The Effects of Differential Diffusion in Counter-flow Premixed Flames with Dilution and Hydrogen Enrichment

Ehsan Abbasi-Atibeh

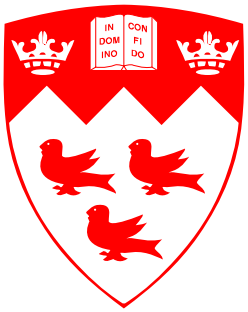

Department of Mechanical Engineering

McGill University

Montreal, QC, Canada

April 2019

A thesis submitted to McGill University in partial fulfillment of the requirements of the degree of Doctor of Philosophy

© 2019 Ehsan Abbasi-Atibeh

Abstract

The continued combustion of fossil fuels to fulfill global energy demand is being questioned because of the well-known problem of greenhouse-gas (GHG) emissions, which introduces new carbon, in the form of carbon dioxide (CO_2), into the environment causing climate change. However, the inherent advantages of combustion-based engines, e.g., energy and power densities, make it hard for other power systems to compete; hence, a leading strategy is to avoid burning fossil fuels by using alternative renewable fuels, such as hydrogen and renewable biofuels. Adaptability with alternative renewable fuels that have variable compositions is referred to as *fuel flexibility*, which is an important parameter of next-generation combustor design. However, fuel flexibility significantly affects combustor operability properties, such as blowout, flashback, and dynamic stability, mainly due to variations in turbulent burning rates. Changing the fuel and oxidizing-gas mixture composition affects flame characteristics and burning rates through changing: (1) mixture reactivity, which is represented by unstretched laminar flame speed, and (2) mixture diffusivity, i.e., the diffusivity of the deficient reactant and diffusivity of heat. The disparity between thermal and mass diffusivities at the flame front is known as "differential diffusion", which causes stretch sensitivity, and thermal-diffusive instabilities, in flame-front propagation, and is represented by Lewis number, a ratio of thermal-to-mass diffusivities.

This thesis investigates the effects of differential diffusion and stretch sensitivity on propagation, stabilization, and structure of lean turbulent premixed flames in the thin reaction zone regime. In the context of fuel flexibility, various fuels and oxidizer-inert mixtures are used to form mixtures with distinct effective Lewis numbers, through changing both fuel diffusivity and thermal diffusivity of the mixture. In these experiments, unstretched laminar flame speed is kept constant during mixture dilution, and hydrogen enrichment of hydrocarbon flames, through changing the mixture equivalence ratio, in order to minimize the effects of chemistry. Furthermore, bulk-flow properties and the temperature boundary condition are kept constant; hence, the study highlights the effects of differential diffusion. Highly strained laminar flame measurements are also reported as a reference for comparison. The experiments are carried out using strained counter-flow flames, in order to study the effects of both components of the flame stretch, i.e., hydrodynamic strain and curvature. Local instantaneous statistics of various flame parameters within the imaged plane are quantified using high-speed particle image velocimetry (PIV) and Mie scattering flame tomography at various levels of turbulence intensity. Data-processing tools are developed through this study to quantify local instantaneous flame parameters, presented as probability density functions using sufficiently large data sets to ensure statistical accuracy. These statistics include flame location, flame velocity, and flame-front topology, such as flame stretch, flame-front curvature, and flame surface area.

The statistics of various parameters of turbulent flames with distinct effective Lewis number show that the effects of differential diffusion on the burning rates and the structure of turbulent premixed flames are important in highly turbulent flames in the thin reaction zone of combustion, where turbulent heat and mass transport are enhanced, and turbulence does not mask the effects of differential diffusion in this regime. These effects are not linear; most results remain almost constant in mixtures with effective Lewis number larger than unity and increase significantly in thermo-diffusively unstable mixtures with effective Lewis number smaller than 0.75. Furthermore, the results for various flame-parameter statistics, which are measured over a wide range of Lewis numbers, are not dependent on the fuel or oxidizing-gas mixture and can be described fully by the effective Lewis number and turbulence intensity. In addition, it was shown that, at constant turbulence intensities, differential diffusion leads to increasing flame surface area, and that, differential diffusion increases the burning rate of turbulent flames in thermo-diffusively unstable mixtures through two main mechanisms: (1) increasing the local flamelet displacement velocity, and (2) increasing the flame surface area. The proportion of different mechanisms of differential diffusion effects on the burning rate of premixed flames is also discussed based on instantaneous local measurements.

This thesis shows the need to advance the combustion theory to produce models that can capture the effects of differential diffusion for flames in real-world combustion systems, in order to predict the performance of future fuel-flexible combustors. The experimental results of this thesis provide a valuable dataset for the validation of such theories.

Résumé

L'effet de la combustion des carburants fossiles, nécessaire afin de suffire à la demande mondiale d'énergie, sur le réchauffement planétaire est bien connu. En brûlant, ces derniers émettent du dioxyde de carbone (CO_2), dans l'atmosphère ce qui entraîne l'effet de serre. Toutefois, ses nombreux avantages, notamment la densité énergétique, font de la combustion un mode de conversion d'énergie difficilement remplaçable. Une solution alternative aux ressources fossiles est l'utilisation de carburants sans carbone, comme l'hydrogène et les biocarburants renouvelables. Dans ce contexte, la capacité des systèmes de combustion de prochaine génération à s'adapter à ces différents carburants, dont la composition peut varier de façon importante, est cruciale. Plus particulièrement, le changement de la célérité de flamme turbulente en fonction du carburant peut causer des problèmes d'opération comme l'extinction, le retour de flamme, ainsi que des instabilités de combustion. La composition du mélange combustible affecte la célérité de flamme turbulente en modifiant (1) la réactivité, qui correspond à la célérité de flamme laminaire, et (2) la diffusivité de la chaleur et du réactif limitant. La disparité entre les flux de diffusion thermique et massique, connue sous l'appellation de diffusivité différentielle, rend la propagation de la flamme sensible à l'étirement local. La diffusivité différentielle est caractérisée par le nombre adimensionnel de Lewis, qui correspond au ratio des diffusitivés thermique et massique du réactif limitant.

Cette dissertation étudie les effets de la diffusion différentielle et de l'étirement local sur la propagation, la stabilisation, et la structure de flammes prémélangées, pauvres et turbulentes dans le régime de zones minces de réaction. Différents mélanges de carburants, comburant, et gaz inertes sont assemblés pour modifier les diffusivités thermique et massique et, conséquemment, le nombre de Lewis. Durant les expériences où les concentrations de gaz inertes et d'hydrogène sont variées, la richesse du mélange est ajustée afin de maintenir la célérité de flamme laminaire constante, et ainsi minimiser l'impact de la cinétique chimique sur les résultats. De même, les températures des réactants et du plan de stagnation, et les propriétés de l'écoulement sont gardées constantes pour tous les tests. De cette façon, la présente étude met en lumière les effets de la diffusion différentielle sur la combustion turbulente. Les expériences sont exécutées avec un brûleur à jets à contre-courant, ce qui permet d'étudier les effets des deux composantes de l'étirement de la flamme, soit la contrainte hydrodynamique et la courbure. La vélocimétrie par imagerie de particules haute fréquence ainsi que la tomographie par diffusion de Mie sont employées pour mesurer différentes propriétés de flamme pour une multitude d'intensités de turbulence. Des méthodes d'analyse de données développées dans le cadre de la présente étude permettent d'en extraire les valeurs locales instantanées, qui sont ensuite présentées sous forme de densités de probabilité incluant un ensemble de données suffisamment grand pour garantir la justesse statistique. Des

densités de probabilité sont fournies pour la position de flamme, sa célérité, ainsi que sa topologie, notamment l'étirement, la courbure et la densité de son front. Pour fin de comparaison, des mesures de célérité sont aussi fournies pour des flammes laminaires hautement étirées.

Les résultats expérimentaux démontrent que les effets de la diffusion différentielle sont importants pour les flammes hautement turbulentes dans le régime de zones minces de réaction, et que la turbulence n'y masque pas l'impact de la diffusion différentielle. Les statistiques extraites des résultats bruts sur une plage de nombres de Lewis plus grande qu'observée communément dans les systèmes de combustion ne dépendent pas du type de carburant ou de comburant. Elles sont plutôt complètement déterminées par le nombre de Lewis et l'intensité de turbulence. De plus, il est démontré que la diffusion différentielle entraîne un accroissement de la densité de la surface de la flamme pour une intensité de turbulence constante. Aussi, la diffusion différentielle accentue la vitesse de combustion des flammes turbulentes dans des mélanges thermo-diffusivement instables de deux façons: (1) en augmentant la célérité locale, et (2) en accroissant la densité de la surface de la flamme. Leur contribution respective est examinée en se basant sur les mesures locales instantanées.

Les résultats expérimentaux présentés dans cette dissertation pourront servir à vérifier la capacité des modèles de combustion turbulente, incluant les effets de la diffusion différentielle, à prédire la propagation des flammes turbulentes dans les simulations de mécanique des fluides numérique.

Acknowledgements

My work leading to the completion of this dissertation would have been insignificant without the intellectual efforts and moral support of my supervisor. I gratefully acknowledge the contributions, inspiration, and guidance provided by my supervisor, Prof. Jeffrey M. Bergthorson, who always supported me throughout this study. I admire his intelligence and dedication at work, and I am fortunate to have worked with him.

I would also like to thank Dr. Gilles Bourque for his guidance for the work in this thesis. Past and current colleagues of the Alternative Fuels Laboratory (AFL), who contributed their time and ideas, deserve a special thanks. I particularly acknowledge the assistance and constructive feedback of Philippe Versailles, Sean D. Salusbury, and Sandeep Jella in performing the experiments and simulations.

I am indebted to my parents and brothers: Hassan, Sousan, Peyman, and Erfan, and my friend, Mohsen, for their constant support and encouragement.

Finally, this thesis is dedicated to my wife, Aysan, for her unconditional love and support, and to my son, Mehrsam, who was just born as I completed this phase of my education.

In the end, I would like to acknowledge the financial support from the Natural Sciences and Engineering Research Council of Canada (grant no. I242349C0G) and Siemens Canada Limited under the Collaborative Research and Development program (NSERC-CRD). Support of the McGill Engineering Doctoral Awards (MEDA) program is also gratefully acknowledged.

Contribution of author

This thesis is presented as a *manuscript-based thesis* consisting of three papers. All the papers are co-authored by Professor Jeffrey M. Bergthorson, who provided research guidance and editorial review in his capacity as a research supervisor. The author has been the lead experimentalist in turbulent premixed combustion and fuel flexibility research of the Alternative Fuels Laboratory (AFL), at McGill University, in collaboration with Siemens Canada Limited through an NSERC Collaborative Research and Development (CRD) project. The full bibliographic information of manuscripts is as follows:

Publication [1]: E. Abbasi-Atibeh, S. Jella, and J. M. Bergthorson. "Fuel variation effects in propagation and stabilization of turbulent counter-flow premixed flames". In: *Journal of Engineering for Gas Turbines and Power* 141 (2018), pp. 031024. http://dx.doi.org/10.1115/1.4041136.

Publication [2]: E. Abbasi-Atibeh and J. M. Bergthorson. "Differential diffusion effects in counter-flow premixed hydrogen-enriched methane and propane flames". In: *Proceedings of the Combustion Institute* 37 (2019), pp. 2399−2406. https://doi.org/10.1016/j.proci.2018.08.006.

Publication [3]: E. Abbasi-Atibeh and J. M. Bergthorson. "The effects of differential diffusion in counter-flow premixed flames with dilution and hydrogen enrichment". Submitted to *Combustion and Flame* (2019).

The hot-exhaust opposed-flow turbulent flame rig (HOTFR), used in this study [1-3], consists of two main sections, in an axial opposed-flow configuration: (1) the fresh reactants nozzle assembly placed at the bottom, and (2) the hot-product ceramic burner at the top. Various components of the bottom nozzle assembly in HOTFR are modified versions of the components previously designed by the AFL, which were re-designed and optimized by the candidate, and were built through this study. The hot-product ceramic burner was initially designed and manufactured by the candidate through this thesis, and due to its superior capabilities, a similar burner is under construction for application in the Metal Fuels Laboratory, at McGill University.

Two turbulence-generating plates are used in these experiments, the multi-circular turbulence-generating plate (MCJ-TGP) with five jets [1] and the star-shaped plate (S-TGP) [2-3]. The former was previously designed and built at the AFL while the latter was designed by the candidate. The temperature measurement setup was also designed and built by the candidate to measure the temperature of hot exhaust gases at the ceramic nozzle exit using multiple R-type thermocouples with different wire (bead) diameters.

The laser-based diagnostic setup, i.e., high-speed particle image velocimetry (2D-PIV) and Mie scattering flame tomography using oil droplet seeding, as well as data-processing tools for analyzing the experimental data, were developed by the author.

The first paper [1] is co-authored by Sandeep Jella (Siemens Canada Limited, and Ph.D. candidate, Department of Mechanical Engineering, McGill University) recognizing his contribution in computational fluid dynamics (CFD) simulations, and writing the related sections in this paper [1].

The code used for calculation of spatial calibration coefficient, in order to quantify the PIV flow velocity field, was developed by Dr. Philippe Versailles (Siemens Canada Limited, and a former colleague at the AFL laboratory, Department of Mechanical Engineering, McGill University), and provided to the author.

Beyond the noted contributions, the whole work presented in this dissertation, including all the experiments, data processing, and analysis, was completed and written by the author.

Contents

Abstract i

Résumé iii

Acknowledgements v

Contribution of author vi

1 Introduction and background 1
- 1.1 Fuel-flexible ultra-low-emission combustors . . . 1
- 1.2 Turbulent flow and premixed combustion . . . 3
  - 1.2.1 Turbulent flow . . . 3
  - 1.2.2 Laminar premixed flames . . . 5
  - 1.2.3 Turbulent premixed combustion . . . 6
- 1.3 Lewis number, stretch sensitivity, and differential diffusion in premixed flames . . . 8
  - 1.3.1 Lewis number . . . 8
  - 1.3.2 Stretch sensitivity and differential diffusion in premixed flames . . . 10
- 1.4 Burning rate of turbulent premixed flames . . . 11
  - 1.4.1 Damköhler's hypothesis and the theory of leading points . . . 11
  - 1.4.2 Various definitions of turbulent flame velocity . . . 13
- 1.5 Flame-front cellular instabilities . . . 16
- 1.6 Thesis objectives and overview . . . 17

References . . . 21

2 Methodology 29
- 2.1 Hot-exhaust opposed-flow turbulent flame rig . . . 29
- 2.2 Mixture properties and experimental conditions . . . 33
- 2.3 Diagnostic method and processing techniques . . . 34
  - 2.3.1 Particle image velocimetry . . . 34
  - 2.3.2 Processing techniques . . . 38
    - 2.3.2.1 Mie scattering flame tomography . . . 38
    - 2.3.2.2 Local instantaneous velocity measurements . . . 41
    - 2.3.2.3 Local instantaneous hydrodynamic strain rate measurements . . . 43

References . . . 46

3 Fuel variation effects in propagation and stabilization of turbulent counter-flow premixed flames **49**
3.1 Abstract . . . 49
3.2 Introduction . . . 50
3.3 Experimental method . . . 52
3.3.1 Turbulent counter-flow burner . . . 52
3.3.2 Particle image velocimetry and processing techniques . . . 56
3.3.3 Computational model description and setup . . . 58
3.4 Results and discussion . . . 62
3.4.1 Results and discussion - experiments . . . 62
3.4.2 Results and discussion - computations . . . 65
3.5 Conclusions . . . 68
References . . . 70

Link between chapters 3 and 4 **74**

4 Differential diffusion effects in counter-flow premixed hydrogen-enriched methane and propane flames **75**
4.1 Abstract . . . 75
4.2 Introduction . . . 76
4.3 Experimental method . . . 77
4.3.1 Hot-exhaust opposed-flow turbulent flame rig . . . 78
4.3.2 Diagnostic method and processing techniques . . . 80
4.3.2.1 Particle image velocimetry . . . 80
4.3.2.2 Processing techniques . . . 81
4.4 Results and discussion . . . 84
4.5 Conclusions . . . 88
References . . . 90

Link between chapters 4 and 5 **94**

5 The effects of differential diffusion in counter-flow premixed flames with dilution and hydrogen enrichment **95**
5.1 Abstract . . . 95
5.2 Introduction . . . 96
5.3 Experimental method . . . 99
5.3.1 Hot-exhaust opposed-flow turbulent flame rig . . . 101
5.3.2 Diagnostic method and processing techniques . . . 104
5.3.2.1 Particle image velocimetry . . . 104
5.3.2.2 Processing techniques . . . 107
5.4 Results and discussion . . . 109
5.4.1 Flame-front location . . . 109
5.4.2 Local flamelet displacement velocity . . . 112
5.4.3 Turbulent flame structure . . . 114

5.4.3.1 Flame-front curvature . . . 116
5.4.3.2 Flame-surface area . . . 116
5.4.4 Flame-front stretch . . . 118
5.4.5 Turbulent burning rate . . . 120
5.4.6 Discussion − The effects of differential diffusion on turbulent burning rates 122
5.5 Conclusions . . . 124
References . . . 126

6 Conclusions **135**
6.1 Summary of results . . . 135
6.2 Contributions . . . 138
6.3 Future research directions . . . 139

A The design details of HOTFR **142**
A.1 Top burner design details . . . 142
A.2 Turbulence-generating plates design details . . . 146
A.3 Bottom nozzle design details . . . 146

B Temperature measurement of the hot exhaust gases at the ceramic burner exit **155**

C Uncertainty in particle image velocimetry (PIV) **158**

D Uncertainty in flame-front tracking **164**

E The effects of deviations from adiabatic conditions at the stagnation surface on flame speed **166**

References **169**

List of Figures

1.1 Borghi diagram showing turbulent premixed combustion regimes and estimated experimental regions of each chapter . . . 7
1.2 Schematic of flame stretch theory showing positively stretched flamelets for fuel and oxidizer mixtures at $\mathrm{Le} \ll 1$, $\mathrm{Le} \approx 1$, and $\mathrm{Le} > 1$ . . . 11
1.3 Schematic showing the effects of turbulence on the flame propagation . . . 12
1.4 Turbulent flame velocity correlations with increasing turbulence level . . . 14

2.1 Schematic of HOTFR and sample laminar and turbulent CH_4-air flames at $\phi = 0.8$ 30
2.2 Designs of turbulence-generating plates . . . 31
2.3 Schematic of the PIV setup . . . 35
2.4 Processing techniques: a sample PIV image indicating the test domain, an example flame front, and PIV velocity vectors . . . 36
2.5 PIV calibration target . . . 38
2.6 Sample PIV velocity profiles for premixed laminar and turbulent CH_4-air flames . . 39
2.7 Processing techniques: a portion of a sample PIV image near the flame front illustrating measurements of convective velocity upstream of the flame front and axial hydrodynamic strain rate . . . 42
2.8 Processing techniques: 5 successive flame fronts and a schematic showing flame-front velocity (S_F) calculation . . . 44

3.1 Schematic of the hot exhaust opposed-flow turbulent flame rig (HOTFR), and stabilized CH_4-air turbulent flames at increasing turbulence intensities . . . 52
3.2 Processing techniques using PIV images showing a sample velocity vector field, a sample flame-front contour, and schematics showing S_u and S_F meaurements . . . 55
3.3 Borghi diagram showing premixed turbulent combustion regimes and experimental regions . . . 57
3.4 Lewis number influence on laminar and turbulent methane flames showing SDR and reaction rates . . . 59
3.5 Lewis number influence on temperature and species of CH_4 and H_2 laminar flames 60
3.6 Lewis number influence on heat release of laminar H_2 flames . . . 60
3.7 CFD model of the turbulent jet, lifted flame front, and temperature contours . . . 61
3.8 PDFs of instantaneous leading edge displacement velocity and flame position . . . 62
3.9 Most probable flame location and flame brush thickness correlations at increasing $u'/S_\mathrm{L}^\mathrm{o}$ . . . 64

3.10 Effect of strain and turbulence intensity on temperature profiles 66
3.11 Effect of strain on laminar chemical source of progress variable 66
3.12 Turbulent flame location and brush thickness 67

4.1 Schematic of HOTFR and S-TGP 79
4.2 Mean and rms velocities at the nozzle exit in the radial direction generated using S-TGP 81
4.3 Processing techniques showing a sample PIV image, a quantized PIV image with an example flame front, and schematics showing S_{u} and S_{F} meaurements 82
4.4 PDFs of Z_{f}, $\langle Z_{\mathrm{f}} \rangle$ correlations, and flame thickness for CH_4-H_2-air and C_3H_8-H_2-air flames at increasing H_2-enrichment 85
4.5 PDFs of S_{T}, and $\langle S_{\mathrm{T}} \rangle$ and $S_{\mathrm{u-ref}}$ correlations for CH_4-H_2-air and C_3H_8-H_2-air flames at increasing H_2-enrichment 86
4.6 Components of flame stretch, $\langle K_{\mathrm{s}} \rangle$ and $\langle \kappa \rangle$ correlations, for CH_4-H_2-air and C_3H_8-H_2-air flames at increasing H_2-enrichment 88

5.1 Schematic of HOTFR showing S-TGP locations in the inner plenum 102
5.2 Processing techniques showing a sample PIV image and velocity vectors, an example flame front, and schematics showing velocity meaurements 104
5.3 Mean and rms velocities in the radial direction generated using S-TGP 106
5.4 PDFs of flame location at various $\mathrm{Le}_{\mathrm{eff}}$, and the correlations of the mean flame location against $\mathrm{Le}_{\mathrm{eff}}$, at two levels of turbulence intensity 111
5.5 Laminar and turbulent flame thichness at various $\mathrm{Le}_{\mathrm{eff}}$ 112
5.6 PDFs of S_{T} at various $\mathrm{Le}_{\mathrm{eff}}$, and the correlations of $\langle S_{\mathrm{T}} \rangle$ and $S_{\mathrm{u-ref}}$ against $\mathrm{Le}_{\mathrm{eff}}$, at two levels of turbulence intensity 113
5.7 Mie scattering images and extracted flame fronts at distinct $\mathrm{Le}_{\mathrm{eff}}$ at two levels of turbulence intensity 115
5.8 Flame-front curvature correlations against $\mathrm{Le}_{\mathrm{eff}}$ at two levels of turbulence intensity 117
5.9 Correlations of $\langle \Sigma \rangle$ against $\mathrm{Le}_{\mathrm{eff}}$, and $\langle |\kappa| \rangle$, at two levels of turbulence intensity . . 118
5.10 Components of flame stretch, and their correlatons against $\mathrm{Le}_{\mathrm{eff}}$, at two levels of turbulence intensity 119
5.11 Correlaions of $S_{\mathrm{T-LC}}$ against $\mathrm{Le}_{\mathrm{eff}}$, and the relative contribution of the parameters of $S_{\mathrm{T-LC}}$, at two levels of turbulence intensity 121

A.1 Design drawing of the stainless steel jacket holding the ceramic burner 143
A.2 Design drawing of the wax-negative used to make the casting mold of the ceramic nozzle 144
A.3 Design drawing of the base plate of the ceramic burner 145
A.4 Design drawing of the star-shaped turbulence-generating plate 147
A.5 Various components of the bottom nozzle assembly 148
A.6 Design drawing of the inner nozzle for premixed fuel and oxidizing-gas mixture . . 149
A.7 Design drawing of the co-flow nozzle 150
A.8 Design drawing of the inner plenum for premixed fuel and oxidizing-gas mixture . 151
A.9 Design drawing of the co-flow plenum 152

A.10 Design drawing of the diffuser 153
A.11 Design drawing of the bottom nozzle base plate 154

B.1 Temperature profiles at the ceramic burner exit 157

C.1 Sample uncertainty calculations, caused by the correlation statistics in the PIV software 163

E.1 The effects of deviations from adiabatic stagnation surface on $S_{\mathrm{u-ref}}$ measurements 168

List of Tables

3.1 Properties of the laminar flames 53
3.2 Experimental conditions of turbulent C_3H_8-air, CH_4-air flames, and H_2-air flames . 54

4.1 Properties of CH_4+H_2+air and C_3H_8+H_2+air mixtures at constant $S_L^o = 0.195$ m/s . 78
4.2 Experimental conditions of turbulent CH_4+H_2+air and C_3H_8+H_2+air flames 80

5.1 Mixture properties and experimental conditions at $S_L^o = 0.115$ m/s 100

C.1 Uncertainty details, caused by particle inertia, for PIV measurements in Chapter 3 . 160
C.2 Uncertainty details, caused by particle inertia, for PIV measurements in Chapter 5 . 161

D.1 Various sources of uncertainty in flame-front tracking 165

Nomenclature

a	Acceleration	m^2/s
A	Surface area	m^2
A_L	Laminar flame surface area	m^2
A_T	Turbulent flame surface area	m^2
c	Temperature progress variable	
$\overline{c}$	Mean temperature progress variable	
$\widetilde{c}$	Mean reaction progress variable	
$\widetilde{c''^2}$	Mean reaction progress variable variance	
c_p	Specific heat	$\mathrm{kJ}/(\mathrm{kg}\cdot\mathrm{K})$
C	PIV spatial calibration coefficient	$\mathrm{pixel}/\mathrm{mm}$
C_KW	Knudsen-Weber slip-correction factor	
d	Diameter	mm
$\mathcal{D}$	Diffusivity of the deficient reactant	m^2/s
Da_T	Turbulent Damköhler number	
E	Oil droplet evaporation constant	
F	Force	N
h	TGP distance from the nozzle exit	mm
h_fg	Specific enthalpy of vaporization	kJ/kg
I_F	Imaging speed	$\mathrm{frame}\cdot\mathrm{s}^{-1}$
I_o	Local stretch factor	s^{-1}
I_W	The smallest PIV interrogation window size	pixel
k	Normal direction to the $r-z$ plane	
K	Stretch rate	s^{-1}
$\langle K\rangle$	Mean flame stretch rate	s^{-1}
K_s	Hydrodynamic strain rate	s^{-1}
$K_\mathrm{s-a}$	Local axial hydrodynamic strain rate	s^{-1}
$\langle K_\mathrm{s-a}\rangle$	Mean axial hydrodynamic strain rate	s^{-1}
$K_\mathrm{s-t}$	Local tangential hydrodynamic strain rate	s^{-1}
$\langle K_\mathrm{s-t}\rangle$	Mean tangential hydrodynamic strain rate	s^{-1}
Ka_T	Turbulent Karlovitz number	

l_{evap}	Uncertainty in the flame-front tracking imposed by the droplet evaporation time	mm
l_{Filt}	Uncertainty in the flame-front tracking imposed by the filtering process during post-processing	mm
l_{I}	Uncertainty in the flame-front tracking imposed by over-saturation	mm
l_{p}	Mean tracer particle distance in the test domain	mm
l_{Total}	Total uncertainty in the flame-front tracking	mm
L	Integral length scale	mm
Le	Lewis number	
$\mathrm{Le}_{\mathrm{eff}}$	Effective Lewis number	
m	Mass	kg
$\dot{m}_{\mathrm{r}}$	Total mass flow rate of reactants	$\mathrm{kg/s}$
M	Molecular weight	$\mathrm{kg/kmol}$
n	Normal direction to the flame surface	
Nu	Nusselt number	
Prtl	Prandtl number	
q	Numerical constant	
$\dot{Q}$	Heat release	$\mathrm{GW/m^3}$
r	Radial coordinate	
R	Radius	mm
Re_{E}	Engineering Reynolds number	
Re_{T}	Turbulent Reynolds number	
$R_{\mathrm{uu}}(r)$	Transverse autocorrelation coefficient in the radial direction	
$R_{\mathrm{uu}}(z)$	Longitudinal autocorrelation coefficient in the axial direction	
$R_{\mathrm{vv}}(r)$	Longitudinal autocorrelation coefficient in the radial direction	
$R_{\mathrm{vv}}(z)$	Transverse autocorrelation coefficient in the axial direction	
S	Flame velocity	$\mathrm{m/s}$
S_{F}	Local flamelet velocity in the flow coordinate system	$\mathrm{m/s}$
$S_{\mathrm{L}}^{\mathrm{o}}$	Unstretched laminar flame velocity	$\mathrm{m/s}$
S_{u}	Convective velocity of the flow upstream of the flame front	$\mathrm{m/s}$
$S_{\mathrm{u-ref}}$	Stretched laminar flame speed	$\mathrm{m/s}$
S_{T}	Local flamelet displacement velocity	$\mathrm{m/s}$
$\langle S_{\mathrm{T}} \rangle$	Mean local flamelet displacement velocity	$\mathrm{m/s}$
$S_{\mathrm{T-GC}}$	Global consumption velocity	$\mathrm{m/s}$

$S_{\mathrm{T-LC}}$	Turbulent burning rate, or turbulent local consumption velocity	$\mathrm{m/s}$
$\langle S_{\mathrm{T-LC}} \rangle$	Mean turbulent burning rate	$\mathrm{m/s}$
t	Time	s
T	Temperature	K
T_{ad}	Adiabatic flame temperature	K
T_{CB}	Temperature of the hot exhaust gases at the nozzle exit	K
T_{s}	Flash-point temperature of the seeding oil	K
T_{TC}	Thermocouple reading temperature	K
u	Instantaneous velocity fluctuation in the axial direction	$\mathrm{m/s}$
u'	Root-mean-square of the velocity fluctuation in the axial direction	$\mathrm{m/s}$
$u'/\overline{U}$	Turbulence intensity in the axial direction	
u_{g}	Unburned gas velocity	$\mathrm{m/s}$
u_{P}	Tracer particle velocity	$\mathrm{m/s}$
U	Instantaneous flow velocity in the axial direction	$\mathrm{m/s}$
$\overline{U}$	Mean flow velocity in the axial direction	$\mathrm{m/s}$
U_{CB}	Exhaust gas velocity at the exit of the ceramic burner	$\mathrm{m/s}$
U_{NE}	Bulk-flow velocity at the nozzle exit centerline	$\mathrm{m/s}$
v	Instantaneous velocity fluctuation in the radial direction	$\mathrm{m/s}$
v'	Root-mean-square of the velocity fluctuation in the radial direction	$\mathrm{m/s}$
V	Instantaneous flow velocity in the radial direction	$\mathrm{m/s}$
$\overline{V}$	Mean flow velocity in the radial direction	$\mathrm{m/s}$
w	Instantaneous velocity fluctuation in the normal direction to the $r-z$ plane	$\mathrm{cm/s}$
w'	Root-mean-square of the velocity fluctuation in the normal direction to the $r-z$ plane	$\mathrm{m/s}$
W	Instantaneous flow velocity in the normal direction to the $r-z$ plane	$\mathrm{m/s}$
$\overline{W}$	Mean flow velocity in the normal direction to the $r-z$ plane	$\mathrm{m/s}$
X	Mole fraction	
Y	Mass fraction	
z	Axial coordinate	
Z_{f}	Local flame-front location within the imaged plane	mm
$\langle Z_{\mathrm{f}} \rangle$	Mean flame-front location	mm

Z_{SP}	Local stagnation-plane location within the imaged plane	mm
$\langle Z_{\mathrm{SP}} \rangle$	Mean stagnation-plane location	mm
α	Thermal diffusivity	m^2/s
β	The angle between the flame-surface normal and its projection	sr
γ	Thermocouple temperature correction coefficient	
δ_{L}	Diffusive flame thickness	mm
δ_{T}	Turbulent flame brush thickness	mm
ϵ	Energy dissipation rate per unit mass	$\mathrm{m}^2/\mathrm{s}^3$
η	Kolmogorov length scale	mm
κ	Flame-front curvature	m^{-1}
$\langle \kappa \rangle$	Mean flame-front curvature	m^{-1}
$\langle \lvert\kappa\rvert \rangle$	Mean absolute flame-front curvature	m^{-1}
λ	Thermal conductivity	$\mathrm{W}/(\mathrm{m} \cdot \mathrm{K})$
μ	Dynamic viscosity	$\mathrm{kg}/(\mathrm{m} \cdot \mathrm{s})$
ν	Kinematic viscosity	m^2/s
ρ	Density	kg/m^3
σ	Standard deviation of the flame-location PDFs	
σ_{u}	Fluid velocity gradient	s^{-1}
Σ	The increase in FSA of turbulent flames compared to that of a laminar flame: $\Sigma = A_{\mathrm{T}}/A_{\mathrm{L}}$	
$\langle \Sigma \rangle$	Mean Σ	
τ_{c}	Timescale of the chemical reaction	ms
τ_{evap}	Oil droplet lifetime at the flame front, or droplet evaporation time	ms
τ_{F}	Timescale of the turbulent transport	ms
τ_{s}	Relaxation time, or stokes time	ms
τ_η	Kolmogorov time scale	ms
ϕ	Equivalence ratio	
$\dot{\omega}_c$	Chemical source term	s^{-1}

Subscripts

b	Burned
h	Hole
i	Instantaneous
ig	Ignition
N	Nozzle
P	Particle
SD	Stokes drag
SP	Stagnation plane
TC	Thermocouple
TP	Thermophoresis
u	Unburned

Acronyms

1D	One-dimensional
2D	Two-dimensional
3D	Three-dimensional
AFL	The Alternative Fuels Laboratory
CFD	Computational fluid dynamics
CMOS	Complementary metal-oxide-semiconductor
DNS	Direct numerical simulation
EGR	Exhaust gas recirculation
FGM	Flamelet-generated manifolds
FPV	Flamelet progress variable
FSA	Flame surface area
GHG	Greenhouse gas
GTE	Gas-turbine engines
HOTFR	The hot-exhaust opposed-flow turbulent flame rig
IC	Internal combustion
LES	Large-eddy simulation
MCJ	Multi-circular jet
MFC	Mass flow controller
NCJ	Non-circular jet
Nd:YLF	Neodymium-doped yttrium lithium fluoride

PDF	Probability density function
PIV	Particle image velocimetry
PLIF	Planar laser-induced fluorescence imaging
RANS	Reynolds-averaged Navier–Stokes
rms	Root-mean-square
RSM	Reynolds stress transport model
SDR	Scalar dissipation rate
S-TGP	Star-shaped turbulence-generating plate
TGP	Turbulence-generating plate

For my true love, Aysan

Chapter 1

Introduction and background

1.1 Fuel-flexible ultra-low-emission combustors

The annual per capita demand for energy is expected to peak by 2030, but the world's underlying population growth has energy demand increasing by 48 % and 30 % by 2040 compared to 2012 [1] and 2016 [2], respectively. The trend towards electrification for energy distribution and utilization is expected to continue, though combustion of fossil fuels, as the primary energy source, will represent more than 80 % of that total [2]. The challenges facing combustion of fossil fuels are well known in terms of greenhouse-gas (GHG) emissions and pollutants, such as nitric oxides (NO_x), carbon monoxide (CO), unburned hydrocarbons, and soot. Consumption of fossil fuels needs to be reduced as it introduces new carbon, in the form of CO_2, into the environment causing climate change.

The global energy demand can be supplied by a variety of renewable energy sources, such as solar, water, wind, and geothermal, using numerous available technologies that can produce carbon-free energy in sufficient quantities [3]. However, many of these renewable sources are intermittent, which implies a need for storage and redistribution of energy to fulfill real-time energy demand in any location [4]. Currently, the efficient storage of renewable energy in energy carriers, that have sufficiently high energy and power densities, are easy to transport, and are convenient for a wide variety of applications, remains a challenge [4, 5].

End users in specific application areas, e.g., transportation, face challenges in transitioning away from combustion. Technologies such as batteries are advancing toward functional and cost parity with the combustion-based engines, but the inherent advantages of fuels for combustion, e.g., energy and power densities, make it hard for other power systems to compete. A leading strategy is to avoid burning fossil fuels by using renewable fuels from various resources, that are produced through conversion of renewable energy into chemical energy, that can be restored through combustion of the energy carriers. Examples of these energy carriers are hydrogen, H_2, and synthesized

biofuels, such as biogas (methane (CH_4), diluted in CO_2), syngas (CO and H_2 diluted in CO_2 and nitrogen, N_2), and alcohols [6]. These biofuels can be produced from biomass, which is grown by conversion of solar energy through photosynthesis [7], or direct application of solar energy to produce H_2 and CO through splitting water and CO_2, producing H_2 from thermal decomposition of fossil fuels, as well as other synthesized hydrocarbons [8]. Furthermore, renewable energy sources can be used to recycle metal oxides into metals as energy carriers, that can be used in the Wet Cycle (the reaction with water as an intermediate stage to produce hot H_2 and steam), or in the Dry Cycle (direct combustion with air) [5].

Combustion of alternative renewable fuels that have variable fuel-oxidizer-inert compositions, such as low-carbon fuels, biogas, syngas, and hydrogen, is being adopted through increasing the proportion of these fuels in the fuel market and increased customer demand for operability with these fuels. Specifically, increasing H_2 production from alternative and renewable sources, such as biomass, from coal conversion processes, or metal-water reaction, has generated interest in H_2 as a clean alternative for fossil fuels. On the other hand, dilution is an important parameter of low-emission combustors, in order to reduce the temperature and NO_x emission, which significantly changes thermo-diffusive properties of the combustible mixture. Dilution is used in mild combustion, staged combustion, and exhaust gas recirculation (EGR). In combustion systems using EGR, the exhaust gases are recycled back into the engine to preheat and dilute the reactants.

Adaptability with fuel mixtures that have variable fuel-oxidizer-inert compositions is referred to as *fuel flexibility*, which is an important parameter of next-generation combustor design and is currently at the forefront of energy research. Fuel flexibility will, ultimately, result in designing higher-performance fuel-flexible combustors, and lowered costs of energy production to fulfill global energy demand while reducing emissions and the carbon footprint of various energy technologies; hence, mitigating the global climate change. In addition, regional energy security, accessibility, and equity are key concerns that have made fuel flexibility an important feature of newly designed combustors.

On the other hand, in combustors running on lean premixed combustion, the fuel-air mixture is precisely controlled, and lower combustion temperature of lean mixtures along with better mixing reduces pollutants, such as NO_x and soot. Therefore, next-generation ultra-low-emission combustors running on lean premixed combustion of alternative fuels from renewable resources, which take advantage of high-efficiency conversion technologies and improved performance, is a promising approach to fulfill global energy demand with tremendous potential for applications in ground and sea transportation, industrial furnaces, aviation, and power generation.

However, building fuel flexibility into a product entails significant operability and emission challenges. Current designs for ultra-low-emission combustors do not generally allow for broad

fuel flexibility, due primarily to an insufficient understanding regarding the effects of unconventional fuel compositions on combustor operability properties, such as blowout, flashback, and dynamic stability, mainly due to variations in turbulent burning rates. This manifests both as difficulties in heuristically designing fuel-flexible combustors and inaccuracy/unreliability in numerical techniques for simulating combustor behavior using computational fluid dynamic (CFD) simulations of turbulent reacting flows.

1.2 Turbulent flow and premixed combustion

1.2.1 Turbulent flow

Laminar and turbulent flows are characterized by Reynolds number (Re), which quantifies the relative importance of the inertial and viscous forces in different flow conditions. Turbulence is characterized by high levels of fluctuating velocity and vorticity at high Re, where convective forces are larger than viscous forces, which increases the tendency to instability. Instabilities create larger eddies in the flow, which break down to smaller eddies, and ultimately, the smallest eddies lose their kinetic energy by viscous shear stresses, where turbulent kinetic energy is converted into heat [9, 10].

The fluid dynamics of turbulent flow are characterized by several length and time scales induced by the size of eddies in the turbulent flow. Most of the energy and momentum in a turbulent flow is transported by the largest eddies in the flow, referred to as integral length scale (L), which is constrained by the physical geometry of the system. Integral length scale is typically on the order of the characteristic length of the apparatus.

In turbulent flows, the integral length scale is estimated as the longest correlation between velocity fluctuations at two points of the flow at two different spatial locations. In two-dimensional (2D) flow, longitudinal (when fluctuating component of the velocity and r are parallel) autocorrelation coefficient in the radial, r, and the axial, z, directions are $R_{\mathrm{vv}}(r)$ and $R_{\mathrm{uu}}(z)$, respectively, and transverse (when fluctuating component of the velocity and r are perpendicular) autocorrelation coefficient in r and z directions are $R_{\mathrm{uu}}(r)$ and $R_{\mathrm{vv}}(z)$, respectively. The transverse autocorrelation coefficient in the radial direction is defined as [9, 11]:

$$R_{\mathrm{uu}}(r) = \frac{\langle u(z,t)\; u(z+r,t)\rangle}{\left[\langle u(z,t)\rangle^2\; \langle u(z+r,t)\rangle^2\right]^{1/2}} \tag{1.1}$$

where u is the instantaneous velocity fluctuation in the axial direction. In most turbulent flows, L is believed to be comparable to the transverse Eulerian integral scale [9, 11]: $L = \int_0^\infty R_{\mathrm{uu}}(r,t)\ \mathrm{d}r$. It is expected that the degree of correlation will decrease by increasing r, and $R_{\mathrm{uu}}(r) \to 0$ beyond a finite distance, after some fluctuations around zero. Therefore, in experiments, L is estimated by integrating $R_{\mathrm{uu}}(r)$ from a spatial location, r, up to the first zero-crossing as discussed in [9, 11]: $L = \int R_{\mathrm{uu}}(r,t)\ \mathrm{d}r$. A sufficiently large experimental domain is necessary in the calculation of $R_{\mathrm{uu}}(r)$ to obtain the zero-crossing.

Kolmogorov length scale (η) is the smallest hydrodynamic turbulence length scale where viscous energy dissipation occurs, which depends on the energy dissipation rate per unit mass (ϵ) and kinematic viscosity (ν) [9, 10]: $\eta = (\nu^3/\epsilon)^{1/4}$. The energy dissipation rate is the rate of energy supply to the small-scale eddies, and is on the order of $u^2\,(u/L)$, where kinetic energy per unit mass and its transfer rate through the large-scale turbulence are proportional to u^2 and u/L, respectively. An estimation for the ratio of largest to smallest hydrodynamic length scales in a turbulent flow can be derived as [9]: $L/\eta \approx \mathrm{Re_T}^{3/4}$, where $\mathrm{Re_T}$ is the turbulent Reynolds number, and is calculated based on u' (the root-mean-square (rms) of velocity fluctuations in the axial direction): $\mathrm{Re_T} = u'\,L/\nu$. Kolmogorov time scale (τ_η) is also defined for small-scale eddies using ϵ and ν [9, 10]: $\tau_\eta = (\nu/\epsilon)^{1/2}$.

Turbulence intensity in the axial direction is defined as: $u'/\overline{U}$. u is calculated using Reynolds decomposition [9, 10]: $U(r,z,k,t) = \overline{U}(r,z,k) + u(r,z,k,t)$, where U is the instantaneous flow velocity in the axial direction at radial (r), axial (z), and the normal direction to the $r-z$ plane (k) location at time t, and $\overline{U}$ is the mean flow velocity in the axial direction. Accordingly, rms of velocity fluctuations in the radial direction (v') and out-of-plane direction (w') are calculated using V, $\overline{V}$, and v, and W, $\overline{W}$, and w, respectively. Near isotropic turbulence in any spatial location is defined as $u' \approx v' \approx w'$. Turbulent flows are discussed in detail in [9, 11].

Simulating turbulent flow characteristics of practical systems in a laboratory-scale experimental system requires generating a highly turbulent flow in a relatively confined system, and at significantly smaller bulk-flow rates. One possible option to generate high-intensity turbulence in a confined system is to use high-blockage turbulence-generating plates (TGP) upstream of the test section [12–16]. The sudden constriction introduced by the high-blockage plates forces an increase in the jet velocity resulting in high Reynolds numbers, leading to highly turbulent flow in the downstream region. These perforated plates are designed to maximize $\mathrm{Re_T}$ at a given engineering Reynolds number ($\mathrm{Re_E}$), which is based on the bulk velocity and the characteristic length of the apparatus; hence, to deliver the highest possible turbulence intensity while preserving isotropic turbulence and axisymmetric uniformity. Higher turbulence intensity allows laboratory-scale experiments closer to the relevant conditions of practical systems, such as gas-turbine engines (GTE)

and other combustors.

Multiple TGP designs, multi-circular jet (MCJ) and non-circular jet (NCJ), were studied in detail by Coppola and Gomez [12], where they demonstrated that nearly isotropic turbulence statistics and high turbulence intensity are feasible using high-blockage plates. It was illustrated that, in order to induce the largest possible $u'/\overline{U}$ at a given flow rate while preserving radial homogeneity in the velocity profiles, the MCJ plates should be designed to allow high blockage-ratio through a small number of jets. Furthermore, MCJ and NCJ plates should be placed close to the test section, and with minimal jet-wall interactions. Coppola and Gomez [12] illustrated that, overall, the NCJ-TGPs achieved higher $u'/\overline{U}$ and a better radial uniformity with a lower blockage ratio in comparison with MCJ-TGPs.

1.2.2 Laminar premixed flames

A laminar premixed flame is a thin, nearly one-dimensional (1D) surface, which includes the reaction zone, where the chemical energy is released through combustion, hot products are convected downstream of the flame, and heat diffuses upstream toward the incoming unburned mixture, and the preheat zone, where the incoming reactants are heated by heat diffusion. In premixed flames, the reaction zone thickness is usually one-tenth of the preheat zone thickness [17].

The unstretched laminar flame velocity ($S_{\mathrm{L}}^{\mathrm{o}}$) is a fundamental combustion parameter, which was described by the thermal flame theory of Mallard and Le Châtelier [18]:

$$S_{\mathrm{L}}^{\mathrm{o}} = \sqrt{\alpha\,\dot{\omega}\,\frac{T_{\mathrm{b}} - T_{\mathrm{ig}}}{T_{\mathrm{ig}} - T_{\mathrm{u}}}} \tag{1.2}$$

where α is the thermal diffusivity, $\dot{\omega}$ is the reaction rate, and T_{b}, T_{ig}, and T_{u} are the burned-gas temperature, the ignition temperature, and the temperature of unburned reactants, respectively. The unstretched laminar flame speed is the speed of a flat, freely propagating adiabatic laminar flame front through a premixed, quiescent fuel and oxidizing-gas mixture, which is independent of apparatus geometry. Unstretched laminar flame speed is an intrinsic property of a given fuel and oxidizing-gas mixture, and is representative of the complex chemical kinetics and thermal properties of the mixture. Since $S_{\mathrm{L}}^{\mathrm{o}}$ is an ideal phenomenon, its direct measurements in the laboratory environment is challenging, but it can be computed with 1D free-flame simulations using chemical models, e.g., $S_{\mathrm{L}}^{\mathrm{o}}$ can be computed using Cantera [19]. Using $S_{\mathrm{L}}^{\mathrm{o}}$, the diffusive flame thickness (δ_{L}) is defined as: $\delta_{\mathrm{L}} = \lambda/(c_{\mathrm{p}}\,\rho_{\mathrm{u}} S_{\mathrm{L}}^{\mathrm{o}})$, where λ is the thermal conductivity, c_{p} is the specific heat, and ρ_{u} is the density of the unburned reactants.

1.2.3 Turbulent premixed combustion

Combustion occurs in turbulent regime in most industrial applications. Compared to laminar flames, turbulent flames involve complex turbulence-chemistry interactions. Understanding and modeling of such systems is a challenging task due to the unsteady, multi-component, and multi-dimensional nature of these flows.

One technique to extend laminar flame models in order to build models of turbulent combustion is the *flamelet concept*. In flamelet models [20–22], in order to decouple small-scale chemistry from large-scale features in the turbulent flow, it is assumed that the structure of a stretched premixed laminar flame is preserved, and that the turbulent premixed flame front is composed of many locally laminar flames [17], that are just stretched and curved by the turbulent eddies. A laminar flamelet is defined as a portion of the flame front, which has a preheat zone and a reaction zone, where gradients in the normal direction are significantly larger than tangential gradients, and molecular diffusion is significantly larger than mass transport by turbulent eddies within the layer [17].

Turbulent Karlovitz number ($\mathrm{Ka_T}$) and turbulent Damköhler number ($\mathrm{Da_T}$) are principal non-dimensional quantities describing turbulence-chemistry interactions. Turbulent Damköhler number ($\mathrm{Da_T}$) relates the timescale of the turbulent transport phenomena to the chemical reaction timescale: $\mathrm{Da_T} = \tau_\mathrm{F}/\tau_\mathrm{c}$, where $\tau_\mathrm{F} = L/u'$ and $\tau_\mathrm{c} = \delta_\mathrm{L}/S_\mathrm{L}^\mathrm{o}$. Turbulent Karlovitz number is defined as the ratio of chemical timescale (τ_c) and the Kolmogorov time scale (τ_η): $\mathrm{Ka_T} = \tau_\mathrm{c}/\tau_\eta$, and is calculated as (Prandtl number ≈ 1):

$$\mathrm{Ka_T} = (L/\delta_\mathrm{L})^{-2}\ \mathrm{Re_T}^{1.5} \tag{1.3}$$

The relation between $\mathrm{Da_T}$ and $\mathrm{Ka_T}$ can be expressed as: $\mathrm{Re_T} = \mathrm{Da_T^2}\ \mathrm{Ka_T^2}$ [17]. Gas-turbine engines and other combustors operate at $\mathrm{Da_T} < 1$, since high bulk velocities will reduce τ_F. Furthermore, in highly turbulent flows, the size of turbulent eddies is extended toward the smaller scales (i.e., lower η and τ_η), which corresponds to high $\mathrm{Ka_T}$. Therefore, in this thesis, we aim at performing tests closer to the relevant operating conditions of GTEs and other practical systems, at $\mathrm{Da_T} < 1$ and $1 < \mathrm{Ka_T} < 100$, in a laboratory scale apparatus.

Karlovitz number is also estimated in terms of length scales: $\mathrm{Ka_T} = (\delta_\mathrm{L}/\eta)^2$, which indicates the tendency of the eddies to penetrate the preheat zone of the flame. Karlovitz number, along with velocity and length scale ratios, defines different regimes of turbulent premixed combustion in the Borghi diagram [17, 23], as shown in Fig. 1.1. On the Borghi diagram, $\mathrm{Ka_T} < 1$ indicates that the eddies of Kolmogorov length scale are significantly large compared to the flame thickness;

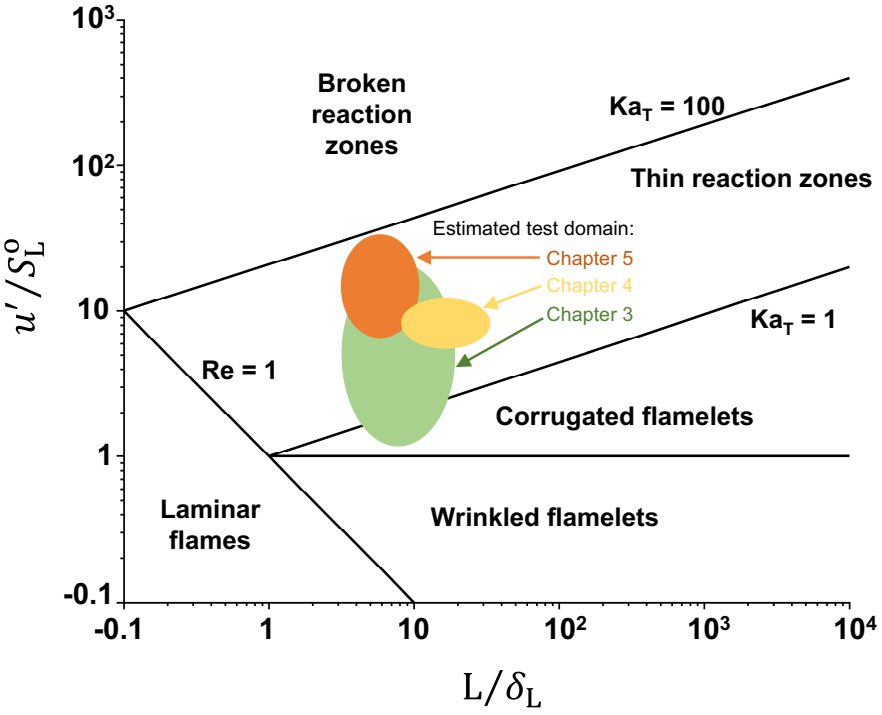

Figure 1.1 Borghi diagram showing turbulent premixed combustion regimes and estimated experimental regions of each chapter.

hence, the eddies do not penetrate the preheat zone and have only a wrinkling effect on the flame-front structure. This zone corresponds to the wrinkled and corrugated flamelet regimes, where the fluctuating velocity component of the turbulent flow is smaller than, or on the order of, the laminar flame speed, respectively. In theory, for $\mathrm{Ka_T} > 1$, eddies of the Kolmogorov length scale will become sufficiently small that they might penetrate the reactive-diffusive flame structure. This regime corresponds to the thin and broken reaction zones on the Borghi diagram. In the thin reaction zone regime, eddies of the Kolmogorov length scale are larger than the reaction zone, but have become smaller than the flame thickness; hence, these eddies might penetrate the flame structure, broaden the preheat zone, and enhance heat and species transport in the preheat zone of the flame [17]. The broken (distributed) reaction zone regime, on the other hand, corresponds to the region where eddies have become small enough to penetrate and disrupt the reaction zone. In turbulent premixed flame studies, the higher turbulence intensity extends experiments to the higher $\mathrm{Ka_T}$, and ensures premixed combustion closer to relevant conditions of GTEs and other combustors. The estimated experimental domain discussed in Chapters 3, 4, and 5 are illustrated on the Borghi diagram in Fig. 1.1.

The theoretical discussion above shows that, in the thin reaction zone regime, the eddies penetrate the preheat zone of the flame and thicken the flame front (i.e., thin reaction zone hypothesis), which contradicts the flamelet model, as the turbulent heat and mass transport become larger than diffusion at the flame front. The validity of the flamelet model in the thin reaction zone ($1 < \mathrm{Ka_T} < 100$) is discussed in several studies [24–33]. Experimental [29] and numerical analysis [30] of flame thickness illustrated that flame thickness decreased with increasing turbulence intensity and $\mathrm{Ka_T}$, which contradicts the thin reaction zone hypothesis. Furthermore, as discussed by Driscoll [28], much larger and stronger turbulent eddies than Kolmogorov eddies might be needed to penetrate the preheat zone, and cause deviations from flamelet structure, as Kolmogorov eddies are typically so weak, and may be destroyed by weak viscous forces during one eddy turnover time. Therefore, $\mathrm{Ka_T} > 1$ might not be the criteria to identify the ability of turbulent eddies to penetrate the preheat zone of the flame. As illustrated by Driscoll [28], the validity of the flamelet model is shown for nearly all cases, where images of the reaction zone are available, while evidence of non-flamelet behavior is sparse. In contrast, the interactions of turbulent eddies and the preheat zone are shown in [25, 27], where temperature profiles illustrate that eddies have enhanced the heat transport from the reaction zone to the areas upstream of the preheat zone. This controversy in the combustion literature motivates further study on the validity of the flamelet model in the thin reaction zone regime. The flamelet model is closely relevant to the concept of stretch sensitivity in the propagation of premixed flames and thermal-diffusive instabilities, which is the focus of this study.

In investigating flame-vortex interactions, it should be noted that the high-temperature zone near the flame front leads to a reduced $\mathrm{Re_T}$, as the mixture density decreases. Measurements in the high-temperature zone also affect $\mathrm{Ka_T}$ and $\mathrm{Da_T}$ calculations. Therefore, $\mathrm{Re_T}$, $\mathrm{Ka_T}$, and $\mathrm{Da_T}$ are temperature-sensitive parameters that need to be calculated immediately upstream of the flame-brush thickness in flame experiments in order to result in realistic values.

1.3 Lewis number, stretch sensitivity, and differential diffusion in premixed flames

1.3.1 Lewis number

In the context of fuel flexibility, changing the fuel and oxidizing-gas mixture composition has two major impacts on flame characteristics, which significantly affect combustor operability properties, such as blowout, flashback, and dynamic stability, mainly due to variations in turbulent

burning rates: (1) it changes the mixture reactivity, and (2) it changes the mixture diffusivity. Fuel flexibility changes chemical properties and the reactivity of the mixture, which is represented by the unstretched laminar flame speed ($S_{\mathrm{L}}^{\mathrm{o}}$) of a given fuel and oxidizing-gas mixture. The effects of mixture reactivity and flame speed are well studied, e.g., laminar flame studies of H_2-enriched hydrocarbon flames [34–38] show that, adding H_2, which is a very reactive fuel with a high laminar flame speed, to the fuel mixture enhances the flame speed and burning rates of the flame, and extends the flammability limit toward the lean side enabling the engine to operate at leaner conditions. Fuel flexibility also changes the transport properties of the mixture, which are the diffusivity of the deficient reactant (fuel in lean, and oxidizer in rich, combustion) ($\mathcal{D}$) and the diffusivity of heat (α). The disparity between α and $\mathcal{D}$ at the flame front is known as *differential diffusion*, which is represented by Lewis number ($\mathrm{Le} = \alpha/\mathcal{D}$). Most previous studies reported the combined effects of mixture reactivity and diffusivity properties, whereas, fewer studies have focused only on the effects of differential diffusion on the propagation and structure of premixed flames. The main focus of this thesis is to investigate the effects of differential diffusion on flame characteristics imposed by variable fuel and oxidizing-gas compositions (i.e., fuel flexibility).

Lewis number is the balance between thermal diffusivity of the mixture and mass diffusivity of the deficient reactant (fuel in lean, and oxidizer in rich combustion) at the flame front, and determines thermo-diffusive properties of the mixture, which is calculated as: $\mathrm{Le} = \alpha/\mathcal{D} = \lambda/(\rho c_{\mathrm{p}}\mathcal{D})$. Models of gas dynamics show that molecular weight and molecular radius of the deficient species and the bulk gas are important parameters in characterizing Le [39, 40]. Using a simple model, Le of deficient species, A, diffusing into the bulk gas, B, is calculated as [39, 40]:

$$\mathrm{Le} \propto \left(1 + \frac{R_{\mathrm{A}}}{R_{\mathrm{B}}}\right)^2 \sqrt{1/\left(1 + \frac{M_{\mathrm{B}}}{M_{\mathrm{A}}}\right)} \tag{1.4}$$

where M is the molecular weight, and R is the radius of the molecule. This simple equation shows that a lighter and smaller molecule (e.g., H_2) diffusing into the bulk gas N_2, is representative of small Le ($\mathrm{Le} \ll 1$) while a heavier and larger molecule (e.g., propane, C_3H_8) diffusing into the bulk gas N_2 will result in large Le ($\mathrm{Le} > 1$).

Lean premixed flames with variable fuel compositions, where multiple fuels are present in the reactants, implies that an effective Lewis number ($\mathrm{Le}_{\mathrm{eff}}$) needs to be defined in determining mixture characteristics. Three main formulations are presented for $\mathrm{Le}_{\mathrm{eff}}$ of lean mixtures with multiple fuels: (1) weighted average of the mixture Lewis numbers calculated for each fuel based on non-dimensional heat release [41], (2) volumetric-fraction-weighted average of the mixture Lewis numbers calculated for each fuel [42], and (3) mixture Lewis number calculation based

on the volumetric-fraction-weighted average of the fuel diffusivities [43]. In this study, $\mathrm{Le_{eff}}$ is defined based on the volumetric-fraction-weighted average of the Lewis numbers of the two fuels for H_2-enrichment of CH_4 and C_3H_8 fuels [43, 44]: $\mathrm{Le_{eff}} = X_{\mathrm{C_nH_m}}\mathrm{Le_{C_nH_m}} + X_{\mathrm{H_2}}\mathrm{Le_{H_2}}$, where X is the mole fraction in the fuel stream, $X_{\mathrm{C_nH_m}} + X_{\mathrm{H_2}} = 1$.

1.3.2 Stretch sensitivity and differential diffusion in premixed flames

Differential diffusion causes stretch sensitivity in flame-front propagation, leading to thermal-diffusive instabilities, and is characterized by Lewis number. Unlike $S_{\mathrm{L}}^{\mathrm{o}}$, which is an ideal phenomenon, any laminar or turbulent flame in the laboratory environment, or practical systems, will experience some stretch and heat loss. Stretch rate (K), is defined as the normalized differential change in flame surface area as a function of time: $K = (1/A)\,(\mathrm{d}A/\mathrm{d}t)$ [45], which is a function of flame curvature (κ) and hydrodynamic strain (K_s) (tangential strain rate due to a non-uniform flow field across the flame) [46]:

$$K = S\kappa + K_{\mathrm{s}} \tag{1.5}$$

where S is the local characteristic flame velocity in laboratory coordinates. The two components of flame stretch depend on the geometry and can be decoupled with a proper choice of experimental apparatus. For instance, the effects of turbulence, bulk hydrodynamic strain, and the combined effects of both can be studied in turbulent jet flames, laminar counter-flow flames, and turbulent counter-flow flames, respectively.

In flame stretch theory, consistent with the flamelet model [20–22], as illustrated in Fig. 1.2, at a positively stretched leading portion of the turbulent flame with $\mathrm{Le} \approx 1$, the molecular diffusion into the reaction zone is in balance with thermal diffusion from the reaction zone, and the flame temperature is equal to the adiabatic flame temperature (T_{ad}). In mixtures with $\mathrm{Le} > 1$ (thermo-diffusively stable mixture), thermal diffusion from the positively stretched portion of the turbulent flame front is larger than fuel diffusion into the stretched area. The rate of thermal energy loss is greater than chemical energy gain provided by molecular diffusion into the reaction zone, which reduces the temperature and results in decreasing flame velocity. In mixtures with $\mathrm{Le} \ll 1$ (thermo-diffusively unstable mixtures), while the leading portion of the flame front is positively stretched, molecular diffusion into the stretched area is larger than thermal energy loss through diffusion, which increases the local equivalence ratio (ϕ), and, consequently, temperature and flame velocity increase. Stretch sensitivity of flames is an important parameter that affects the flame structure [27,

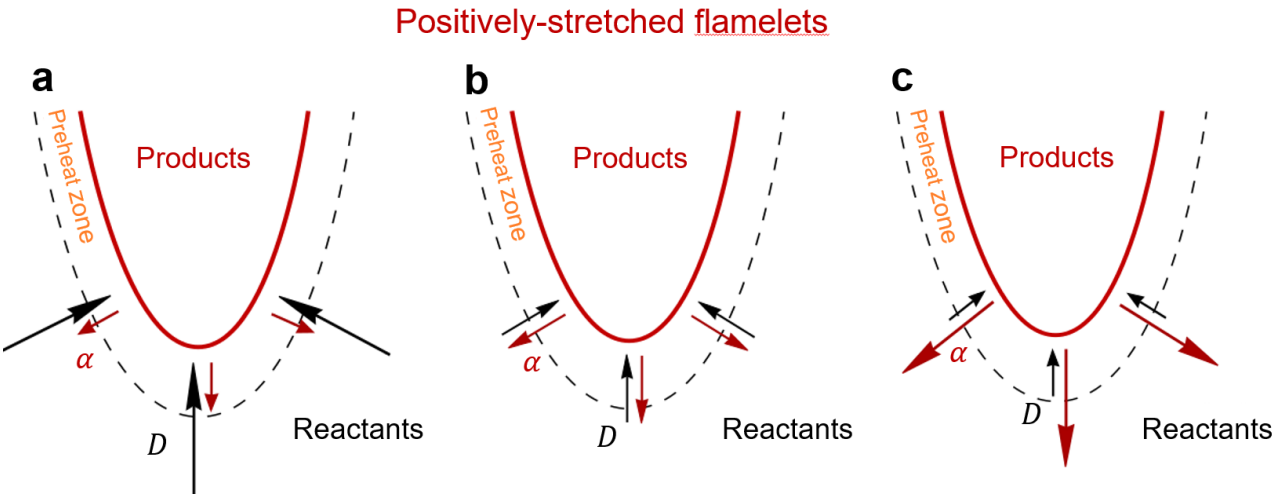

Figure 1.2 Schematic of flame stretch theory showing positively stretched flamelets at the turbulent premixed flame front: fuel and oxidizer mixtures at (a) $\mathrm{Le} \ll 1$, (b) $\mathrm{Le} \approx 1$, and (c) $\mathrm{Le} > 1$.

28, 30, 33, 47–50], e.g., flame-front curvature [26, 51], and burning rates in laminar and turbulent flames [49, 52–60].

1.4 Burning rate of turbulent premixed flames

Flame speed is a fundamental parameter for combustor design and turbulent combustion modeling, which determines the burning rate of the flame, and the rate at which the chemical energy of the fuel is released. Intense burning is technologically desirable, which increases the energy density in practical systems. The fundamental understanding of the interactions between turbulence, flame-front hydrodynamic instabilities, and thermal-diffusive instabilities due to the effects of differential diffusion, and their effects on flame burning rates, a topic that is only recently emerging, is of great importance to answer the question: *"How fast can we burn?"*.

1.4.1 Damköhler's hypothesis and the theory of leading points

The increase in the velocity of turbulent flames compared to laminar flames is illustrated schematically in Fig. 1.3. Figure 1.3 (a) shows an unstretched laminar flame with the surface area, A_{L}, propagating at a speed of $S_{\mathrm{L}}^{\mathrm{o}}$. When this flame is wrinkled by turbulence, in order to explain the propagation of turbulent flames, Damköhler's hypothesis [52] was proposed based on the idea that, in the flamelet regime, the increase in flame surface area is the dominant mechanism for flame velocity enhancement in turbulent flames, and that the local flamelet velocities remain close to $S_{\mathrm{L}}^{\mathrm{o}}$.

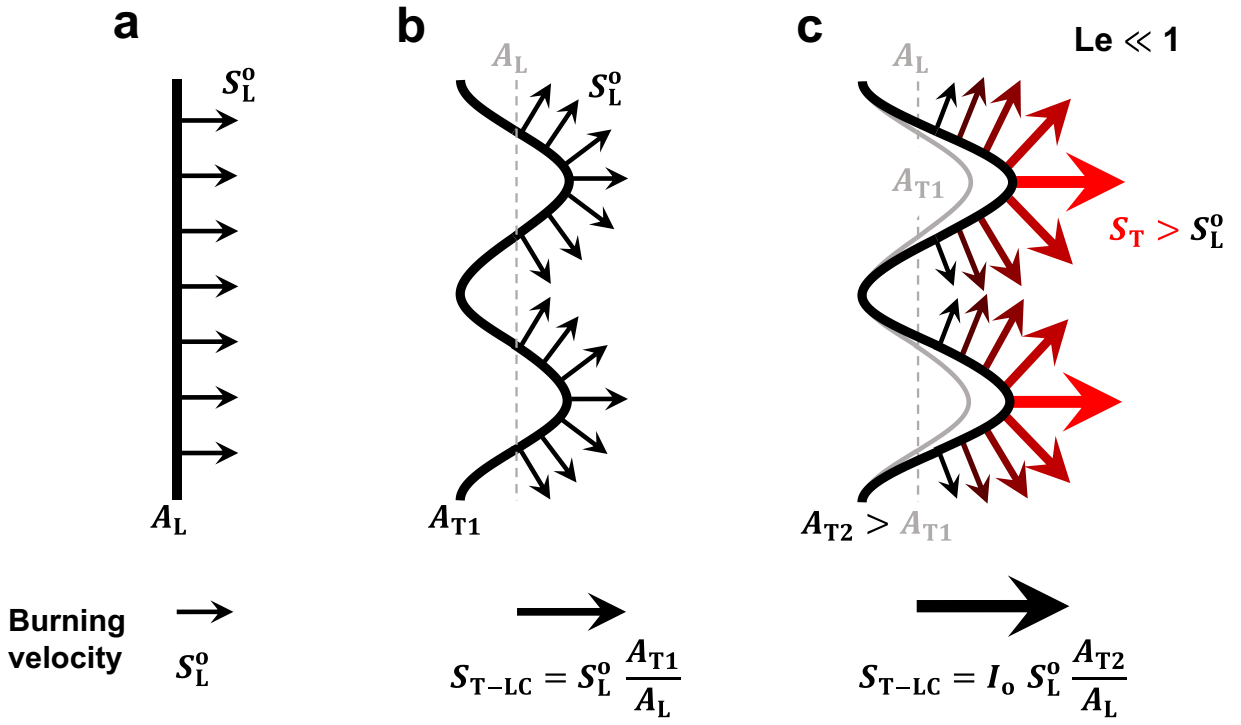

Figure 1.3 Schematic showing the effects of turbulence on the flame propagation: (a) unstretched laminar flame propagating at S_L^o, (b) classical Damköhler's hypothesis [52], (c) theory of leading points, considering the effects of differential diffusion on local flamelet velocities and the flame surface area.

Damköhler's hypothesis is illustrated in Fig.1.3 (b): $S_{T-LC} = S_L^o\,(A_T/A_L)$, where S_{T-LC} is the overall propagation velocity (burning rate) of a turbulent flame, and the turbulent flame surface area (A_T) is larger than A_L.

However, previous studies showed that the increase in flame surface area alone is insufficient to explain increasing burning rates with increasing turbulence intensity, and that differential diffusion also affects the burning rates of laminar [61–63] and turbulent [51, 64–69] flames. These studies show that, at the positively stretched portion of the flame front in thermo-diffusively unstable mixtures, local flamelet velocities (S_T) can have values significantly larger than S_L^o. The effects of differential diffusion on turbulent premixed flame propagation can be explained by the *theory of leading points*, which was first proposed by Kuznetsov [70] to describe turbulent premixed flame propagation, and was expanded in [71], and investigated in recent studies [56, 63]. Leading points are the most forward-lying points of the flame front into the reactants, which are positively curved and stretched, and are considered to be locally 1D flamelets. The leading points concept, consistent with the flamelet model [20–22], assumes that the burning rate and overall propagation velocity of

a turbulent premixed flame are controlled by the velocity of the leading points, which is particularly revealing for thermo-diffusively unstable mixtures with $\mathrm{Le} < 1$. Since the leading edge is stretched and positively curved, the local flamelet velocities at the leading points will increase due to the effects of differential diffusion. The effects of differential diffusion in increasing the velocity of the leading points, as well as its inherent effects on flame surface area enhancement is shown in Fig.1.3 (c): $S_{\mathrm{T-LC}} = S_{\mathrm{L}}^{\mathrm{o}}\, I_{\mathrm{o}}\, (A_{\mathrm{T}}/A_{\mathrm{L}})$, where, I_{o} is the local stretch factor, and can be estimated as the ratio of the local flamelet velocity to the unstretched laminar flame speed: $I_{\mathrm{o}} \approx S_{\mathrm{T}}/S_{\mathrm{L}}^{\mathrm{o}}$. For thermo-diffusively stable flames ($\mathrm{Le} \geq 1$), $I_{\mathrm{o}} \approx 1$, leading to the classical $S_{\mathrm{T-LC}}$ scaling described by Damköhler. In this study, one goal is to investigate the validity of the leading points theory, and the inherent effects of differential diffusion in increasing flame surface area at constant turbulence intensities.

The effects of stretch sensitivity on the turbulent premixed flame propagation are clearly shown by turbulent flame velocity correlations versus various levels of turbulence, where mixtures with different thermo-diffusive properties (distinct Lewis numbers) have different velocities at constant levels of turbulence ($u'/S_{\mathrm{L}}^{\mathrm{o}}$). These correlations show a general scatter of the datasets when mixtures with distinct Lewis numbers are used. Examples of these correlations are illustrated in Fig. 1.4. In Fig. 1.4 (a) [66], variations in turbulent flame velocities are shown at increasing u' for H_2-air, CH_4-air, C_3H_8-air flames with different Lewis numbers in the range of $0.4 < \mathrm{Le} < 1.6$, where mixtures are diluted with N_2 to keep $S_{\mathrm{L}}^{\mathrm{o}}$ constant at 0.15 m/s in all flames. Figure 1.4 (b) [63] is another example showing these correlations for H_2+CO fuel blends in air, leading to distinct Lewis numbers, at increasing $u'/S_{\mathrm{L}}^{\mathrm{o}}$, and constant $S_{\mathrm{L}}^{\mathrm{o}} = 0.34$ m/s. Also included in Fig. 1.4 (b) are turbulent flame velocity predictions of several models, which generally fail to accurately predict these experimental correlations. Figures 1.4 (a) and 1.4 (b) show that, while turbulent flame velocity increases with increasing turbulence level for a given fuel-oxidizer-inert mixture, the correlations do not collapse. Variations in these correlations, originating from the effects of differential diffusion in mixtures with distinct Lewis number, further strengthen the motivation for this study.

1.4.2 Various definitions of turbulent flame velocity

A precise definition of turbulent flame velocity is crucial in turbulent combustion experiments to avoid conflicting results from complementary experimental studies. There are three common definitions of turbulent flame velocity, in the form of consumption velocity or displacement velocity, depending on the experimental configuration [28]: (1) global consumption velocity ($S_{\mathrm{T-GC}}$), (2) local consumption velocity, or burning rate ($S_{\mathrm{T-LC}}$), and (3) local flamelet displacement velocity

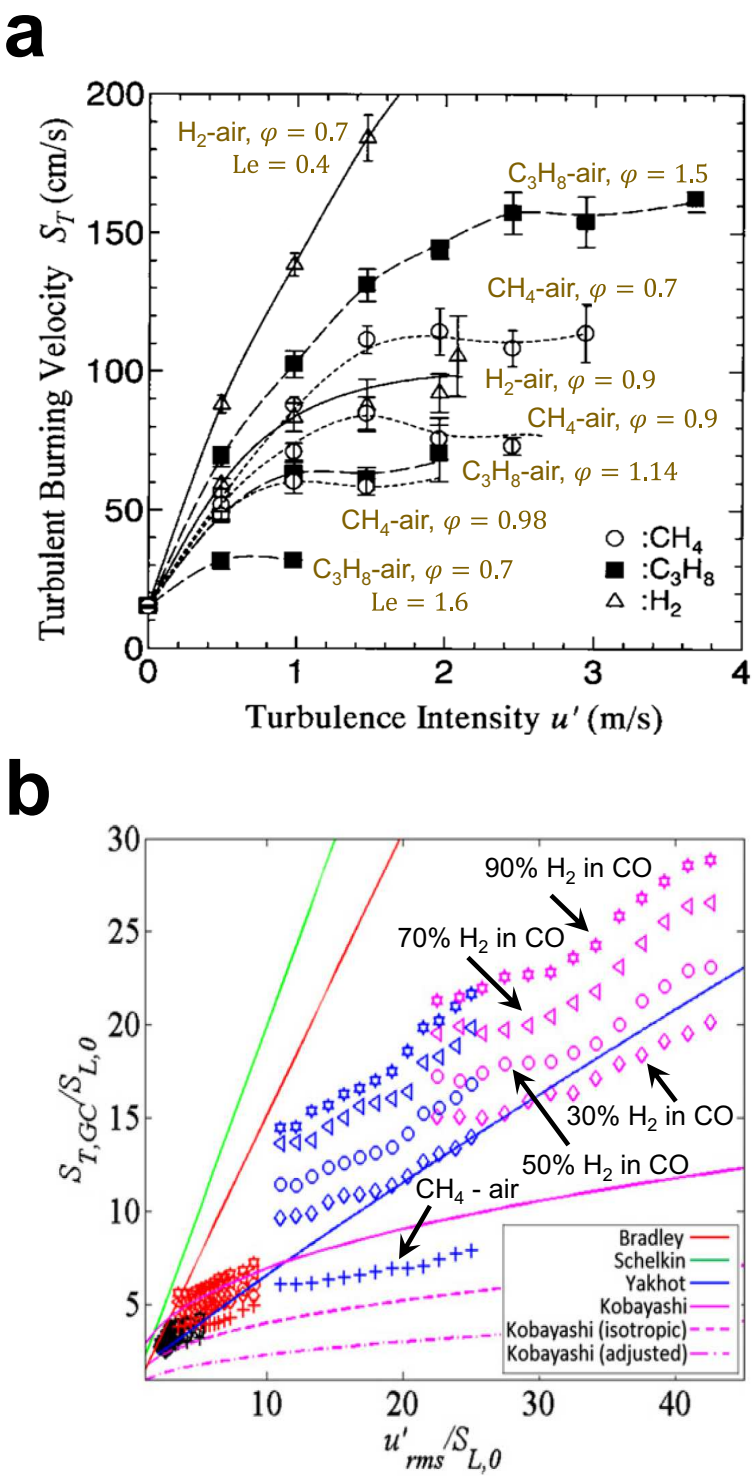

Figure 1.4 Turbulent flame velocity correlations with increasing turbulence level: (a) Turbulent flame velocity vs u' at constant $S_L^o = 0.15$ m/s for mixtures at distinct Lewis numbers, reprinted and modified from [66], and (b) Normalized turbulent flame velocity vs (u'/S_L^o) at constant $S_L^o = 0.34$ m/s for H_2+CO fuel blends in air at distinct Lewis numbers, reprinted and modified from [63].

(S_{T}). It should be noted that, for any turbulent premixed flame, the magnitudes of the three velocities are not equal [72, 73], however, all three definitions can be used to compare experiments and simulations for validation purposes, where both have identical geometry, and use the same definition of turbulent burning velocity. Various definitions of the turbulent burning velocity are measured and reported in [28, 63, 74–78].

Global consumption velocity is a global quantity calculated based on the total mass flow rate of reactants ($\dot{m}_{\mathrm{r}}$) as [28]: $S_{\mathrm{T-GC}} = \dot{m}_{\mathrm{r}}/(\rho\, A)$, where ρ is the density of the unburned reactants, and A is the area of a flame contour calculated at an arbitrary average temperature progress variable (typically $\overline{c} = 0.5$). This definition of flame velocity is commonly used in the Bunsen burner.

Local consumption velocity ($S_{\mathrm{T-LC}}$) is the local instantaneous turbulent burning rate of the flame, which includes both the effects of differential diffusion on local flamelet velocities, as well as the increase in flame surface area [28, 79, 80]:

$$S_{\mathrm{T-LC}} = I_{\mathrm{o}}\, S_{\mathrm{L}}^{\mathrm{o}}\, \frac{A_{\mathrm{T}}}{A_{\mathrm{L}}} \tag{1.6}$$

where, I_{o} is the local stretch factor, which depends on differential diffusion, A_{T} is the turbulent flame surface area, and A_{L} is the laminar flame surface area.

Local flamelet displacement velocity (S_{T}), in a counter-flow apparatus used in this thesis (please see Chapter 2) is the local instantaneous propagation velocity of a portion of the flame front ($c \approx 0$ iso-surface, where c is the temperature progress variable), in the flow coordinate system, relative to the convection velocity of the flow in the direction normal to the flame surface ($\mathbf{n}$) [28, 81–83]: $S_{\mathrm{T}} = (S_{\mathrm{flame}} + S_{\mathrm{convection}}) \cdot \mathbf{n}$. The local stretch factor (I_{o}) in Eq. 1.6 can be estimated as the ratio of the local flamelet displacement velocity to the unstretched laminar flame speed [28, 80]: $I_{\mathrm{o}} \approx (S_{\mathrm{T}}/S_{\mathrm{L}}^{\mathrm{o}})$, which is a function of differential diffusion.

Equation 1.6 indicates that the effects of stretch on the propagation and structure of turbulent premixed flames in the flamelet regime originate from two main mechanisms: (1) the effects of differential diffusion on local flamelet displacement velocities, and (2) the effects of flame surface area. One of the main objectives of this thesis is to experimentally investigate these two mechanisms and their interactions, in order to explore the effects of differential diffusion on the burning rate of turbulent premixed flames in the thin reaction zone regime of the turbulent premixed combustion [17, 23], where $1 < \mathrm{Ka}_{\mathrm{T}} < 100$ and $\mathrm{Da}_{\mathrm{T}} < 1$.

1.5 Flame-front cellular instabilities

It is known that premixed flames are often subjected to intrinsic flame-front cellular-instabilities [41, 84–89] that arise from a combination of the thermal-diffusive and the Darrieus–Landau hydrodynamic instabilities. Thermal-diffusive instabilities are caused by the effects of differential diffusion and stretch sensitivity on the propagation of premixed flames, and are a function of Lewis number. As discussed in Eq. 1.5, these instabilities affect the burning velocity of premixed flames through the external influence of turbulence (i.e., flame-front curvature) and bulk hydrodynamic strain. On the other hand, Darrieus–Landau hydrodynamic instabilities are triggered by a sharp density change across the flame front, without the external influence of turbulence nor hydrodynamic strain. The spontaneous formation of cellular structures, generated by these instabilities, wrinkles the flame front leading to an enhanced flame velocity and rapid flame acceleration. The increase in flame velocity at the onset of hydrodynamic instabilities is attributed to an increase in flame surface area, where the increase in local burning rate caused by flame stretch is often neglected, due to large flame cells (on the scale of several centimeters); hence, a very small effective curvature/stretch [88, 90, 91]. These effects are of particular importance in accidental explosions within the context of industrial safety.

The effects of thermal-diffusive instabilities on increasing the flame propagation velocity of mixtures with $\mathrm{Le} < 1$ are coupled to the effects of Darrieus–Landau hydrodynamic instabilities. While hydrodynamic instabilities are typically stabilized for small-scale flames at atmospheric pressure due to the diffusional thickness of the flame front, these effects are of fundamental significance and practical importance at high-pressure combustion environments, such as GTEs and internal combustion (IC) engines for which these instabilities can be substantially enhanced due to very thin flames. Furthermore, recent studies [88, 90] show that turbulence allows instabilities to grow faster than they would spontaneously, and that turbulence may act to accentuate the burning rate by promoting intrinsic flame instabilities.

This study investigates how the cellular instabilities and turbulence interact in small-scale flames. The results of this study should also be extendable to the effects of differential diffusion on hydrodynamic instabilities since both turbulence, and flame-front hydrodynamic instabilities can wrinkle the flame, increase the flame-front curvature, and augment its propagation velocity and burning rate.

1.6 Thesis objectives and overview

The effects of differential diffusion on the burning rate and structure of turbulent premixed flames are still not clear. Many researchers state that these effects should disappear once turbulence is strong; hence, there is no mutual understanding in the combustion literature regarding the effects of differential diffusion in the thin reaction zone regime ($1 < \mathrm{Ka_T} < 100$ and $\mathrm{Da_T} < 1.$) [17, 23], where turbulent heat and mass transport are enhanced. Therefore, understanding the interactions between turbulence and thermal-diffusive instabilities, caused by differential diffusion, in the thin reaction zone regime, and independent of mixture reactivity, is one of the main objectives of this thesis. Furthermore, the relative contribution of different mechanisms of differential diffusion effects on the overall burning rate of premixed flames, i.e., the effects on local flamelet velocities and the effects on increasing flame surface area, is discussed at constant turbulence intensities.

In addition, there are two main gaps in the majority of turbulent premixed flame experiments: (1) chemical effects are not isolated from differential diffusion effects, and (2) the local instantaneous measurements of turbulent flame velocity, burning rate, flame location and structure parameters, such as flame stretch, flame-front curvature, and flame surface area are thinly scattered in the current combustion research literature, and the measurements reported in the majority of studies are focused on global time-averaged quantities, that do not necessarily yield local information on the physics of turbulent flame propagation [28]. This thesis will address these two gaps in the current turbulent premixed combustion research.

In the context of fuel flexibility, this study experimentally investigates the effects of differential diffusion on flame velocity, burning rates, and structure parameters of turbulent premixed flames, such as flame stretch, flame-front curvature, and flame surface area, by variations in transport properties of the combustible mixtures originating from variable fuel and oxidizing-gas compositions. The experiments are carried out using aerodynamically stabilized lifted flames against hot exhaust gases in an axial counter-flow apparatus [13, 14, 92–96], where the flames are not affected by conductive heat loss to the burner. Strained counter-flow flames are used in these experiments, in order to study the effects of both components of the flame stretch, i.e., bulk and local hydrodynamic strain and local curvature. Mixtures with very distinct effective Lewis number ($\mathrm{Le_{eff}}$) in the range of $0.3 < \mathrm{Le_{eff}} < 3.1$, representative of different mixture thermo-diffusive properties, are studied, which spans a wide range of Lewis numbers. Furthermore, these experiments are done at various levels of turbulence intensity to investigate the effects of turbulence on the premixed flame propagation for mixtures with distinct $\mathrm{Le_{eff}}$. Laminar flame measurements are also reported as a reference for comparison.

In these experiments, unstretched laminar flame speed is kept constant during mixture dilution, and H_2 enrichment of hydrocarbon flames, through changing the mixture equivalence ratio in each series of experiments, in order to minimize the effects of chemical properties of the mixture. Furthermore, bulk-flow properties and the temperature boundary condition are also kept constant; hence, the experiments specifically focus on the effects of differential diffusion on flame propagation independent of mixture reactivity.

Two-dimensional high-speed particle image velocimetry (2D-PIV) and Mie scattering flame tomography are applied to quantify the flow velocity field within the imaged plane using oil droplet seeding, enabling simultaneous flame-location and velocity measurements. Data-processing tools are developed through this study to extract local instantaneous statistics of various flame parameters within the imaged plane, such as flame location, local flamelet velocity, and structure parameters of turbulent premixed flames, including flame stretch, flame-front curvature, and flame surface area. These processing techniques enable local instantaneous measurements to be statistically represented, using sufficiently large datasets, in the form of probability density functions (PDF).

This dissertation is presented as a *manuscript-based thesis* in six chapters:

Chapter 1 This chapter starts with an introduction to fuel flexibility and presents a background on turbulent premixed combustion and turbulent burning rates. Furthermore, it includes a review of the current literature on stretch sensitivity and differential diffusion in premixed flames. The gaps in the current turbulent premixed combustion research, the main objectives of the study, and an overview of the thesis are presented in this chapter.

Chapter 2 This chapter presents a detailed methodology of this study. The hot-exhaust opposed-flow turbulent flame rig (HOTFR) and two-dimensional high-speed particle image velocimetry (2D-PIV) are discussed in detail. Furthermore, a description and a thorough analysis of processing techniques, developed through this thesis to extract local instantaneous statistics of various flame parameters within the imaged plane, are presented in this chapter.

Chapter 3 The work reported in this chapter describes a study of flame stabilization characteristics of lean turbulent premixed flames with variable Lewis number, which are stabilized under various turbulence levels. The experiments are carried out using pure fuel mixtures of hydrogen-air ($\mathrm{Le} \ll 1$), methane-air ($\mathrm{Le} \approx 1$), and propane-air ($\mathrm{Le} > 1$). In the final part of this paper, these flames are modeled using preliminary computational fluid dynamic (CFD) simulations based on the flamelet generated manifolds (FGM) model in a Reynolds-averaged Navier–Stokes (RANS) context. The ability of turbulent combustion models to predict lifted, aerodynamically stabilized

flames will be validated in future studies using large-eddy simulation (LES) and more complex turbulent premixed combustion models.

This chapter was published in the *ASME Journal of Engineering for Gas Turbines and Power*, and was presented in the *ASME Turbo Expo 2018: Turbine Technical Conference and Exposition* (paper GT2018-77139), Oslo, Norway.

Publication (1): E. Abbasi-Atibeh, S. Jella, and J. M. Bergthorson. "Fuel variation effects in propagation and stabilization of turbulent counter-flow premixed flames". In: *Journal of Engineering for Gas Turbines and Power* 141 (2018), pp. 031024. http://dx.doi.org/10.1115/1.4041136.

Chapter 4 This chapter investigates the effects of differential diffusion and stretch sensitivity on flame velocities and stabilization of lean premixed flames at a constant turbulence level, where variations of $\mathrm{Le}_{\mathrm{eff}}$ are mainly due to a change in fuel diffusivity of the mixture. In these experiments, highly strained turbulent hydrogen-enriched methane-air and propane-air flames in the thin reaction zone regime of turbulent premixed combustion are stabilized in a counter-flow apparatus. During hydrogen enrichment, the unstretched laminar flame speed of the mixtures is kept constant through decreasing the mixture equivalence ratio, which minimizes the effects of chemical properties of the mixture on the propagation and stabilization of premixed flames; hence, the study highlights the effects of variations in fuel diffusivity of the mixtures in fuel flexibility experiments. A brief discussion on the structure parameters of turbulent premixed hydrogen-enriched flames, including flame stretch and flame-front curvature is also presented in this chapter.

This study was presented in the *Turbulent Flames Section* of the *37th International Symposium on Combustion* in August 2018, which was held in Dublin, Ireland, and was published in the *Proceedings of the Combustion Institute*.

Publication (2): E. Abbasi-Atibeh and J. M. Bergthorson. "Differential diffusion effects in counter-flow premixed hydrogen-enriched methane and propane flames". In: *Proceedings of the Combustion Institute* 37 (2019), pp. 2399−2406. https://doi.org/10.1016/j.proci.2018.08.006.

Chapter 5 In this chapter, turbulent premixed flames of various fuel-oxidizer-inert mixtures in the thin reaction zone regime with variations in both fuel diffusivity and mixture thermal diffusivity, representative of very distinct effective Lewis number, are aerodynamically stabilized in a counter-flow apparatus. In the context of fuel flexibility, various fuels and fuel blends are used in combination with various oxidizer-inert mixtures to form mixtures with a wide range of effective Lewis numbers ($0.3 < \mathrm{Le}_{\mathrm{eff}} < 3.1$), through hydrogen enrichment and dilution. In these experiments, unstretched laminar flame speed (through changing the mixture equivalence ratio),

bulk-flow properties, and stagnation surface temperature are kept constant, in order to highlight the effects of differential diffusion during mixture dilution and hydrogen enrichment of hydrocarbon flames. Experiments are done at two different levels of turbulence intensity to investigate the effects of turbulence on the premixed flame propagation of mixtures with distinct $\mathrm{Le}_{\mathrm{eff}}$. Laminar flame measurements are also reported as a reference for comparison.

The effects of differential diffusion on various flame parameters of lean premixed laminar and turbulent flames, such as flame location, local flamelet displacement velocity, local consumption velocity or flame burning rate, and flame-structure parameters, including flame stretch, flame-front curvature, and flame surface area, are investigated. Furthermore, the relative proportion of different mechanisms of differential diffusion effects on the burning rate of premixed flames is discussed based on instantaneous local measurements.

This chapter is submitted to *Combustion and Flame* in March 2019.

Publication (3): E. Abbasi-Atibeh and J. M. Bergthorson. "The effects of differential diffusion in counter-flow premixed flames with dilution and hydrogen enrichment". Submitted to *Combustion and Flame* (2019).

Chapter 6 This chapter presents a discussion of the results and major conclusions and contributions of the thesis and suggests future research directions.

The resulting datasets reported in this thesis are expected to form benchmark cases both for technology innovation as well as a numerical model development for validating the ability of turbulent combustion models to predict turbulent premixed flames, which includes the effects of differential diffusion, through CFD simulations. The improved scientific understanding of the fundamental issues behind combustor operability and flame stability with variable fuel compositions and improved predictive capabilities of turbulent combustion models will enable designing fuel-flexible combustors with reduced emissions, higher performance, and at a lower cost.

References

[1] US Energy Information Administration. *International Energy Outlook 2016 With Projections to 2040*. Tech. rep. Report DOE/EIA-0484(2016). Washington D.C., 2016, p. 276.

[2] British Petroleum. *BP energy outlook 2018 edition*. Tech. rep. Available: https://www.bp.com/energyoutlook, Accessed: 2018-11-24.

[3] M.Z. Jacobson and M.A. Delucchi. "Providing all global energy with wind, water, and solar power, Part I: Technologies, energy resources, quantities and areas of infrastructure, and materials". In: *Energy Policy* 39 (2011), pp. 1154–1169.

[4] H. Ibrahim, A. Ilinca, and J. Perron. "Energy storage systems-characteristics and comparisons". In: *Renewable and Sustainable Energy Reviews* 12 (2008), pp. 1221–1250.

[5] J.M. Bergthorson. "Recyclable metal fuels for clean and compact zero-carbon power". In: *Progress in Energy and Combustion Science* 68 (2018), pp. 169–196.

[6] J.M. Bergthorson and M.J. Thomson. "A review of the combustion and emissions properties of advanced transportation biofuels and their impact on existing and future engines". In: *Renewable and Sustainable Energy Reviews* 42 (2015), pp. 1393–1417.

[7] L. Brennan and P. Owende. "Biofuels from microalgae - A review of technologies for production, processing, and extractions of biofuels and co-products". In: *Renewable and Sustainable Energy Reviews* 14 (2010), pp. 557–577.

[8] Y. Hou, R. Vidu, and P. Stroeve. "Solar energy storage methods". In: *Industrial & Engineering Chemistry Research* 50 (2011), pp. 8954–8964.

[9] H. Tennekes and J.L. Lumley. *A First Course in Turbulence*. The MIT Press, Cambridge, USA, 1972.

[10] S.B. Pope. *Turbulent flows*. Cambridge University Press, Cambridge, UK, 2000.

[11] J.O. Hinze. *Turbulence*. McGraw-Hill, New York, USA, 1975.

[12] G. Coppola and A. Gomez. "Experimental investigation on a turbulence generation system with high-blockage plates". In: *Experimental Thermal and Fluid Science* 33 (2009), pp. 1037–1048.

[13] G. Coppola, B. Coriton, and A. Gomez. "Highly turbulent counterflow flames: A laboratory scale benchmark for practical systems". In: *Combustion and Flame* 156 (2009), pp. 1834–1843.

[14] E. Mastorakos, A.M.K.P. Taylor, and J.H. Whitelaw. "Extinction of turbulent counterflow flames with reactants diluted by hot products". In: *Combustion and Flame* 102 (1995), pp. 101–114.

[15] P. Geipel, K.H.H. Goh, and R.P. Lindstedt. "Fractal-generated turbulence in opposed jet flows". In: *Flow, Turbulence and Combustion* 85 (2010), pp. 397–419.

[16] K.H.H. Goh, P. Geipel, and R.P. Lindstedt. "Lean premixed opposed jet flames in fractal grid generated multiscale turbulence". In: *Combustion and Flame* 161 (2014), pp. 2419–2434.

[17] N. Peters. *Turbulent combustion*. Cambridge university press, Cambridge, UK, 2000.

[18] E. Mallard and H. Le Chatelier. "On the propagation velocity of burning in gaseous explisove mixture". In: *Comptes Rendus Chimie* 93 (1881), pp. 145–148.

[19] D.G. Goodwin, H.K. Moffat, and R.L. Speth. *Cantera: A software toolkit for chemical kinetics, thermodynamics, and transport processes*. Version 2.2.1, http://www.cantera.org, 2016.

[20] N. Peters. "Laminar flamelet concepts in turbulent combustion". In: *Proceedings of the Combustion Institute* 21 (1988), pp. 1231–1250.

[21] N. Peters. "Laminar diffusion flamelet models in non-premixed turbulent combustion". In: *Progress in Energy and Combustion Science* 10 (1984), pp. 319–339.

[22] S.K. Liew, K.N.C. Bray, and J.B. Moss. "A flamelet model of turbulent non-premixed combustion". In: *Combustion Science and Technology* 27 (1981), pp. 69–73.

[23] R. Borghi. "On the structure and morphology of turbulent premixed flames". In: *Recent Advances in the Aerospace Sciences* (1985), pp. 117–138.

[24] Ö.L. Gülder and G.J. Smallwood. "Flame surface densities in premixed combustion at medium to high turbulence intensities". In: *Combustion Science and Technology* 179 (2007), pp. 191–206.

[25] Ö.L. Gülder. "Contribution of small scale turbulence to burning velocity of flamelets in the thin reaction zone regime". In: *Proceedings of the Combustion Institute* 31 (2007), pp. 1369–1375.

[26] F.T. Yuen and Ö.L. Gülder. "Dynamics of lean-premixed turbulent combustion at high turbulence intensities". In: *Combustion Science and Technology* 182 (2010), pp. 544–558.

[27] F.T.C. Yuen and Ö.L. Gülder. "Turbulent premixed flame front dynamics and implications for limits of flamelet hypothesis". In: *Proceedings of the Combustion Institute* 34 (2013), pp. 1393–1400.

[28] J.F. Driscoll. "Turbulent premixed combustion: Flamelet structure and its effect on turbulent burning velocities". In: *Progress in Energy and Combustion Science* 34 (2008), pp. 91–134.

[29] A. Soika, F. Dinkelacker, and A. Leipertz. "Measurement of the resolved flame structure of turbulent premixed flames with constant Reynolds number and varied stoichiometry". In: *Proceedings of the Combustion Institute* 27 (1998), pp. 785–792.

[30] L.P.H. De Goey, T. Plessing, R.T.E. Hermanns, and N. Peters. "Analysis of the flame thickness of turbulent flamelets in the thin reaction zones regime". In: *Proceedings of the Combustion Institute* 30 (2005), pp. 859–866.

[31] M.S. Mansour, N. Peters, and Y.-C. Chen. "Investigation of scalar mixing in the thin reaction zones regime using a simultaneous CH-LIF/Rayleigh laser technique". In: *Proceedings of the Combustion Institute* 27 (1998), pp. 767–773.

[32] F. O'young and R.W. Bilger. "Scalar gradient and related quantities in turbulent premixed flames". In: *Combustion and Flame* 109 (1997), pp. 682–700.

[33] R. Sankaran, E.R. Hawkes, J.H. Chen, T. Lu, and C.K. Law. "Structure of a spatially developing turbulent lean methane–air Bunsen flame". In: *Proceedings of the Combustion Institute* 31 (2007), pp. 1291–1298.

[34] Z. Huang, Y. Zhang, K. Zeng, B. Liu, Q. Wang, and D. Jiang. "Measurements of laminar burning velocities for natural gas–hydrogen–air mixtures". In: *Combustion and Flame* 146 (2006), pp. 302–311.

[35] E. Hu, Z. Huang, J. He, C. Jin, and J. Zheng. "Experimental and numerical study on laminar burning characteristics of premixed methane–hydrogen–air flames". In: *International Journal of Hydrogen Energy* 34 (2009), pp. 4876–4888.

[36] C. Tang et al. "Laminar burning velocities and combustion characteristics of propane–hydrogen–air premixed flames". In: *International Journal of Hydrogen Energy* 33 (2008), pp. 4906–4914.

[37] P. Strakey, T. Sidwell, and J. Ontko. "Investigation of the effects of hydrogen addition on lean extinction in a swirl stabilized combustor". In: *Proceedings of the Combustion Institute* 31 (2007), pp. 3173–3180.

[38] F. Halter, C. Chauveau, and I. Gökalp. "Characterization of the effects of hydrogen addition in premixed methane/air flames". In: *International Journal of Hydrogen Energy* 32 (2007), pp. 2585–2592.

[39] R.J. Kee, M.E. Coltrin, and P. Glarborg. *Chemically reacting flow: theory and practice*. John Wiley & Sons, Hoboken, New Jersey, USA, 2005.

[40] J.R. Welty, C.E. Wicks, G. Rorrer, and R.E. Wilson. *Fundamentals of momentum, heat, and mass transfer*. John Wiley & Sons, Hoboken, New Jersey, USA, 2009.

[41] C.K. Law, G. Jomaas, and J.K. Bechtold. "Cellular instabilities of expanding hydrogen/ propane spherical flames at elevated pressures: theory and experiment". In: *Proceedings of the Combustion Institute* 30 (2005), pp. 159–167.

[42] S.P.R. Muppala, M. Nakahara, N.K. Aluri, H. Kido, J.X. Wen, and M.V. Papalexandris. "Experimental and analytical investigation of the turbulent burning velocity of two-component fuel mixtures of hydrogen, methane and propane". In: *International Journal of Hydrogen Energy* 34 (2009), pp. 9258–9265.

[43] F. Dinkelacker, B. Manickam, and S.P.R. Muppala. "Modelling and simulation of lean premixed turbulent methane/hydrogen/air flames with an effective Lewis number approach". In: *Combustion and Flame* 158 (2011), pp. 1742–1749.

[44] N. Bouvet, F. Halter, C. Chauveau, and Y. Yoon. "On the effective Lewis number formulations for lean hydrogen/hydrocarbon/air mixtures". In: *International Journal of Hydrogen Energy* 38 (2013), pp. 5949–5960.

[45] B. Karlovitz, D.W. Denniston Jr, D.H. Knapschaefer, and F.E. Wells. "Studies on turbulent flames: A. Flame propagation across velocity gradients B. Turbulence measurement in flames". In: *Proceedings of the Combustion Institute* 4 (1953), pp. 613–620.

[46] M. Matalon. "On flame stretch". In: *Combustion Science and Technology* 31 (1983), pp. 169–181.

[47] A. Buschmann, F. Dinkelacker, T. Schäfer, M. Schäfer, and J. Wolfrum. "Measurement of the instantaneous detailed flame structure in turbulent premixed combustion". In: *Proceedings of the Combustion Institute* 26 (1996), pp. 437–445.

[48] Ö.L. Gülder and G.J. Smallwood. "Flame surface densities in premixed combustion at medium to high turbulence intensities". In: *Combustion Science and Technology* 179 (2007), pp. 191–206.

[49] R.W. Pitz, S. Hu, and P. Wang. "Tubular premixed and diffusion flames: Effect of stretch and curvature". In: *Progress in Energy and Combustion Science* 42 (2014), pp. 1–34.

[50] J. Hult et al. "Measurement of flame surface density for turbulent premixed flames using PLIF and DNS". In: *Proceedings of the Combustion Institute* 31 (2007), pp. 1319–1326.

[51] A. Marshall, J. Lundrigan, P. Venkateswaran, J. Seitzman, and T. Lieuwen. "Fuel effects on leading point curvature statistics of high hydrogen content fuels". In: *Proceedings of the Combustion Institute* 35 (2015), pp. 1417–1424.

[52] G. Damköhler. "The effect of turbulence on the combustion rate in gas compounds". In: *Z. Elektrochem. Angew. Phys. Chem.* 46 (1940), pp. 601–626.

[53] C.K. Law. "Dynamics of stretched flames". In: *Proceedings of the Combustion Institute* 22 (1989), pp. 1381–1402.

[54] J.H. Tien and M. Matalon. "On the burning velocity of stretched flames". In: *Combustion and Flame* 84 (1991), pp. 238–248.

[55] F.A. Williams. "Progress in knowledge of flamelet structure and extinction". In: *Progress in Energy and Combustion Science* 26 (2000), pp. 657–682.

[56] A.N. Lipatnikov and J. Chomiak. "Molecular transport effects on turbulent flame propagation and structure". In: *Progress in Energy and Combustion Science* 31 (2005), pp. 1–73.

[57] C.K. Law. *Combustion physics*. Cambridge university press, Cambridge, UK, 2010.

[58] P.A. Libby and F.A. Williams. "Structure of laminar flamelets in premixed turbulent flames". In: *Combustion and Flame* 44 (1982), pp. 287–303.

[59] Y.-C. Chen and R.W. Bilger. "Experimental investigation of three-dimensional flame-front structure in premixed turbulent combustion: II. Lean hydrogen/air Bunsen flames". In: *Combustion and Flame* 138 (2004), pp. 155–174.

[60] A. Amato, M. Day, R.K. Cheng, J. Bell, and T. Lieuwen. "Leading edge statistics of turbulent, lean, H_2–air flames". In: *Proceedings of the Combustion Institute* 35 (2015), pp. 1313–1320.

[61] J.D. Regele, E. Knudsen, H. Pitsch, and G. Blanquart. "A two-equation model for non-unity Lewis number differential diffusion in lean premixed laminar flames". In: *Combustion and Flame* 160 (2013), pp. 240–250.

[62] S.D. Salusbury and J.M. Bergthorson. "Maximum stretched flame speeds of laminar premixed counter-flow flames at variable Lewis number". In: *Combustion and Flame* 162 (2015), pp. 3324–3332.

[63] P. Venkateswaran, A. Marshall, D.H. Shin, D. Noble, J. Seitzman, and T. Lieuwen. "Measurements and analysis of turbulent consumption speeds of H_2/CO mixtures". In: *Combustion and Flame* 158 (2011), pp. 1602–1614.

[64] R.G. Abdel-Gayed, D. Bradley, M.N. Hamid, and M. Lawes. "Lewis number effects on turbulent burning velocity". In: *Proceedings of the Combustion Institute* 20 (1984), pp. 505–512.

[65] D. Bradley. "How fast can we burn?" In: *Proceedings of the Combustion Institute* 24 (1992), pp. 247–262.

[66] H. Kido, M. Nakahara, K. Nakashima, and J. Hashimoto. "Influence of local flame displacement velocity on turbulent burning velocity". In: *Proceedings of the Combustion Institute* 29 (2002), pp. 1855–1861.

[67] R.S. Barlow, M.J. Dunn, M.S. Sweeney, and S. Hochgreb. "Effects of preferential transport in turbulent bluff-body-stabilized lean premixed CH_4/air flames". In: *Combustion and Flame* 159 (2012), pp. 2563–2575.

[68] E. Boschek, P. Griebel, and P. Jansohn. "Fuel variability effects on turbulent, lean premixed flames at high pressures". In: *Proceedings of the ASME Turbo Expo: Turbine Technical Conference and Exposition. GT2007–27496* (2007).

[69] F. Dinkelacker, B. Manickam, and S.P.R. Muppala. "Modelling and simulation of lean premixed turbulent methane/hydrogen/air flames with an effective Lewis number approach". In: *Combustion and Flame* 158 (2011), pp. 1742–1749.

[70] V.R. Kuznetsov, V.A. Sabel'nikov, and P.A. Libby. *Turbulence and Combustion*. Hemisphere Publishing, Moscow, Russia, 1986.

[71] V.P. Karpov, A.N. Lipatnikov, and V.L. Zimont. "Flame curvature as a determinant of preferential diffusion effects in premixed turbulent combustion". In: *Advances in Combustion Science (Progress in Astronautics and Aeronautics)* 173 (1997), pp. 235–250.

[72] I.G. Shepherd and R.K. Cheng. "The burning rate of premixed flames in moderate and intense turbulence". In: *Combustion and Flame* 127 (2001), pp. 2066–2075.

[73] C.J. Lawn and R.W. Schefer. "Scaling of premixed turbulent flames in the corrugated regime". In: *Combustion and Flame* 146 (2006), pp. 180–199.

[74] H. Kobayashi, T. Tamura, K. Maruta, T. Niioka, and F.A. Williams. "Burning velocity of turbulent premixed flames in a high-pressure environment". In: *Proceedings of the Combustion Institute* 26 (1996), pp. 389–396.

[75] K. Yamamoto, M. Ozeki, N. Hayashi, and H. Yamashita. "Burning velocity and OH concentration in premixed combustion". In: *Proceedings of the Combustion Institute* 32 (2009), pp. 1227–1235.

[76] J. Furukawa, T. Hirano, and F.A. Williams. "Burning velocities of flamelets in a turbulent premixed flame". In: *Combustion and Flame* 113 (1998), pp. 487–491.

[77] J. Furukawa and F.A. Williams. "Flamelet effects on local flow in turbulent premixed Bunsen flames". In: *Combustion Science and Technology* 175 (2003), pp. 1835–1858.

[78] Y. Ikeda, J. Kojima, T. Nakajima, F. Akamatsu, and M. Katsuki. "Measurement of the local flamefront structure of turbulent premixed flames by local chemiluminescence". In: *Proceedings of the Combustion Institute* 28 (2000), pp. 343–350.

[79] K.N.C. Bray and R.S. Cant. "Some applications of Kolmogorov's turbulence research in the field of combustion". In: *Proceedings of the Royal Society of London Series A* 434 (1991), pp. 217–240.

[80] S. Kheirkhah and Ö.L. Gülder. "Consumption speed and burning velocity in counter-gradient and gradient diffusion regimes of turbulent premixed combustion". In: *Combustion and Flame* 162 (2015), pp. 1422–1439.

[81] H. Kolla, J.W. Rogerson, and N. Swaminathan. "Validation of a turbulent flame speed model across combustion regimes". In: *Combustion Science and Technology* 182 (2010), pp. 284–308.

[82] P.J. Trunk, I. Boxx, C. Heeger, W. Meier, B. Böhm, and A. Dreizler. "Premixed flame propagation in turbulent flow by means of stereoscopic PIV and dual-plane OH-PLIF at sustained kHz repetition rates". In: *Proceedings of the Combustion Institute* 34 (2013), pp. 3565–3572.

[83] G. Hartung, J. Hult, R. Balachandran, M.R. Mackley, and C.F. Kaminski. "Flame front tracking in turbulent lean premixed flames using stereo PIV and time-sequenced planar LIF of OH". In: *Applied Physics B* 96 (2009), pp. 843–862.

[84] L.D. Landau. "On the theory of slow combustion". In: *Acta Physicochim (USSR)* 19 (1944), pp. 77–85.

[85] A.G. Istratov and V.B. Librovich. "On the stability of propagation of spherical flames". In: *Journal of Applied Mechanics and Technical Physics* 7 (1966), pp. 43–50.

[86] D. Bradley, T.M. Cresswell, and J.S. Puttock. "Flame acceleration due to flame-induced instabilities in large-scale explosions". In: *Combustion and Flame* 124 (2001), pp. 551–559.

[87] W.K. Kim, T. Mogi, K. Kuwana, and R. Dobashi. "Self-similar propagation of expanding spherical flames in large scale gas explosions". In: *Proceedings of the Combustion Institute* 35 (2015), pp. 2051–2058.

[88] C.R. Bauwens, J.M. Bergthorson, and S.B. Dorofeev. "On the interaction of the Darrieus–Landau instability with weak initial turbulence". In: *Proceedings of the Combustion Institute* 36 (2017), pp. 2815–2822.

[89] F. Wu, G. Jomaas, and C.K. Law. "An experimental investigation on self-acceleration of cellular spherical flames". In: *Proceedings of the Combustion Institute* 34 (2013), pp. 937–945.

[90] Z. Liu, S. Yang, C.K. Law, and A. Saha. "Cellular instability in Le< 1 turbulent expanding flames". In: *Proceedings of the Combustion Institute* 37 (2019), pp. 2611–2618.

[91] S. Yang, A. Saha, F. Wu, and C.K. Law. "Morphology and self-acceleration of expanding laminar flames with flame-front cellular instabilities". In: *Combustion and Flame* 171 (2016), pp. 112–118.

[92] E. Mastorakos, A.M.K.P. Taylor, and J.H. Whitelaw. "Extinction and temperature characteristics of turbulent counterflow diffusion flames with partial premixing". In: *Combustion and Flame* 91 (1992), pp. 40–54.

[93] K. Sardi, A.M.K.P. Taylor, and J.H. Whitelaw. "Conditional scalar dissipation statistics in a turbulent counterflow". In: *Journal of Fluid Mechanics* 361 (1998), pp. 1–24.

[94] D. Geyer, A. Kempf, A. Dreizler, and J. Janicka. "Turbulent opposed-jet flames: A critical benchmark experiment for combustion LES". In: *Combustion and Flame* 143 (2005), pp. 524–548.

[95] F. Hampp and R.P. Lindstedt. "Quantification of combustion regime transitions in premixed turbulent DME flames". In: *Combustion and Flame* 182 (2017), pp. 248–268.

[96] A. Kempf, H. Forkel, J.-Y. Chen, A. Sadiki, and J. Janicka. "Large-eddy simulation of a counterflow configuration with and without combustion". In: *Proceedings of the Combustion Institute* 28 (2000), pp. 35–40.

Chapter 2

Methodology

2.1 Hot-exhaust opposed-flow turbulent flame rig

In this study, the effects of differential diffusion and stretch sensitivity on the propagation, stabilization, and structure of lean turbulent premixed flames are investigated using strained counter-flow flames, in order to study the effects of both components of the flame stretch, i.e., hydrodynamic strain and curvature. In the axial counter-flow configuration, turbulent flames are stretched due to both bulk strain rate and the stretch effects of turbulent eddies through increasing flamelet curvature, while in laminar flames, stretching is mainly due to the bulk hydrodynamic strain rate.

The experiments are carried out using aerodynamically stabilized lifted flames in a hot-exhaust opposed-flow turbulent flame rig (HOTFR) under atmospheric pressure. Similar rigs were previously used in turbulent combustion research at Yale University [1], Imperial College [2–5], University of Cambridge [6–9], and Darmstadt University of Technology [10, 11]. The burner setup is designed to stabilize laminar and turbulent premixed flames from the bottom nozzle against a stream of hot combustion products from a pre-burner inside a ceramic nozzle at the top, in an axial opposed-flow configuration, where the lifted flames are not affected by conductive heat loss to the burners. A co-flow of inert gas, helium (He) or nitrogen (N_2), is used to shroud the reacting mixture and the flame from the surrounding air in order to reduce the effect of the shear layer and stabilize the flame edge. A schematic of the burner setup, as well as sample laminar and turbulent CH_4-air flames at $\phi = 0.8$, are shown in Fig. 2.1.

The rig has a compact design, where the aerodynamically stabilized flames have well-defined boundary conditions, and excellent optical accessibility, which is a key factor in maximizing spatial resolution in flame-location and velocity-field measurements using laser diagnostic techniques. The stagnation plane of hot products allows stabilization of near-adiabatic highly strained laminar and turbulent flames, which is suitable for studying stretch sensitivity on the premixed flame propagation. Furthermore, it allows flames to be stabilized at higher bulk-flow velocities and turbulence

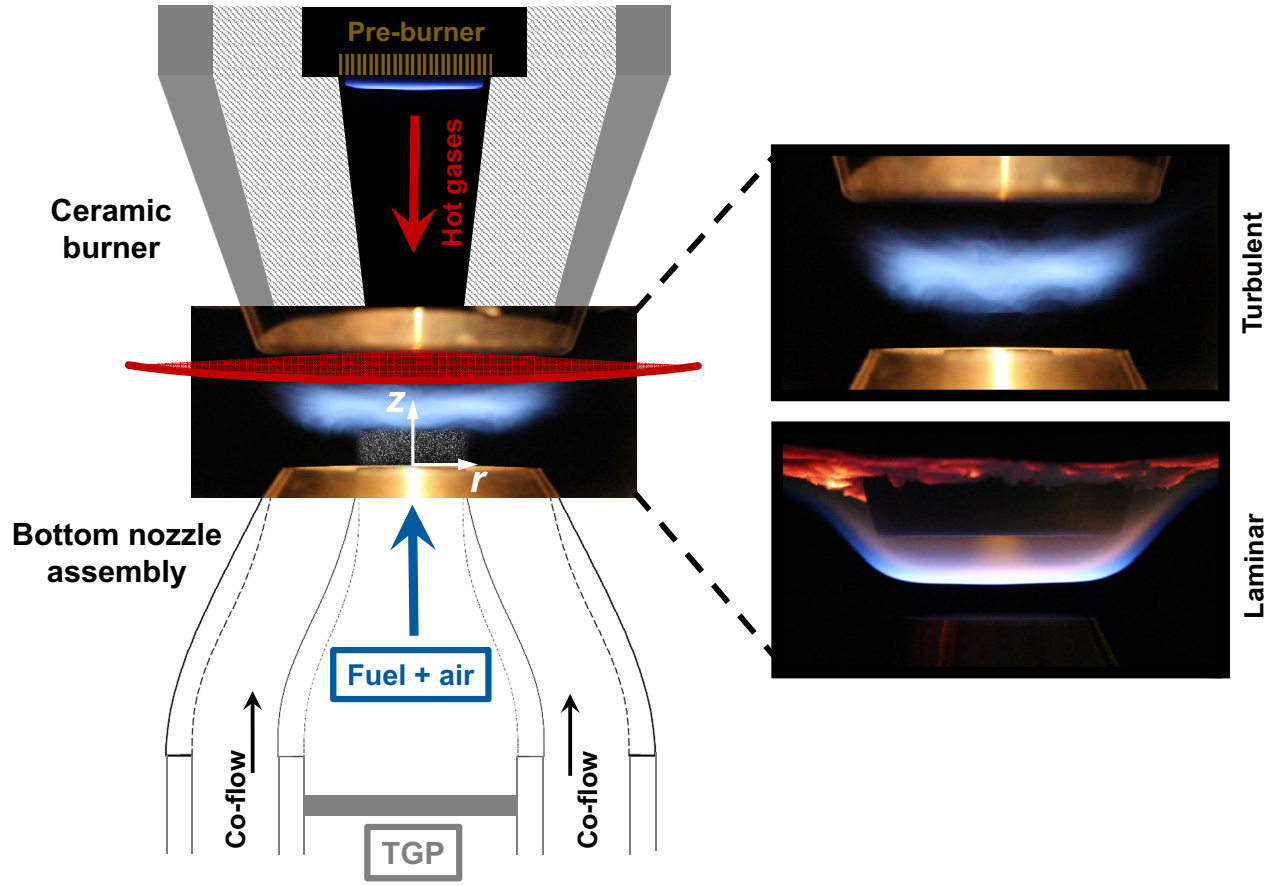

Figure 2.1 Schematic of HOTFR, showing the turbulence-generating plate located upstream of the nozzle contraction, and the direction of the fuel and oxidizing-gas mixture, hot gases, and the co-flow. Sample laminar and turbulent CH_4-air flames at $\phi = 0.8$ are illustrated.

intensities to extend turbulent premixed flames to higher Karlovitz numbers, and into the thin reaction zone regime of the Borghi diagram [12, 13]. These characteristics make the rig convenient both for diagnostics and validating CFD models.

At the bottom section of HOTFR, two concentric inner and outer nozzles deliver the premixed fuel and oxidizing-gas mixture, and the co-flow, respectively, through two separate concentric plena. The inner fuel and oxidizing-gas nozzle has an exit diameter of $d_{\mathrm{N}} = 20\,\mathrm{mm}$, which is attached to the inner plenum of diameter 60 mm, with a contraction ratio of 9:1. Various components of the bottom nozzle are illustrated in Fig. A.5. The interior contour of the nozzle contraction is defined by polynomials that minimize the formation of Taylor-Görtler vortices [14] in the concave portion of the profile, and minimize the angle-of-attack in the convex portion [15]. This contoured design minimizes the bulk-flow instabilities and damps the transition to turbulence, which makes

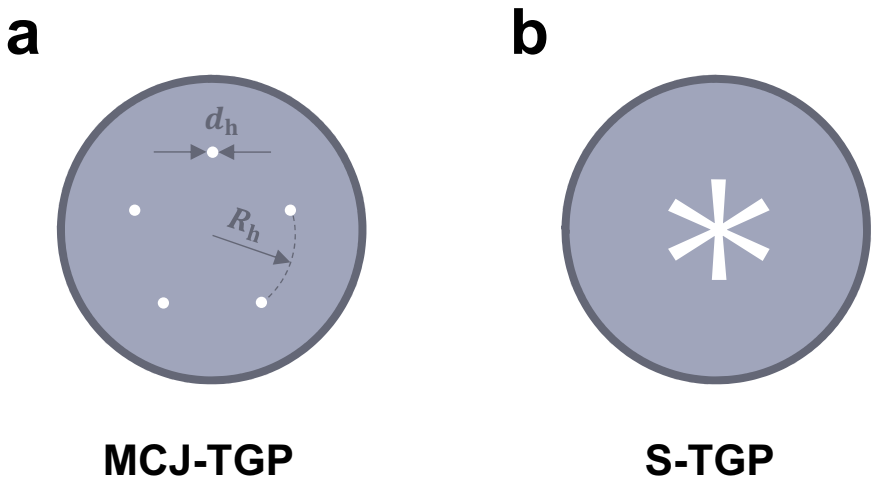

Figure 2.2 TGP designs: (a) MCJ-TGP, where $d_\mathrm{h} = 1.7\,\mathrm{mm}$ and $R_\mathrm{h} = 15\,\mathrm{mm}$, and (b) S-TGP. Design details for S-TGP are found in Appendix A.

the rig suitable for accurate laminar flame experiments in the absence of the turbulence-generating system. The inner and outer plena are filled with alumina (Al_2O_3) beads ($d = 1\,\mathrm{mm}$) to fully laminarize the inlet jets, and to assure uniformity of the flow in the laminar flame experiments. For design details of the bottom nozzle assembly, please see Appendix A.

As discussed in Chapter 1, turbulence is generated using two different designs of high-blockage turbulence-generating plates (TGP), which are located upstream of the bottom nozzle exit in the inner plenum (Fig. 2.1). In the first experimental campaign reported in Chapter 3, a multi-circular plate (MCJ-TGP) is used [1, 16], which has 5 jets with a hole diameter of $d_\mathrm{h} = 1.7\,\mathrm{mm}$ on a radius of $R_\mathrm{h} = 15\,\mathrm{mm}$, with an open area of 0.35 %. In Chapters 4 and 5, turbulence was generated using a star-shaped turbulence-generating plate (S-TGP) with an open area of 2.4 %, which allows higher $u'/\overline{U}$ and a more uniform radial flow compared to MCJ-TGP [16]. The two different TGP designs are illustrated schematically in Fig. 2.2. Since steady-state turbulence decays with distance, the TGPs can be placed at different vertical distances from the nozzle exit, using spacers of different heights, in order to generate various turbulence intensities at constant bulk-flow velocity and bulk hydrodynamic strain rate. Higher turbulence intensity allows premixed combustion in the thin reaction zone of the Borghi diagram [12, 13], and closer to relevant conditions of GTEs and other combustors. In laminar flame experiments, the TGP is removed without changing the flow conditions or mixture compositions.

At the top nozzle assembly, the ceramic burner is made of zirconia (ZrO_2) and is enclosed inside a stainless steel jacket. A water-cooled ceramic honeycomb, embedded inside the ceramic nozzle, acts as a flame-holder; it is located at a vertical distance from the ceramic nozzle exit of

90 mm, as illustrated in Fig. 2.1. Hot exhaust gases from the pre-burner are accelerated to the test domain through a ceramic nozzle with a contraction ratio of 6.25:1. The design details of the top nozzle assembly are found in Appendix A. The separation distance between the two nozzles is adjusted to minimize bulk-flow oscillations, reduce mixing with the inert co-flow or surrounding air, and maintain high strain rates. The separation distance used in the experiments of Chapters 3 and 4 is 1.4 d_{N}, which is reduced to 1.225 d_{N} in Chapter 5.

The momentum balance of the impinging flows from the top and the bottom nozzles sets the location of the stagnation plane. A CH_4-air mixture at $0.7 \leq \phi \leq 0.95$ and $1842\,\mathrm{K} \leq T_{\mathrm{ad}} \leq 2192\,\mathrm{K}$ is used to feed the top nozzle. The top nozzle exit velocity (U_{CB}) and the temperature of the hot exhaust gases at the nozzle exit (T_{CB}) are adjusted to balance the momentum, and deliver the exhaust gases at nozzle exit temperatures in the range of $1400\,\mathrm{K} < T_{\mathrm{CB}} < 2012\,\mathrm{K}$, in these experiments. Libraries are developed through this study that relates the equivalence ratio of the CH_4-air flame and the mass flow rate of the fuel and oxidizing-gas mixture to the flame height on the ceramic honeycomb, in order to define the stability range of the flame, and prevent flashback and blowout. The experiments are started when the surface temperature of the stainless steel nozzle sheathing the ceramic burner reaches around 475 K, measured with a K-type thermocouple on its surface.

The temperature of hot exhaust gases at the ceramic nozzle exit is measured using R-type thermocouples with three different wire (bead) diameters of $d_{\mathrm{TC1}} = 51\,\mu$m, $d_{\mathrm{TC2}} = 127\,\mu$m, and $d_{\mathrm{TC3}} = 203\,\mu$m, at 5 mm distance from the nozzle exit. The temperature readings are corrected for heat losses by extrapolating the measured temperature to a zero junction diameter. Please see Appendix B for the details on the temperature reading corrections for heat losses, and radial temperature profiles within the test domain. Radial temperature profiles are relatively constant, and the repeatability in measuring T_{CB} is $\sim 1\,\%$ of the reading.

Fuels, oxidizing-gas mixture, and inerts are delivered to the top and the bottom nozzles using mass flow controllers (MFC) at room temperature, which are calibrated using a Bios DryCal ML-800-44 dry-piston calibrator before each set of runs, in order to minimize uncertainty in mixture composition. The absolute uncertainty in each MFC's flow rate is reduced to 0.50 % through this calibration process, which reduces the absolute uncertainty in mixture composition to less than 1 %. A portion of the air stream at the bottom nozzle passes through the TSI oil droplet generator Model 9307-6 and is seeded with micron-sized oil droplets as tracer particles for laser diagnostics. The number of Laskin nozzles used in the atomizer controls the seeding density.

2.2 Mixture properties and experimental conditions

In this study, in order to investigate the effects of differential diffusion on the burning rate and structure of lean turbulent premixed flames imposed by variable fuel-oxidizer-inert compositions in the context of fuel flexibility, mixtures with a wide range of effective Lewis numbers are used. To form mixtures with different thermo-diffusive properties, various fuels and fuel blends, through hydrogen enrichment and dilution, are used in combination with various oxidizer-inert mixtures to study variations in both fuel diffusivity and mixture thermal diffusivity. The comprehensiveness of this study allows general conclusions to be drawn on the effects of differential diffusion on the turbulent premixed flame propagation, rather than generating fuel-specific conclusions.

In this thesis, flame characteristics, such as diffusive flame thickness (δ_{L}) and adiabatic flame temperature (T_{ad}), and mixture properties, such as effective Lewis number ($\mathrm{Le_{eff}}$), $\mathrm{Re_T}$, $\mathrm{Ka_T}$, and $\mathrm{Da_T}$ are calculated using Cantera [17]. Furthermore, unstretched laminar flame speed ($S_{\mathrm{L}}^{\mathrm{o}}$) is computed using free-flame simulations in Cantera [17]. GRI-Mech 3.0 and AramcoMech 1.3 reaction mechanisms are used for computations involving CH_4 and C_3H_8, respectively.

Mixture properties and experimental conditions used in these experiments are briefly discussed in this chapter, with detailed explanations presented in *Experimental method* sections in Chapters 3, 4, and 5.

Chapter 3 In this chapter, pure fuel mixtures of H_2-air at $\phi = 0.19$, CH_4-air at $\phi = 0.6$, and C_3H_8-air at $\phi = 0.7$ are used, which represent distinct Lewis numbers of $\mathrm{Le} \ll 1$, $\mathrm{Le} \approx 1$, and $\mathrm{Le} > 1$, respectively. These mixtures were selected based on a previous laminar flame study [18] in the Alternative Fuels Laboratory (AFL) at McGill University, and $S_{\mathrm{L}}^{\mathrm{o}}$ is calculated by extrapolating the experimental results of the stretched laminar flame speeds [18] to zero stretch. Chapter 3 investigates the effects of various turbulence levels, $u'/S_{\mathrm{L}}^{\mathrm{o}}$, on the propagation and stabilization of lean turbulent premixed flames of various commonly used pure fuels in the air, representative of distinct Lewis numbers. These experiments focus on the effects of differential diffusion imposed by increasing turbulence level in mixtures with distinct fuel diffusivity, where various $u'/S_{\mathrm{L}}^{\mathrm{o}}$ values are generated by increasing bulk-flow velocity. Details of mixture properties and experimental conditions are discussed in Chapter 3.

Chapter 4 In this chapter, the aim is to investigate the effects of differential diffusion on local flamelet velocities and stabilization of lean turbulent premixed H_2-enriched CH_4-air and C_3H_8-air flames in the thin reaction zone regime at a constant turbulence level. By using fuel blends in the air, CH_4-H_2 and C_3H_8-H_2, variations in the effective Lewis number of the mixtures are mainly due to a change in fuel diffusivity of the mixture. During H_2 enrichment, in these experiments, unstretched laminar flame speed is kept constant, in order to minimize the effects of chemical

properties of the mixture. Furthermore, bulk-flow properties and the temperature boundary condition are kept constant; hence, the effects of differential diffusion are highlighted. To form mixtures, a CH_4-air flame at $\phi = 0.7$ and a C_3H_8-air flame at $\phi = 0.659$ are selected as reference mixtures, both having a predicted $S_L^o = 0.195$ m/s, at 300 K. During the enrichment process, H_2 is added to the fuel component of the reference mixtures in increments of $10\,\%$ (by volume). At each H_2 content, the mixture equivalence ratio is reduced through iterative free-flame simulations to result in $S_L^o = 0.195 \pm 0.0002$ m/s. For details of the mixtures, please see Chapter 4.

Chapter 5 Experiments in this chapter highlight the effects of differential diffusion at two different turbulence levels on local flamelet velocities, burning rates, flame location, and structure of lean turbulent premixed flames in the thin reaction zone regime, by keeping unstretched laminar flame speed, bulk-flow properties, and the temperature boundary condition constant. In the context of fuel flexibility, various fuel-oxidizer-inert mixtures, with variations in both fuel diffusivity and mixture thermal diffusivity, are studied through H_2 enrichment and dilution. These mixtures are representative of very distinct $\mathrm{Le_{eff}}$ in the range of $0.3 < \mathrm{Le_{eff}} < 3.1$, which spans over a wide range of Lewis numbers. To form mixtures with constant S_L^o, similar to the methodology used in Chapter 4, a CH_4-air flame at $\phi = 0.6$ and $\mathrm{Le_{eff}} \approx 1$ is selected as a reference flame with predicted $S_L^o = 0.115$ m/s at 300 K. Free-flame simulations are used to determine fuel-oxidizer-inert mixtures at $S_L^o = 0.115 \pm 0.0002$ m/s, through H_2 enrichment of hydrocarbon fuels and dilution with various inerts. Properties of the mixtures are presented in Chapter 5. Mixtures with the lower reactivity ($S_L^o = 0.115$), compared to Chapter 4, are used in this chapter, in order to prevent flashback, and extend the experiments to the higher H_2 content mixtures.

2.3 Diagnostic method and processing techniques

2.3.1 Particle image velocimetry

In these experiments, the flow velocity field is quantified using two-dimensional high-speed particle image velocimetry (2D-PIV) within the imaged plane. In PIV, canola oil is atomized using a Laskin nozzle atomizer, and seeded into the flow as tracer particles. The average size of the droplets is $\approx 1\,\mu$m according to the atomizer's specifications. At the test section, atomized oil droplets are illuminated using a thin sheet of visible frequency-doubled neodymium-doped yttrium lithium fluoride (Nd:YLF) laser at 527 nm wavelength. The laser has two heads, pulsing at a repetition rate of 10 kHz and 7.5 mJ per pulse, at each head. The two laser heads allow imaging speed of 20 kHz by keeping the time delay between images constant. The Mie scattered light is captured using a Photron Fastcam SA5 high-speed complementary metal-oxide-semiconductor

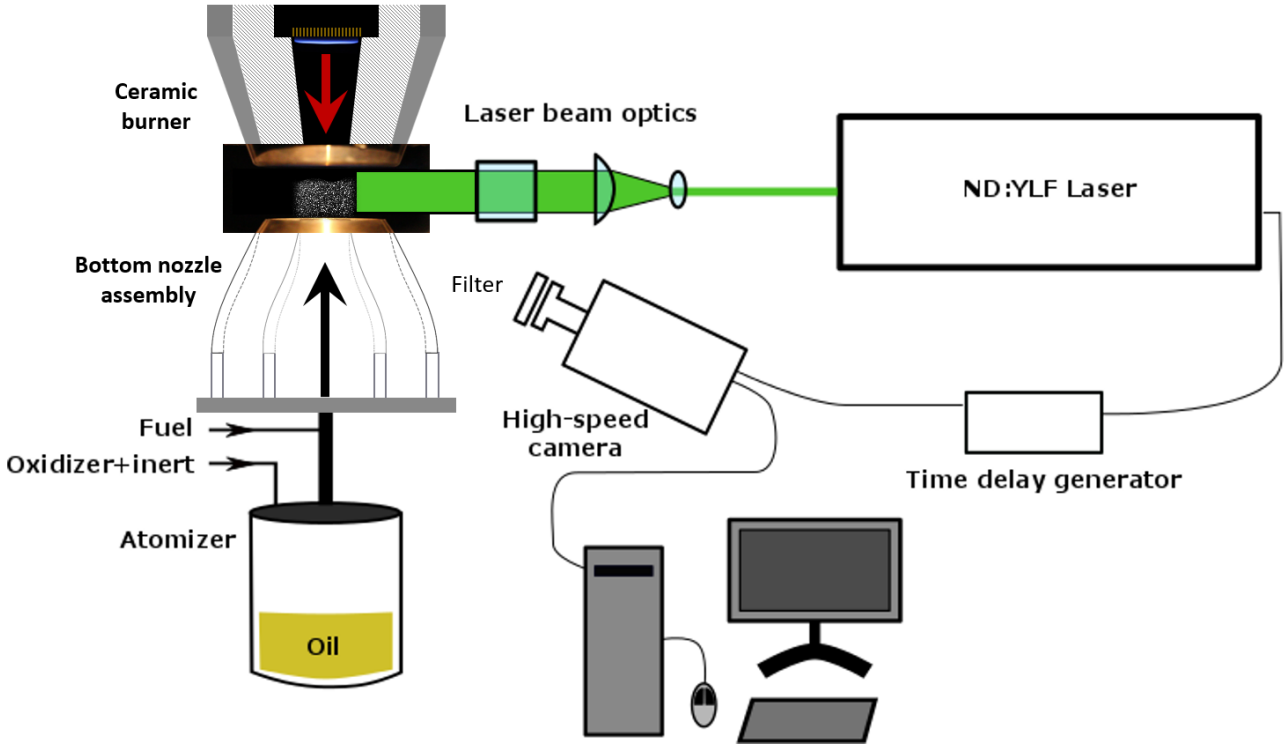

Figure 2.3 Schematic of the PIV setup.

(CMOS) camera. The frequency of the laser matches the frequency of the camera, where the laser heads are triggered by the camera using a time delay generator. In these experiments, an imaging speed (I_{F}) of 3.5-14 kfps, 12 kfps, and 10 kfps, are used in Chapters 3, 4, and 5, respectively. The laser beam is re-directed in order to pass through the test section using several appropriate optics and is focused into a thin sheet of around 1 mm thick. A bandpass filter is also used on the camera lens with transmissivity $\geq$ 95 % in the range of 527 ± 20 nm to reduce flame luminosity in PIV images. The PIV setup is illustrated schematically in Fig. 2.3.

The time delay between illumination pulses must be long enough to provide sufficient resolution in determining the displacement of tracer elements between successive image pairs, and also short enough to prevent particles that are moving in an out-of-plane direction from leaving the laser sheet between subsequent images. Therefore, the frequency of laser pulses is adjusted to result in a large enough tracer particle displacement ($\approx$ 10 pixels based on the bulk-flow velocity), which is equivalent to imaging speed in the range of 3.5 kfps $\leq I_{\mathrm{F}} \leq$ 12 kfps in these experiments. The PIV imaging frequency is kept greater than $I_{\mathrm{F}} > 2 \times (1/\tau_\eta)$, where $1/\tau_\eta$ is the the frequency of the Kolmogorov eddies. These criteria ensure that imaging is fast enough to capture the PIV vector field even at the smallest hydrodynamic turbulence length scale. The duration of each laser-pulse

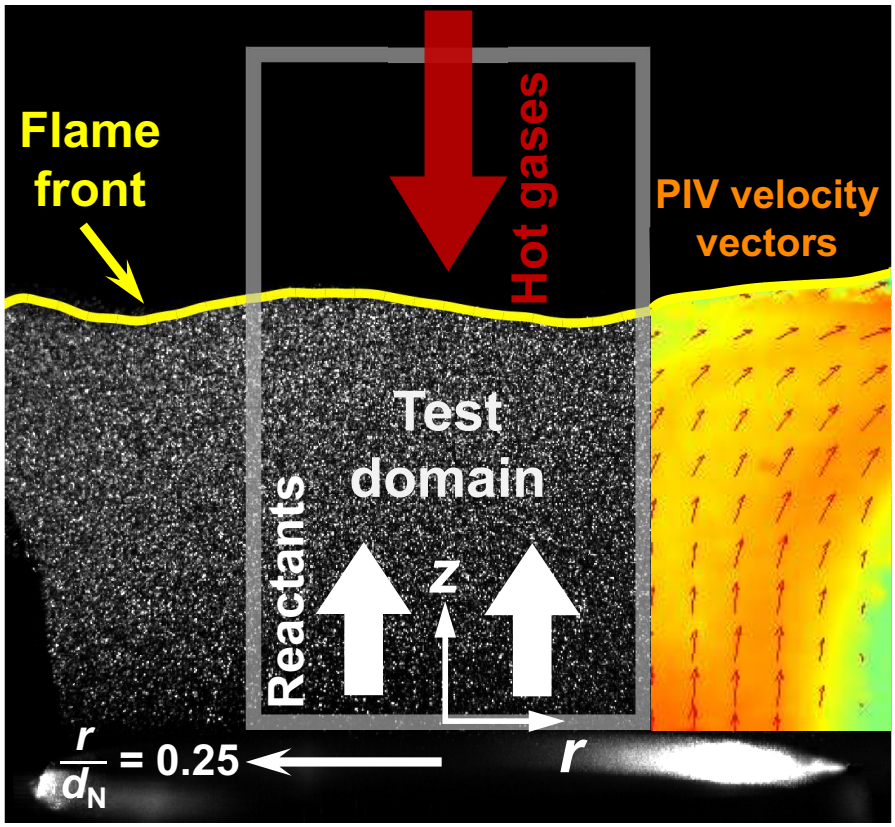

Figure 2.4 Processing techniques: a sample PIV image indicating the test domain, an example flame front, and PIV velocity vectors (the density of the velocity vectors is reduced by 8 times for better visibility).

exposure is short enough to freeze the motion of the atomized oil droplets.

In turbulent flame experiments, 8 000 to 10 000, and in laminar flame experiments, 500 to 1 000 PIV image pairs are post-processed using DaVis 8.2 (a LaVision PIV software package) to calculate the two-component velocity vector field within the plane of the laser sheet. A large number of PIV image pairs is used in data processing to approach the PDF of various flame-parameter statistics. In order to increase the signal-to-noise ratio in calculating instantaneous axial (U) and radial (V) velocities at time t_i, three successive PIV images at t_{i-1}, t_i, and t_{i+1} are considered, and a second-order central-differencing method is used to estimate particle displacement vectors at time t_i. A sample PIV image is illustrated in Fig. 2.4, showing the radial boundaries of the test domain between $-0.25 \leq (r/d_{\mathrm{N}}) \leq 0.25$. Within the plane of the laser sheet, the origin of the 2D coordinate system is located at the center of the bottom nozzle, where r is the radial direction, and the z-axis is normal to the exit plane of the bottom nozzle.

While a large interrogation window size results in too much spatial averaging, a small window size results in too much in-plane pair loss. To this end, a larger interrogation window of size 96 $\times$

96 pixels is refined using a grid-refinement cross-correlation technique to a smallest 16×16 pixel grid in five passes. This sophisticated multi-pass algorithm, with a window overlap of 75 %, repeatedly evaluates the image in order to find the local mean displacements at larger interrogation windows, then, iteratively increases the spatial resolution and evaluates smaller interrogation windows to increase the accuracy, and prevent in-plane pair losses. Vector post-processing techniques are also used to iteratively distinguish the spurious vectors and replace them with interpolated values. The smallest interrogation window size (I_{W}) is chosen to be 16×16 pixel grid to be small enough to avoid the significant influence of velocity gradients. In PIV technique, in order to obtain optimal measurements and to apply the standard statistical PIV evaluation, a homogeneous distribution of tracer elements at a medium density is required to prevent massive multi-scattering from a heavily seeded flow [19]. The inlet flow and the number of Laskin nozzles in the atomizer are adjusted to result in suitable particle density per each interrogation window of approximately $8 - 10$ oil droplets [19].

In order to quantify the PIV flow velocity field, the spatial calibration coefficient (C (pixel/mm)) is determined using images of a Thorlabs grid distortion target with a center-to-center grid-spacing of 1000 ± 1 μm (0.5 mm dot-size), as illustrated in Fig. 2.5. The location of the dots on the calibration image (Fig. 2.5 (b)) is obtained with the gray-scale intensity centroid calculation described in [20], performed on the negative of the calibration image. C is calculated as the average, over all dot-to-dot interstices in the image. The spatial calibration coefficient is 30.7 pixel/mm, 44.7 pixel/mm, and 46.6 pixel/mm in experiments carried out in Chapters 3, 4, and 5, respectively. The resolution of the PIV measurements is improved through modifications on the camera lens system. Statistically independent velocity data is measured at a PIV grid-spacing equal to the smallest interrogation window size ($I_{\mathrm{W}} = 16$ pixels $\approx 521\,\mu$m, $358\,\mu$m, and $343\,\mu$m, in Chapters 3, 4, and 5, respectively), which is considered as the spatial resolution of PIV in these experiments.

In PIV measurements, the velocity lag of tracer particles in regions of high velocity gradients due to particle inertia (relaxation time or Stokes time), as well as uncertainties originating from the correlation statistics from the PIV software, introduces some uncertainty in the flow velocity measurement. While small particles follow the flow better, the scattered light intensity increases with increasing particle size, according to Mie scattering theory [19]. Therefore, there is always a compromise between the velocity-lag of tracer particles and the light illumination factor. Details of uncertainty analysis in the flow velocity measurement are discussed in Appendix C. These calculations result in an uncertainty of approximately 1.5 % in the unburned gas velocity in turbulent flame experiments.

A set of sample PIV validation profiles for laminar and turbulent premixed CH_4-air flames, at $\phi = 0.6$ and $S_{\mathrm{L}}^{\mathrm{o}} = 0.115$ m/s, is illustrated in Fig. 2.6. The mass-averaged bulk-flow velocity at

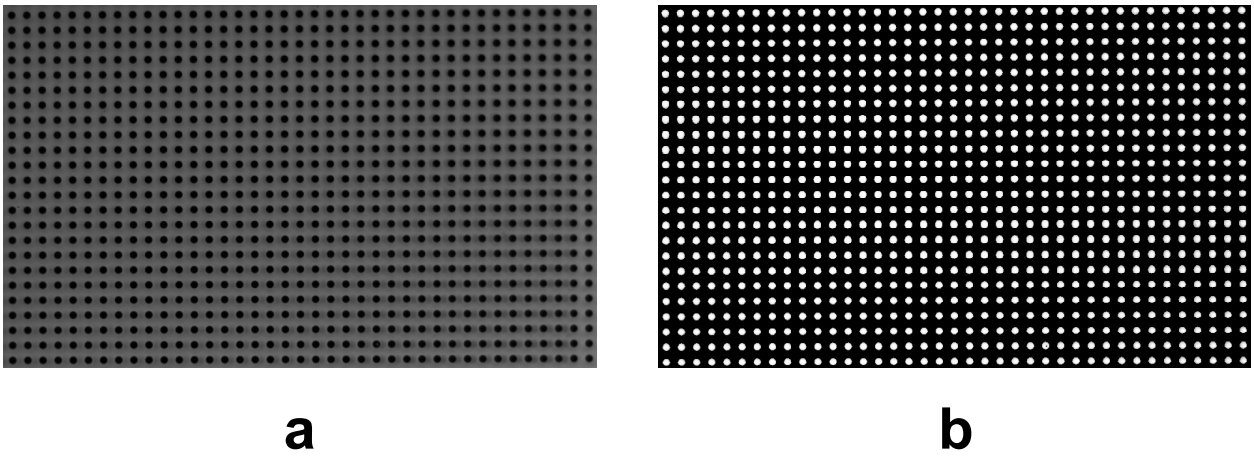

Figure 2.5 PIV calibration target.: (a) image of the target recorded with the SA5 camera, and (b) computer-generated target on the negative of the calibration image. The images are not to scale.

the nozzle exit is 4 m/s. In Fig. 2.6 (a), the mean axial velocities ($\overline{U}$) at the center of the nozzle exit are plotted in the axial direction, and up to the edge of the flame brush in both laminar and turbulent flames. The laminar flame location is steady, while the turbulent flame brush is unsteady and has a higher average burning intensity; hence, the turbulent profile stops far upstream of the laminar one. The velocities decrease as the flow approached the stagnation surface, and the mean velocities overlap for the laminar and turbulent flames. The mean axial ($\overline{U}$) and radial ($\overline{V}$) velocities are plotted against r in Figs. 2.6 (b) and 2.6 (c), respectively, at various axial distances from the nozzle exit (z). In the counter-flow geometry, as the flow approaches the stagnation surface, the streamlines diverge; hence, $\overline{U}$ decreases while $\overline{V}$ increases with increasing z, as illustrated in Fig. 2.6. At various z, $\overline{U}$ profiles are almost flat, and $\overline{V}$ profiles are linear, within the limits of the test domain ($-0.25 \leq (r/d_{\mathrm{N}}) \leq 0.25$). As illustrated in Fig. 2.6 (b), the mean axial velocity within the limits of the test domain at the nozzle exit is approximately 4.5 m/s, which is larger than the mass-averaged bulk-flow velocity of 4 m/s, due to the lower velocities in the boundary layer near the nozzle walls.

2.3.2 Processing techniques

2.3.2.1 Mie scattering flame tomography

Particle image velocimetry and Mie scattering flame tomography allow simultaneous flame location detection and velocity field measurement [21–23], which enables a time-resolved study of the turbulence-chemistry interactions. Atomized oil droplets seeded into the flow evaporate at the

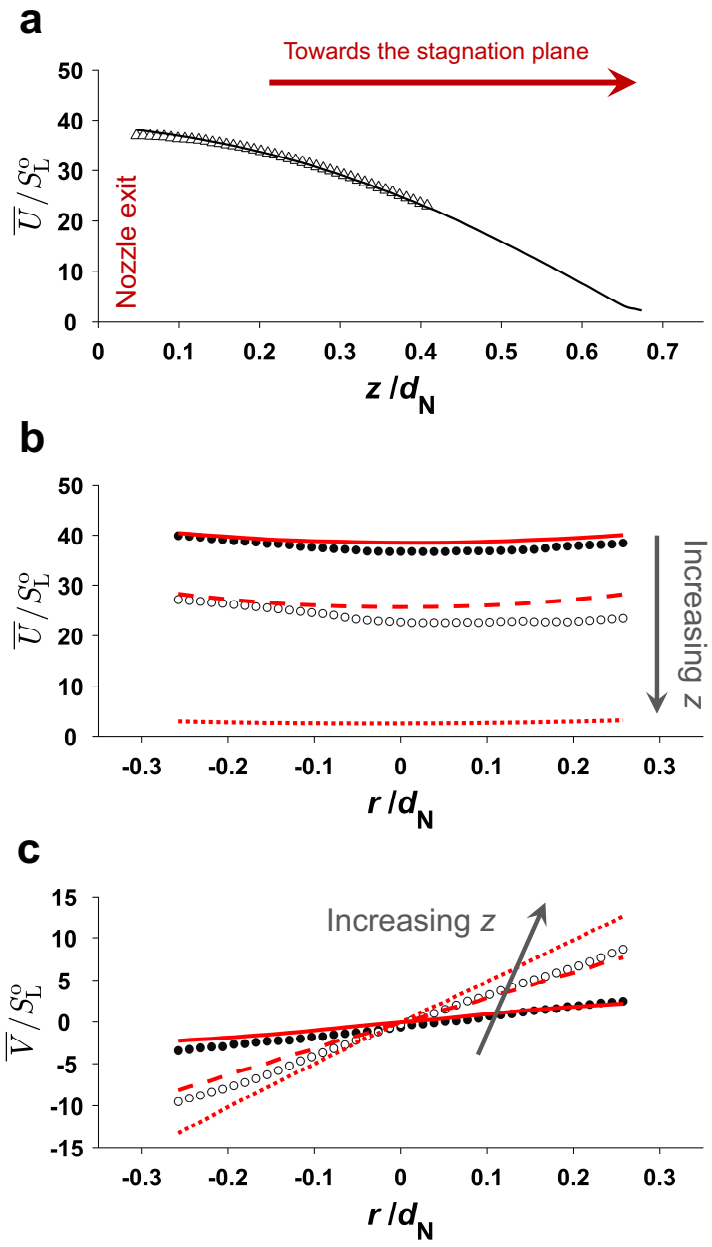

Figure 2.6 Sample PIV velocity profiles for laminar and turbulent premixed CH_4-air flames, at $\phi = 0.6$ and $S_L^o = 0.115$ m/s, (a) the centerline $\overline{U}$ profiles in axial direction for laminar (solid line) and turbulent (triangle), (b) $\overline{U}$, and (c) $\overline{V}$ at various z: turbulent flame at the nozzle exit (solid circle), and upstream of the flame brush (hollow circle). Laminar flame at the nozzle exit (solid line), at mid-distance toward the stagnation surface (dashed line), and upstream of the flame brush (dotted line).

flame front and terminate the Mie scattering of light. Flame surface tracking methods, developed in this study, are used to localize and track the flame front. An example flame front is shown in Fig. 2.4. In this technique, it is assumed that combustion occurs inside a relatively thin layer and that a continuous reaction zone exists. Planar laser-induced fluorescence imaging of hydroxyl radicals (OH-PLIF) is another commonly used technique in turbulent premixed flame studies, where the flame front is identified at the maximum OH gradient in the flame region. One can expect a shift in flame-location statistics, on the order of a flame thickness, when comparing statistics carried out using OH-PLIF and Mie scattering tomography.

In flame-front tracking using Mie scattering tomography, PIV images are first converted to an intensity image, where the pixel intensities range from 0 (black) to 1 (full intensity or white). The normalized image is binarized using the normalized edge threshold (intensity progress variable) of 0.075. The binarized image has the pixel intensity of 0 or 1 and is smoothed using an edge-preserving filtering algorithm, i.e., a combination of Gaussian and Median filters, in order to reduce its sensitivity to noise. Gaussian filtering is commonly used in image processing as it preserves the edges of the image. Laplacian of Gaussian (log) filter is applied to highlight regions of rapid intensity change, which is often used for edge detection. A proper choice of the log filter kernel may sharpen the light-intensity gradients of the flame front and simplify the flame-front tracking. The standard deviation of the Gaussian filter is, iteratively, changed to result in a sufficiently smoothed and continuous flame front. Zero crossings of the log filter correspond to the locations of the maximum gradient and localize the edges. Finally, the instantaneous 2D flame contour within the imaged plane is determined by tracking the image pixels marked as the flame front using the Pavlidis edge-finding algorithm [24]. The stagnation plane location in non-reacting flows is measured using the same methodology, as the oil droplets evaporate at the stagnation plane, due to the hot exhaust gases.

The main uncertainty sources in finding instantaneous flame location are the mean tracer particle distance in the test domain, the oil droplet lifetime at the flame front, uncertainties imposed by filtering processes during the post-processing procedure, and over-saturated pixels from larger oil droplets in PIV images, resulting in a total uncertainty of less than 0.5 δ_{L} in these experiments, where δ_{L} is the laminar flame thickness. The details of uncertainty analysis in flame-front tracking are discussed in Appendix D.

Flame-front tracking methods are also used to extract 2D flame-front topology within the imaged plane, such as local instantaneous flame-front curvature in flame-contour coordinates and normal directions to the flame contour. This data is extracted at each pixel of the flame front using a 4^{th}-order polynomial fitted over a flame-front portion, that is 13-pixel long, and centered at the

desired pixel. Flame-front curvature is calculated as [9, 25, 26]:

$$\kappa = \frac{r'z'' - z'r''}{\left(r'^2 + z'^2\right)^{3/2}} \tag{2.1}$$

where the first and the second derivatives are calculated in flame-contour coordinates. In this study, κ is positive when a curved flamelet is convex toward the reactants and is negative when a curved segment of the flame front is concave toward the reactants.

Instantaneous flame location within the imaged plane is also used to estimate the increase in flame surface area (FSA) of turbulent flames compared to the laminar flames, which is defined as the ratio between the 2D projection of a turbulent flame surface area and an idealized laminar flame in the test section: $A_{\mathrm{T}}/A_{\mathrm{L}}$, where $A_{\mathrm{L}} \approx 10\,\mathrm{mm}$.

2.3.2.2 Local instantaneous velocity measurements

In Eq. 1.6, I_{o} is the local stretch factor, which can be estimated as the ratio of the local stretched flamelet velocity to the unstretched laminar flame speed [23, 27]. In these experiments, I_{o} is defined as the normalized local flamelet displacement velocity: $I_{\mathrm{o}} \approx S_{\mathrm{T}}/S_{\mathrm{L}}^{\mathrm{o}}$, which is a function of differential diffusion. The local instantaneous flamelet displacement velocity (S_{T}) is the propagation velocity of the local flamelet (S_{F}), in the flow coordinate system, relative to the convective velocity of the flow (S_{u}) in the direction normal to the flame surface ($\mathbf{n}$) [27–30]: $S_{\mathrm{T}} = (S_{\mathrm{F}} + S_{\mathrm{u}})\cdot\mathbf{n}$. In order to calculate S_{T}, S_{u} and S_{F} need to be determined. In this study, single-plane PIV imaging within the plane of the laser sheet measures the 2D projection of S_{T}, which is the apparent local flamelet displacement velocity within the imaged plane in the laboratory coordinate system, and is referred to as "local flamelet velocity" for brevity. In laminar flame experiments, $S_{\mathrm{F}} = 0$; hence, S_{u}, which is the unburned gas velocity upstream of the flame front, equals stretched laminar flame velocity, and is referred to as $S_{\mathrm{u-ref}}$.

In the counter-flow geometry, as the premixed jet approaches the stagnation plane, the unburned gas velocity is reduced to a local velocity minimum, after which the flow accelerates through the preheat zone as the density drops due to dilatation. The flame is aerodynamically stabilized at the location where the flame speed is equal to the convective velocity of the flow. The instantaneous two-component unburned gas velocity upstream of the flame front (S_{u}) is calculated in laminar and turbulent flames using the velocity grid network in the vicinity of the normal line to the flame surface within 1.25 mm upstream of the flame front at each location along the flame contour, as seen in Fig. 2.7.

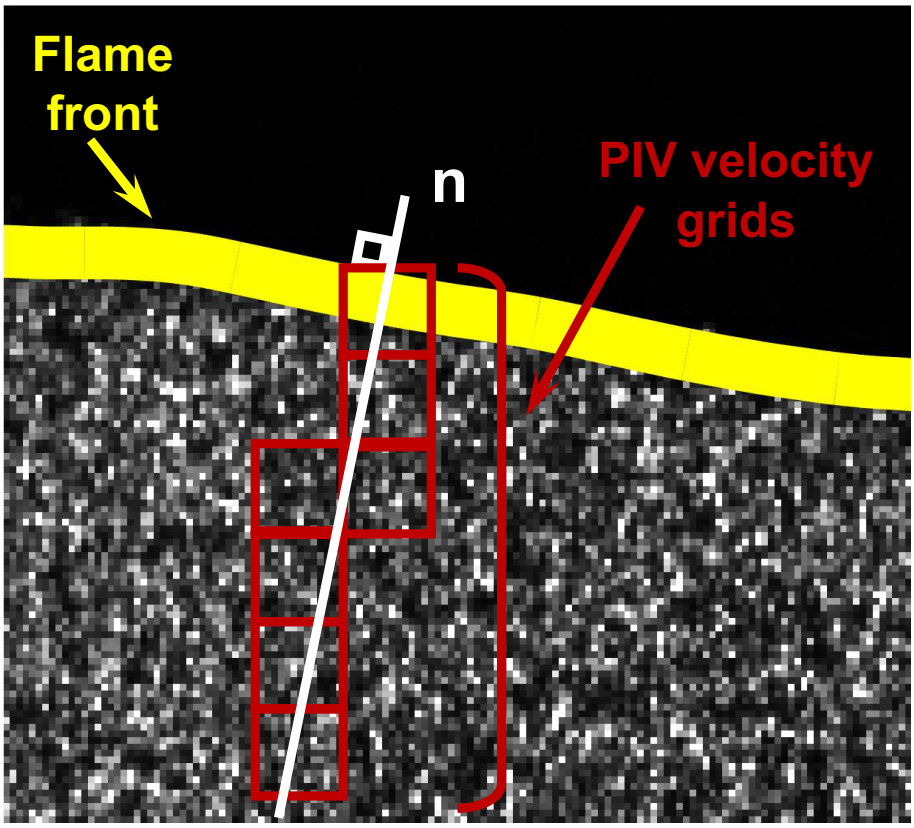

Figure 2.7 Processing techniques: a portion of a sample PIV image near the flame front illustrating measurements of S_{u} and $K_{\mathrm{s-a}}$ (PIV velocity vectors are available at the grid corners).

If S_{u} is extracted within the regions of elevated temperatures in the preheat zone, it needs to be corrected for density changes. However, a sudden change in tracer particle density across the flame front, thermophoretic effects in the high-temperature-gradient region of a flame, and a significant decrease in the signal-to-noise ratio of PIV velocity vectors at the high-temperature region due to vaporization of the oil droplets influence the accuracy of PIV in this region. Therefore, the local minimum velocity at the edge of the preheat zone in the unburned region is considered as the most appropriate local convective velocity. In turbulent flames, this minimum is not always recognized due to the filtering effect of the flame wrinkling; therefore, the average of the two closest measured velocities is considered as the convective velocity. S_{u} is positive when the unburned gas velocity is toward the flame and is negative in the opposite direction.

In order to determine local instantaneous flamelet velocity in the flow coordinate system (S_{F}), image processing techniques, similar to the methods proposed in [31, 32], are used. These techniques are optimized to apply a high-order finite differencing method in the reconstruction of the

flamelet's path between consecutive flame fronts to improve the signal-to-noise ratio in S_{F} calculations of highly turbulent flames. To calculate (S_{F}) at time t_i, 5 successive flame fronts, 2 upstream at t_{i-2} and t_{i-1}, and 2 downstream at t_{i+1} and t_{i+2} are considered. The flamelet's path between 5 consecutive flame fronts within the imaged plane is estimated using four continuous third-order polynomials to reconstruct the flame motion using a continuous streamline, which is perpendicular to all five flame fronts, and the total length is a minimum. For each location along the flame contour at t_i, in increments of 4 pixels in the flame-contour coordinate, the length of a third-order polynomial is minimized between this location and the neighboring front, which is constrained by the normal direction to both fronts, as well as their location. The same procedure is used to determine all four third-order polynomials, which estimates the flamelet's pathway from t_{i-2} to t_{i+2}. A fourth-order finite differencing method is used to estimate the local displacement at each location along the flame contour at t_i, which is used in the calculation of S_{F}. The axial component of S_{F} in the z-direction can be estimated as:

$$S_{\mathrm{F}-z} = \left.\frac{\partial z}{\partial t}\right|_{t_i} = \frac{8\left(z_{t_{i+1}} - z_{t_{i-1}}\right) - \left(z_{t_{i+2}} - z_{t_{i-2}}\right)}{12\Delta t} + O\left(\Delta t^{\,4}\right) \tag{2.2}$$

where Δt is the original inter-frame time interval of the camera. This method is illustrated schematically in Fig. 2.8. S_{F} is considered positive when the flame moves toward the unburned gas and is considered negative in the opposite direction. Spurious flame-front velocity vectors are distinguished using a MATLAB script, and, iteratively, removed and replaced by interpolated velocity vectors. S_{F} and S_{u} are used in the calculation of S_{T}.

2.3.2.3 Local instantaneous hydrodynamic strain rate measurements

In the counter-flow geometry, the instantaneous axial hydrodynamic strain rate ($K_{\mathrm{s-a}}$) is calculated in laminar and turbulent flames using the velocity grid network in the vicinity of the normal line to the flame surface at each location along the flame contour. Projected velocities in the unburned region, over the normal lines to the flame surface, are computed within 1.25 mm upstream of the flame front, as seen in Fig. 2.7. These calculations are done at each segment of the flame front in increments of 4 pixels in the flame-contour coordinate. Along the normal line, the projection and spatial location of each four velocity vectors at the corners of highlighted squares are distance-weighted with respect to the normal line, in order to estimate 5-9 independent velocity vectors and their spatial location along the normal line. The local instantaneous axial hydrodynamic strain rate is computed as the slope of a linear fit to the projected velocities, and their location on the

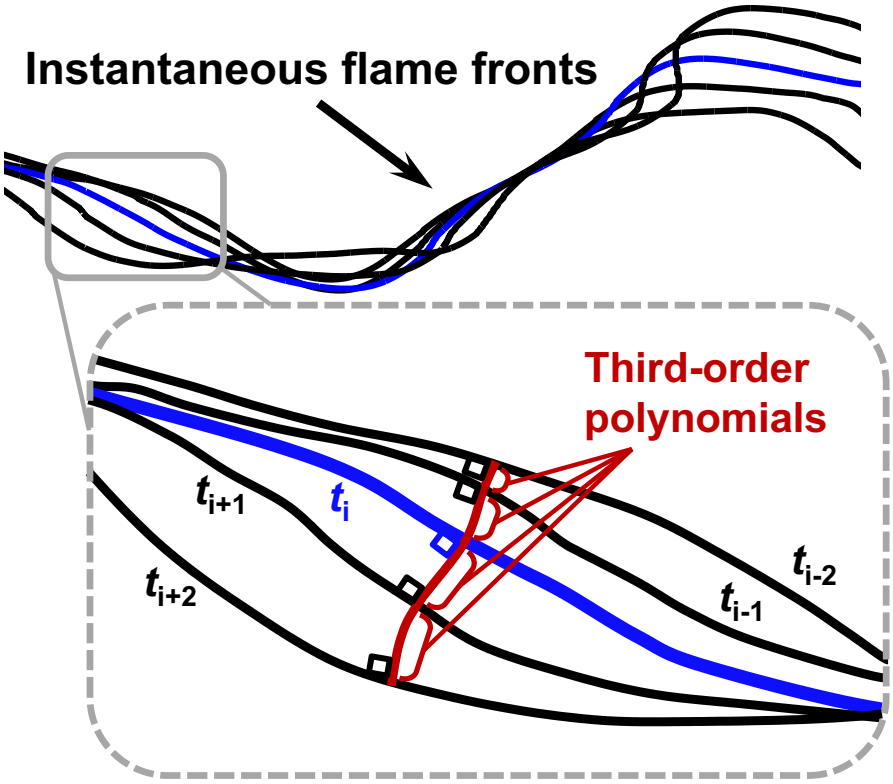

Figure 2.8 Processing techniques: 5 successive flame fronts and a schematic showing S_{F} calculation.

normal line, from 1.25 mm upstream of the flame front, and up to the local velocity minimum, or the closest reliable velocity data to the flame surface.

The local instantaneous tangential hydrodynamic strain rate ($K_{\mathrm{s-t}}$) imposed on laminar and turbulent flames is also calculated in the unburned region over the tangent line to the flame surface at each location along the flame contour in increments of 4 pixels in the flame-contour coordinate. To calculate $K_{\mathrm{s-t}}$ imposed on each segment of the flame front, two velocity vectors centered at this location in the flame-contour coordinate are considered, that are at least 16 pixels apart to ensure the statistical independence of the velocity vectors. A second-order central-differencing method is used to estimate $K_{\mathrm{s-t}}$ (compression or stretch) imposed on this location along the flame contour, using projected velocities onto the tangent line and the distance between the two velocity vectors.

In this study, PIV velocity grids used in data processing must have velocity data measured at that spatial location, and must also be located in the unburned gas region of all three PIV images involved in the second-order finite differencing method used to calculate velocity vectors at each time t. These criteria ensure that velocities used in the calculation of S_{u}, $K_{\mathrm{s-a}}$, and $K_{\mathrm{s-t}}$ are reliable, and the velocity vectors are measured before the evaporation of the oil droplets.

Local instantaneous statistics of various parameters, such as flame location, flame velocity, strain rate, flame-front curvature, and flame surface area are quantified and reported in the form of probability density functions (PDF), where on the order of one million data points are used to improve the statistical accuracy and approach the underlying PDF of various flame-parameter statistics. Angular brackets ($\langle\,\rangle$) are used throughout this thesis to present the *expected value, i.e., mean* of these PDFs.

References

[1] G. Coppola, B. Coriton, and A. Gomez. “Highly turbulent counterflow flames: A laboratory scale benchmark for practical systems”. In: *Combustion and Flame* 156 (2009), pp. 1834–1843.

[2] E. Mastorakos, A.M.K.P. Taylor, and J.H. Whitelaw. “Extinction of turbulent counterflow flames with reactants diluted by hot products”. In: *Combustion and Flame* 102 (1995), pp. 101–114.

[3] E. Mastorakos, A.M.K.P. Taylor, and J.H. Whitelaw. “Extinction and temperature characteristics of turbulent counterflow diffusion flames with partial premixing”. In: *Combustion and Flame* 91 (1992), pp. 40–54.

[4] K. Sardi, A.M.K.P. Taylor, and J.H. Whitelaw. “Conditional scalar dissipation statistics in a turbulent counterflow”. In: *Journal of Fluid Mechanics* 361 (1998), pp. 1–24.

[5] F. Hampp and R.P. Lindstedt. “Quantification of combustion regime transitions in premixed turbulent DME flames”. In: *Combustion and Flame* 182 (2017), pp. 248–268.

[6] L.W. Kostiuk, K.N.C. Bray, and T.C. Chew. “Premixed turbulent combustion in conterflowing streams”. In: *Combustion Science and Technology* 64 (1989), pp. 233–241.

[7] L.W. Kostiuk, K.N.C. Bray, and R.K. Cheng. “Experimental study of premixed turbulent combustion in opposed streams: Part I—Nonreacting flow field”. In: *Combustion and Flame* 92 (1993), pp. 377–395.

[8] L.W. Kostiuk, K.N.C. Bray, and R.K. Cheng. “Experimental study of premixed turbulent combustion in opposed streams: Part II–Reacting flow field and extinction”. In: *Combustion and Flame* 92 (1993), pp. 396–409.

[9] L.W. Kostiuk, I.G. Shepherd, and K.N.C. Bray. “Experimental study of premixed turbulent combustion in opposed streams. Part III–Spatial structure of flames”. In: *Combustion and Flame* 118 (1999), pp. 129–139.

[10] D. Geyer, A. Kempf, A. Dreizler, and J. Janicka. “Turbulent opposed-jet flames: A critical benchmark experiment for combustion LES”. In: *Combustion and Flame* 143 (2005), pp. 524–548.

[11] A. Kempf, H. Forkel, J.-Y. Chen, A. Sadiki, and J. Janicka. “Large-eddy simulation of a counterflow configuration with and without combustion”. In: *Proceedings of the Combustion Institute* 28 (2000), pp. 35–40.

[12] R. Borghi. "On the structure and morphology of turbulent premixed flames". In: *Recent Advances in the Aerospace Sciences* (1985), pp. 117–138.

[13] N. Peters. *Turbulent combustion*. Cambridge university press, Cambridge, UK, 2000.

[14] H.W. Liepmann. *Investigations on laminar boundary-layer stability and transition on curved boundaries*. Tech. rep. NACA Wartime Report W-107. ACR No. 3H30. 1943.

[15] J.M. Bergthorson. *Experiments and modeling of impinging jets and premixed hydrocarbon stagnation flames*. PhD thesis, California Institute of Technology, 2005.

[16] G. Coppola and A. Gomez. "Experimental investigation on a turbulence generation system with high-blockage plates". In: *Experimental Thermal and Fluid Science* 33 (2009), pp. 1037–1048.

[17] D.G. Goodwin, H.K. Moffat, and R.L. Speth. *Cantera: A software toolkit for chemical kinetics, thermodynamics, and transport processes*. Version 2.2.1, http://www.cantera.org, 2016.

[18] S.D. Salusbury and J.M. Bergthorson. "Maximum stretched flame speeds of laminar premixed counter-flow flames at variable Lewis number". In: *Combustion and Flame* 162 (2015), pp. 3324–3332.

[19] M. Raffel, C.E. Willert, S. Wereley, and J. Kompenhans. *Particle image velocimetry: a practical guide*. Springer, 2013.

[20] P. Versailles. *CH formation in premixed flames of C_1–C_4 alkanes: assessment of current chemical modeling capability against experiments*. PhD thesis, McGill University, 2018.

[21] T. Lachaux, F. Halter, C. Chauveau, I. Gökalp, and I.G. Shepherd. "Flame front analysis of high-pressure turbulent lean premixed methane–air flames". In: *Proceedings of the Combustion Institute* 30 (2005), pp. 819–826.

[22] S.A. Filatyev, J.F. Driscoll, C.D. Carter, and J.M. Donbar. "Measured properties of turbulent premixed flames for model assessment, including burning velocities, stretch rates, and surface densities". In: *Combustion and Flame* 141 (2005), pp. 1–21.

[23] S. Kheirkhah and Ö.L. Gülder. "Consumption speed and burning velocity in counter-gradient and gradient diffusion regimes of turbulent premixed combustion". In: *Combustion and Flame* 162 (2015), pp. 1422–1439.

[24] T. Pavlidis. *Algorithms for graphics and image processing*. Springer Science & Business Media, 2012.

[25] M.Z. Haq, C.G.W. Sheppard, R. Woolley, D.A. Greenhalgh, and R.D. Lockett. "Wrinkling and curvature of laminar and turbulent premixed flames". In: *Combustion and Flame* 131 (2002), pp. 1–15.

[26] Y.-C. Chen. "Measurements of flame-front curvature based on Fourier transformation". In: *Combustion Theory and Modelling* 11 (2007), pp. 333–349.

[27] J.F. Driscoll. "Turbulent premixed combustion: Flamelet structure and its effect on turbulent burning velocities". In: *Progress in Energy and Combustion Science* 34 (2008), pp. 91–134.

[28] H. Kolla, J.W. Rogerson, and N. Swaminathan. "Validation of a turbulent flame speed model across combustion regimes". In: *Combustion Science and Technology* 182 (2010), pp. 284–308.

[29] P.J. Trunk, I. Boxx, C. Heeger, W. Meier, B. Böhm, and A. Dreizler. "Premixed flame propagation in turbulent flow by means of stereoscopic PIV and dual-plane OH-PLIF at sustained kHz repetition rates". In: *Proceedings of the Combustion Institute* 34 (2013), pp. 3565–3572.

[30] G. Hartung, J. Hult, R. Balachandran, M.R. Mackley, and C.F. Kaminski. "Flame front tracking in turbulent lean premixed flames using stereo PIV and time-sequenced planar LIF of OH". In: *Applied Physics B* 96 (2009), pp. 843–862.

[31] R. Abu-Gharbieh, G. Hamarneh, T. Gustavsson, and C.F. Kaminski. "Flame front tracking by laser induced fluorescence spectroscopy and advanced image analysis". In: *Optics Express* 8 (2001), pp. 278–287.

[32] R. Abu-Gharbieh, G. Hamarneh, T. Gustavsson, and C.F. Kaminski. "Level set curve matching and particle image velocimetry for resolving chemistry and turbulence interactions in propagating flames". In: *Journal of Mathematical Imaging and Vision* 19 (2003), pp. 199–218.

Chapter 3

Fuel variation effects in propagation and stabilization of turbulent counter-flow premixed flames

Publication (1)[1]**:** E. Abbasi-Atibeh, S. Jella, and J. M. Bergthorson. *Journal of Engineering for Gas Turbines and Power* 141 (2018), pp. 031024. http://dx.doi.org/10.1115/1.4041136.

3.1 Abstract

Sensitivity to stretch and differential diffusion of chemical species are known to influence the premixed flame propagation, even in the turbulent environment where mass diffusion can be greatly enhanced. In this context, it is convenient to characterize flames by their Lewis number, a ratio of thermal-to-mass diffusivities. The work reported in this paper describes a study of flame stabilization characteristics when the Lewis number is varied. The test data is comprised of $\mathrm{Le} \ll 1$ (hydrogen), $\mathrm{Le} \approx 1$ (methane), and $\mathrm{Le} > 1$ (propane) flames stabilized at various turbulence levels. The experiments were carried out in a hot exhaust opposed-flow turbulent flame rig (HOTFR), which consists of two axially-opposed, symmetric jets. The stagnation plane between the two jets allows the aerodynamic stabilization of a flame, and clearly identifies fuel influences on turbulent flames. Furthermore, high-speed particle image velocimetry (PIV), using oil droplet seeding, allowed simultaneous recordings of velocity (mean and rms) and flame-front location. These experiments, along with the data-processing tools developed through this study, illustrated that, in the mixtures with $\mathrm{Le} \ll 1$, turbulent flame speed increases considerably compared to the laminar

[1]**Copyright © 2019 by Siemens Canada Ltd.**

flame speed due to the differential diffusion effects, where higher burning rates compensate for the steepening average velocity-gradients, and keeps these flames almost stationary as bulk flow velocity increases. These experiments are suitable for validating the ability of turbulent combustion models to predict lifted, aerodynamically-stabilized flames. In the final part of this paper, we model the three fuels at two turbulence intensities using the flamelet generated manifolds (FGM) model in a Reynolds-averaged Navier–Stokes (RANS) context. Computations reveal that the qualitative flame stabilization trends reproduce the effects of turbulence intensity, however, more accurate predictions are required to capture the influences of fuel variations and differential diffusion.

3.2 Introduction

Most of the world's required energy in industrial systems and transportation is provided through combustion. Lean premixed combustion is a promising approach for reducing pollutants, such as nitric oxides, NO_x, and soot. Lean premixed ultra-low-emission gas-turbine engines (GTE) play a significant role in the power generation industry. However, fuel flexibility of these lean premixed combustors is also an important feature of these engines, as lean premixed turbulent combustion of mixtures with different chemistry and transport properties, originating from various non-renewable (fossil fuels) and renewable sources, brings large uncertainty in the design process and operability properties of these engines. Fuel flexibility addresses two main issues: (1) difference in chemical properties of the combustible mixture (fuel+air), which is clearly seen in hydrogen-enrichment of hydrocarbon fuels in laminar flame studies [1, 2], and (2) difference in transport properties (diffusivity of deficient species), which plays an important role in the propagation of premixed flames. The effect of transport properties is clearly seen in the study carried out by Boschek *et al.* [3], where it was illustrated that, with increasing the hydrogen, H_2, concentration in methane, CH_4, flames, the laminar flame speed increased linearly while the turbulent flame speed rapidly diverged from the behavior of laminar flames at higher H_2 concentrations, and increased non-linearly toward much higher velocities.

A turbulent flame is stretched due to the bulk hydrodynamic strain (K_s), and the stretch effects of turbulent eddies in the flow, which can be expressed by flame curvature (κ) [4]: $K = S_{\mathrm{L}}\kappa + K_s$, where K is the flame stretch rate. The effects of stretch are highly important in the propagation of premixed flames in both laminar flames [5–7], and in turbulent flames [8–11].

The stretch sensitivity in the flame propagation is shown by the Lewis number (Le), which defines the balance between the thermal diffusivity of the mixture (α), and the mass diffusivity of

the deficient reactant ($\mathcal{D}$) (fuel in lean, and oxidizer in rich combustion), at the flame front. The disparity between thermo-diffusive properties, α and $\mathcal{D}$, is known as *differential diffusion*.

Many researchers have studied the effects of Lewis number in the propagation of turbulent flames [12–16]. A number of studies reported differential diffusion effects with a focus on measuring the burning velocity and consumption speed of turbulent flames [9, 17], as well as on the local flamelet velocity, and flame-front structure measurements [18, 19]. However, the time-averaged measurements of turbulent flame properties reported in the majority of these studies, do not necessarily yield local information on the physics of turbulent flame propagation at an instantaneous scale [20]. Therefore, in this study, statistical methods are used to describe instantaneous local properties of turbulent premixed flames, such as flame location and turbulent flame speed, based on probability density functions (PDF). These experiments investigate the effects of differential diffusion on the propagation of turbulent premixed flames of lean H_2-air, CH_4-air, and C_3H_8-air mixtures, representative of low ($\mathrm{Le} \ll 1$), unity ($\mathrm{Le} \approx 1$), and high ($\mathrm{Le} > 1$) Lewis numbers, respectively.

These experiments are conducted in a powerfully simple geometry of hot exhaust opposed-flow turbulent flame rig (HOTFR) [21–23]. The rig has a compact geometry, excellent optical accessibility, and well-defined boundary conditions, where aerodynamically-stabilized lifted flames are not affected by conductive heat loss to the burner. Furthermore, the counter-flowing hot exhaust gases enable turbulent flames to be stabilized at higher bulk flow velocities and turbulence intensities, which enables turbulent flame experiments to be extended to higher Karlovitz numbers (Ka), and assures sustaining turbulent combustion in the thin reaction zone regime of the Borghi diagram [24]. These characteristics make the rig convenient both for diagnostics, and computational studies, and allows experiments closer to relevant conditions of GTEs and other combustors.

The experiments provide data to evaluate design tools in the field of turbulent combustion, specifically fuel flexibility. Accordingly, computations for all three fuels, at two different turbulence intensities (lowest and highest for each fuel), were carried out to complement the experiments and obtain additional insight. The computations make use of the flamelet-progress variable (FPV) approach, a regularly used framework in the industry due to its low computational overhead. The economy comes from being able to tabulate chemistry based on the assumption that a turbulent flame may be considered as an ensemble of locally laminar *flamelets*, whose structure can be pre-calculated for a range of strain rates, equivalence ratios, and heat loss effects [25, 26], parametrized by a reaction progress variable, and referenced during run time. A priori flamelet calculations use *flamelet generated manifolds* (FGM) [27], as a chemistry reduction technique, while creating a database of strained flamelets in composition space. Since finite-rate chemistry effects can be incorporated at the flame front, this method is capable of predicting lifted flames. It is of

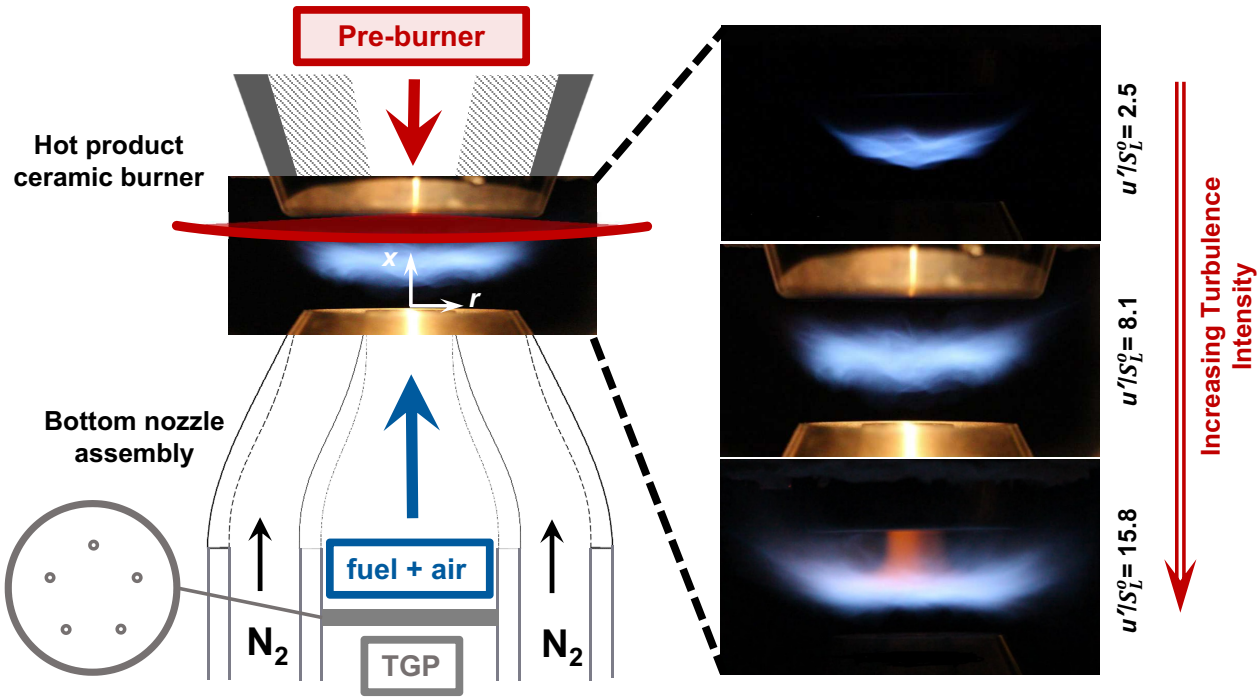

Figure 3.1 Schematic of the hot exhaust opposed-flow turbulent flame rig (HOTFR) and stabilized CH_4-air turbulent flames at increasing turbulence intensities.

interest, therefore, to evaluate its ability to reproduce the flame stabilization trends observed in the experiments described in this paper.

3.3 Experimental method

3.3.1 Turbulent counter-flow burner

In these experiments, lean premixed turbulent flames of H_2-air at equivalence ratio of $\phi = 0.19$, CH_4-air at $\phi = 0.6$, and C_3H_8-air at $\phi = 0.7$ are stabilized in a hot exhaust opposed-flow turbulent flame rig (HOTFR) under atmospheric pressure. These mixtures are representative of distinct Lewis numbers of $\mathrm{Le} \ll 1$, $\mathrm{Le} \approx 1$, and $\mathrm{Le} > 1$, respectively. The rig consists of two axially-opposed, symmetric turbulent round jets. The two jets issue from a stainless steel nozzle on one side (the reactant mixture side) and a ceramic burner nozzle on the opposing side (hot product side). A schematic of HOTFR is illustrated in Fig. 3.1. The premixed fuel and air mixture from the bottom nozzle accelerates toward the test domain, and the flame impinges against hot exhaust gases from the ceramic burner at the top. The balance of momentum at the stagnation plane between the two jets allows the formation of an aerodynamically-stabilized flame. The excellent optical access

Table 3.1 Properties of the laminar flames.

	C_3H_8 + Air	CH_4+ Air	H_2 + Air
ϕ	0.7	0.6	0.19
Le	1.860	0.976	0.334
δ_{L} (mm)	0.247	0.433	0.516
T_{ad} (K)	1889	1668	898
$S_{\mathrm{L}}^{\mathrm{o}}$ (m/s)	0.197	0.115	0.875
S_{L} (at 576 K) (m/s)	0.378	0.221	0.168

allows well-defined boundary conditions, and clearly identifies fuel influences on turbulent flames. The stabilizing effect of the hot products allows higher turbulence intensities.

The premixed fuel and air nozzle assembly at the bottom consists of two concentric sets of plena and nozzles. The inner nozzle, with an exit diameter of $d_{\mathrm{N}} = 20$ mm and the contraction ratio of 9:1, is attached to a plenum of diameter 60 mm, and delivers the premixed fuel and air mixture to feed the turbulent flame. The nozzle centerline bulk flow velocity at the nozzle exit (U_{NE}) varies between 0.9 m/s $\leq U_{\mathrm{NE}} \leq$ 5.6 m/s in these experiments. The outer nozzle (co-flow nozzle) provides a flow of nitrogen, N_2, as a co-flow to shroud the flame from the surrounding environment and stabilize the edge of the flame. Furthermore, the flame is only studied within the radial boundaries of $-0.25 \leq (r/d_{\mathrm{N}}) \leq 0.25$, away from the flame edge and the shear layer with the co-flow. A portion of air delivered to the bottom nozzle is passed through an atomizer, where Laskin nozzles are used to generate atomized oil droplets as seeding particles in laser diagnostics. In order to generate high intensity turbulence at the test domain, a multi-circular turbulence generating plate (TGP) is used [21, 28], as illustrated in Fig. 3.1. The plate has 5 jets with a hole diameter of 1.7 mm on a radius of 15 mm, with an open area of 0.4 %. The TGP is located in the inner plenum at a vertical distance from the nozzle exit of 123 mm.

The exhaust gases are generated using a water-cooled pre-burner inside a ceramic nozzle with a contraction ratio of 6.25:1, and at a vertical distance from the nozzle exit of 90 mm. CH_4-air mixtures at equivalence ratios of $0.75 \leq \phi \leq 0.85$ are used to feed the ceramic burner. The nozzle exit velocity (U_{CB}) and the equivalence ratio of the mixture is adjusted to balance the momentum, and deliver the exhaust gases at nozzle exit temperatures (T_{CB}) of 1400 K$< T_{\mathrm{CB}} <$ 1900 K.

The required fuel, air, and inert flows are delivered to the rig using mass flow controllers (MFC), calibrated using a Bios DryCal ML-800-44 dry-piston calibrator to reduce uncertainty in mixture composition. Multiple opposed-flow jets of fuel-air mixtures, along with mixing vessels upstream of the nozzles, help to maximize the mixing of the fuel and air in a confined system. Furthermore, alumina, Al_2O_3, beads with a diameter of 1 mm are used upstream of the nozzles'

Table 3.2 Experimental conditions of turbulent C_3H_8-air flames at $\phi = 0.7$, CH_4-air flames at $\phi = 0.6$, and H_2-air flames at $\phi = 0.19$.

	$U/S_{\mathrm{L}}^{\mathrm{o}}$	$u'/S_{\mathrm{L}}^{\mathrm{o}}$	L/δ_{L}	$\mathrm{Re_T}$	$\mathrm{Ka_T}$	T_{CB} [K]
C_3H_8	4.6	1.4	8.6	12.7	0.6	1504
	13.5	4.6	8.6	41.0	3.6	1824
	21.1	6.5	8.7	59.3	6.1	1916
	26.4	9.1	10.3	97.2	9.1	1907
CH_4	8.8	2.5	5.7	14.4	1.7	1455
	25.1	8.1	5.5	45.3	9.9	1738
	35.8	11.2	5.2	59.9	16.8	1797
	48.7	15.8	6.6	106.6	25.1	1841
H_2	13.1	3.5	4.1	12.4	2.6	1396
	32.2	10.9	4.5	42.8	13.8	1760
	42.9	16.2	5.2	73.5	22.9	1806
	63.4	19.8	4.8	81.7	32.7	1786

exit in the plena to enhance the mixing.

Properties of fuel and air mixtures, used in this study, are listed in Table 3.1. Lewis number is calculated as: $\mathrm{Le} = \alpha/\mathcal{D} = \lambda/(\rho c_{\mathrm{p}}\mathcal{D})$, where λ is the thermal conductivity, c_{p} is the specific heat, and ρ is the density of the unburned reactants. Lewis number, adiabatic flame temperature (T_{ad}), and diffusive flame thickness ($\delta_{\mathrm{L}} \approx \alpha/S_{\mathrm{L}}^{\mathrm{o}}$) are calculated using free-flame simulations in Cantera [29]. Unstretched laminar flame speed ($S_{\mathrm{L}}^{\mathrm{o}}$) is calculated by extrapolating the experimental results of the stretched laminar flame speeds reported in [30] to a zero stretch.

The temperature of hot exhaust gases at the ceramic nozzle exit (T_{CB}), is measured using R-type thermocouples with three different wire (bead) diameters at 5 mm distance from the nozzle exit. The temperature readings are corrected for heat losses by extrapolating the measured temperature to a zero diameter. Please see Appendix B for the details on the correction of temperature readings. These calculations are done according to the details found in [31, 32]. The estimated values of T_{CB} are reported in Table 3.2.

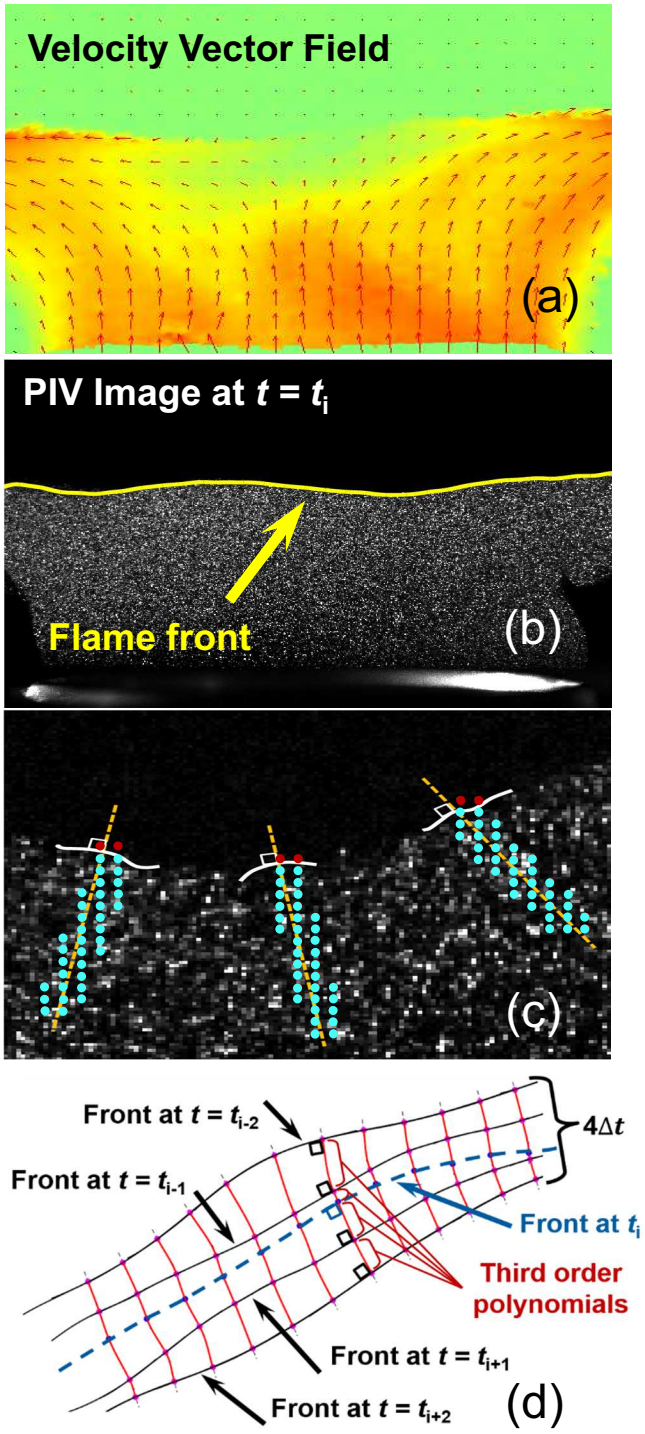

Figure 3.2 Processing techniques using PIV images: (a) a sample velocity vector field (down-sampled for clarity), (b) a sample flame front contour, (c) S_u measurement upstream of the flame front, and (d) 5 successive flame fronts centered at time t_i and a schematic showing S_F calculation.

3.3.2 Particle image velocimetry and processing techniques

In these experiments, the flow velocity field is quantified using two-dimensional high-speed particle image velocimetry (2D-PIV) within the imaged plane. In this method, a Nd:YLF laser at 527 nm-wavelength is used to illuminate oil droplets seeded into the flow, and the Mie scattered light is captured by a high-speed CMOS camera (see Fig. 3.2 (b)). The imaging frequency ranges from 3.5 kfps to 14 kfps, and around 10 000 PIV image pairs are post-processed using DaVis (a PIV software package) to calculate the velocity vector fields, as illustrated in Fig. 3.2 (a). The smallest interrogation window used in PIV calculations is a 16 $\times$ 16 pixel grid, and the pixel-to-mm ratio is 30.7, yielding the PIV spatial resolution of ≈ 521 μm.

Turbulent flow statistics of the mean ($\overline{U}$) and root-mean-square (rms) of velocity fluctuations (u' in the axial direction and v' in the radial direction) are calculated using instantaneous velocity vector measurements through Reynolds decomposition: $U(r,x,t) = \overline{U}(r,x) + u(r,x,t)$, where r and x are the radial and axial positions, respectively, at time t. The integral length scale (L) is also estimated using rms velocities by integrating the autocorrelation coefficient from zero up to the first zero-crossing as discussed in [33, 34]: $L = \int R_{\mathrm{uu}}(r,t)\ \mathrm{d}r$. These results are listed in Table 3.2. In these experiments, turbulence intensity (u'/U) varies between $44\,\% \leq (u'/U) \leq 60\,\%$. For uncertainty analysis of the flow velocity measurement, please see Appendix C.

Atomized canola oil droplets are used as seeding particles in PIV. At the flame front, oil droplets evaporate and disappear from the Mie scattering images, which allows surface tracking methods to determine instantaneous flame front contours within the plane of the laser sheet, as seen in Fig. 3.2 (b). A similar method was used in previous studies for characterizing the flame front, see for example [35, 36]. In flame front tracking, binarized PIV images are smoothed using edge preserving filtering, in order to reduce its sensitivity to noise. Laplacian Of Gaussian (LOG) filter is, then, applied to highlight regions of rapid intensity change, which is often used for edge detection. Zero crossings of the LOG filter correspond to positions of maximum gradient and localize the edges. Finally, instantaneous flame front position is determined by tracking the flame front using an edge-finding algorithm. A similar method was used by Balusamy *et al.* [35] to track the propagation of spherical flames using an adopted filtering technique. Flame front topology properties, such as normal directions to the flame front, flame surface density, and curvature are extracted from this data. For uncertainty analysis in flame surface tracking, please see Appendix C.

The two-component unburned gas velocity upstream of the flame front (S_{u}) is calculated based on the velocity vector field data in the vicinity of the normal lines to the flame front, as illustrated in Fig. 3.2 (c). Flame position (Z_{f}) data is also used to calculate instantaneous apparent flame front velocity within the imaged plane (S_{F}). As illustrated schematically in Fig. 3.2 (d), in order to

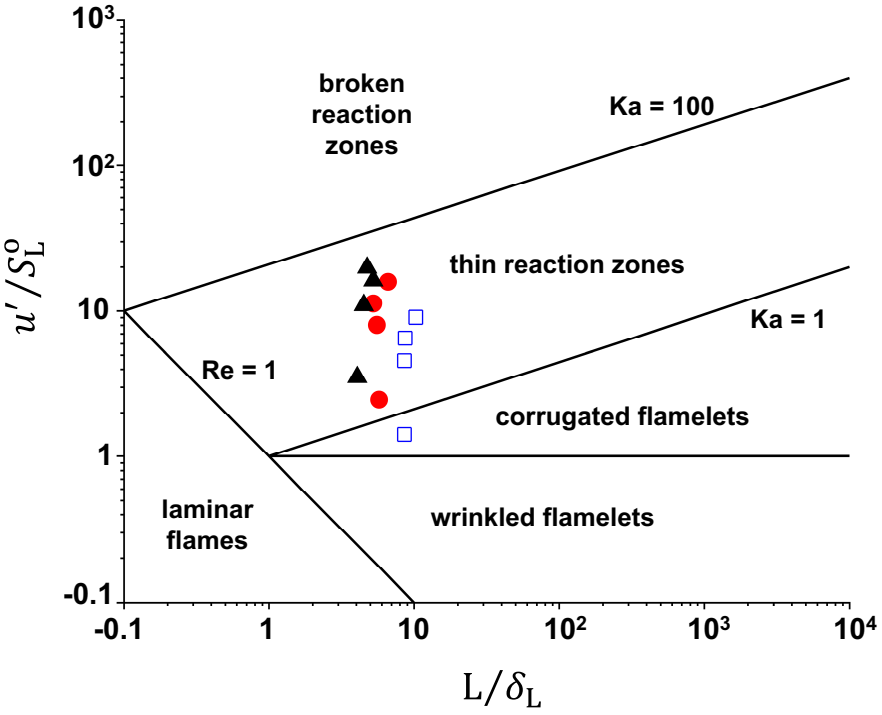

Figure 3.3 Borghi diagram showing premixed turbulent combustion regimes: experimental region of C_3H_8-air (□), CH_4-air (●), and H_2-air (▲) flames.

calculate S_F for a flamelet at time t_i, 5 successive flame contours (centered at t_i) are considered, and third-order polynomials are fit between each pair of successive fronts, starting at the flamelet grid, at time t_i, and extending toward upstream and downstream flame fronts. These polynomials are calculated such that, they are perpendicular to both successive flame fronts, have a minimum length, and pass through the flamelet grid at time t_i, as well as the intersection grids of the flamelet's path and the flame front contours, specified by the minimum path length. Therefore, each flamelet's path consists of 4 continuous third-order polynomials, which are perpendicular to all 5 flame fronts and the total length is a minimum. The length of the estimated streamline is used to calculate the displacement velocity of the flamelet using a fourth-order finite difference method.

Although previously proposed methods [35, 37] and the current approach utilize different image source, and flame surface tracking methods, they all track the flamelet's path between consecutive flame-front contours to reconstruct the flame-front motion using successive image sequences. However, in the current approach, the application of a higher-order finite differencing method, in flame-front velocity calculations, improves the signal-to-noise ratio.

S_F and S_u are, then, used to calculate instantaneous apparent local turbulent flame displacement velocity within the imaged plane, along the normal line to the flame surface contour (S_T) [20, 38]:

$S_{\mathrm{T}} = (S_{\mathrm{F}} + S_{\mathrm{u}}) \cdot \vec{n}$. A similar method was also used and validated in [35] to measure local laminar burning velocity of stretched spherical flames.

Turbulent Karlovitz number ($\mathrm{Ka_T}$) is a key non-dimensional quantity describing turbulence-chemistry interactions. $\mathrm{Ka_T}$ is defined as the ratio of chemical time scale (τ_{c}) to the time scale related with the smallest eddies in the flow, known as Kolmogorov eddies, and is calculated as: $\mathrm{Ka_T} = (L/\delta_{\mathrm{L}})^{-2}\ \mathrm{Re_T}^{1.5}$, where $\mathrm{Re_T}$ is the turbulent Reynolds number.

$\mathrm{Ka_T}$, rms velocities, L, and chemistry related properties (δ_{L} and $S_{\mathrm{L}}^{\mathrm{o}}$) are suitable parameters in describing different regimes of turbulent premixed combustion in the Borghi diagram [24, 39]. The experimental conditions listed in Table 3.2 are summarized in the Borghi diagram (Fig. 3.3). $\mathrm{Ka_T} < 1$ indicates that the eddies of Kolmogorov length scale are significantly large compared to the flame thickness; hence, the eddies do not penetrate into the preheat zone and have only a wrinkling effect on the flame front structure. This zone corresponds to the wrinkled and corrugated flamelet regions. On the other hand, $\mathrm{Ka_T} > 1$ demonstrates that eddies of the Kolmogorov length scale have become sufficiently small, and they might penetrate into the reactive-diffusive flame structure. This region corresponds to the thin and the broken reaction zone regimes on the Borghi diagram. As illustrated in Fig. 3.3, the experimental conditions in this study are in the thin reaction zone regime of the Borghi diagram, to quantify measurements closer to the relevant operating conditions of GTEs.

3.3.3 Computational model description and setup

The Favre-averaged equations for continuity, momentum, and energy were solved, together with the flamelet-progress variable equations using a commercial code, ANSYS 18.2. A Reynolds stress transport model (RSM) is used for turbulence predictions, as it minimizes turbulence modeling issues with the mixed (laminar-turbulent) nature of the counter-flow system. Figure. 3.7 (a) shows contours of the fluctuating velocity field. Turbulent and laminar regions of the flow are reproduced, and no spurious fluctuations can be seen in the laminar region. For brevity, the combustion model will be briefly summarized. The recent, comprehensive review of van Oijen *et al.* [27] may be consulted for full details, and the work by Jella *et al.* [40] for more specifics on the flamelet-generation method used in this article.

The flame is tracked by the mean reaction progress variable ($\widetilde{c}$), and its variance ($\widetilde{c''^2}$), which are used to convolve a conventional beta-pdf with the laminar (FGM) reaction rate. The progress variable is defined as $\widetilde{c} = \widetilde{Y}_{\mathrm{CO}} + \widetilde{Y}_{\mathrm{CO_2}}$ for the hydrocarbon flames, and $\widetilde{c} = \widetilde{Y}_{\mathrm{H_2O}}$ for the hydrogen flames. Details on the closure for the source and sink terms in the transport of $\widetilde{c}$ and $\widetilde{c''^2}$ may be found in [40]. In the limit of perfect mixing, the chemical source term is modeled as: $\overline{\dot{\omega}}_c =$

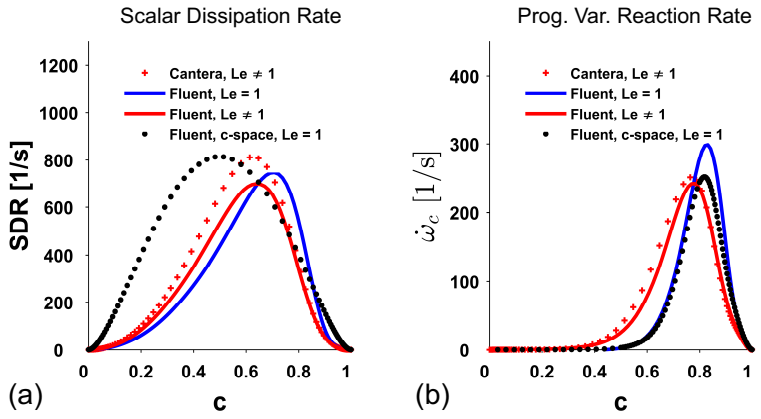

Figure 3.4 Le influence on laminar and turbulent methane flames at $\phi = 0.55$: (a) SDR and (b) reaction rate.

$\int_0^1 \dot{\omega}_c(\zeta)\ P(\zeta)\ d\zeta$, where ζ is the sample space variable for $\widetilde{c}$, $\dot{\omega}_c$ is the FGM reaction rate, and $P(\zeta)$ is the probability shape obtained from the beta-pdf. The FGM equations in composition space are solved as described by Nguyen *et al.* [41], assuming unity Lewis numbers. An important consequence that results from this transformation is the need to prescribe the scalar dissipation rate (SDR), χ_c, defined as $\chi_c = D_c(\nabla c \cdot \nabla c)$, which accounts for molecular mixing in the composition space. In this work, the peak value of χ_c is computed from a physical space simulation, and an error function distribution [41] is used to calculate its variation through the flame. Since Fluent is hardcoded to generate $\mathrm{Le} = 1$ flamelets in the c-space with an analytical SDR, we quantify the impact of the coordinate transformation using physical space solutions. Strained counter-flow flames, corresponding to boundary conditions without TGP, were calculated in Cantera as a cross-check of the Fluent $\mathrm{Le} \neq 1$ physical space and c-space solutions, but for the sake of space, we refer to [40] for these results and reproduce the most relevant points below. The UCSD-San Diego 2016 mechanism has been used for all computations in this study.

Figure 3.4 summarizes the effect of $\mathrm{Le} = 1$ on two important quantities that directly impact the flame speed: χ_c and $\dot{\omega}_c$ for a lean methane flame ($\phi = 0.55$). The main consequence of $\mathrm{Le} = 1$ for lean methane flames is the lowering of reactivity due to the neglect of differential diffusion. This is seen as a shifted peak for the SDR, in the range of $0.2 < c < 0.8$, between the plots in Fig. 3.4. The differences between the physical space SDR and the error-function approximation do not appear to heavily influence the results in this case, although differences in species profiles should be expected. In the case of laminar hydrogen flames, much larger differences are seen between profiles of temperature and species (OH) in Fig. 3.5 (b), and in heat release ($\dot{Q}$) in Fig. 3.6. $\dot{Q}$ is observed to distribute over a larger range of c, and reach a maximum c in the case of $\mathrm{Le} \neq 1$. This implies that flamelet reaction rates that assume $\mathrm{Le} = 1$ will under-predict the reaction rate.

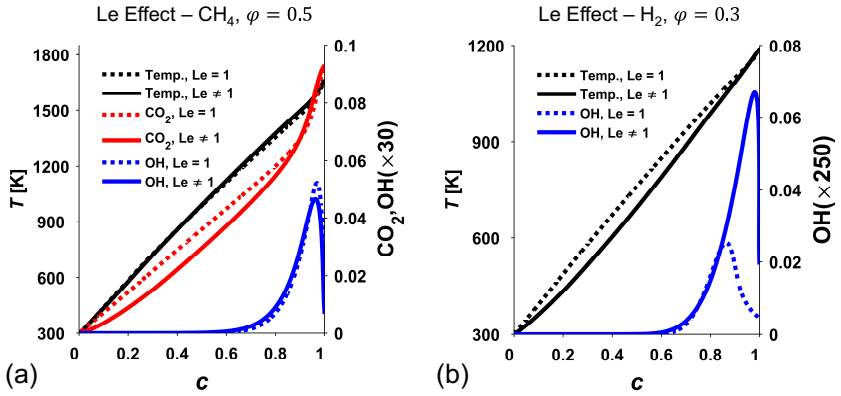

Figure 3.5 Le influence on temperature and species: laminar flames of (a) CH_4 and (b) H_2.

Therefore, while $\mathrm{Le} = 1$ assumption might be a reasonable representation of the flame structure for methane flames, hydrogen flames are not likely to yield correct results with the present CFD methodology.

Accordingly, non-unity Le flamelets should be used, as noted by Donini [26]. Goldin *et al.* [42] point out that in this case, the enthalpy equation is required to account for flamelet enthalpy changes, and that a large turbulent eddy viscosity can easily mask molecular diffusivity influences. In order to investigate this further, major changes to the flamelet-progress variable implementation

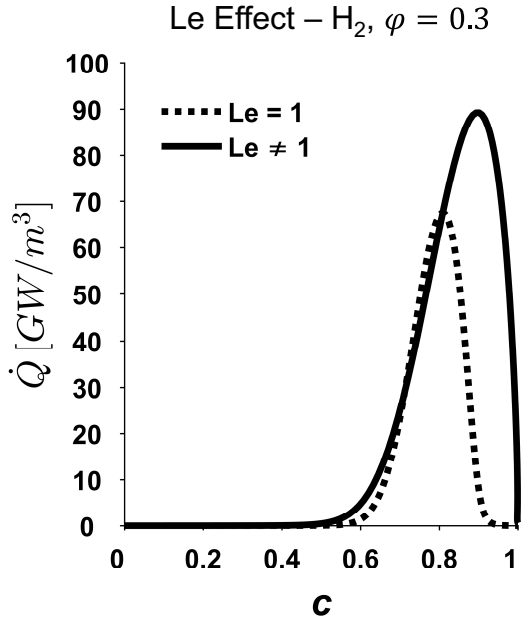

Figure 3.6 Le influence on heat release: laminar H_2 flames.

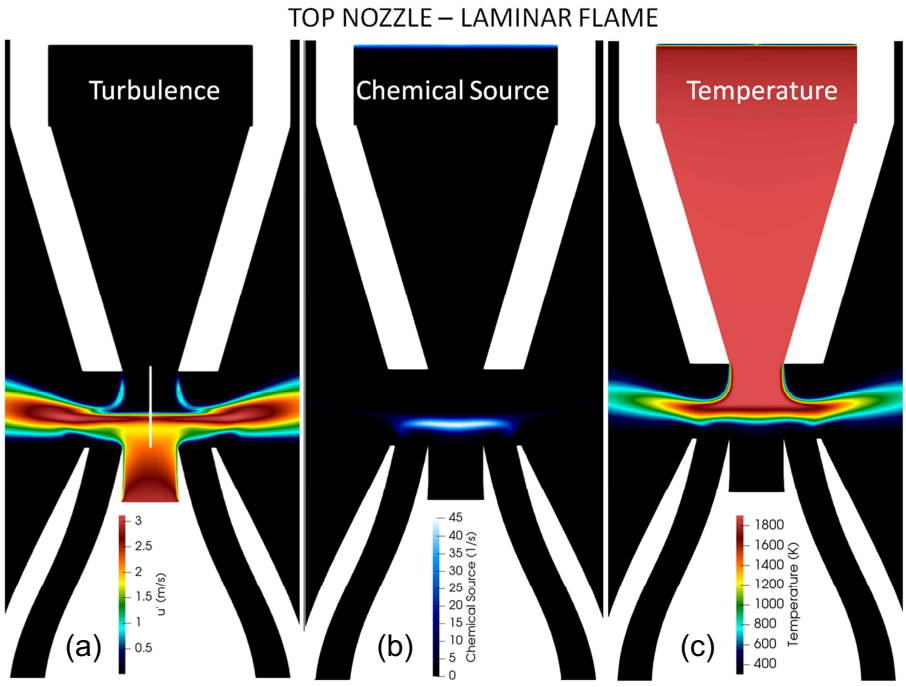

Figure 3.7 CFD model: (a) turbulent jet, (b) lifted flame front visualized by chemical source term, and (c) temperature contours.

in the Fluent code are required, or flamelets should be generated externally. For the present, we restrict discussion to our findings with respect to the assumption of $\mathrm{Le} = 1$ and reserve a more focused investigation of flamelet methods for the next step.

The flow and combustion model equations were discretized using second-order upwinding for convective terms, and second-order central differencing for the diffusion terms. 2D axisymmetric forms of the equations were solved taking advantage of the statistically 2D axisymmetric flow. Boundary conditions for flow and turbulence were imposed using experimental measurements. 3D RANS simulations with full resolution of TGP did not yield any significant advantage. In addition, the nozzle exit conditions were designed to be statistically isotropic to facilitate the most minimal computational domain. A simplified computational domain is shown for a propane flame in Fig. 3.7. The nature of the computations in this work are fundamental checks of the unity Le assumption (typically assumed in commercial codes such as Fluent) in flamelet generation, and its effect on predicting flame stabilization trends. A detailed analysis in 3D will be reserved for future work with more advanced turbulence modeling.

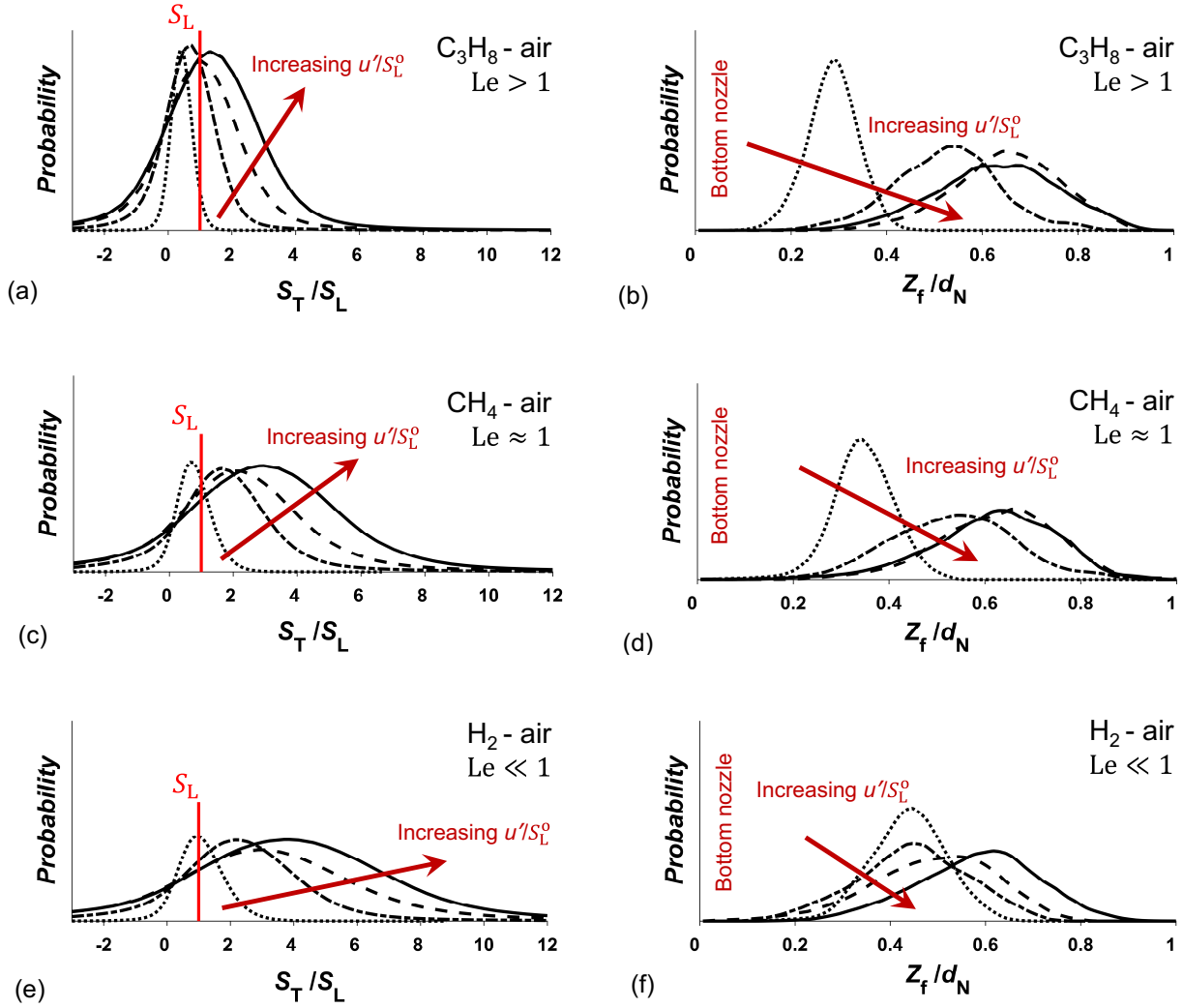

Figure 3.8 PDFs of instantaneous leading edge displacement velocity (S_T) (left), and flame position (Z_f) (right) for: (a-b) C_3H_8-air, (c-d) CH_4-air, and (e-f) H_2-air flames at increasing u'/S_L^o. Please see Table 3.2 for u'/S_L^o values.

3.4 Results and discussion

3.4.1 Results and discussion - experiments

The effects of stretch sensitivity and differential diffusion on the propagation and stabilization of turbulent premixed flames through fuel variation are investigated in this study. In these experiments, instantaneous apparent flame position and velocity statistics within the imaged plane are extracted from PIV data. 10 000 PIV images are processed for each experiment to improve the

statistical accuracy, and approximately 1 million data points are included to approach the probability density function of the statistics. For calculating the instantaneous apparent turbulent flame velocity within the plane of the laser sheet (S_{T}), vector summation of both unburned gas velocity upstream of the flame front (S_{u}), and the instantaneous apparent flame front velocity within the imaged plane (S_{F}) are considered in the direction perpendicular to the flame surface to quantify S_{T}. In these experiments, bulk flow velocity is increased at each step, which increases $u'/S_{\mathrm{L}}^{\mathrm{o}}$ and the bulk strain rate; hence, enhances the stretch imposed on the flames under study.

PDFs of S_{T} and Z_{f} for the three different fuel mixtures at increasing $u'/S_{\mathrm{L}}^{\mathrm{o}}$ are shown side-by-side in Fig. 3.8 (a)-3.8 (f). The key features of the PDFs of S_{T} are the most probable velocity (expected velocity) ($\langle S_{\mathrm{T}} \rangle$), and the distribution of PDFs compared to S_{L}. In general, increasing $u'/S_{\mathrm{L}}^{\mathrm{o}}$, increases leading edge displacement velocity, as well as local consumption speed in turbulent flames, which is in agreement with previous studies, for example see [12, 14, 20].

With increasing $u'/S_{\mathrm{L}}^{\mathrm{o}}$, PDFs of S_{T} are widened and move toward higher velocities. In H_2-air and CH_4-air flames with $\mathrm{Le} \leq 1$, as $u'/S_{\mathrm{L}}^{\mathrm{o}}$ increases, PDFs of S_{T} significantly widen, and $\langle S_{\mathrm{T}} \rangle$ considerably passes S_{L} values, which indicates the propensity of flames with $\mathrm{Le} \leq 1$ to burn faster and to move upstream toward the unburned mixture. While normalized $\langle S_{\mathrm{T}} \rangle$ is higher in H_2-air ($\mathrm{Le} \ll 1$) compared to CH_4-air flames ($\mathrm{Le} \approx 1$) at constant turbulence, the differences are smaller than the change in turbulent burning rates seen in PDFs of Z_{f} shown in Fig. 3.8 (d) and 3.8 (f). Furthermore, in C_3H_8-air flames ($\mathrm{Le} > 1$), with increasing $u'/S_{\mathrm{L}}^{\mathrm{o}}$, PDFs of S_{T} only slightly move toward higher velocities. It should be noted that S_{T} is normalized by S_{L} that has been corrected for density changes from room temperature to 576 K, which is the temperature at which the oil droplets evaporate.

PDFs of Z_{f} for the three different fuel mixtures at increasing $u'/S_{\mathrm{L}}^{\mathrm{o}}$ are shown in Figs. 3.8 (b), 3.8 (d), and 3.8 (f), where $Z_{\mathrm{f}} = 0$ is located at the exit plane of the bottom nozzle. These PDFs are rich in physical information, and give statistics of the flame-location distribution and the range of movement. The most probable flame location (expected flame location) ($\langle Z_{\mathrm{f}} \rangle$), and the flame brush thickness (δ_{T}), can be extracted from these PDFs. δ_{T} is defined as: $\delta_{\mathrm{T}} = \pm 2 \times \sigma$, where σ is the standard deviation of the flame-location PDF distribution. δ_{T} contains 95.4 % of the observed Z_{f} values. Furthermore, the skewness of the PDFs indicate a preference for the flame to locate upstream or downstream of $\langle Z_{\mathrm{f}} \rangle$. By increasing bulk flow velocity and $u'/S_{\mathrm{L}}^{\mathrm{o}}$, turbulent flames are subjected to a steeper average velocity-gradients, which pushes the flames toward the hot stagnation surface, and PDfs are widened.

In order to quantify these statistics, $\langle Z_{\mathrm{f}} \rangle$ correlations at increasing $u'/S_{\mathrm{L}}^{\mathrm{o}}$ are summarized in Fig. 3.9. Figure 3.9 (a) illustrates that increasing $u'/S_{\mathrm{L}}^{\mathrm{o}}$, and stretching the flame through increasing

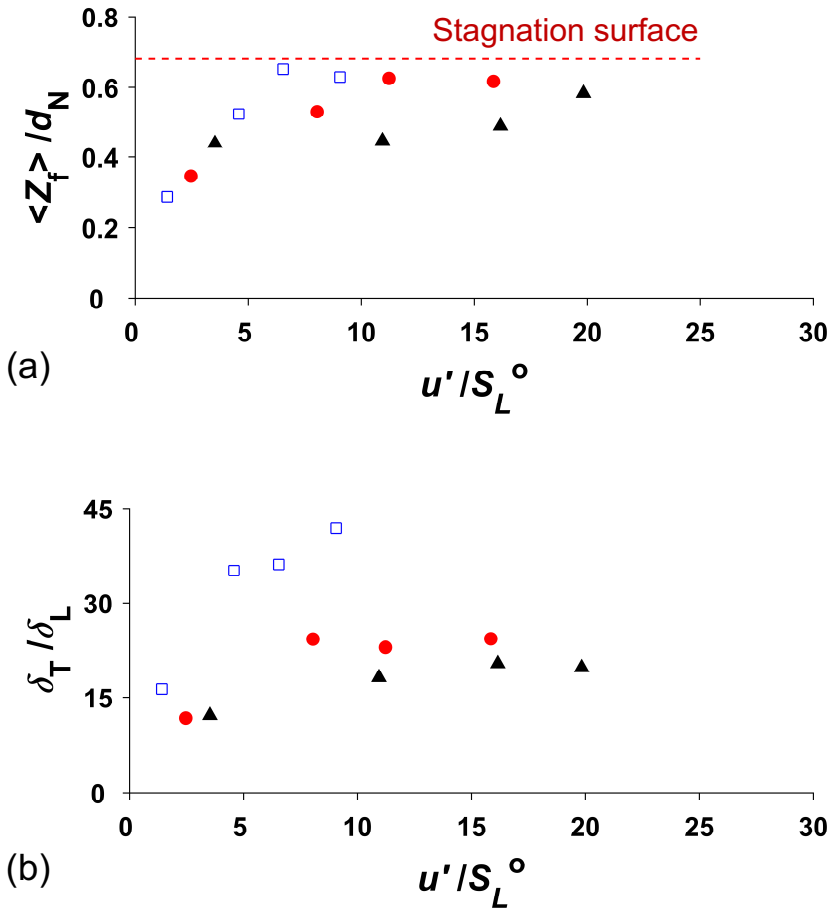

Figure 3.9 (a) Most probable flame location ($\langle Z_{\rm f} \rangle$) and (b) flame brush thickness ($\delta_{\rm T}$) correlations at increasing $u'/S_{\rm L}^{\rm o}$: C_3H_8-air (□), CH_4-air (●), and H_2-air (▲) flames.

bulk hydrodynamic strain, as well as turbulence stretch effects, significantly affects the propagation of various fuel mixtures with distinct Le. With increasing $u'/S_{\rm L}^{\rm o}$, C_3H_8-air flames (Le > 1) are skewed and move significantly downstream due to larger than unity Le. In mixtures with Le > 1, thermal diffusion from the positively-stretched portion of the turbulent flame front is larger than fuel diffusion into the stretched area. The rate of thermal energy loss is greater than chemical energy gain provided by the molecular diffusion into the reaction zone, which reduces the temperature and results in decreasing the flame speed, and consequently, the flame moves downstream. In CH_4-air flames with Le ≈ 1, this relocation is less pronounced with steepening average velocity-gradients, since the molecular transport into the reaction zone is balanced with thermal diffusion

from the reaction zone, and the flame temperature corresponds to T_{ad}.

However, as illustrated in Fig. 3.8 (f) and Fig. 3.9 (a), H_2-air flames remain stationary up to very high bulk velocities ($U/S_{\mathrm{L}}^{\mathrm{o}} = 42.9$ and $u'/S_{\mathrm{L}}^{\mathrm{o}} = 16.2$), which shows that mixtures with $\mathrm{Le} \ll 1$ are sensitive to the stretch effects due to differential diffusion, and the flamelets make larger incursions upstream against the steepening velocity-gradient. This is clearly seen in Fig. 3.8 (f), where PDFs of flame location in the case of H_2-air flames, are spread closer to the bottom nozzle, and $Z_{\mathrm{f}}/d_{\mathrm{N}}$ obtains values as small as 0.25, at increasing $u'/S_{\mathrm{L}}^{\mathrm{o}}$. In mixtures with $\mathrm{Le} \ll 1$, while the flame front is positively stretched, molecular diffusion into the leading points of the flame is larger than thermal diffusion losses, which increases the local equivalence ratio (ϕ), and consequently, temperature and flame speed increase. It is also indicated in Fig. 3.9 (a) that, at the highest $U/S_{\mathrm{L}}^{\mathrm{o}}$ and $u'/S_{\mathrm{L}}^{\mathrm{o}}$ tested in this study, Z_{f} is close to the stagnation surface in all mixtures due to a very high bulk flow velocity.

Figure 3.8 (f) and Fig. 3.9 (a) further validate a significant increase in turbulent burning rates in mixtures with $\mathrm{Le} \ll 1$ at increasing bulk flow velocity and $u'/S_{\mathrm{L}}^{\mathrm{o}}$, as the flames remain stationary at steepening average velocity-gradients. This increase in local turbulent burning rates (and consequently, global turbulent burning rates) is thought to be due to both an increase in local turbulent displacement velocities due to the effects of differential diffusion and stretch sensitivity (as shown in Fig. 3.8 (e)), as well as an increase in flame surface density due to an enhancement in local flamelet curvature, as discussed in [20].

Flame brush thickness (δ_{T}) increases with increasing $u'/S_{\mathrm{L}}^{\mathrm{o}}$ as seen in Fig. 3.9 (b). In mixtures with $\mathrm{Le} > 1$, δ_{T} increases faster with increasing $u'/S_{\mathrm{L}}^{\mathrm{o}}$, compared to $\mathrm{Le} \approx 1$ and $\mathrm{Le} \ll 1$ mixtures, respectively. Thickening trend of δ_{T} with $u'/S_{\mathrm{L}}^{\mathrm{o}}$ is in agreement with previous studies, see for example [36, 43].

3.4.2 Results and discussion - computations

Computations were carried out for the lowest and the highest turbulence intensities for each fuel. Prior to turbulent combustion calculations, counter-flow laminar flames were computed using Cantera in physical space with differential diffusion effects included via detailed chemistry. The Cantera results indicate qualitatively similar behavior to the experiment with respect to flame stabilization at low and high strain rates, and follow the trends seen in Fig. 3.8. At low strain rate, C_3H_8-air flame stabilizes first, followed by CH_4-air and H_2-air flames, though the differences are small. At the highest strain levels, all flames stabilize close to the stagnation plane due to a very high bulk flow velocity.

Figures 3.10 (a) and 3.10 (b) compare the laminar flame profiles of temperature rise (x axis is the distance between the two nozzles) in the left column. At low strain conditions, the highly

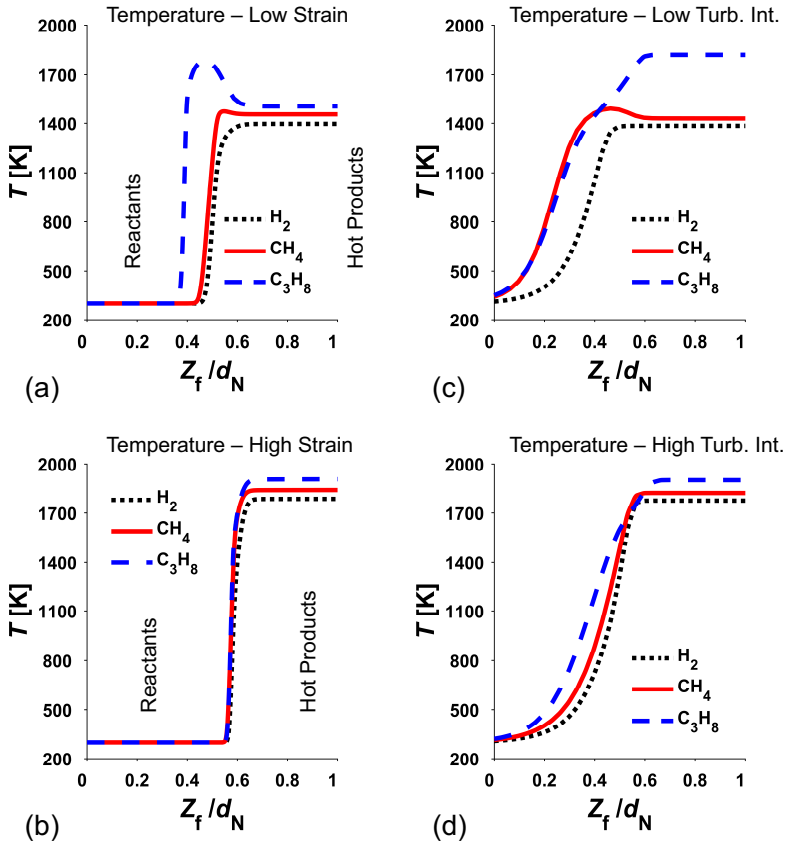

Figure 3.10 Effect of strain and turbulence intensity on temperature profiles.

reactive C_3H_8-air jet ignites well before the other two fuels. A bump in its profile is seen before the post-flame region merges with the hot products from the top nozzle. CH_4-air flame shows a much smaller bump, and the temperature rise for the lean H_2-air case cannot be noticed, due to its

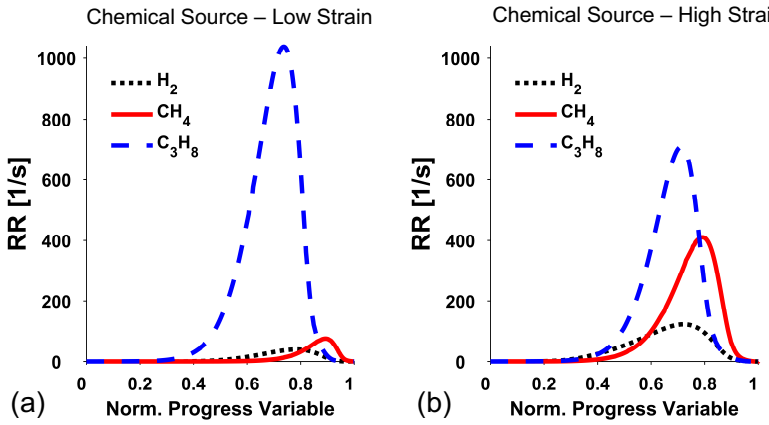

Figure 3.11 Effect of strain on laminar chemical source of progress variable.

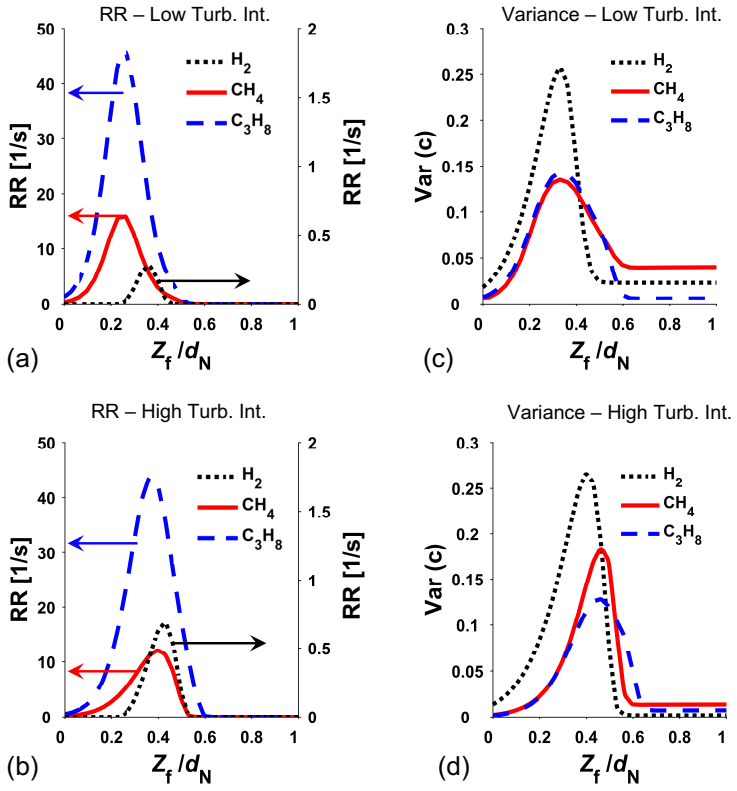

Figure 3.12 Turbulent flame location and brush thickness.

low T_{ad}. Nevertheless, the computations show a small, but non-negligible reaction rate within the flame-front, as seen in Fig. 3.11 (a), which increases with strain rate (Fig. 3.11 (b)).

In Figs. 3.10 (c) and 3.10 (d), the effect of turbulence intensity on the temperature profiles can be seen. Whereas, there is a certain distance the unburned reactants travel along the axis between the two nozzles ($\approx 0.4\,(Z_{\mathrm{f}}/d_{\mathrm{N}})$), a temperature rise is noticed as soon as the reactants exit the bottom nozzle. This is of chemical origin and not due to mixing, as the turbulent chemical source terms, shown in Figs. 3.12 (a) and 3.12 (b), indicate a ramping up as soon as the reactants exit the nozzle. The H_2-air flames are an exception, however. The temperature rise is markedly slower relative to the others, most likely due to its very lean condition ($T_{\mathrm{ad}} \sim 898$ K), and stabilized by a much cooler (1386 K) stream of products. At high strain values, all flames stabilize at the same location indicating that bulk strain effects appear to dominate differential diffusion. For the selected cases, the effect of turbulence intensity coupling with differential diffusion effects is not immediately obvious from the computations for the lowest and the highest turbulence intensities, and more cases will need to be computed to isolate the fuel influences.

The flame location and brush thickness may be estimated using the variance predictions. Figures 3.12 (c) and 3.12 (d) show that H_2-air flames exhibit the largest variance at low, as well as,

high turbulence levels. There is relatively less difference between the hydrocarbon flames, and the differences in Fig. 3.12 may not be explained independently of the laminar hot product boundary conditions. With respect to flame location, flames move downstream as in the experiments, but not to the same extent. At low intensity, the peaks of the reaction rate (a measure of where the flame front is on average) plots in Figs. 3.12 (a) and 3.12 (b), exhibit correct trends compared to the experiment: H_2-air flames are slightly more downstream compared to CH_4-air and C_3H_8-air flames, which essentially coincide with respect to their statistically most likely location, as shown by the experimental PDFs of $Z_{\rm f}$. At higher turbulence intensity, the flames (especially C_3H_8-air) do not move as far downstream as the experiments indicate, although their locations relative to each other are in reasonable agreement with experiment. At present, the reason for this deviation from experiment is unclear, but given the differences between unity and non-unity Le solutions, it is expected that the effects of differential diffusion are significant for this flame configuration. Three dimensional effects may also be a reason.

The combustion model, as far as the default implementation in Fluent is concerned, treats the flame as a passive scalar with the influence of fuel isolated to the chemical source term. The dependence of the molecular diffusivity of c, and flamelet generation on differential diffusion, as well as scalar dissipation effects in transport of c''^2 must be examined before a comprehensive understanding can emerge. The present calculations also show that the flames are more susceptible to straining effects, as the laminar flame simulations follow the experiment quite well.

3.5 Conclusions

Sensitivity to stretch and the effects of differential diffusion of various fuels on the propagation and stabilization of turbulent lean premixed flames in the thin reaction zone regime were studied in a reactants-to-product counter-flow apparatus. Furthermore, the FGM model was used to simulate three fuels at two turbulence intensities in a RANS context.

The statistics of the local instantaneous flame position and turbulent flamelet velocities are observed to be sensitive to the effects of differential diffusion at increasing flame stretch. With increasing flame stretch, and due to the effects of differential diffusion in the mixtures with $\mathrm{Le} \ll 1$, turbulent flame velocities increase considerably compared to the laminar flame speed, which indicates a propensity of the flamelets to make larger incursions upstream against the steepening average velocity-gradient.

PDFs of flame location show a significant increase in turbulent burning rates in mixtures with

$\mathrm{Le} \ll 1$, where H_2-air flames are almost stationary and compensating for the steepening average velocity-gradient imposed by increasing bulk flow, meaning that the turbulent flame speed is increasing to compensate for the increase in the bulk flow velocity. In contrast, the downstream movement of CH_4-air ($\mathrm{Le} \approx 1$) and C_3H_8-air ($\mathrm{Le} > 1$) flames toward the stagnation surface is much steeper compared to H_2-air flames. However, as illustrated by PDFs of flame velocity, the differences in local turbulent displacement velocities between H_2-air ($\mathrm{Le} \ll 1$) and CH_4-air ($\mathrm{Le} \approx 1$) flames are smaller than the change in turbulent burning rates seen in the PDFs of flame location.

The normalized flame brush thickness increases with increasing $u'/S_{\mathrm{L}}^{\mathrm{o}}$, and this increase is the largest for C_3H_8-air flames ($\mathrm{Le} > 1$) and the smallest for H_2-air flames ($\mathrm{Le} \ll 1$).

Computations indicate that strained counter-flow laminar flames with detailed chemistry are able to reproduce the experimental trends, and turbulence does not mask this behavior. While qualitative trends look encouraging and reproduce the effect of turbulence intensity, fuel influences definitely require the inclusion of differential diffusion for accurate predictions.

Reliable quantitative experimental results, which are quantified and reported as probability density functions using processing techniques, proposed in this study, are suitable for validating combustion models that are based on flame-front displacement velocity such as G-equation, reaction progress variable such as FGM-based modeling, and turbulent flame speed correlations.

Acknowledgment

This research was funded by the Natural Sciences and Engineering Research Council of Canada and Siemens Canada Limited under the Collaborative Research and Development program (NSERC-CRD). The McGill Engineering Doctoral Awards (MEDA) program is also gratefully acknowledged for the support during this research study.

Funding data

- Natural Sciences and Engineering Research Council of Canada (I242349C0G).
- Siemens Canada Limited (I242215C0G).

References

[1] E. Hu, Z. Huang, J. He, C. Jin, and J. Zheng. "Experimental and numerical study on laminar burning characteristics of premixed methane–hydrogen–air flames". In: *International Journal of Hydrogen Energy* 34 (2009), pp. 4876–4888.

[2] C. Tang et al. "Laminar burning velocities and combustion characteristics of propane–hydrogen–air premixed flames". In: *International Journal of Hydrogen Energy* 33 (2008), pp. 4906–4914.

[3] E. Boschek, P. Griebel, and P. Jansohn. "Fuel variability effects on turbulent, lean premixed flames at high pressures". In: *Proceedings of the ASME Turbo Expo: Turbine Technical Conference and Exposition. GT2007–27496* (2007).

[4] M. Matalon. "On flame stretch". In: *Combustion Science and Technology* 31 (1983), pp. 169–181.

[5] C.K. Law. "Dynamics of stretched flames". In: *Proceedings of the Combustion Institute* 22 (1989), pp. 1381–1402.

[6] F.A. Williams. "Progress in knowledge of flamelet structure and extinction". In: *Progress in Energy and Combustion Science* 26 (2000), pp. 657–682.

[7] C.K. Law. *Combustion physics*. Cambridge university press, Cambridge, UK, 2010.

[8] A. Marshall, J. Lundrigan, P. Venkateswaran, J. Seitzman, and T. Lieuwen. "Fuel effects on leading point curvature statistics of high hydrogen content fuels". In: *Proceedings of the Combustion Institute* 35 (2015), pp. 1417–1424.

[9] P. Venkateswaran, A. Marshall, J. Seitzman, and T. Lieuwen. "Pressure and fuel effects on turbulent consumption speeds of H_2/CO blends". In: *Proceedings of the Combustion Institute* 34 (2013), pp. 1527–1535.

[10] P.A. Libby and F.A. Williams. "Structure of laminar flamelets in premixed turbulent flames". In: *Combustion and Flame* 44 (1982), pp. 287–303.

[11] Y.-C. Chen and R.W. Bilger. "Experimental investigation of three-dimensional flame-front structure in premixed turbulent combustion: II. Lean hydrogen/air Bunsen flames". In: *Combustion and Flame* 138 (2004), pp. 155–174.

[12] R.G. Abdel-Gayed, D. Bradley, M.N. Hamid, and M. Lawes. "Lewis number effects on turbulent burning velocity". In: *Proceedings of the Combustion Institute* 20 (1984), pp. 505–512.

[13] A.N. Lipatnikov and J. Chomiak. "Molecular transport effects on turbulent flame propagation and structure". In: *Progress in Energy and Combustion Science* 31 (2005), pp. 1–73.

[14] P. Venkateswaran, A. Marshall, D.H. Shin, D. Noble, J. Seitzman, and T. Lieuwen. "Measurements and analysis of turbulent consumption speeds of H_2/CO mixtures". In: *Combustion and Flame* 158 (2011), pp. 1602–1614.

[15] R.S. Barlow, M.J. Dunn, M.S. Sweeney, and S. Hochgreb. "Effects of preferential transport in turbulent bluff-body-stabilized lean premixed CH_4/air flames". In: *Combustion and Flame* 159 (2012), pp. 2563–2575.

[16] S.D. Salusbury, E. Abbasi-Atibeh, and J.M. Bergthorson. "The effect of Lewis number on instantaneous flamelet speed and position statistics in counter-flow flames with increasing turbulence". In: *Proceedings of the ASME Turbo Expo: Turbine Technical Conference and Exposition. GT2017-64821* (2017).

[17] F.T.C. Yuen and Ö.L. Gülder. "Premixed turbulent flame front structure investigation by Rayleigh scattering in the thin reaction zone regime". In: *Proceedings of the Combustion Institute* 32 (2009), pp. 1747–1754.

[18] J. Furukawa, T. Hirano, and F.A. Williams. "Burning velocities of flamelets in a turbulent premixed flame". In: *Combustion and Flame* 113 (1998), pp. 487–491.

[19] Y. Ikeda, J. Kojima, T. Nakajima, F. Akamatsu, and M. Katsuki. "Measurement of the local flamefront structure of turbulent premixed flames by local chemiluminescence". In: *Proceedings of the Combustion Institute* 28 (2000), pp. 343–350.

[20] J.F. Driscoll. "Turbulent premixed combustion: Flamelet structure and its effect on turbulent burning velocities". In: *Progress in Energy and Combustion Science* 34 (2008), pp. 91–134.

[21] G. Coppola, B. Coriton, and A. Gomez. "Highly turbulent counterflow flames: A laboratory scale benchmark for practical systems". In: *Combustion and Flame* 156 (2009), pp. 1834–1843.

[22] E. Mastorakos, A.M.K.P. Taylor, and J.H. Whitelaw. "Extinction of turbulent counterflow flames with reactants diluted by hot products". In: *Combustion and Flame* 102 (1995), pp. 101–114.

[23] F. Hampp and R.P. Lindstedt. "Quantification of combustion regime transitions in premixed turbulent DME flames". In: *Combustion and Flame* 182 (2017), pp. 248–268.

[24] R. Borghi. "On the structure and morphology of turbulent premixed flames". In: *Recent Advances in the Aerospace Sciences* (1985), pp. 117–138.

[25] H. Kolla and N. Swaminathan. "Strained flamelets for turbulent premixed flames, I: Formulation and planar flame results". In: *Combustion and Flame* 157 (2010), pp. 943–954.

[26] A. Donini, R.J.M. Bastiaans, J.A. van Oijen, and L.P.H. de Goey. "Differential diffusion effects inclusion with flamelet generated manifold for the modeling of stratified premixed cooled flames". In: *Proceedings of the Combustion Institute* 35 (2015), pp. 831–837.

[27] J.A. van Oijen, A. Donini, R.J.M. Bastiaans, J.H.M. ten Thije Boonkkamp, and L.P.H. de Goey. "State-of-the-art in premixed combustion modeling using flamelet generated manifolds". In: *Progress in Energy and Combustion Science* 57 (2016), pp. 30–74.

[28] G. Coppola and A. Gomez. "Experimental investigation on a turbulence generation system with high-blockage plates". In: *Experimental Thermal and Fluid Science* 33 (2009), pp. 1037–1048.

[29] D.G. Goodwin, H.K. Moffat, and R.L. Speth. *Cantera: A software toolkit for chemical kinetics, thermodynamics, and transport processes*. Version 2.2.1, http://www.cantera.org, 2016.

[30] S.D. Salusbury and J.M. Bergthorson. "Maximum stretched flame speeds of laminar premixed counter-flow flames at variable Lewis number". In: *Combustion and Flame* 162 (2015), pp. 3324–3332.

[31] G.E. Glawe, R. Holanda, and L.N. Krause. *Recovery and radiation corrections and time constants of several sizes of shielded and unshielded thermocouple probes for measuring gas temperature*. Tech. rep. NASA: NASA-TP-1099, E-9289. 1978.

[32] D. Bradley and K.J. Matthews. "Measurement of high gas temperatures with fine wire thermocouples". In: *Journal of Mechanical Engineering Science* 10 (1968), pp. 299–305.

[33] H. Tennekes and J.L. Lumley. *A First Course in Turbulence*. The MIT Press, Cambridge, USA, 1972.

[34] J.O. Hinze. *Turbulence*. McGraw-Hill, New York, USA, 1975.

[35] S. Balusamy, A. Cessou, and B. Lecordier. "Direct measurement of local instantaneous laminar burning velocity by a new PIV algorithm". In: *Experiments in Fluids* 50 (2011), pp. 1109–1121.

[36] S. Kheirkhah and Ö.L. Gülder. "Consumption speed and burning velocity in counter-gradient and gradient diffusion regimes of turbulent premixed combustion". In: *Combustion and Flame* 162 (2015), pp. 1422–1439.

[37] R. Abu-Gharbieh, G. Hamarneh, T. Gustavsson, and C.F. Kaminski. "Level set curve matching and particle image velocimetry for resolving chemistry and turbulence interactions in propagating flames". In: *Journal of Mathematical Imaging and Vision* 19 (2003), pp. 199–218.

[38] H. Kolla, J.W. Rogerson, and N. Swaminathan. "Validation of a turbulent flame speed model across combustion regimes". In: *Combustion Science and Technology* 182 (2010), pp. 284–308.

[39] N. Peters. *Turbulent combustion*. Cambridge university press, Cambridge, UK, 2000.

[40] S. Jella, J.M. Bergthorson, W.Y. Kwong, and A. Steinberg. "RANS and LES modeling of a linear-array swirl burner using a flamelet-progress variable approach". In: *Proceedings of the ASME Turbo Expo: Turbine Technical Conference and Exposition. GT2018-75896* (2018).

[41] P.-D. Nguyen, L. Vervisch, V. Subramanian, and P. Domingo. "Multidimensional flamelet-generated manifolds for partially premixed combustion". In: *Combustion and Flame* 157 (2010), pp. 43–61.

[42] G. Goldin, Z. Ren, H. Forkel, L. Lu, V. Tangirala, and H. Karim. "Modeling CO with flamelet-generated manifolds: Part 1—flamelet configuration". In: *Proceedings of the ASME Turbo Expo: Turbine Technical Conference and Exposition. GT2012-69528* (2012).

[43] H. Guo, B. Tayebi, C. Galizzi, and D. Escudié. "Burning rates and surface characteristics of hydrogen-enriched turbulent lean premixed methane–air flames". In: *International Journal of Hydrogen Energy* 35 (2010), pp. 11342–11348.

Link between chapters 3 and 4

In Chapter 3, the effects of turbulence and stretch sensitivity on the propagation and stabilization of lean turbulent premixed flames with variable Lewis numbers were investigated in a counter-flow apparatus at increasing turbulence level. In these experiments, as the first incursion into the field of fuel flexibility, pure fuel-air mixtures of hydrogen-air ($\mathrm{Le} \ll 1$), methane-air ($\mathrm{Le} \approx 1$), and propane-air ($\mathrm{Le} > 1$), representative of various thermo-diffusive properties, were studied. In the final part of this paper, these flames were modeled using preliminary CFD simulations based on the FGM model in a RANS context. In these experiments, turbulence intensity was increased by increasing the bulk-flow velocity. The results demonstrated that the statistics of the local instantaneous flame location and turbulent flamelet velocities are sensitive to the effects of differential diffusion at increasing turbulence level.

In the previous chapter, the combined effects of mixture reactivity and diffusivity properties were reported for pure fuel-air flames at increasing turbulence level. In Chapter 4, in the context of fuel flexibility, fuel blends of hydrogen, which is a clean alternative for fossil fuels, and conventional hydrocarbons, i.e., methane and propane, will be studied in the air, where the variations of $\mathrm{Le_{eff}}$ are mainly due to a change in fuel diffusivity of the mixtures. Furthermore, the unstretched laminar flame speed of the mixtures is kept constant, through decreasing the mixture equivalence ratio, in order to minimize the effects of chemical properties of the mixture on the propagation and stabilization of premixed flames. Furthermore, turbulence intensity is kept constant through keeping the bulk-flow properties constant, and the temperature boundary condition is also kept constant, in order to only focus on the effects of differential diffusion (variations in the fuel diffusivity of the mixtures) in fuel-flexibility experiments in the thin reaction zone regime. In addition, the spatial resolution of the PIV measurements is improved from $\approx 521\,\mu$m, in Chapter 3, to $\approx 358\,\mu$m, in Chapter 4, through modifications on the camera lens system. The experiments in Chapter 4 will investigate the effects of differential diffusion on the flame location and local flamelet velocities for lean premixed H_2-enriched CH_4-air and C_3H_8-air flames with distinct effective Lewis numbers. A brief discussion on the structure parameters of turbulent premixed flames, including flame stretch and flame-front curvature will also be presented.

Chapter 4

Differential diffusion effects in counter-flow premixed hydrogen-enriched methane and propane flames

Publication (2): E. Abbasi-Atibeh and J. M. Bergthorson. *Proceedings of the Combustion Institute* 37 (2019), pp. 2399−2406.
https://doi.org/10.1016/j.proci.2018.08.006.

4.1 Abstract

The effects of differential diffusion and stretch sensitivity on the propagation and stabilization of lean premixed hydrogen-enriched methane-air and propane-air flames are studied in a turbulent counter-flow apparatus. In these experiments, the unstretched laminar flame speed is kept constant through decreasing the mixture equivalence ratio, in order to minimize the effects of chemistry and highlight the effects of differential diffusion during hydrogen-enrichment. Bulk flow properties are also kept constant between laminar and turbulent flames. High-speed particle image velocimetry (PIV) is applied to quantify the flow velocity field using oil droplet seeding, enabling simultaneous flame-location detection and velocity measurements. Data-processing tools are developed through this study to quantify instantaneous local measurements of flame location, flame curvature, and apparent turbulent flame velocity within the imaged plane. Probability density functions (PDFs) of instantaneous flame location showed that, in hydrogen-enriched methane-air flames (effective Lewis number < 1), differential diffusion increases the turbulent burning rates throughout the whole hydrogen-enrichment range. However, in hydrogen-enriched propane-air flames, these effects are only observed at hydrogen content above $60\,\%$ (by volume), where the effective Lewis number falls below unity. PDFs of flame location also illustrated that the effects of differential

diffusion become significant when the effective Lewis number < 0.8. In contrast, PDFs of turbulent flame velocities only showed a slight increase in local instantaneous velocities with increasing hydrogen content. Furthermore, it was illustrated that differential diffusion affects the flame-front topology by increasing instantaneous flamelet curvature at below unity Lewis numbers, consistent with flame stability theory.

Keywords: Differential diffusion; Hydrogen-enrichment; Premixed turbulent combustion; Particle image velocimetry (PIV).

4.2 Introduction

Fuel flexibility of newly-designed engines is an important parameter of combustor performance due to increasing demand for renewable alternative fuels, and also energy security concerns. However, turbulent combustion of mixtures with different chemistry and transport properties brings large uncertainty in the design of fuel-flexible combustors, mainly due to variations in turbulent burning rates, which significantly affect combustor operability issues, such as blow out, flash back, and dynamic stability.

Changing the fuel composition has two major impacts on the flame propagation: (1) it changes the chemical properties of the mixture, which increases the flame velocity with increasing H_2 content in laminar hydrocarbon flames [1, 2], and (2) it changes the transport properties (diffusivity of the deficient species and heat), which plays an important role in the propagation of premixed flames [3–7], and is known as *differential diffusion*.

Differential diffusion effects on the propagation of premixed flames are coupled with stretch sensitivity at the flame front. Stretch rate (K), is defined as the normalized differential change in flame surface area as a function of time: $K = (1/A)\,(\mathrm{d}A/\mathrm{d}t)$, and can be expressed as a function of flame curvature (κ) and hydrodynamic strain (K_s) [8]: $K = S_\mathrm{L}\kappa + K_\mathrm{s}$. The effects of stretch are highly important in the propagation of premixed flames, which have been studied in detail for laminar flames [9, 10], and for turbulent flames [11, 12]. Lewis number (Le), defined as: $\mathrm{Le} = \alpha/\mathcal{D}$, determines the relative role of heat and mass diffusivities (thermo-diffusive properties) at the flame front, and controls the stretch sensitivity of premixed flames.

In this study, the effects of differential diffusion on the propagation and stabilization of highly-stretched H_2-enriched CH_4-air and C_3H_8-air flames are studied. H_2-enrichment at various volume ratios forms mixtures with different fuel diffusivity illustrative of distinct Le.

H_2-enriched flames have been investigated in a number of studies [13, 14]; however, in the majority of these studies, chemical effects are not isolated from differential diffusion effects. Furthermore, turbulent flame velocity measurements, reported in the majority of studies, are focused on global time-averaged measurements, that do not yield local information on the physics of turbulent flame propagation [15].

Therefore, in this study, the effects of differential diffusion are highlighted by keeping the unstretched laminar flame speed ($S_{\mathrm{L}}^{\mathrm{o}}$) constant during H_2-enrichment. Furthermore, instantaneous local measurements of apparent flame position and turbulent flame velocity components within the imaged plane are used to study the effects of differential diffusion at constant bulk flow properties in a hot-exhaust counter-flow rig.

4.3 Experimental method

Experiments in this study investigate lean premixed turbulent and laminar combustion of H_2-enriched CH_4-air and C_3H_8-air flames under atmospheric pressure. A CH_4-air flame at $\phi = 0.7$ and a C_3H_8-air flame at $\phi = 0.659$ are selected as reference mixtures, both having a predicted $S_{\mathrm{L}}^{\mathrm{o}} = 0.195$ m/s. During the enrichment process, H_2 is added to the reference mixtures in increments of 10 % (by volume), while $S_{\mathrm{L}}^{\mathrm{o}}$ is kept constant at 0.195 m/s, through decreasing the mixture equivalence ratio (ϕ). The bulk flow velocity at the nozzle exit is also kept constant in all experiments at 4.5 m/s. Properties of these mixtures are listed in Table 4.1. Keeping $S_{\mathrm{L}}^{\mathrm{o}}$ constant minimizes the effects of chemical properties of the mixture on the propagation and stabilization of premixed flames, and highlights the effects of differential diffusion, in order to study the effects of thermo-diffusive properties of the fuel in fuel flexibility experiments. H_2 content in turbulent flame experiments was increased up to the flash-back limit of 70 % and 90 % for CH_4-H_2-air and C_3H_8-H_2-air flames, respectively.

Lewis number is defined as: $\mathrm{Le} = \alpha/\mathcal{D} = \lambda/(\rho c_{\mathrm{p}} \mathcal{D})$, and is calculated at room temperature and pressure of 300 K and 1 atm, respectively. λ is the thermal conductivity, c_{p} is the specific heat, ρ is the density of the unburned reactants, and $\mathcal{D}$ is the fuel diffusivity. The effective Le is defined based on volumetric-fraction-weighted average formulation [16]: $\mathrm{Le}_{\mathrm{eff}} = X_{\mathrm{C_nH_m}} \mathrm{Le}_{\mathrm{C_nH_m}} + X_{\mathrm{H_2}} \mathrm{Le}_{\mathrm{H_2}}$, where X is the mole fraction in the fuel stream. As listed in Table 4.1, $\mathrm{Le}_{\mathrm{eff}}$ decreases with increasing H_2 content in the fuel stream from 0.97 for CH_4-air, and from 1.86 for C_3H_8-air, down to 0.376 for pure H_2.

Diffusive flame thickness ($\delta_{\mathrm{L}} = \lambda/(c_{\mathrm{p}}\, \rho_{\mathrm{u}} S_{\mathrm{L}}^{\mathrm{o}})$), and adiabatic flame temperature (T_{ad}) are calculated using free-flame simulations in Cantera [17], and listed in Table 4.1. GRI-Mech 3.0 and

Table 4.1 Properties of CH_4+H_2+air and C_3H_8+H_2+air mixtures at constant $S_L^o = 0.195$ m/s.

H_2 (%)	CH_4+H_2+air				C_3H_8+H_2+air			
(by Vol.)	ϕ	Le_{eff}	δ_L (mm)	T_{ad} (K)	ϕ	Le_{eff}	δ_L (mm)	T_{ad} (K)
0	0.7	0.97	0.271	1842	0.659	1.86	0.248	1817
20	0.668	0.85	0.280	1800	0.647	1.56	0.252	1799
40	0.628	0.73	0.291	1746	0.630	1.27	0.259	1774
60	0.578	0.61	0.306	1679	0.602	0.97	0.270	1733
80	0.513	0.50	0.327	1593	0.547	0.67	0.291	1650
100	0.423	0.38	0.363	1481	0.423	0.38	0.363	1481

AramcoMech 1.3 reaction mechanisms are used for computations involving CH_4 and C_3H_8, respectively.

4.3.1 Hot-exhaust opposed-flow turbulent flame rig

Experiments are conducted in a hot-exhaust opposed-flow turbulent flame rig (HOTFR) [18–24]. The rig is designed to stabilize turbulent flames against a hot product flow in an axial counter-flow configuration. In HOTFR, the flow from the premixed fuel and air nozzle at the bottom impinges against hot products from a pre-burner inside the ceramic burner at the top. A co-flow of inert gas is used to reduce the effect of the shear layer, stabilize the flame edge, and shroud the opposed flow from surrounding air. The exit diameter of the premixed fuel and air nozzle (d_N) is 20 mm, and the separation distance between the two nozzles is $1.4\,d_N$. A schematic of HOTFR is shown in Fig. 4.1.

A CH_4-air mixture at $\phi = 0.75$, and $T_{ad} = 1924$ K is used to feed the top nozzle, and the nozzle exit velocity ($U_{CB} \approx 13$ m/s) is kept constant in all experiments. The temperature of hot exhaust gases at the ceramic nozzle exit is measured using R-type thermocouples, and corrected for heat losses: $T_{CB} = 1837$ K. Radial temperature profiles are fairly constant, and the repeatability of T_{CB} readings are verified through multiple measurements with an uncertainty of ~ 1 % of the reading. Please see Appendix B for details of temperature measurements.

Turbulence in the test area is generated using a star-shaped high-blockage turbulence generating plate (S-TGP) with an open area of 2.4 % [25], as illustrated in Fig. 4.1. Higher turbulence intensity assures combustion in the thin reaction zone regime of the Borghi diagram [26], and allows experiments closer to relevant conditions of gas-turbine engines (GTE) and other combustors. S-TGP is removed in laminar flame experiments while flow conditions and mixture compositions are preserved.

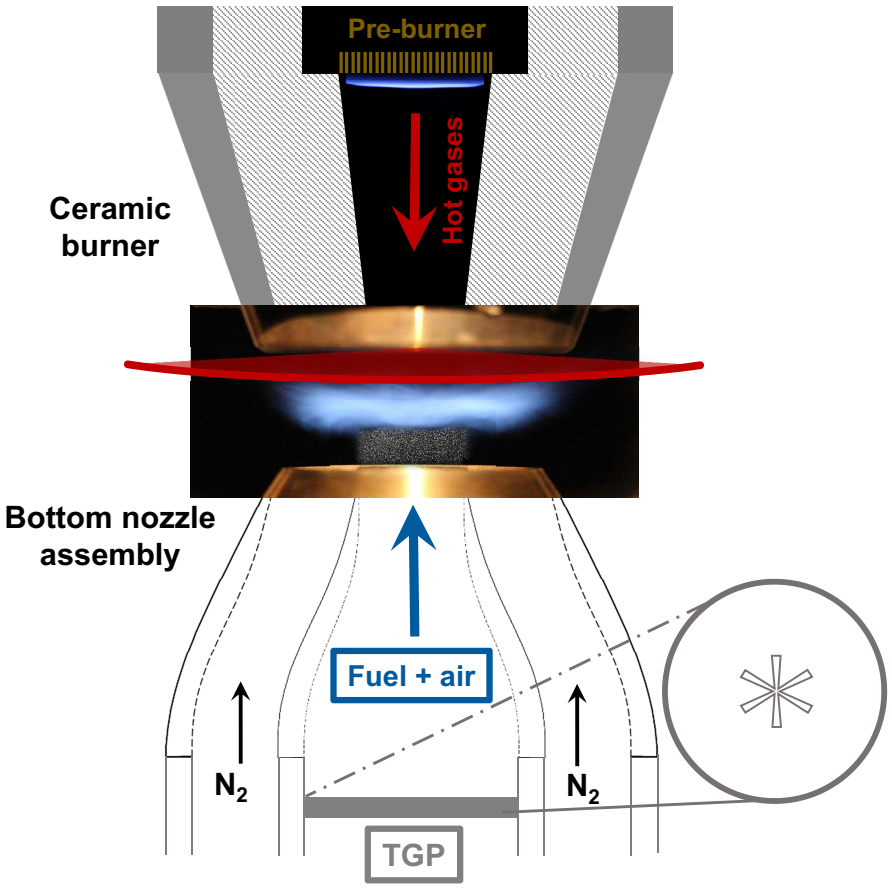

Figure 4.1 Schematic of HOTFR and S-TGP.

In turbulent experiments, S-TGP distance from the nozzle exit (h) was set at $h/d_{\mathrm{TGP}} = 2.4$, where d_{TGP} is the diameter of the plate. This distance was chosen to be larger than that found to minimize large-scale bulk-flow oscillations, as shown in [25] using energy spectra of S-TGP for various h. These large-scale oscillations are caused by vortex shedding from the TGP holes and are minimized by using a single-jet TGP design and increased h [27]. Furthermore, the contoured design of the nozzles is also effective in damping jet-wake interactions downstream of the TGP.

The rig has a compact geometry and excellent optical accessibility, where aerodynamically-stabilized lifted flames are not affected by conductive heat loss to the burners, and are stabilized against a uniform flow of hot combustion products. Therefore, it provides clear boundary conditions and a compact experimental zone that reduces the complexity, and makes it ideal for validating computational fluid dynamics (CFD) models.

Table 4.2 Experimental conditions of turbulent CH_4+H_2+air and C_3H_8+H_2+air flames at $S_L^o = 0.195$ m/s using S-TGP.

	H_2 [%] (by Vol.)	U/S_L^o	u'/S_L^o	$u'/\overline{U}$	L/δ_L	L/η	Re_T	Ka_T	Da_T
CH_4+H_2+air	0	23.1	8.4	0.36	9.9	29.0	89.0	8.6	1.2
	70	21.6	7.3	0.34	10.0	28.2	85.9	8.0	1.4
C_3H_8+H_2+air	0	23.5	7.8	0.33	11.3	29.5	91.0	6.8	1.5
	90	21.8	7.4	0.34	10.3	28.9	88.5	7.9	1.4

4.3.2 Diagnostic method and processing techniques

4.3.2.1 Particle image velocimetry

The flow velocity field is quantified using two-dimensional high-speed particle image velocimetry (2D-PIV) within the imaged plane. Atomized oil droplets ($\approx 1\,\mu$m) are seeded into the flow, through an atomizer, as tracer particles, and are illuminated using a Nd:YLF laser at 527 nm wavelength. The Mie scattered light is captured using a high-speed CMOS camera at imaging speed of 12 kfps. 10 000 PIV image pairs are post-processed using the DaVis PIV software package to calculate the two-component velocity vector field within the plane of the laser sheet at each turbulent run, whereas 500 images are used in each laminar experiment. The smallest interrogation window used in PIV calculations is a 16 $\times$ 16 pixel grid with a window overlap of 75 %. The pixel-to-mm ratio is 44.7, yielding a PIV spatial resolution of $\approx 358\,\mu$m, and a grid-spacing of $\approx 89.5\,\mu$m in these experiments.

Turbulent flow statistics of the mean velocity ($\overline{U}$) and root-mean-square (rms) of velocity fluctuations (u' in the axial direction and v' in the radial direction) are calculated, and the results are listed in Table 4.2 for pure hydrocarbon flames and H_2-enriched flames near the flash-back region, where $\overline{U}$ and u' are averaged over the test domain at 0.7 mm above the nozzle exit, and upstream of the flame brush, respectively. Details of uncertainty analysis in the flow velocity measurement are discussed in Appendix C. These calculations result in an uncertainty of approximately 1.5 %, in the unburned gas velocity in turbulent flame experiments.

The performance of the S-TGP in generating turbulence is illustrated in Fig. 4.2. u' and v' velocity profiles show that turbulence statistics in the test domain is nearly isotropic ($u' \approx v'$), and axial turbulence intensity fluctuates slightly within the range of $31\,\% \leq u'/\overline{U} \leq 36\,\%$, as listed in Table 4.2.

The integral length scale (L) is estimated using the autocorrelation coefficient [28, 29]. An

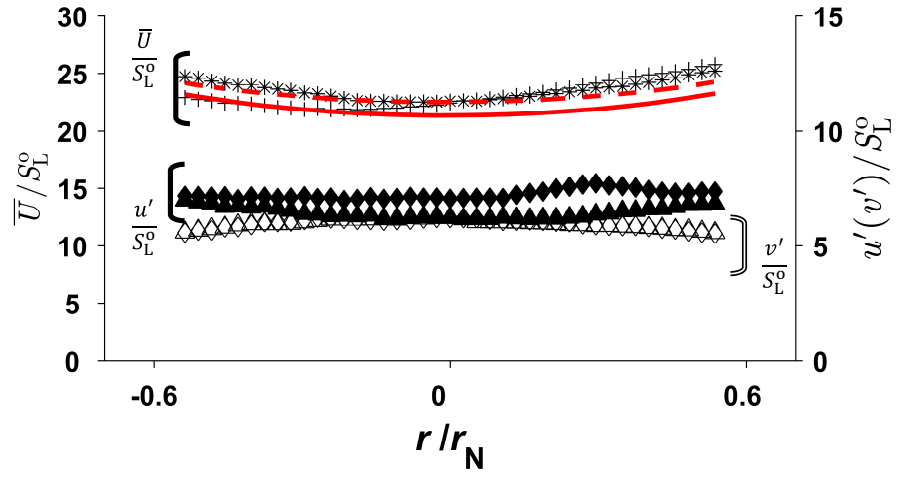

Figure 4.2 Nozzle exit u' (♦ and ▲), v' (◊ and △), turbulent $\overline{U}$ (+ and $*$), and laminar $\overline{U}$ (solid and dash) of CH_4+air and C_3H_8+air flames, respectively, in radial direction.

estimation for the ratio of largest to smallest hydrodynamic length scales in a turbulent flow can be derived as [28]: $L/\eta \approx \mathrm{Re_T}^{3/4}$, where η is the Kolmogorov length scale, and $\mathrm{Re_T}$ is the turbulent Reynolds number: $\mathrm{Re_T} = u'\,L/\nu$. $\mathrm{Re_T}$ is calculated upstream of the flame brush, in the preheat zone at $T \approx 576\,\mathrm{K}$, which is the flash point of the oil used for seeding, whereas, the cold flow equivalent of $\mathrm{Re_T}$ is around 240. Studying turbulence-chemistry interactions in this range of $\mathrm{Re_T}$ is of specific interest in the validation of flamelet models, in the region where mixing and chemical time scales are comparable.

Turbulent Karlovitz number: $\mathrm{Ka_T} = (L/\delta_\mathrm{L})^{-2}\,\mathrm{Re_T}^{1.5}$, and turbulent Damköhler number: $\mathrm{Re_T} = \mathrm{Da_T^2}\,\mathrm{Ka_T^2}$ [30] are listed in Table 4.2. $\mathrm{Ka_T}$ and $\mathrm{Da_T}$ are also calculated at $T \approx 576\,\mathrm{K}$. According to the experimental conditions listed in Table 4.2, these flames are located in the thin reaction zone regime of the Borghi diagram [26, 30].

4.3.2.2 Processing techniques

Mie scattering of light from atomized oil droplets allows simultaneous flame-location detection and velocity-field measurements [31, 32]. Atomized oil droplets seeded into the flow evaporate at the flame front and terminate the light scattering. Hence, the pixel light intensities from the PIV images can be processed using flame-surface tracking methods to track the flame front. In this technique, it is assumed that combustion occurs inside a relatively thin layer, and that the flamelet

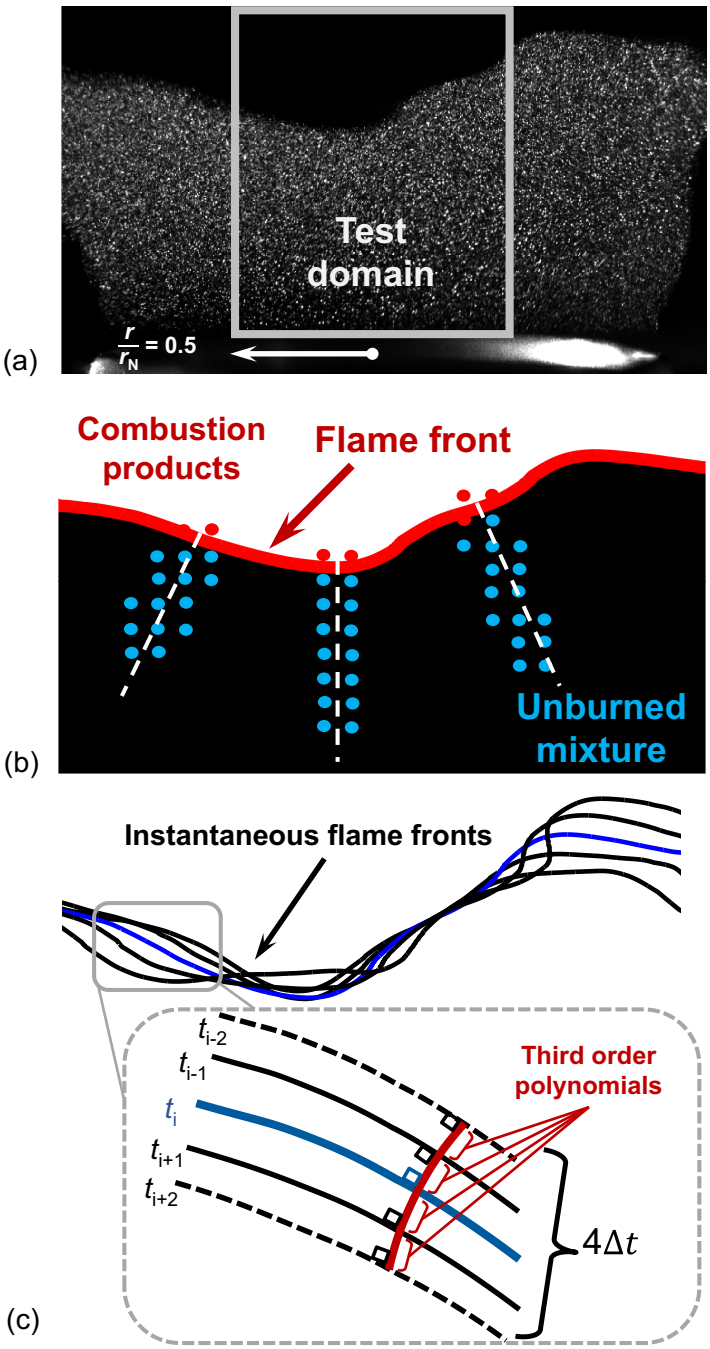

Figure 4.3 Processing techniques: (a) a sample PIV image indicating the test domain, (b) a quantized PIV image with an example flame front illustrating the schematic of S_u measurement, and (c) 5 successive flame fronts and a schematic showing S_F calculation.

model [30] is valid. A sample PIV image is illustrated in Fig. 4.3 (a), showing the test domain at $-0.25 \leq (r/d_{\mathrm{N}}) \leq 0.25$.

In flame-front tracking, an edge-detection algorithm is applied to find locations of maximum pixel-intensity gradient on a PIV image, and localize the edges, resulting in instantaneous flame-front topology within the imaged flame. A quantized PIV image with the resulting flame front is shown in Fig. 4.3 (b). The main uncertainty sources of this method are the mean tracer particle distance, the oil droplet lifetime at the flame front, uncertainties imposed by filtering process during post processing, and over-saturated pixels from larger oil droplets in PIV images, resulting in a total uncertainty of less than $0.5\,\delta_{\mathrm{L}}$. The details of uncertainty analysis in flame-front tracking are discussed in Appendix D.

The local turbulent flame displacement velocity (S_{T}) is the propagation velocity of the local flamelet (S_{F}) relative to the convection velocity of the flow (S_{u}) in the direction normal to the flame surface ($\mathbf{n}$) [15, 33–35]: $S_{\mathrm{T}} = (S_{\mathrm{F}} + S_{\mathrm{u}}) \cdot \mathbf{n}$. S_{T} measurement is discussed in detail in the study of Trunk *et al.* [34]. However, in the current study, the 2D projection of S_{T} is measured using 2D-PIV and single-plane imaging, which is the apparent turbulent flame velocity within the imaged plane, and is noted as S_{T} for simplicity.

Hartung *et al.* [35] showed that the 2D projection of S_{T} is, indeed, a sensitive parameter in turbulence-chemistry interactions, and that more complex 3D measurements might not result in significant extra information. The experiments have the advantage of relative simplicity and superior precision compared to complex 3D measurements, which present a suitable method for quantification of turbulence-chemistry interactions with a specific potential in the validation of CFD simulations. They also provide adequate data to address the effects of differential diffusion on the flame propagation in the context of fuel flexibility, which is the main focus of this study.

The instantaneous two-component unburned gas velocity upstream of the flame front (S_{u}) is calculated using the velocity grid network in the vicinity of the normal line, as seen in Fig. 4.3 (b). Due to a significant decrease in signal-to-noise ratio, and increased uncertainty in PIV velocity vectors within the regions of elevated temperatures in the preheat zone [34], a local velocity minimum at the edge of the preheat zone is considered as the most appropriate local convective velocity. However, in turbulent flames, this minimum is not always recognized due to the movement of the flame, and the average of the two closest velocity vectors to the flame is considered as S_{u} upstream of the flame front.

Axial hydrodynamic strain rate (K_{s}) is computed by a linear fitting to the projected velocity values in the unburned region along the normal line. These calculations are done within 1.5 mm upstream of the flame front (equivalent to 5-9 independent velocity data), over 10 000 PIV images to approach the PDF of K_{s}.

In order to measure instantaneous apparent flame front velocity (S_{F}), the flamelet's path between 5 consecutive flame fronts within the imaged plane is estimated using 4 continuous third-order polynomials to reconstruct the flame motion, which are perpendicular to all 5 flame fronts and the total length is a minimum [36]. A fourth-order finite difference method is used to calculate displacement data for each segment of the flame, which is used in the calculation of S_{F}. This method is illustrated schematically in Fig. 4.3 (c). S_{F} is considered positive when the velocity is toward the unburned gas, and is considered negative in the opposite direction.

In laminar flame experiments, the unburned gas velocity upstream of the flame front ($S_{\mathrm{u-ref}}$) is measured as the minimum of the averaged velocity profile, along the nozzle centerline.

4.4 Results and discussion

PDFs of instantaneous flame location within the imaged plane (Z_{f}) at increasing H_2-enrichment are shown in Figs. 4.4 (a) and 4.4 (b), where $Z_{\mathrm{f}} = 0$ is located at the exit plane of the bottom nozzle. PDFs of Z_{f} give statistics of the flame location, and the range of flame movement. The expected flame location ($\langle Z_{\mathrm{f}} \rangle$), as well as the flame brush thickness, $\delta_{\mathrm{T}} = 4 \times \sigma$, where σ is the standard deviation of the PDFs, can be extracted. Furthermore, the skewness of the PDFs indicates a propensity for the flame location to be upstream or downstream of $\langle Z_{\mathrm{f}} \rangle$.

As shown in Figs. 4.4 (a) and 4.4 (b), PDFs of the pure hydrocarbon flames are skewed toward the stagnation surface, as they are pushed to the hot exhaust gases by the steep average velocity-gradients. In H_2-enriched flames, with increasing H_2-enrichment, PDFs of Z_{f} move toward the bottom nozzle and become less skewed, which shows that the enriched flames have a higher tendency to burn faster and climb up the velocity gradient toward the unburned mixture. This relocation is clearly seen in CH_4-H_2-air flames at H_2 content as low as 20 %, whereas in C_3H_8-H_2-air flames, PDFs of Z_{f} show a slight tendency to move toward the fresh reactants up to H_2 contents of 60 %, and a considerable movement toward the bottom nozzle at H_2 contents above 60 %.

In order to quantify these effects, $\langle Z_{\mathrm{f}} \rangle$ of turbulent and laminar flames, as well as δ_{T} and δ_{L} variations, are summarized in Figs. 4.4 (c) and 4.4 (d). Figure 4.4 (c) illustrates that highly-strained laminar flames also move further upstream toward the unburned reactants with increasing H_2 content. Cold-flow experiments show that the momentum change in opposed-jet streams during the enrichment from 0 % to 100 %, results in a relocation of the stagnation surface of less than $0.02 \langle Z_{\mathrm{f}} \rangle / d_{\mathrm{N}}$ toward the bottom nozzle. $\langle Z_{\mathrm{f}} \rangle$ decreases linearly in CH_4-H_2-air flames, as $\mathrm{Le}_{\mathrm{eff}}$ is also decreasing linearly from a value close to one to 0.38 for the pure H_2-air flame. In C_3H_8-H_2-air flames, in contrast, the slope appears to change after 70 % of H_2 content once differential

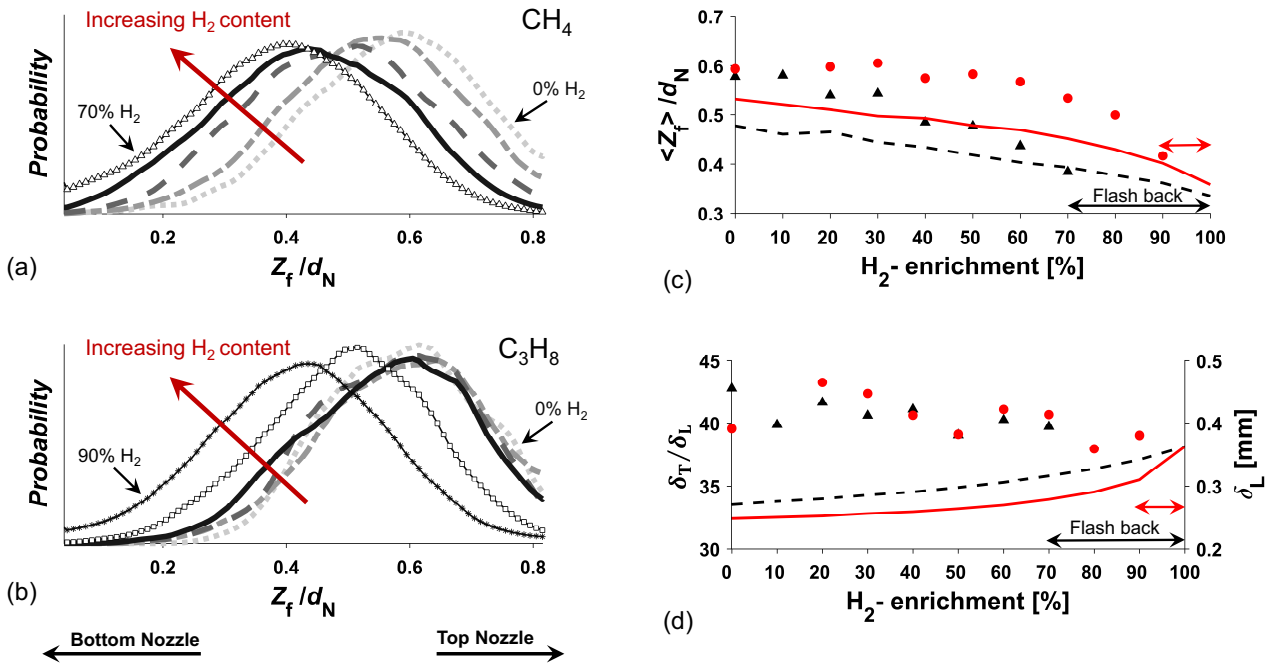

Figure 4.4 PDFs of Z_{f} for turbulent: (a) CH_4-H_2-air, and (b) C_3H_8-H_2-air flames at increasing H_2-enrichment of 0 % (dot), 20 % (dash-dot), 40 % (dash), 60 % (solid), 70 % (△), 80 % (□), and 90 % (∗). (c) $\langle Z_{\mathrm{f}} \rangle$ of turbulent (symbol) and laminar (line): CH_4-H_2-air (▲ and dash), and C_3H_8-H_2-air (● and solid) flames, respectively. (d) δ_{T} of turbulent (symbol) and δ_{L} of laminar (line): CH_4-H_2-air (▲ and dash), and C_3H_8-H_2-air (● and solid) flames, respectively.

diffusion effects become effective at $\mathrm{Le}_{\mathrm{eff}} < 1$. Similar behavior is observed in turbulent C_3H_8-H_2-air flames, where $\langle Z_{\mathrm{f}} \rangle$ is almost constant up to H_2-enrichment of 60 %, and drops significantly after 70 % ($\mathrm{Le}_{\mathrm{eff}} \leq 0.82$), whereas, in CH_4-H_2-air flames, decreasing trend in $\langle Z_{\mathrm{f}} \rangle$ is observed at H_2 content of as low as 20 %, and is more significant after 30 % ($\mathrm{Le}_{\mathrm{eff}} \leq 0.79$). Flash-back regions are illustrated in Figs. 4.4 (c) and 4.4 (d) for turbulent flames.

Normalized δ_{T} (Fig. 4.4 (d)) is almost constant, while δ_{L} slightly increases with increasing H_2-enrichment at constant laminar flame speed.

PDFs of S_{T} are illustrated in Figs. 4.5 (a) and 4.5 (b). The key features of these PDFs are the most probable apparent turbulent flame velocity ($\langle S_{\mathrm{T}} \rangle$), and the distribution of PDFs compared to $S_{\mathrm{L}}^{\mathrm{o}}$. These PDFs include the velocity data up to 60 % and 80 % of enrichment for CH_4-H_2-air and C_3H_8-H_2-air flames, respectively, as extensive wrinkling of the enriched flames at distances too close to the nozzle exit, at the near flash-back limit, significantly decreases the signal-to-noise ratio in S_{u}, S_{F}, and S_{T} measurements.

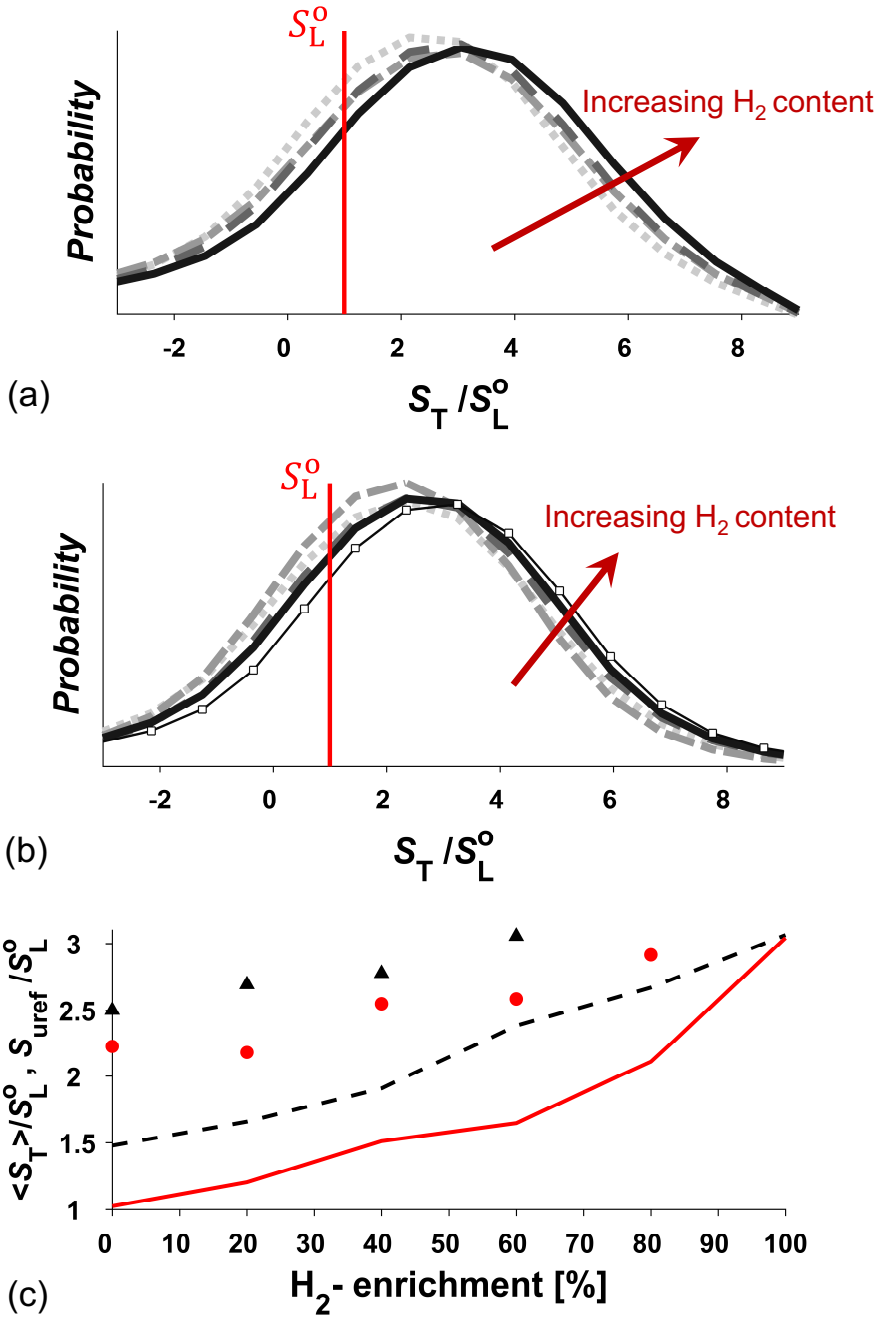

Figure 4.5 PDFs of S_T for turbulent: (a) CH_4-H_2-air, and (b) C_3H_8-H_2-air flames at increasing H_2-enrichment of 0 % (dot), 20 % (dash-dot), 40 % (dash), 60 % (solid), and 80 % (□). (c) $\langle S_T \rangle$ (▲ and ●) and S_{u-ref} (dash and solid) correlations of CH_4-H_2-air and C_3H_8-H_2-air flames at increasing H_2-enrichment, respectively.

As illustrated in Fig. 4.5 (a), PDF of S_{T} in CH_4-air flame shows values in the range of $-2 \lesssim S_{\mathrm{T}}/S_{\mathrm{L}}^{\mathrm{o}} \lesssim 8$, consistent with the local 3D turbulent displacement velocity measurements reported in [34], which further validates the current measurements. Direct numerical simulation (DNS) study of 2D stoichiometric CH_4-air flames [37] also supports the existence of negative S_{T} values, in the highly curved regions.

PDFs of S_{T} in H_2-enriched CH_4-air flames move toward slightly higher velocities by increasing H_2 content. However, in C_3H_8-H_2-air flames, PDFs of S_{T} are not sensitive to the effects of differential diffusion at low H_2 contents, and start to move toward higher velocities at higher H_2 content. PDFs of S_{T} are normally distributed and look almost similar for both flame mixtures.

$\langle S_{\mathrm{T}} \rangle$ and $S_{\mathrm{u-ref}}$ are plotted versus H_2 content in Fig. 4.5 (c). In general, $\langle S_{\mathrm{T}} \rangle$ is larger than $S_{\mathrm{u-ref}}$, due to the fact that turbulent flames also have local curvature to enhance the local flamelet burning rate. In turbulent flames, $\langle S_{\mathrm{T}} \rangle$ is 2 to 3 times larger than $S_{\mathrm{L}}^{\mathrm{o}}$, which indicates the propensity of these flames to burn faster when stretched, as also shown in [35].

As shown in Fig. 4.5 (c), $\langle S_{\mathrm{T}} \rangle$ is larger in CH_4-H_2-air compared to C_3H_8-H_2-air flames, and it shows a slight increase with increasing H_2 content due to the differential diffusion effects. $\langle S_{\mathrm{T}} \rangle$ values closely correlate with PDFs of Z_{f} (Fig. 4.4 (c)).

The trends in $S_{\mathrm{u-ref}}$ of laminar flames at increasing H_2-enrichment are in agreement with Z_{f} correlations shown in Fig. 4.4 (c), and $S_{\mathrm{u-ref}}$ remains closer to $S_{\mathrm{L}}^{\mathrm{o}}$ in the absence of turbulence for the pure hydrocarbon flames. Highly-strained laminar flames are sensitive to thermo-diffusive effects at $\mathrm{Le_{eff}} < 1$, where $\mathcal{D}$ is larger than α, which increases local ϕ; consequently, temperature and flame velocity increase. Therefore, at constant flame stretch, $S_{\mathrm{u-ref}}$ linearly increases and $\langle Z_{\mathrm{f}} \rangle$ linearly decreases at increasing H_2 content for CH_4-H_2-air flames with $\mathrm{Le_{eff}} < 1$. However, in C_3H_8-H_2-air flames, the slope appears to change once $\mathrm{Le_{eff}} < 1$.

In the counter-flow geometry, laminar flames are stretched mainly due to the bulk strain rate: $K_{\mathrm{s}} = \mathrm{d}U/\mathrm{d}x$, where U is the bulk axial velocity and x is the axial distance. However, in turbulent flames, stretching is due to both bulk strain rate and the stretch effects of turbulent eddies through increasing flamelet curvature (κ). The two components of flame stretch, K_{s} and $\langle |\kappa| \rangle$, are illustrated in Figs. 4.6 (a) and 4.6 (b).

In general, Figs. 4.6 (a) and 4.6 (b) show that the bulk strain rate is larger than the stretch caused by curvature in highly-strained turbulent counter-flow flames. $\langle K_{\mathrm{s}} \rangle$ remains almost constant in laminar and turbulent flames, and is higher in turbulent flames compared to laminar cases. Furthermore, in CH_4-H_2-air flames, $\langle |\kappa| \rangle S_{\mathrm{L}}^{\mathrm{o}}$ increases with increasing H_2 content, while in C_3H_8-H_2-air flames, $\langle |\kappa| \rangle S_{\mathrm{L}}^{\mathrm{o}}$ is constant up to 60 % of H_2 content, after which $\mathrm{Le_{eff}} < 1$, and $\langle |\kappa| \rangle S_{\mathrm{L}}^{\mathrm{o}}$ increases sharply. The increase in stretch sensitivity leads to a flame making more frequent incursions to the unburned reactants in mixtures with $\mathrm{Le_{eff}} < 1$. Increasing local flamelet curvature also

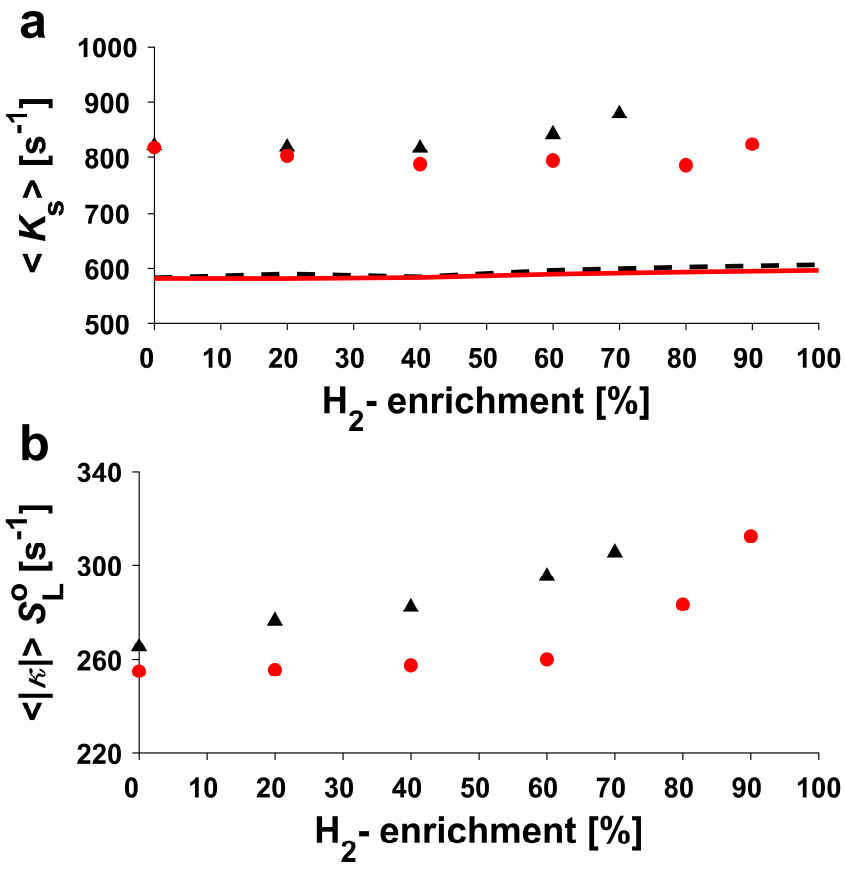

Figure 4.6 Components of flame stretch: (a) $\langle K_s \rangle$ of turbulent and laminar: CH_4-H_2-air (▲ and dash), and C_3H_8-H_2-air (● and solid) flames, (b) $\langle |\kappa| \rangle$ of CH_4-H_2-air (▲) and C_3H_8-H_2-air (●) turbulent flames, respectively.

increases the global turbulent burning rates due to an increase in flame surface density [38], which make the flames to burn faster and move further upstream to the high-speed region close to the nozzle, eventually causing flash back in mixtures with high H_2 content.

4.5 Conclusions

The effects of differential diffusion on laminar and turbulent flame velocities and stabilization of lean premixed flames were investigated in a counter-flow apparatus. H_2-enriched CH_4-air flames and C_3H_8-air flames, representative of distinct $\mathrm{Le_{eff}}$, were studied at constant laminar flame speeds.

PDFs of instantaneous flame location illustrate that the effects of differential diffusion are only observed in H_2-enriched C_3H_8-air flames when $\mathrm{Le_{eff}} < 1$ at H_2 contents of larger than 60 % (by

volume), whereas a continuous drop in flame location was observed in H_2-enriched CH_4-air flames, all having $\mathrm{Le}_{\mathrm{eff}} < 1$, at increasing H_2-enrichment. Furthermore, PDFs of flame location show that the effects of differential diffusion become significant when $\mathrm{Le}_{\mathrm{eff}} \lesssim 0.8$.

PDFs of local instantaneous apparent turbulent flame velocity closely correlate with the PDFs of flame location. While local turbulent flame velocities are larger in CH_4-H_2-air compared to C_3H_8-H_2-air flames, the PDFs show a slight increase with increasing H_2 content due to the effects of differential diffusion, and have values 2 to 3 times larger than $S_{\mathrm{L}}^{\mathrm{o}}$.

In highly-strained turbulent counter-flow flames, differential diffusion affects the flame-front topology in mixtures with $\mathrm{Le}_{\mathrm{eff}} < 1$. While bulk strain rates remain nearly constant, we observe a clear increase in the flame-front curvature when $\mathrm{Le}_{\mathrm{eff}}$ falls below unity, which then allows the flames to burn faster and propagate further upstream toward the unburned reactants, specifically in mixtures with $\mathrm{Le}_{\mathrm{eff}} \lesssim 0.8$, eventually leading to flash back.

Acknowledgment

This research was funded by the Natural Sciences and Engineering Research Council of Canada (grant no. I242349C0G) and Siemens Canada Limited (grant no. I242215C0G) under the Collaborative Research and Development program (NSERC-CRD). Support of the McGill Engineering Doctoral Awards (MEDA) program is also gratefully acknowledged.

References

[1] Z. Huang, Y. Zhang, K. Zeng, B. Liu, Q. Wang, and D. Jiang. "Measurements of laminar burning velocities for natural gas–hydrogen–air mixtures". In: *Combustion and Flame* 146 (2006), pp. 302–311.

[2] C. Tang et al. "Laminar burning velocities and combustion characteristics of propane–hydrogen–air premixed flames". In: *International Journal of Hydrogen Energy* 33 (2008), pp. 4906–4914.

[3] R.G. Abdel-Gayed, D. Bradley, M.N. Hamid, and M. Lawes. "Lewis number effects on turbulent burning velocity". In: *Proceedings of the Combustion Institute* 20 (1984), pp. 505–512.

[4] A.N. Lipatnikov and J. Chomiak. "Molecular transport effects on turbulent flame propagation and structure". In: *Progress in Energy and Combustion Science* 31 (2005), pp. 1–73.

[5] R.S. Barlow, M.J. Dunn, M.S. Sweeney, and S. Hochgreb. "Effects of preferential transport in turbulent bluff-body-stabilized lean premixed CH_4/air flames". In: *Combustion and Flame* 159 (2012), pp. 2563–2575.

[6] J.D. Regele, E. Knudsen, H. Pitsch, and G. Blanquart. "A two-equation model for non-unity Lewis number differential diffusion in lean premixed laminar flames". In: *Combustion and Flame* 160 (2013), pp. 240–250.

[7] E. Boschek, P. Griebel, and P. Jansohn. "Fuel variability effects on turbulent, lean premixed flames at high pressures". In: *Proceedings of the ASME Turbo Expo: Turbine Technical Conference and Exposition. GT2007–27496* (2007).

[8] M. Matalon. "On flame stretch". In: *Combustion Science and Technology* 31 (1983), pp. 169–181.

[9] C.K. Law. "Dynamics of stretched flames". In: *Proceedings of the Combustion Institute* 22 (1989), pp. 1381–1402.

[10] R.W. Pitz, S. Hu, and P. Wang. "Tubular premixed and diffusion flames: Effect of stretch and curvature". In: *Progress in Energy and Combustion Science* 42 (2014), pp. 1–34.

[11] A. Marshall, J. Lundrigan, P. Venkateswaran, J. Seitzman, and T. Lieuwen. "Fuel effects on leading point curvature statistics of high hydrogen content fuels". In: *Proceedings of the Combustion Institute* 35 (2015), pp. 1417–1424.

[12] F. Dinkelacker, B. Manickam, and S.P.R. Muppala. "Modelling and simulation of lean premixed turbulent methane/hydrogen/air flames with an effective Lewis number approach". In: *Combustion and Flame* 158 (2011), pp. 1742–1749.

[13] F. Halter, C. Chauveau, and I. Gökalp. "Characterization of the effects of hydrogen addition in premixed methane/air flames". In: *International Journal of Hydrogen Energy* 32 (2007), pp. 2585–2592.

[14] C. Mandilas, M.P. Ormsby, C.G.W. Sheppard, and R. Woolley. "Effects of hydrogen addition on laminar and turbulent premixed methane and iso-octane–air flames". In: *Proceedings of the Combustion Institute* 31 (2007), pp. 1443–1450.

[15] J.F. Driscoll. "Turbulent premixed combustion: Flamelet structure and its effect on turbulent burning velocities". In: *Progress in Energy and Combustion Science* 34 (2008), pp. 91–134.

[16] N. Bouvet, F. Halter, C. Chauveau, and Y. Yoon. "On the effective Lewis number formulations for lean hydrogen/hydrocarbon/air mixtures". In: *International Journal of Hydrogen Energy* 38 (2013), pp. 5949–5960.

[17] D.G. Goodwin, H.K. Moffat, and R.L. Speth. *Cantera: A software toolkit for chemical kinetics, thermodynamics, and transport processes*. Version 2.2.1, http://www.cantera.org, 2016.

[18] G. Coppola, B. Coriton, and A. Gomez. "Highly turbulent counterflow flames: A laboratory scale benchmark for practical systems". In: *Combustion and Flame* 156 (2009), pp. 1834–1843.

[19] E. Mastorakos, A.M.K.P. Taylor, and J.H. Whitelaw. "Extinction of turbulent counterflow flames with reactants diluted by hot products". In: *Combustion and Flame* 102 (1995), pp. 101–114.

[20] D. Geyer, A. Kempf, A. Dreizler, and J. Janicka. "Turbulent opposed-jet flames: A critical benchmark experiment for combustion LES". In: *Combustion and Flame* 143 (2005), pp. 524–548.

[21] F. Hampp and R.P. Lindstedt. "Quantification of combustion regime transitions in premixed turbulent DME flames". In: *Combustion and Flame* 182 (2017), pp. 248–268.

[22] E. Mastorakos, A.M.K.P. Taylor, and J.H. Whitelaw. "Extinction and temperature characteristics of turbulent counterflow diffusion flames with partial premixing". In: *Combustion and Flame* 91 (1992), pp. 40–54.

[23] K. Sardi, A.M.K.P. Taylor, and J.H. Whitelaw. "Conditional scalar dissipation statistics in a turbulent counterflow". In: *Journal of Fluid Mechanics* 361 (1998), pp. 1–24.

[24] A. Kempf, H. Forkel, J.-Y. Chen, A. Sadiki, and J. Janicka. "Large-eddy simulation of a counterflow configuration with and without combustion". In: *Proceedings of the Combustion Institute* 28 (2000), pp. 35–40.

[25] G. Coppola and A. Gomez. "Experimental investigation on a turbulence generation system with high-blockage plates". In: *Experimental Thermal and Fluid Science* 33 (2009), pp. 1037–1048.

[26] R. Borghi. "On the structure and morphology of turbulent premixed flames". In: *Recent Advances in the Aerospace Sciences* (1985), pp. 117–138.

[27] B. Böhm, O. Stein, A. Kempf, and A. Dreizler. "In-nozzle measurements of a turbulent opposed jet using PIV". In: *Flow, Turbulence and Combustion* 85 (2010), pp. 73–93.

[28] H. Tennekes and J.L. Lumley. *A First Course in Turbulence*. The MIT Press, Cambridge, USA, 1972.

[29] J.O. Hinze. *Turbulence*. McGraw-Hill, New York, USA, 1975.

[30] N. Peters. *Turbulent combustion*. Cambridge university press, Cambridge, UK, 2000.

[31] S.A. Filatyev, J.F. Driscoll, C.D. Carter, and J.M. Donbar. "Measured properties of turbulent premixed flames for model assessment, including burning velocities, stretch rates, and surface densities". In: *Combustion and Flame* 141 (2005), pp. 1–21.

[32] S. Kheirkhah and Ö.L. Gülder. "Consumption speed and burning velocity in counter-gradient and gradient diffusion regimes of turbulent premixed combustion". In: *Combustion and Flame* 162 (2015), pp. 1422–1439.

[33] H. Kolla, J.W. Rogerson, and N. Swaminathan. "Validation of a turbulent flame speed model across combustion regimes". In: *Combustion Science and Technology* 182 (2010), pp. 284–308.

[34] P.J. Trunk, I. Boxx, C. Heeger, W. Meier, B. Böhm, and A. Dreizler. "Premixed flame propagation in turbulent flow by means of stereoscopic PIV and dual-plane OH-PLIF at sustained kHz repetition rates". In: *Proceedings of the Combustion Institute* 34 (2013), pp. 3565–3572.

[35] G. Hartung, J. Hult, R. Balachandran, M.R. Mackley, and C.F. Kaminski. "Flame front tracking in turbulent lean premixed flames using stereo PIV and time-sequenced planar LIF of OH". In: *Applied Physics B* 96 (2009), pp. 843–862.

[36] R. Abu-Gharbieh, G. Hamarneh, T. Gustavsson, and C.F. Kaminski. "Flame front tracking by laser induced fluorescence spectroscopy and advanced image analysis". In: *Optics Express* 8 (2001), pp. 278–287.

[37] I.R. Gran, T. Echekki, and J.H. Chen. "Negative flame speed in an unsteady 2-D premixed flame: A computational study". In: *Proceedings of the Combustion Institute* 26 (1996), pp. 323–329.

[38] J. Hult et al. "Measurement of flame surface density for turbulent premixed flames using PLIF and DNS". In: *Proceedings of the Combustion Institute* 31 (2007), pp. 1319–1326.

Link between chapters 4 and 5

Experiments in Chapter 4 were focused on the effects of variations in fuel diffusivity of the mixtures on flame location and local flamelet velocities for lean premixed H_2-enriched hydrocarbon flames, at a constant turbulence level. In Chapter 4, mixtures of various fuel blends in the air were studied; hence, variations in $\mathrm{Le_{eff}}$ were mainly due to the variations in fuel diffusivity. In these experiments, local flamelet velocity measurements were not reported for mixtures with $\mathrm{Le_{eff}} \leq 0.5$, due to flashback. It was demonstrated that the effects of differential diffusion in increasing turbulent burning rates were only observed in H_2-enriched C_3H_8-air flames when $\mathrm{Le_{eff}} < 1$ at H_2 contents of larger than $60\,\%$ (by volume), whereas, these effects were observed in H_2-enriched CH_4-air flames over the whole range of H_2 content, all having $\mathrm{Le_{eff}} < 1$. However, PDFs of flame velocity showed that local flamelet displacement velocities only slightly increased with increasing H_2 content due to the effects of differential diffusion. These results further implied that there must also be an effect of differential diffusion on the flame surface area at constant turbulence intensities.

In Chapter 5, the goal is to study the stretch sensitivity of turbulent premixed flames in mixtures with a wide range of effective Lewis numbers, which allows drawing general conclusions on the effects of differential diffusion on the propagation of turbulent premixed flames, rather than generating fuel-specific conclusions. To continue in this direction, fuels and fuel blends, in combination with various oxidizer-inert mixtures, will be used to form mixtures with very distinct $\mathrm{Le_{eff}}$, by varying both fuel diffusivity and thermal diffusivity of the mixture, through H_2 enrichment and dilution. Similar to the previous chapter, the unstretched laminar flame speed of the mixtures, the bulk-flow properties, and the temperature boundary condition will be kept constant, in order to only focus on the effects of differential diffusion. In these experiments, the reactivity of the mixtures will be reduced ($S_\mathrm{L}^\mathrm{o} = 0.115\,\mathrm{m/s}$), which allows stabilizing flames at a wider range of Lewis numbers, and prevents/delays flashback in flames with high H_2 content. Turbulence will be generated using the same S-TGP, used in Chapter 4, at two levels of turbulence intensity. In addition, the spatial resolution of the PIV measurements is further improved by $4\,\%$ to $\approx 343\,\mu$m. In Chapter 5, a set of experiments are proposed to investigate the effects of differential diffusion on various flame parameters of lean premixed flames, such as flame location, local flamelet velocities, consumption velocities (i.e., flame burning rates), with a focus on flame structure parameters, including flame stretch, flame-front curvature, and flame surface area, in the thin reaction zone regime.

Chapter 5

The effects of differential diffusion in counter-flow premixed flames with dilution and hydrogen enrichment

Publication (3): E. Abbasi-Atibeh and J. M. Bergthorson. Submitted to *Combustion and Flame* (2019).

5.1 Abstract

The effects of differential diffusion on local flamelet velocities, turbulent burning rates, and structure of lean turbulent premixed flames in the thin reaction zone regime are investigated using aerodynamically stabilized flames in a counter-flow apparatus. In the context of fuel flexibility, various fuel-oxidizer-inert mixtures with different transport properties, representative of distinct effective Lewis numbers, are studied. In order to minimize the effects of chemistry in these experiments, unstretched laminar flame speed is kept constant during mixture dilution, and hydrogen enrichment of hydrocarbon flames, through changing the mixture equivalence ratio. Furthermore, bulk-flow properties and stagnation surface temperature are kept constant; hence, the study focuses on the effects of differential diffusion. Highly strained laminar flame measurements are also reported as a reference for comparison. Local instantaneous statistics of various flame parameters within the imaged plane, such as flame location, flame velocity, and flame-front topology, are quantified using high-speed particle image velocimetry (PIV) and Mie scattering flame tomography at two levels of turbulence intensity. These parameters are presented as probability density functions using sufficiently large data sets to ensure statistical accuracy. The results for various flame-parameter statistics, which are measured over a wide range of Lewis numbers, show that the effects of differential diffusion are important in turbulent flames in the thin reaction zone regime.

At constant turbulence intensities, differential diffusion increases the burning rates of turbulent flames in thermo-diffusively unstable mixtures through two main mechanisms: (1) increasing local flamelet displacement velocity, and (2) increasing flame-surface area. The relative contribution of these two parameters in increasing turbulent burning rates is approximately 76 % and 24 %, respectively, which is not dependent on the fuel, oxidizing-gas mixture, or turbulence intensity, and the results overlap over a wide range of Lewis numbers.

Keywords: Differential diffusion; Fuel flexibility; Hydrogen enrichment; Lewis number; Premixed turbulent combustion; Flame surface area.

5.2 Introduction

The continued combustion of fossil fuels to fulfill global energy demand is being questioned because of the well-known problem of greenhouse-gas (GHG) emissions and pollutants, such as nitric oxides (NO_x), carbon monoxide (CO), and soot. Consumption of fossil fuels needs to be reduced as it introduces new carbon, in the form of carbon dioxide (CO_2), into the environment causing climate change. However, the inherent advantages of combustion-based engines in some application areas make it hard for other power systems to compete. For instance, combustion of liquid fuels remains attractive for transportation because of the high energy density. A leading strategy is to avoid burning fossil fuels by using hydrogen (H_2) and renewable biofuels, such as biogas, syngas, and alcohols, that can be produced from conversion of various renewable energy sources, such as solar, water, wind, or geothermal, into chemical energy [1–6].

Adaptability with alternative renewable fuels that have variable compositions is referred to as *fuel flexibility*, which is an important parameter of next-generation combustor design. Fuel flexibility will, ultimately, result in higher-performance fuel-flexible combustors that lower costs of energy production, while reducing emissions and the carbon footprint of various energy technologies; hence, mitigating global climate change. However, changing fuels significantly affects combustor operability properties, such as blowout, flashback, and dynamic stability, mainly due to variations in turbulent burning rates. This manifests both as difficulties in heuristically designing fuel-flexible combustors and inaccuracy/unreliability in numerical techniques for simulating combustor behavior using computational fluid dynamic (CFD) simulations.

Changing the fuel and oxidizing-gas mixture composition affects flame characteristics and burning rates through changing: (1) mixture reactivity, and (2) mixture diffusivity. Fuel flexibility changes chemical properties and the reactivity of the mixture, which can be represented by

unstretched laminar flame speed ($S_{\mathrm{L}}^{\mathrm{o}}$) as an intrinsic property of a given fuel and oxidizing-gas mixture. The effects of mixture reactivity on flame speed are well studied, e.g., laminar flame studies of H_2-enriched hydrocarbon flames [7–11] show that adding H_2, which is a very reactive fuel with a high laminar flame speed, to the fuel mixture enhances the flame speed, and extends the flammability limit towards the lean side enabling the engine to operate at leaner conditions. Fuel flexibility also changes the transport properties of the mixture, which are the diffusivity of the deficient reactant (fuel in lean, and oxidizer in rich, combustion) ($\mathcal{D}$) and the diffusivity of heat (α). The disparity between α and $\mathcal{D}$ at the flame front is known as *differential diffusion*, which is represented by the Lewis number ($\mathrm{Le} = \alpha/\mathcal{D}$).

Differential diffusion causes stretch sensitivity in flame-front propagation leading to thermal-diffusive (TD) instabilities. Stretch rate (K), is defined as the normalized differential change in flame-surface area (FSA) as a function of time: $K = (1/A)\,(\mathrm{d}A/\mathrm{d}t)$ [12], which is a function of flame curvature (κ) and hydrodynamic strain ($K_{\mathrm{s-t}}$) (tangential strain rate due to a non-uniform flow field across the flame) [13]:

$$K = \kappa\, S_{\mathrm{T}} + K_{\mathrm{s-t}} \tag{5.1}$$

where S_{T} is the local characteristic flame velocity in laboratory coordinates. Stretch sensitivity of flames is an important parameter that affects the flame structure [14–20], e.g., flame-front curvature [21, 22], and burning rates in laminar and turbulent flames [17, 23–31].

Various definitions of turbulent flame velocity in the form of consumption velocity or displacement velocity are measured and reported in [20, 32–39]. One equation that describes the turbulent burning rate is [20, 40, 41]:

$$S_{\mathrm{T-LC}} = I_{\mathrm{o}}\, S_{\mathrm{L}}^{\mathrm{o}}\, \frac{A_{\mathrm{T}}}{A_{\mathrm{L}}} \tag{5.2}$$

where $S_{\mathrm{T-LC}}$ is the turbulent local burning rate (also referred to as "turbulent local consumption velocity"), I_{o} is the local stretch factor, which depends on differential diffusion, and A_{T} and A_{L} are the turbulent and the laminar flame-surface area, respectively. Equation 5.2 indicates that the effects of stretch on the propagation of turbulent premixed flames in the flamelet regime originate from two main mechanisms: (1) the effects of differential diffusion on local flamelet velocities, and (2) the effects of FSA on local and global burning rates.

Previous studies [22, 32, 38, 39, 42–48] showed that the increase in FSA alone, due to turbulence folding, (i.e., classical Damköhler's hypothesis [23]) is insufficient to explain increasing burning rates with increasing flame stretch, and that differential diffusion also affects the local burning rates of laminar [32, 42, 43] and turbulent [22, 38, 39, 44–48] flames. Some studies [27, 32, 49, 50] have explained the effects of differential diffusion by the theory of leading points, where it is assumed that the burning velocity of a turbulent premixed flame is controlled by the increased

velocity of the positively curved and stretched leading points, which is particularly important for thermo-diffusively unstable mixtures with $\mathrm{Le} < 1$. While some studies show an extreme role of differential diffusion on the structure and propagation of highly turbulent flames (e.g., [51]), some researchers state that these effects are suppressed once turbulence is strong [52, 53] due to the enhanced turbulent heat and mass transport. Controversies are also seen in the literature regarding the effects of differential diffusion and turbulence intensity on the premixed flame-front structure in the thin reaction zone regime. For instance, it was shown that differential diffusion has no effect on flame-front curvature and flame-surface area and that the flame structure is only influenced by turbulence [22, 52], while other studies illustrated significant effects of differential diffusion on the flame-front structure in this regime [38, 54, 55]. Furthermore, recent studies [15, 16] showed no clear dependence of flame-surface density on turbulence intensity, whereas flame-front curvature and flame-surface density were reported to increase with increasing turbulence intensity in other experimental and numerical studies [22, 54]. Hence, there is no common understanding in the combustion literature regarding the effects of differential diffusion in the thin reaction zone regime ($1 < \mathrm{Ka_T} < 100$ and $\mathrm{Da_T} < 1$) [56, 57], where turbulent heat and mass transport are enhanced.

In this study, experiments are performed using strained counter-flow flames, in order to study the effects of both components of flame stretch, i.e., bulk and local hydrodynamic strain rates and local curvature [38, 39, 58–68]. Mixtures with very distinct effective Lewis number ($\mathrm{Le_{eff}}$) in the range of $0.3 < \mathrm{Le_{eff}} < 3.1$ are studied. Most previous studies report the combined effects of mixture reactivity and diffusivity properties, with few studies focused only on the effects of differential diffusion on the propagation and stabilization of premixed flames. In the present experiments, $S_{\mathrm{L}}^{\mathrm{o}}$ is kept constant during mixture dilution, and H_2 enrichment, through changing the mixture equivalence ratio (ϕ), in order to minimize the effects of chemical properties of the mixture. Furthermore, bulk-flow properties and the temperature boundary conditions are also kept constant; hence, the study focuses on the effects of differential diffusion.

Two-dimensional high-speed particle image velocimetry (2D-PIV) and Mie scattering flame tomography are used to quantify the effects of differential diffusion on local flamelet velocities, burning rates, and structure of turbulent premixed flames, within the imaged plane, in the thin reaction zone regime. Data-processing tools, developed through this study, are used to quantify instantaneous local flame properties based on $\mathrm{Le_{eff}}$ variations, and statistically, represent these measurements in the form of probability density functions (PDF) using sufficiently large data sets.

5.3 Experimental method

In these experiments, lean turbulent and laminar premixed flames with distinct $\mathrm{Le_{eff}}$ are investigated at atmospheric pressure. A methane-air (CH_4-air) flame at $\phi = 0.6$ and $\mathrm{Le_{eff}} \approx 1$ is selected as a reference flame with predicted $S_\mathrm{L}^\mathrm{o} = 0.115\,\mathrm{m/s}$ at 300 K, and $T_\mathrm{ad} = 1669\,\mathrm{K}$. Lean mixtures representative of distinct Lewis number ($\mathrm{Le} = \alpha/\mathcal{D} = \lambda/(\rho c_\mathrm{p}\mathcal{D})$, where λ is the thermal conductivity, c_p is the specific heat, and ρ is the density of the unburned reactants) are formed by changing both fuel diffusivity (which is the deficient species in the lean mixtures under study) and thermal diffusivity of the mixture. The former is performed through H_2 enrichment of propane (C_3H_8) in various volume ratios up to pure H_2, and the latter is carried out by using different diluents. The oxidizer-inert mixture always contains 21 % oxygen (O_2) by volume and some of the nitrogen (N_2) in air, 40 % by volume, is replaced by helium (He) or CO_2 to form mixtures with various thermal diffusivities. In H_2-enrichment experiments, $\mathrm{Le_{eff}}$ is defined based on the volumetric-fraction-weighted average of the Lewis numbers of the two fuels [69]: $\mathrm{Le_{eff}} = X_{\mathrm{C_nH_m}}\mathrm{Le_{C_nH_m}} + X_{\mathrm{H_2}}\mathrm{Le_{H_2}}$, where X is the mole fraction in the fuel stream. Properties of the mixtures are presented in Table 5.1. The $\mathrm{Le_{eff}}$ varies within the range of $0.3 < \mathrm{Le_{eff}} < 3.1$, where H_2+CO_2 and C_3H_8+He correspond to the smallest and the largest $\mathrm{Le_{eff}}$, respectively.

In all experiments, S_L^o is kept constant at 0.115 m/s, through changing ϕ. Mixture properties, diffusive flame thickness ($\delta_\mathrm{L} = \lambda/(c_\mathrm{p}\,\rho_\mathrm{u} S_\mathrm{L}^\mathrm{o})$), as well as S_L^o values are calculated using free-flame simulations in Cantera [70]. GRI-Mech 3.0 reaction mechanism is used for CH_4 and pure H_2 computations, and AramcoMech 1.3 reaction mechanism is used for computations involving C_3H_8. The mass-averaged bulk-flow velocity at the nozzle exit is also kept constant in all experiments at 4 m/s.

Table 5.1 Mixture properties and experimental conditions at $S_{\mathrm{L}}^{\mathrm{o}} = 0.115$ m/s.

	Mixtures			Mixture properties			Experimental conditions							
	Fuel [%] (Vol.)	O_2 balance diluent [%] (Vol.)	Diluent [%] (Vol.)	ϕ	T_{ad} (K)	$\mathrm{Le}_{\mathrm{eff}}$	$u'^*/S_{\mathrm{L}}^{\mathrm{o}}$	$u'^*/\overline{U}$	L/δ_{L}	L/η^*	$\delta_{\mathrm{T}}/\delta_{\mathrm{L}}$	$\mathrm{Re}_{\mathrm{T}}^*$	$\mathrm{Ka}_{\mathrm{T}}^*$	$\mathrm{Da}_{\mathrm{T}}^*$
High turbulence	C_3H_8	21	$60\,N_2 + 40\,He$	0.45	1513	3.08	13.7	0.33	3.6	23.1	12.4	65.7	41.4	0.3
	C_3H_8	21	N_2	0.56	1631	1.87	12.2	0.32	6.9	27.5	23.5	83.1	15.8	0.6
	C_3H_8	21	$60\,N_2 + 40\,CO_2$	0.79	1823	1.69	13.4	0.34	8.5	36.0	29.9	118.8	17.8	0.6
	$80\,C_3H_8 + 20\,H_2$	21	$60\,N_2 + 40\,CO_2$	0.77	1795	1.43	12.7	0.31	8.1	33.6	25.8	108.4	17.1	0.6
	$60\,C_3H_8 + 40\,H_2$	21	$60\,N_2 + 40\,CO_2$	0.75	1762	1.16	12.2	0.31	6.9	29.0	27.4	89.2	17.9	0.6
	$40\,C_3H_8 + 60\,H_2$	21	$60\,N_2 + 40\,CO_2$	0.71	1709	0.89	13.1	0.31	6.3	29.3	25.6	90.1	21.8	0.5
	$20\,C_3H_8 + 80\,H_2$	21	$60\,N_2 + 40\,CO_2$	0.63	1617	0.62	13.0	0.33	6.7	31.7	26.0	100.5	22.3	0.5
	$10\,C_3H_8 + 90\,H_2$	21	$60\,N_2 + 40\,CO_2$	0.57	1532	0.48	12.8	0.33	6.8	32.3	25.0	102.7	22.6	0.5
	CH_4	21	$60\,N_2 + 40\,He$	0.47	1542	1.60	14.0	0.35	3.7	23.9	12.9	68.9	42.8	0.3
	CH_4	21	N_2	0.60	1669	0.98	12.9	0.34	6.3	27.5	23.0	82.9	19.2	0.5
	CH_4	21	$60\,N_2 + 40\,CO_2$	0.88	1896	0.86	13.1	0.34	7.5	33.8	26.2	109.3	20.2	0.6
Low turbulence	C_3H_8	21	$60\,N_2 + 40\,CO_2$	0.79	1823	1.69	8.7	0.23	9.1	27.4	21.5	82.8	9.1	1.0
	$50\,C_3H_8 + 50\,H_2$	21	$60\,N_2 + 40\,CO_2$	0.73	1740	1.02	8.5	0.20	6.5	21.5	17.4	59.6	10.8	0.8
	$20\,C_3H_8 + 80\,H_2$	21	$60\,N_2 + 40\,CO_2$	0.63	1617	0.62	8.3	0.20	6.3	21.5	15.6	59.8	11.6	0.8
	H_2	21	$60\,N_2 + 40\,CO_2$	0.48	1440	0.35	8.8	0.23	5.5	22.3	17.9	62.8	16.3	0.6

* Properties are calculated upstream of the flame brush, in the preheat zone at $T \approx 576$ K.

As listed in Table 5.1, ϕ and the adiabatic flame temperature (T_{ad}) of the mixtures are within the range of $0.45 \leq \phi \leq 0.88$ and $1440\,\mathrm{K} \leq T_{\mathrm{ad}} \leq 1896\,\mathrm{K}$, respectively. To name different mixtures throughout this text, O_2 and N_2 are eliminated for brevity, as they exist in all mixtures under study. For instance, the C_3H_8+O_2+N_2+He mixture is summarized as C_3H_8+He. The pure hydrogen flame, H_2+CO_2, ($S_{\mathrm{L}}^{\mathrm{o}} = 0.115\,\mathrm{m/s}$ and $\phi = 0.48$) at the higher turbulence intensity case is not reported due to flashback, whereas, it is included in laminar flames, and in turbulent flames at the lower turbulence intensity.

5.3.1 Hot-exhaust opposed-flow turbulent flame rig

The experiments are carried out using aerodynamically stabilized lifted flames in a hot-exhaust opposed-flow turbulent flame rig (HOTFR) [38, 39, 59, 62, 63, 65–68]. The burner setup is designed to stabilize premixed laminar and turbulent flames of mixtures flowing from the bottom nozzle against a stream of hot combustion products flowing from a pre-burner inside a ceramic nozzle at the top, in an axial opposed-flow configuration. A co-flow of He is used to shroud the reacting mixture and the flame from surrounding air in order to reduce the effect of the shear layer and stabilize the flame edge. A schematic of the burner setup is shown in Fig. 5.1. In this configuration, laminar flames are stretched mainly due to bulk strain rate (K_{s}) while, in turbulent flames, the stretch is due to both bulk strain rate and the stretch effects of turbulent eddies through increasing flamelet curvature (κ).

The rig has a compact design with well-defined boundary conditions and excellent optical accessibility. In HOTFR, the lifted flames are not affected by conductive heat loss to the burner, and the stagnation plane of hot products allows stabilization of near-adiabatic laminar and turbulent flames. Furthermore, this configuration allows highly strained flames to be stabilized at higher bulk-flow velocities, turbulence intensities, and Karlovitz numbers in the thin reaction zone regime of the Borghi diagram [56, 57], and closer to relevant conditions of gas-turbine engines (GTE) and other combustors. These characteristics enable high-resolution laser diagnostic imaging for velocity field measurements, capturing the overall flame structure, and integral scales of highly stretched flames; hence, make the rig convenient both for diagnostics and validating computational fluid dynamic (CFD) models.

At the bottom section, two concentric inner and outer nozzles deliver the premixed fuel and oxidizing-gas mixture, and the co-flow, respectively, through two separate concentric plena. The inner nozzle has an exit diameter of $d_{\mathrm{N}} = 20\,\mathrm{mm}$, which is attached to the inner plenum of diameter 60 mm, with a contraction ratio of 9:1. The interior contour of the nozzle contraction is defined by polynomials that minimize the formation of Taylor-Görtler vortices [71] in the concave

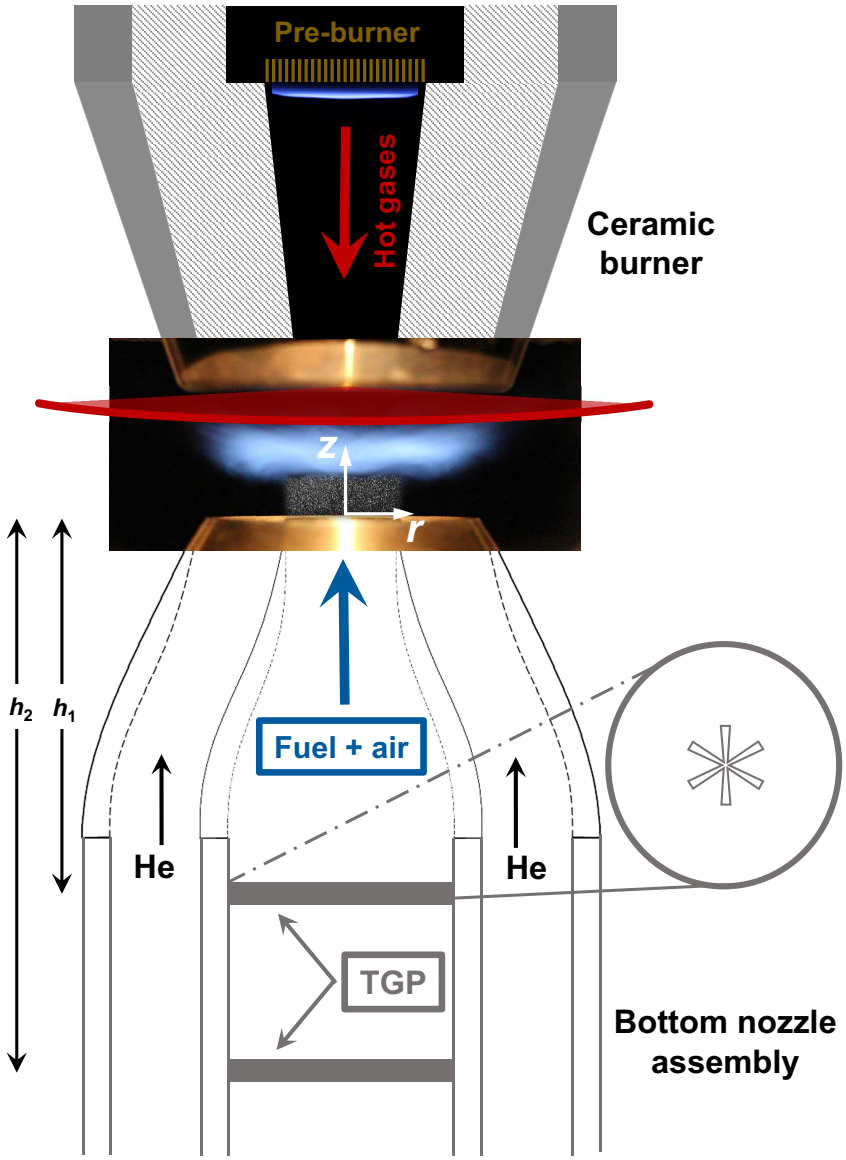

Figure 5.1 Schematic of HOTFR. S-TGP is located upstream of the nozzle contraction, in the inner plenum, at two different distances from the nozzle exit: $h_1 = 142\,\text{mm}$ and $h_2 = 212\,\text{mm}$.

portion of the profile, and minimize the angle-of-attack in the convex portion [72]. This contoured design minimizes flow instabilities and dampens the transition to turbulence, which makes the rig suitable for accurate laminar flame experiments when the turbulence-generating system is removed (e.g., [43]).

Turbulence is generated using a star-shaped high-blockage turbulence-generating plate (S-TGP) with an open area of 2.4 % [66, 73]. The S-TGP is designed to deliver the highest possible

turbulence intensity while producing nearly isotropic turbulence and axisymmetric uniformity. In turbulent experiments, the S-TGP is located at vertical distances upstream of the nozzle exit of $h_1 = 142\,\text{mm}$ and $h_2 = 212\,\text{mm}$, corresponding to the higher and the lower turbulence intensity levels, respectively, since steady-state turbulence decays with distance. Therefore, two different turbulence intensities are achievable at a constant bulk-flow velocity and bulk hydrodynamic strain rate, as indicated in Table 5.1. In laminar flame experiments, the S-TGP is removed without changing the flow conditions or mixture compositions.

In order to minimize any bulk-flow oscillations in turbulent experiments, the S-TGP distance from the nozzle exit is set at $h_1/d_{\text{TGP}} = 2.4$ and $h_2/d_{\text{TGP}} = 3.5$, where d_{TGP} is the effective diameter of the S-TGP. This distance is chosen to be larger than that found to minimize large-scale bulk-flow oscillations, as shown in [73]. Using the energy spectra of S-TGP for various h, it was illustrated [73] that the bulk-flow oscillations (bumps in the region of low-frequency energy) tend to disappear with increasing h to an optimum value of $h/d_{\text{TGP}} \gtrsim 2.3$. Furthermore, using a single-jet TGP design minimizes the pulsation of the axial jet velocity at the nozzle exit, caused by vortex-shedding from the holes of the TGP [74].

At the top section, a CH_4-air flame at $\phi = 0.7$ and $T_{\text{ad}} = 1842\,\text{K}$ is stabilized inside a ceramic nozzle, on a flame holder, and at a vertical distance from the ceramic nozzle exit of 90 mm, as illustrated in Fig. 5.1. Hot exhaust gases from the pre-burner are accelerated to the test domain through the ceramic nozzle with a contraction ratio of 6.25:1. The momentum balance of the impinging flows from the top and the bottom nozzles sets the location of the stagnation plane. The separation distance between the two nozzles is $1.225\,d_{\text{N}}$ to minimize bulk-flow oscillations, reduce mixing with the inert co-flow or surrounding air and maintain high strain rates.

The temperature of hot exhaust gases at the ceramic nozzle exit (T_{CB}) is measured for each experiment using R-type thermocouples with three different wire (bead) diameters at a distance of 5 mm from the nozzle exit. Temperature readings are corrected for heat losses by extrapolating the measured temperatures to a zero bead diameter. The velocity and temperature of the hot exhaust gases at the ceramic nozzle exit are kept constant at $U_{\text{CB}} \approx 12\,\text{m/s}$ and $T_{\text{CB}} = 1786\,\text{K}$, respectively, in all laminar and turbulent flame experiments. Radial temperature profiles are nearly constant, and the repeatability in measuring T_{CB} is $\approx 1\,\%$ of the reading. The effects of deviations from adiabatic conditions at the stagnation surface ($\mid T_{\text{CB}} - T_{\text{ad}} \mid$) on flame speed are discussed in Appendix E.

The fuel, oxidizing-gas mixture, and inerts are delivered using mass flow controllers (MFC) at room temperature, which are calibrated using a Bios DryCal ML-800-44 dry-piston calibrator before each set of runs. Through this calibration process, the absolute uncertainty in mixture composition is reduced to $\approx 0.9\,\%$.

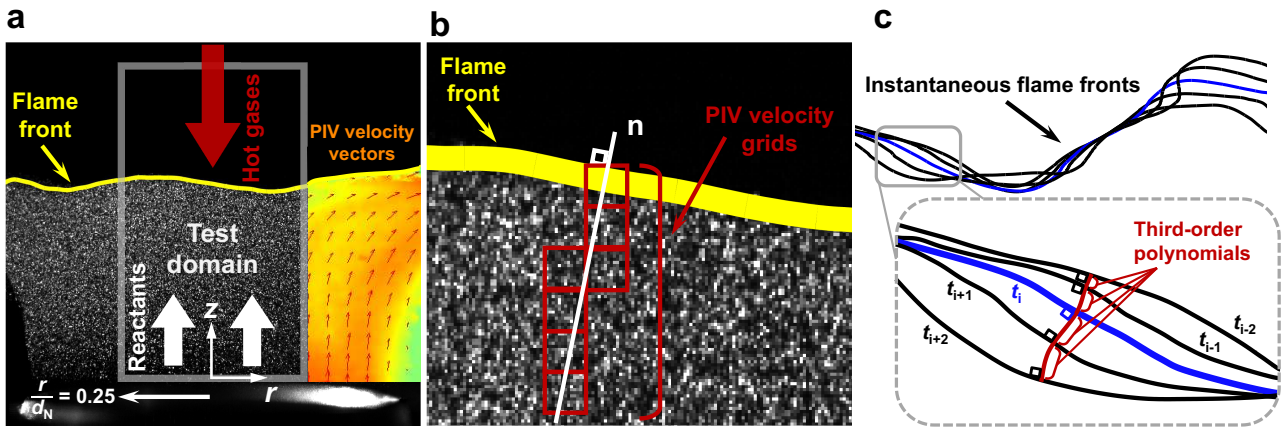

Figure 5.2 Processing techniques: (a) a sample PIV image indicating the test domain, an example flame front, and PIV velocity vectors (the density of the velocity vectors is reduced by 8 times for better visibility.), (b) a portion of a sample PIV image near the flame front illustrating the schematic of S_u measurement (PIV velocity vectors are available at the grid corners), and (c) 5 successive flame fronts and a schematic showing S_F calculation.

5.3.2 Diagnostic method and processing techniques

5.3.2.1 Particle image velocimetry

Velocity fields are measured in laminar and turbulent experiments using two-dimensional high-speed particle image velocimetry (2D-PIV) within the imaged plane. In PIV, oil droplets ($\approx 1\,\mu$m) are atomized and seeded into the flow. At the test section, these droplets are illuminated using a thin sheet ($\approx$ 1 mm) of visible frequency-doubled Nd: YLF laser at 527 nm wavelength pulsing at a repetition rate of 10 kHz. The Mie scattered light is captured using a high-speed camera at an imaging speed of 10 kfps, and a resolution of 768 $\times$ 976 pixels. 8 000 and 1 000 PIV image pairs are post-processed using DaVis 8.2 in each turbulent and laminar experiment, respectively, to calculate the two-component velocity vector field within the plane of the laser sheet. A sample PIV image is illustrated in Fig. 5.2 (a) showing the radial boundaries of the test domain between $-0.25 \leq (r/d_\mathrm{N}) \leq 0.25$. Within the plane of the laser sheet, the origin of the 2D coordinate system is located at the center of the bottom nozzle, where r is the radial direction, and the z-axis is normal to the exit plane of the bottom nozzle.

In PIV post-processing, a larger interrogation window of size 96 $\times$ 96 pixel is refined using a grid-refinement cross-correlation technique to a 16 $\times$ 16 pixel grid in five passes with a window overlap of 75 %. The pixel-to-mm ratio is 46.6, and independent velocity data is measured at a grid-spacing equal to the smallest interrogation window size (16 pixels $\approx$ 343.5 μm), which is

considered as the spatial resolution of PIV in these experiments. In order to increase the signal-to-noise ratio in calculating instantaneous axial (U) and radial (V) velocities at time t_i, three successive PIV images at t_{i-1}, t_i, and t_{i+1} are considered, and a second-order central differencing method is used to estimate particle displacement vectors at time t_i.

Uncertainties associated with PIV are calculated based on the velocity lag of tracer particles in regions of high velocity gradients due to particle inertia (relaxation time or Stokes time), as well as uncertainties originating from the processing algorithm of the PIV software. These calculations result in an uncertainty of approximately 1.5 % in the unburned gas velocity in turbulent flame experiments. Details of the uncertainty analysis in the flow velocity measurement are discussed in [39].

Turbulent flow statistics of the average flow velocity (axial, $\overline{U}$, and radial, $\overline{V}$), and the fluctuating components of the velocity (axial, u, and radial, v) are calculated from PIV data at each grid through Reynolds decomposition [75, 76]: $U(r,z,t) = \overline{U}(r,z) + u(r,z,t)$, where U is the instantaneous flow velocity at radial (r) and axial (z) location at time t. Statistics of u and v are calculated as the root-mean-square (rms) of velocity fluctuations (axial, u', and radial, v'). These results are listed in Table 5.1 for various mixtures, where $\overline{U}$ and u' are averaged over the test domain at 0.7 mm above the nozzle exit, and upstream of the flame brush in the preheat zone at $T \approx 576\,\mathrm{K}$ (i.e., the flash point of oil used for seeding), respectively. Axial turbulence intensity ($u'/\overline{U}$) ranges between $31\% \leq \left(u'/\overline{U}\right) \leq 35\%$ for the higher, and $20\% \leq \left(u'/\overline{U}\right) \leq 23\%$ for the lower, turbulence levels.

The performance of the S-TGP in generating turbulence is illustrated in Fig. 5.3, which shows that $\overline{U}$ is almost constant in the test section in both laminar and turbulent flows, and $u'/\overline{U}$ profiles are flat in the test domain. HOTFR was previously shown [38] to produce turbulence statistics at the nozzle exit that are nearly isotropic ($u' \approx v'$). However, in a highly strained impinging-jet geometry, as the flow approaches the stagnation plane, eddies in the turbulent flow are significantly compressed and stretched. Even if the flow is isotropic at the nozzle exit, it is no longer isotropic in the flame vicinity. Similar phenomena are present in most burner technologies. The uniformity of the turbulent flow at the inlet boundary is essential for future CFD modeling of these experiments.

In turbulent experiments, the integral length scale (L) is estimated by integrating the transverse autocorrelation coefficient of u in the radial direction over the test domain, at $\approx 0.7\,\mathrm{mm}$ above the nozzle exit, from $r/d_\mathrm{N} = -0.25$ up to the first zero-crossing, as discussed in [75, 77]: $L = \int R_\mathrm{uu}(r,t)\,\mathrm{d}r$. The estimated values of L vary between $2.46\,\mathrm{mm} \leq L \leq 3.1\,\mathrm{mm}$, with the average value $\overline{L} = 2.87\,\mathrm{mm}$, which is on the order of the characteristic length of the S-TGP ($\approx 2\,\mathrm{mm}$). The scaled values of L are listed in Table 5.1 for various experimental conditions. An estimation of the ratio of largest to smallest hydrodynamic length scales in a turbulent flow can be derived

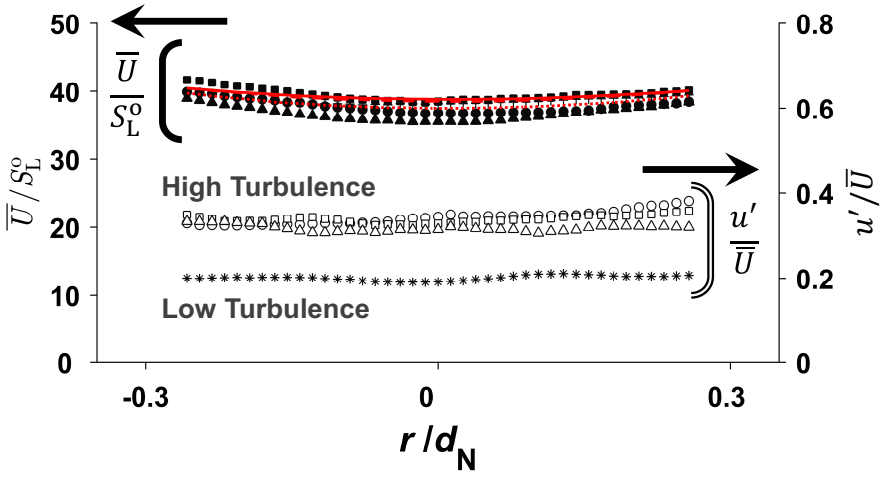

Figure 5.3 Nozzle exit $\overline{U}$ and u' in turbulent flames with distinct $\mathrm{Le_{eff}}$, respectively: CH_4-air (solid circle, hollow circle), C_3H_8-CO_2 (solid square, hollow square), and H_2-CO_2 (solid triangle, hollow triangle) at high turbulence intensity, and C_3H_8-CO_2 with 80 % H_2 content (plus, star) at low turbulence intensity. Nozzle exit $\overline{U}$ in laminar flames: CH_4-air (dashed line), C_3H_8-CO_2 (solid line), and H_2-CO_2 (dotted line).

as [75]: $L/\eta \approx \mathrm{Re_T}^{3/4}$, where η is the Kolmogorov length scale, and $\mathrm{Re_T}$ is the turbulent Reynolds number: $\mathrm{Re_T} = u'\,L/\nu$ (ν is the kinematic viscosity). $\mathrm{Re_T}$ is calculated upstream of the flame brush, in the preheat zone at $T \approx 576\,\mathrm{K}$, yielding $\mathrm{Re_T}$ values in the range of $59 \leq \mathrm{Re_T} \leq 119$, as listed in Table 5.1. The cold flow equivalent of $\mathrm{Re_T}$ is around 383 in the C_3H_8-CO_2 experiment. Studying turbulence-chemistry interactions in this range of $\mathrm{Re_T}$ is of specific interest in the validation of flamelet models, in the region where mixing and chemical time scales are comparable.

Turbulent Damköhler number ($\mathrm{Da_T}$) and turbulent Karlovitz number ($\mathrm{Ka_T}$) are key quantities describing turbulence-chemistry interactions. $\mathrm{Da_T}$ relates the timescale of the turbulent transport phenomena to the chemical reaction timescale: $\mathrm{Da_T} = \tau_\mathrm{F}/\tau_\mathrm{c}$, where $\tau_\mathrm{F} = L/u'$ and $\tau_\mathrm{c} = \delta_\mathrm{L}/S_\mathrm{L}^\mathrm{o}$. $\mathrm{Ka_T}$ is defined as the ratio of τ_c and the Kolmogorov time scale (τ_η): $\mathrm{Ka_T} = \tau_\mathrm{c}/\tau_\eta$, and is calculated as: $\mathrm{Ka_T} = (L/\delta_\mathrm{L})^{-2}\ \mathrm{Re_T}^{1.5}$. $\mathrm{Ka_T}$ indicates the tendency of the eddies to penetrate into the preheat zone of the flame and, along with velocity and length scale ratios, defines different regimes of turbulent combustion in the Borghi diagram [56, 57]. In investigating flame-vortex interactions, the high-temperature zone near the flame front affects $\mathrm{Re_T}$, $\mathrm{Ka_T}$, and $\mathrm{Da_T}$ calculations; therefore, these temperature-sensitive parameters are calculated immediately upstream of the flame brush. In these experiments, $\mathrm{Da_T}$ and $\mathrm{Ka_T}$ range between $0.3 \leq \mathrm{Da_T} \leq 1$ and $9.1 \leq \mathrm{Ka_T} \leq 42.8$,

respectively, showing that these flames are located in the thin reaction zone regime.

5.3.2.2 Processing techniques

Particle image velocimetry and Mie scattering flame tomography allow simultaneous flame-location and velocity-field measurements [38, 39, 41, 78, 79], which enables time-resolved study of the turbulence-chemistry interactions. Atomized oil droplets are seeded into the flow as tracer particles, and then evaporate at the flame front and terminate the Mie scattering of light. Flame-surface tracking methods, developed in this study, are used to localize and track the flame-front motion. The instantaneous flame location within the imaged plane (Z_{f}) is determined in each frame by tracking the regions of maximum intensity gradients at the flame front using the Pavlidis edge-finding algorithm [38, 39, 80]. An example flame front is shown in Figs. 5.2 (a) and 5.2 (b). The main uncertainty sources in finding instantaneous flame location are average tracer particle distance in the test domain, oil droplet lifetime at the flame front, uncertainties imposed by filtering processes during the post-processing procedure, and over-saturated pixels from larger oil droplets in PIV images, resulting in a total uncertainty of less than $0.5\,\delta_{\mathrm{L}}$. The details of the uncertainty analysis in flame-front tracking are discussed in [39].

The instantaneous flame-location measurements are used to estimate the increase in FSA of turbulent flames compared to that of a laminar flame: $\Sigma = A_{\mathrm{T}}/A_{\mathrm{L}}$. Since these measurements are based on 2D-PIV within the plane of the laser sheet, an estimate of Σ is possible by direct measurement of the length of the 2D slice of the FSA (e.g., [81]). It is assumed that both A_{T} and A_{L} are calculated by multiplying the flame length in turbulent flames, and that of an idealized laminar flame with a length of ≈ 10 mm, respectively, by the thickness of the laser sheet. However, this estimated value under-estimates the Σ, since the variations of FSA due to turbulence folding in the depth of the image is not considered. The direct numerical simulation (DNS) study of Bell *et al.* [82] illustrates that the flame surface density estimated using 2D flame surfaces under-estimates the values calculated based on 3-dimensionally resolved flame contours by $25-33\,\%$. In this study, relative values of Σ are used to assess how differential diffusion affects flame topology and burning rates, and the 2D projection of FSA is sufficient for these purposes. Flame-front tracking methods are also used to extract 2D flame topology within the imaged plane, such as local instantaneous flame-front curvature in flame-contour coordinates and normal directions to the flame contour. Flame-front curvature is calculated as [64, 83, 84]:

$$\kappa = \frac{r'z'' - z'r''}{\left(r'^2 + z'^2\right)^{3/2}} \tag{5.3}$$

where first and second derivatives are calculated in flame-contour coordinates. In this study, κ is positive when a curved flamelet is convex towards the reactants.

In counter-flow flames, streamlines diverge as the flow approaches the stagnation surface, and the flames are stretched due to tangential hydrodynamic strain rate ($K_{\mathrm{s-t}}$). The $K_{\mathrm{s-t}}$ is defined as the differential change in the unburned flow velocity as a function of distance at each location along the tangent line to the flame front, which is calculated at increments of 4 pixels in flame-contour coordinates. At each location on the flame-contour, two velocity vectors centered at this location are considered, that are at least 16 pixels apart to ensure the statistical independence of the velocity vectors. A second-order central differencing method is used to estimate $K_{\mathrm{s-t}}$ (compression or stretch), using projected velocities onto the tangent line and the distance between the two velocity vectors.

In Eq. 5.2, I_{o} is the ratio of the local stretched flamelet velocity to $S_{\mathrm{L}}^{\mathrm{o}}$ [20, 41]. In this study, I_{o} is estimated as the normalized local flamelet displacement velocity: $I_{\mathrm{o}} \approx S_{\mathrm{T}}/S_{\mathrm{L}}^{\mathrm{o}}$, which is a function of differential diffusion. In these experiments, the flame surface is measured at the constant droplet evaporation temperature ($T \approx 576\,\mathrm{K}$), not a constant temperature progress variable (c), due to variations in T_{ad} of our mixtures. Therefore, the exact value of I_{o} reported in this study might not be necessarily meaningful, but the relative trends are still important, and this dataset can be used for validation of models, as long as the "validation surface" is set to be equal to the appropriate c value for each experiment. The S_{T} is the propagation velocity of the local flamelet (S_{F}) relative to the convection velocity of the flow (S_{u}) in the direction normal to the flame surface (n) [20, 38, 39, 85–87]: $S_{\mathrm{T}} = (S_{\mathrm{F}} + S_{\mathrm{u}}) \cdot n$. In order to calculate S_{T}, S_{u} and S_{F} need to be determined. In this study, single-plane PIV imaging within the plane of the laser sheet measures the 2D projection of S_{T} within the imaged plane.

In counter-flow flames, a laminar flame stabilizes at some location where the local flow velocity matches the stretched flame speed. As the laminar jet approaches the stagnation plane, the velocity reduces, and its profile shows a minimum, after which the flow accelerates through the preheat zone as the density drops due to dilatation [43]. The location of this velocity minimum is considered to be the location of flame stabilization, and this minimum value of the velocity profile ahead of the flame is taken as the reference flame speed ($S_{\mathrm{u-ref}}$), which is typically used in laminar flame studies as the characteristic flame speed at the given stretch rate. In this paper, stretched laminar flame experiments are used to find the flame location and laminar stretched flame speed for comparison to the turbulent values.

In turbulent flames, the two-component velocity field upstream of the flame is used to find the convective velocity of the flow (S_{u}). The values of S_{u} are calculated using the velocity grid network in the vicinity of the normal line to the flame surface within 1.25 mm upstream of the flame front

at each location along the flame contour, as illustrated in Fig. 5.2 (b). These velocity profiles may not show a local velocity minimum upstream of the flame front due to the unsteady turbulent flow and the filtering effects of flame motion; therefore, S_{u} is found by taking the average of the two closest velocity values to the flame surface. The S_{u} (or $S_{\mathrm{u-ref}}$) is positive when the unburned gas velocity is towards the flame.

In order to determine local instantaneous flamelet velocity in the flow coordinate system within the imaged plane (S_{F}), image-processing techniques, similar to the methods proposed in [88, 89], are used. A high-order finite differencing method is used in the reconstruction of the flamelet's path between consecutive flame fronts to improve the signal-to-noise ratio in S_{F} calculations of highly turbulent flames. To calculate S_{F} at time t_{i}, 5 successive flame fronts, 2 upstream at $t_{\mathrm{i-2}}$ and $t_{\mathrm{i-1}}$, and 2 downstream at $t_{\mathrm{i+1}}$ and $t_{\mathrm{i+2}}$ are considered. The flamelet's path between 5 consecutive flame fronts within the imaged plane is estimated using four continuous third-order polynomials to reconstruct the flame motion using a continuous streamline, which is perpendicular to all five flame fronts, and for which the total length is a minimum. For each location along the flame contour at t_{i}, at increments of 4 pixels in the flame-contour coordinates, the length of a third-order polynomial is minimized between this location and the neighboring front, which is constrained by the normal direction to both fronts. The same procedure is used to determine all four third-order polynomials, which estimates the flamelet's pathway from $t_{\mathrm{i-2}}$ to $t_{\mathrm{i+2}}$. A fourth-order finite difference method is used to estimate the displacement at each location at t_{i}, which is used in the calculation of S_{F}. This method is illustrated schematically in Fig. 5.2 (c). The S_{F} is considered positive when the flame moves towards the unburned gas. S_{F} and S_{u} are used in the calculation of S_{T}.

5.4 Results and discussion

Experiments in this study investigate stretch sensitivity and the effects of differential diffusion on the propagation, stabilization, and structure of lean premixed flames. Various fuel-oxidizer-inert mixtures are selected at constant $S_{\mathrm{L}}^{\mathrm{o}}$, but distinct $\mathrm{Le_{eff}}$, to highlight the effects of differential diffusion. Laminar flame measurements are reported for diluted C_3H_8 flames with CO_2 and He, as well as H_2-enriched C_3H_8 flames.

5.4.1 Flame-front location

The Z_{f} of various mixtures at a wide range of $\mathrm{Le_{eff}}$ ($0.3 < \mathrm{Le_{eff}} < 3.1$) are illustrated in Fig. 5.4 for laminar flames, as well as for turbulent flames at two different turbulence intensities. In the counter-flow geometry, the momentum balance of the impinging-jets defines the location of the

stagnation plane, and flames stabilize close to the stagnation plane because of high bulk-flow velocities. The composition, temperature of hot exhaust gases (T_{CB}), and the top nozzle exit velocity (U_{CB}) are constant in these experiments, which results in a constant momentum of the hot jet in all experiments. Changing the mixture composition of the cold jet, however, changes its momentum, mainly due to variations in mixture density. Therefore, as various mixtures are produced at constant $S_{\mathrm{L}}^{\mathrm{o}}$ but distinct $\mathrm{Le}_{\mathrm{eff}}$, variations in flame location are due to the effects of both movement of the mean stagnation surface location, as well as variations in the burning rate of flames due to the effects of differential diffusion.

In order to highlight the effects of differential diffusion on burning rates, the PDFs of flame location, and the correlations of the mean flame location against $\mathrm{Le}_{\mathrm{eff}}$, are plotted in the stagnation-plane (SP) coordinate system, where $\langle Z_{\mathrm{SP}} \rangle - Z_{\mathrm{f}} = 0$ indicates the flame surface located at the average location of the stagnation plane and $\langle Z_{\mathrm{SP}} \rangle - Z_{\mathrm{f}}$ increases towards the bottom nozzle, as illustrated in Fig. 5.4. The stagnation-plane location is measured by Mie scattering flame tomography of non-reacting flow experiments with preserved flow properties of the oxidizer-inert portion of the unburned laminar and turbulent flows. The fuel is removed from the mixtures to prevent autoignition at the stagnation surface. The standard deviation of $\langle Z_{\mathrm{SP}} \rangle$ is less than $0.036\, d_{\mathrm{N}}$ over the full set of mixtures.

PDFs of flame location at various $\mathrm{Le}_{\mathrm{eff}}$ at the higher, and the lower, turbulence intensity levels are shown in Figs. 5.4 (a) and 5.4 (c), respectively. These PDFs determine the mean flame location ($\langle \langle Z_{\mathrm{SP}} \rangle - Z_{\mathrm{f}} \rangle$), and the flame-brush thickness (δ_{T}). Furthermore, skewness of these PDFs indicates a propensity for the instantaneous flame location to be upstream or downstream of the average location.

Variations of $\langle \langle Z_{\mathrm{SP}} \rangle - Z_{\mathrm{f}} \rangle$ for laminar flames and turbulent flames at the higher turbulence intensity are shown in Fig. 5.4 (b). As shown in Figs. 5.4 (a) and 5.4 (b), PDFs of flame location overlap for $0.9 < \mathrm{Le}_{\mathrm{eff}} < 3.1$, and are skewed towards the stagnation surface, as they are pushed to the hot exhaust gases by steep average velocity gradients; hence, the mean flame location is almost constant in mixtures with $\mathrm{Le}_{\mathrm{eff}} > 1$. As $\mathrm{Le}_{\mathrm{eff}}$ falls below unity, PDFs of flame location significantly move upstream toward the bottom nozzle with decreasing $\mathrm{Le}_{\mathrm{eff}}$, and are less skewed. This relocation is also illustrated by a significant increase in $\langle \langle Z_{\mathrm{SP}} \rangle - Z_{\mathrm{f}} \rangle$ for mixtures with $\mathrm{Le}_{\mathrm{eff}} \ll 1$ shown in Fig. 5.4 (b). In laminar flames at constant $S_{\mathrm{L}}^{\mathrm{o}}$, $\langle \langle Z_{\mathrm{SP}} \rangle - Z_{\mathrm{f}} \rangle$ increases linearly with a shallow slope up to $\mathrm{Le}_{\mathrm{eff}} \approx 0.5$, and rises significantly for the pure H_2 flame ($\mathrm{Le}_{\mathrm{eff}} \approx 0.35$), due to differential diffusion enhancing the stretched flame speed. In thermo-diffusively unstable turbulent flames with $\mathrm{Le}_{\mathrm{eff}} \ll 1$, the global burning velocity considerably increases with decreasing $\mathrm{Le}_{\mathrm{eff}}$; hence, the flames are stabilized closer to the bottom nozzle exit in the steep average bulk-flow velocity gradients. The pure H_2 flame could not be stabilized at the higher turbulence intensity due

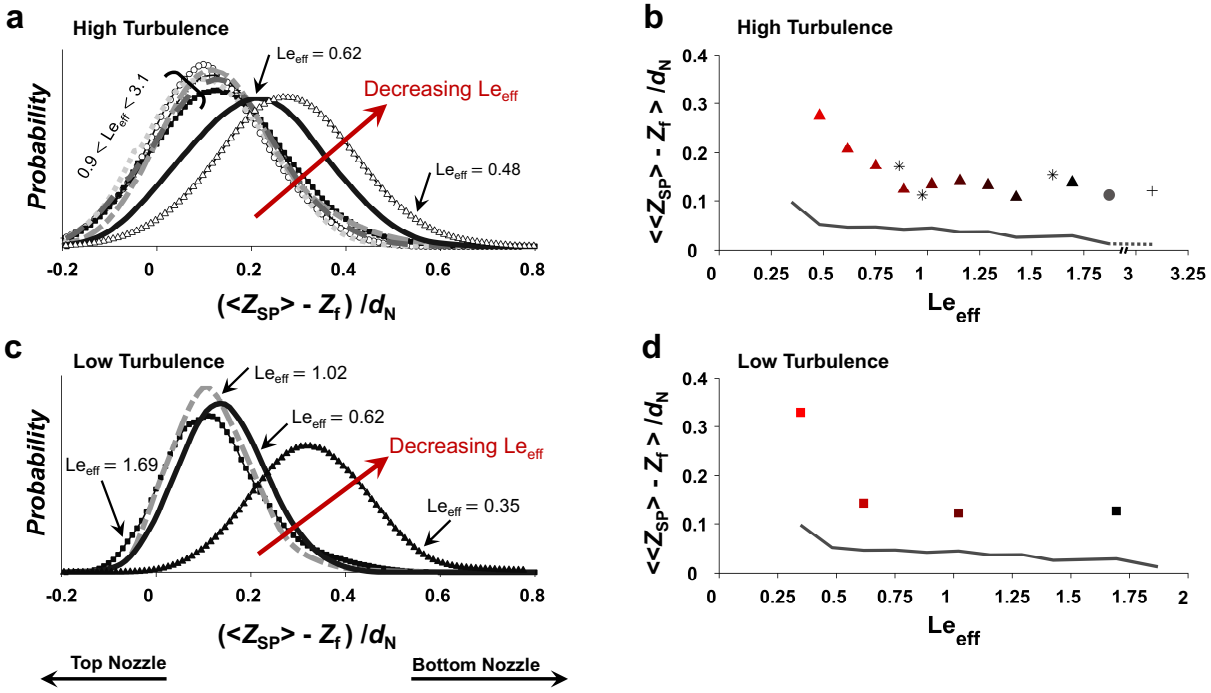

Figure 5.4 PDFs of flame location for flames at various $\mathrm{Le_{eff}}$: (a) high-turbulence case: C_3H_8-He (plus), C_3H_8-air (circle), C_3H_8-CO_2 (square), H_2-enriched C_3H_8-CO_2 flames with various H_2 content (by volume) of 20 % (dotted line), 40 % (dash-dot line), 60 % (dashed line), 80 % (solid line), and 90 % (hollow triangle). (c) low-turbulence case: C_3H_8-CO_2 (square), H_2-enriched C_3H_8-CO_2 flames at 50 % H_2 content (dash-dot line), 80 % (solid line), and H_2-CO_2 (solid triangle). Correlations of $\langle\langle Z_{\mathrm{SP}}\rangle - Z_{\mathrm{f}}\rangle$ in turbulent (symbol) and in laminar (line) flames with respect to $\mathrm{Le_{eff}}$: (b) high-turbulence case: C_3H_8-He (plus), C_3H_8-air (circle), H_2-enriched C_3H_8-CO_2 flames with various H_2 content (by volume) from 0 % to 90 % (triangle), and CH_4 flames (star). The x-axis is broken to show the C_3H_8-He flame (plus) at $\mathrm{Le_{eff}} = 3.08$. (d) low-turbulence case: H_2-enriched C_3H_8-CO_2 flames with $0\% \leq H_2$ in fuel mixture $\leq 100\%$. H_2-enriched C_3H_8-CO_2 flames are color-mapped from black at 0 % H_2 to red at 90 % H_2. Laminar flame measurements are reported for diluted C_3H_8 flames with CO_2 and He, as well as H_2-enriched C_3H_8 flames. For details of the mixtures see Table 5.1.

to flashback, which also shows that the turbulent burning rate is enhanced compared to the other mixtures.

Variations of $\langle\langle Z_{\mathrm{SP}}\rangle - Z_{\mathrm{f}}\rangle$ at the lower turbulence intensity are summarized in Fig. 5.4 (d) for mixtures with $0.35 \leq \mathrm{Le_{eff}} \leq 1.69$. As illustrated in Figs. 5.4 (c) and 5.4 (d), PDFs of flame location at $\mathrm{Le_{eff}} \gtrsim 1$ overlap, and the mean flame location is almost constant. With decreasing $\mathrm{Le_{eff}}$, at $\mathrm{Le_{eff}} \approx 0.6$, the PDF starts to move further towards the fresh reactants, and the pure H_2-CO_2 flame ($\mathrm{Le_{eff}} = 0.35$) stabilizes at the closest distance to the bottom nozzle due to a significant

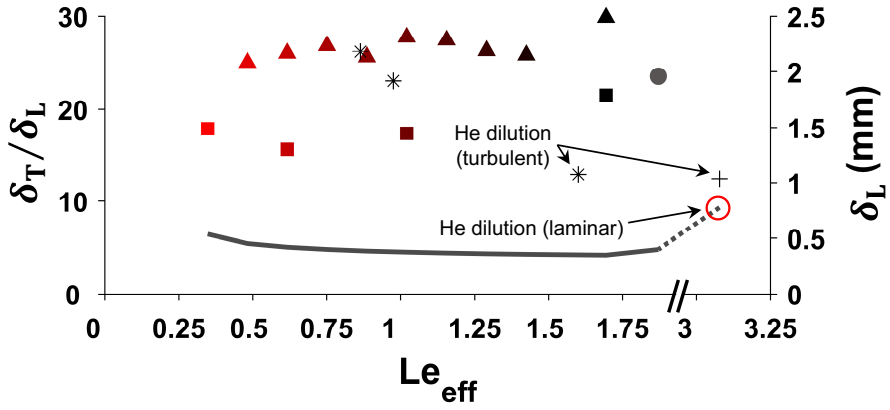

Figure 5.5 δ_T of turbulent (symbol) and δ_L of laminar (line): symbols are the same as Figs. 5.4 (b) and 5.4 (d). Laminar flame measurements are reported for diluted C_3H_8 flames with CO_2 and He, as well as H_2-enriched C_3H_8 flames. The x-axis is broken to show the C_3H_8-He flame (plus) at $Le_{eff} = 3.08$.

increase in turbulent burning rates.

Turbulent flame-brush thickness is calculated using PDFs of flame location: $\delta_T = 4 \times \sigma$, where σ is the standard deviation of the PDFs. In Fig. 5.5, the scaled values of δ_T are plotted, along with the laminar flame thickness (δ_L) for reference. In general, the normalized δ_T is larger in flames at the higher turbulence intensity compared to the same mixtures at the lower turbulence intensity. At each turbulence intensity, while the dimensional values of δ_T show an increase with decreasing Le_{eff}, the scaled values appear flat because the δ_L also increases for reduced Le_{eff}. In mixtures with He dilution, δ_L is considerably larger due to the increased thermal diffusivity of the mixture ($\delta_L \propto \alpha/S_L^o$).

5.4.2 Local flamelet displacement velocity

PDFs of S_T for flames at two levels of turbulence intensity are illustrated in Figs. 5.6 (a)−5.6 (c). These PDFs show the mean local turbulent flame velocity ($\langle S_T \rangle$), and the distribution of PDFs compared to S_L^o. In Fig. 5.6 (a), PDFs of S_T for C_3H_8 and H_2-enriched C_3H_8 flames at the higher turbulence intensity illustrate that the peak moves towards higher local velocities with decreasing Le_{eff} in mixtures with $Le_{eff} < 1$, and S_T significantly passes S_L^o, due to the effects of differential diffusion. However, the PDFs of mixtures with $Le_{eff} > 1$ overlap, and $\langle S_T \rangle$ is almost constant in these mixtures. PDFs of S_T for CH_4 flames at the higher turbulence intensity are illustrated in Fig. 5.6 (b), where Le_{eff} is varied through dilution with different inerts. In these flames, the peaks of

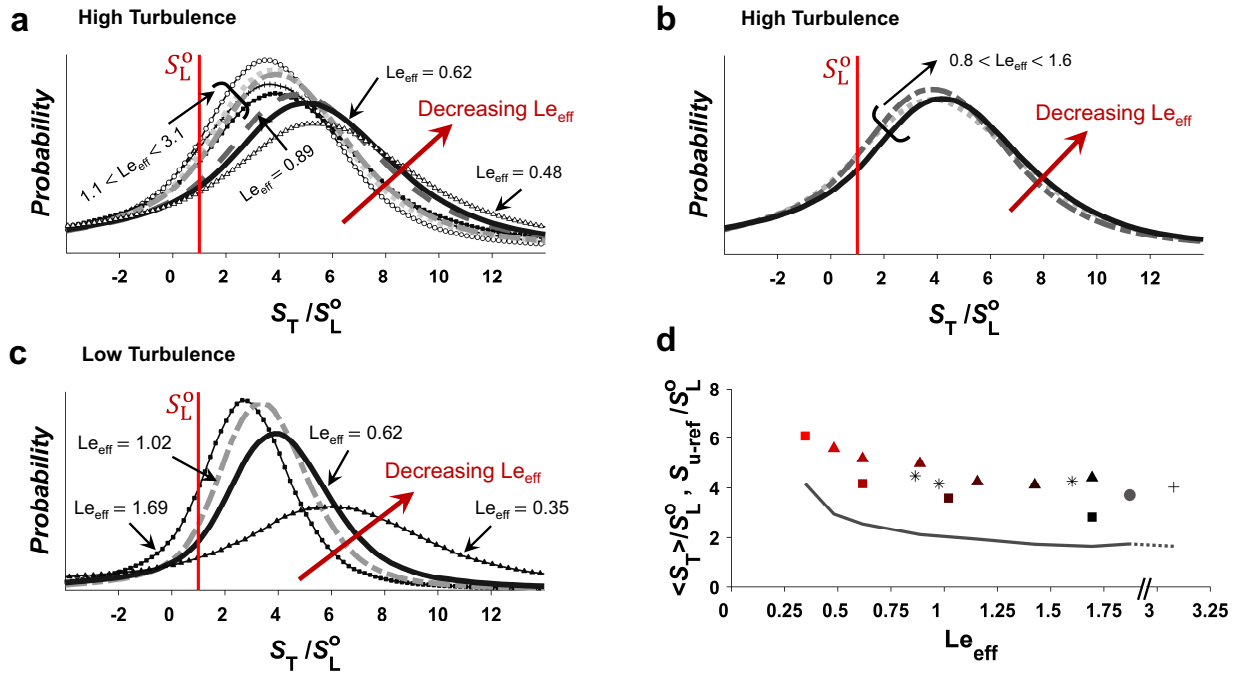

Figure 5.6 PDFs of S_T for flames at various Le_{eff}: (a) C_3H_8 and H_2-enriched C_3H_8 flames in various oxidizer-inert mixtures under high-turbulence level: legend is the same as Fig. 5.4 (a). (b) CH_4 flames in various oxidizer-inert mixtures under high-turbulence level: CH_4-He (dotted line), CH_4-air (dash-dot line), and CH_4-CO_2 (solid line). (c) C_3H_8 and H_2-enriched C_3H_8 flames in CO_2 under low-turbulence level: legend is the same as Fig. 5.4 (c). (d) $\langle S_T \rangle$ in turbulent (symbols) and S_{u-ref} in laminar (line) correlations with respect to Le_{eff}: symbols are the same as Figs. 5.4 (b) and 5.4 (d). Laminar flame measurements are reported for diluted C_3H_8 flames with CO_2 and He, as well as H_2-enriched C_3H_8 flames. The x-axis is broken to show the C_3H_8-He flame (plus) at $Le_{eff} = 3.08$. For details of the mixtures see Table 5.1.

the PDFs only slightly move towards higher velocities, as Le_{eff} decreases from 1.6 to 0.86. These PDFs show values in the range of $-2 \lesssim (S_T/S_L^o) \lesssim 12$, consistent with 3D turbulent displacement velocity measurements reported in [86]. At the lower turbulence intensity shown in Fig. 5.6 (c), PDFs of S_T are narrower compared to the higher turbulence case in mixtures with $Le_{eff} > 1$. With increasing H_2 enrichment in C_3H_8-CO_2 from 0 % ($Le_{eff} = 1.69$) to 100 % ($Le_{eff} = 0.35$), PDFs of S_T significantly widen and the peaks move towards higher velocities. Evidently, negative S_T values are less likely, and account for only $\approx 14\,\%$ of all S_T measurements. A DNS study of 2D stoichiometric CH_4-air flames [90] show negative S_T values in highly curved concave regions towards the reactants.

In order to quantify these effects, $\langle S_T \rangle$ of turbulent flames, as well as S_{u-ref} of laminar flames,

are plotted against $\mathrm{Le_{eff}}$ in Fig. 5.6 (d), where $\langle S_\mathrm{T}\rangle/S_\mathrm{L}^\mathrm{o} \approx \langle I_\mathrm{o}\rangle$ (Eq. 5.2). $S_{\mathrm{u-ref}}/S_\mathrm{L}^\mathrm{o}$ values are larger than 1 because of stretch and hydrodynamic effects on the laminar counter-flow flames [43]. In general, $\langle S_\mathrm{T}\rangle$ is larger than $S_{\mathrm{u-ref}}$, as local curvature generated by eddies in turbulent flames enhances the local flamelet velocities. Furthermore, $\langle S_\mathrm{T}\rangle$ is larger at the higher turbulence intensity compared to the lower intensity, due to an increase in local curvature effects with increasing turbulence intensity.

As illustrated in Fig. 5.6 (d), $S_{\mathrm{u-ref}}/S_\mathrm{L}^\mathrm{o}$ variations with decreasing $\mathrm{Le_{eff}}$ correlate well with the laminar flame location variations shown in Figs. 5.4 (b) and 5.4 (d), with a sharp increase at $\mathrm{Le_{eff}} \ll 1$. At the higher turbulence intensity, the normalized $\langle S_\mathrm{T}\rangle$ is almost constant at ≈ 4 in flames with $\mathrm{Le_{eff}} > 1$, whereas in flames with $\mathrm{Le_{eff}} < 1$, it increases with decreasing $\mathrm{Le_{eff}}$ up to 5.6 for C_3H_8-CO_2 with 90 % H_2 enrichment. The S_T results are consistent with the study of Daniele *et al.* [91], who reported the local flamelet velocities for fuels ranging from CH_4 to syngas blends. In thermo-diffusively stable mixtures ($\mathrm{Le_{eff}} > 1$), thermal diffusion from the positively stretched portion of the flame front is larger than fuel diffusion into the stretched area; hence, the rate of thermal energy loss is greater than chemical energy gain provided by molecular diffusion into the reaction zone, which reduces the temperature, and results in decreasing the flame velocity. In thermo-diffusively unstable mixtures ($\mathrm{Le_{eff}} < 1$), at a positively stretched portion of the flame front, molecular diffusion into the stretched area is larger than thermal energy loss through diffusion, which increases the local ϕ and temperature; hence, the velocity of the leading points increases [51]. At the lower turbulence intensity, $\langle S_\mathrm{T}\rangle/S_\mathrm{L}^\mathrm{o}$ peaks at the pure H_2 flame ($\mathrm{Le_{eff}} = 0.35$). In general, as illustrated in Fig. 5.6 (d), the effect of Lewis number on the local flame velocity of stretched flames is not linear, with sharp increases in the local flame velocity of mixtures with $\mathrm{Le_{eff}} \lesssim 0.75$, due to the effects of differential diffusion.

5.4.3 Turbulent flame structure

The effects of $\mathrm{Le_{eff}}$ on turbulent flame-front curvature (κ), and creating/enhancing FSA, are illustrated in Figs. 5.7 (a)−5.7 (f), where sample Mie scattering images and extracted flame fronts for mixtures with distinct $\mathrm{Le_{eff}}$ are demonstrated at two levels of turbulence intensity. The representative frames are chosen so that the average absolute curvature within the test domain of the chosen frame at time t is close to the mean absolute curvature over the whole image sequence, i.e., $\overline{|\kappa|}_t \approx \langle|\kappa|\rangle$. These instantaneous frames illustrate a significant increase in flame-front curvature and FSA for thermo-diffusively unstable mixtures with $\mathrm{Le_{eff}} \ll 1$ at each turbulence intensity.

The uncertainties in κ and Σ measurements originate from the uncertainties in the flame-front tracking method, which defines the resolution of the measurement technique in recognizing κ and

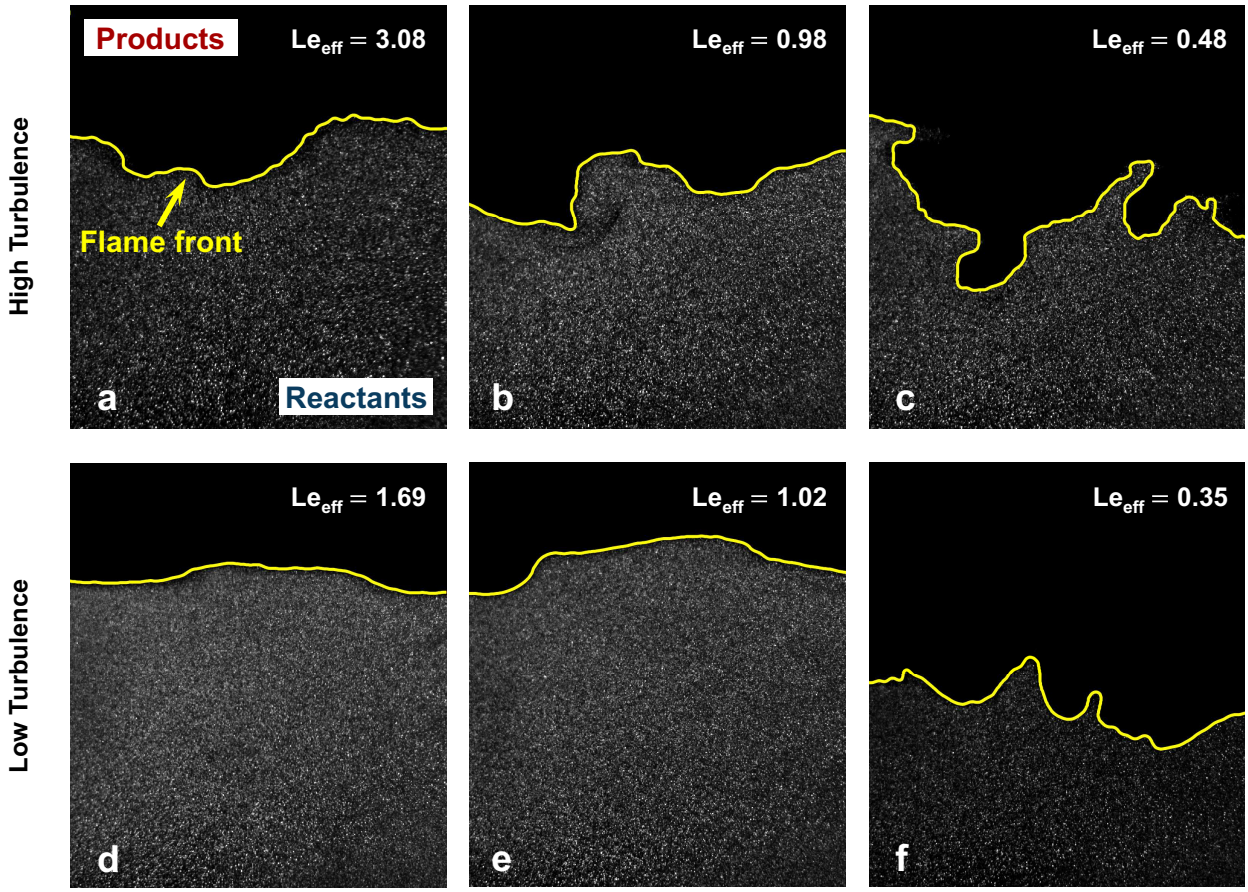

Figure 5.7 Sample Mie scattering images and extracted flame fronts for mixtures with distinct $\mathrm{Le_{eff}}$ at two levels of turbulence intensity. High turbulence intensity: (a) C_3H_8-He flame ($\mathrm{Le_{eff}} = 3.08$), (b) CH_4-air flame ($\mathrm{Le_{eff}} = 0.98$), (c) H_2-enriched C_3H_8-CO_2 flame with 90 % H_2 content ($\mathrm{Le_{eff}} = 0.48$). Low turbulence intensity: (d) C_3H_8-CO_2 ($\mathrm{Le_{eff}} = 1.69$), (e) H_2-enriched C_3H_8-CO_2 flame with 50 % H_2 content ($\mathrm{Le_{eff}} = 1.02$), and (f) H_2-CO_2 flame ($\mathrm{Le_{eff}} = 0.35$). In these frames, $\overline{|\kappa|}_t \approx \langle|\kappa|\rangle$.

Σ. In these experiments, the total uncertainty in tracking the flame location is less than $0.5\,\delta_\mathrm{L}$ (≈ 0.2 mm) [38, 39], which implies that the maximum κ that can be measured is $\approx 5000\,\mathrm{m}^{-1}$. The flame-front curvature associated with the same scale as the average flame thickness, and the average integral length scale, are $(1/\delta_\mathrm{L}) \approx 2500\,\mathrm{m}^{-1}$, and $(1/L) \approx 350\,\mathrm{m}^{-1}$, respectively, which are well below the maximum resolution limit. Available measurements of flame-front wrinkles, summarized in [20], show that the characteristic length of wrinkles in the flame front is never as small as the Kolmogorov length scale or even the Taylor scale. Driscoll [20] also points out that only turbulent eddies larger than 20 % of L are strong enough to wrinkle the flame, and create/increase flame-front perturbations. Kolmogorov eddies are too weak, and they may be easily destroyed by viscosity; hence, they are not strong enough to perturb the flame nor to create wrinkles. The

discussion above shows that the measurement technique employed has a sufficient resolution to quantify the effects of differential diffusion and turbulence on both κ and Σ.

5.4.3.1 Flame-front curvature

In turbulent flames, eddies enhance the stretch imposed on flames through increasing flamelet curvature. The effects of differential diffusion on flame-front curvature are illustrated in Fig. 5.8. Curvature PDFs display a symmetric profile with a near-zero mean in all turbulent flames ($\langle\kappa\rangle \approx 0$), as illustrated in Fig. 5.8 (a). It was illustrated in previous studies that the skewness of the local flame curvature PDF is a suitable parameter for identifying the presence of Darrieus–Landau (DL) hydrodynamic instabilities [92, 93]. The large negative curvature values associated with the DL instabilities lead to a PDF profile with a distinct asymmetry, where $\langle\kappa\rangle < 0$. Therefore, Fig. 5.8 (a) shows that the fluctuations are not associated with the DL instabilities, and the flame-front curvature is equally negative as it is positive for all $\mathrm{Le_{eff}}$ values. Fogla *et al.* [94] also showed that with increasing turbulence intensity, DL instabilities are weakened, and the effects of turbulence become more prominent. On the other hand, Fig. 5.8 (b) illustrates that, at both turbulence intensities, $\langle|\kappa|\rangle$ is almost constant in thermo-diffusively stable mixtures with $\mathrm{Le_{eff}} > 1$, whereas it significantly increases with decreasing $\mathrm{Le_{eff}}$ in thermo-diffusively unstable mixtures with $\mathrm{Le_{eff}} < 1$, due to variations in mixtures transport properties. As illustrated in Fig. 5.8 (b), at the higher turbulence intensity, the average magnitude of the flame curvature, $\langle|\kappa|\rangle$, is larger compared to the lower intensity case, consistent with Fig. 5.7. At the higher turbulence intensity case, the size spectrum of the turbulent eddies extends towards smaller scales, the small eddies are stronger, and the dissipation of their energy by viscous forces are delayed; hence, these eddies are more effective in increasing κ. The discussion above shows that turbulent flames in the thin reaction zone regime are controlled by both turbulence and the effects of differential diffusion in thermo-diffusively unstable mixtures ($\mathrm{Le_{eff}} < 1$), whereas they are controlled solely by turbulence in thermo-diffusively stable mixtures ($\mathrm{Le_{eff}} > 1$) [95].

5.4.3.2 Flame-surface area

Variations of the mean FSA of turbulent flames normalized by the FSA of a laminar flame ($\langle\Sigma\rangle \approx \langle A_\mathrm{T}\rangle/A_\mathrm{L}$) with respect to $\mathrm{Le_{eff}}$ are shown in Fig. 5.9 (a). This figure shows that increasing turbulence intensity increases $\langle\Sigma\rangle$ due to the effects of more-intense eddies in creating FSA, consistent with recent studies (e.g., [94]). Figure 5.9 (a) illustrates that, in mixtures with $\mathrm{Le_{eff}} > 1$, $\langle\Sigma\rangle$ is almost constant; whereas, as $\mathrm{Le_{eff}}$ falls below unity, $\langle\Sigma\rangle$ increases with decreasing $\mathrm{Le_{eff}}$ at both turbulence intensities. This figure also demonstrates that the increase in $\langle\Sigma\rangle$ by changing $\mathrm{Le_{eff}}$

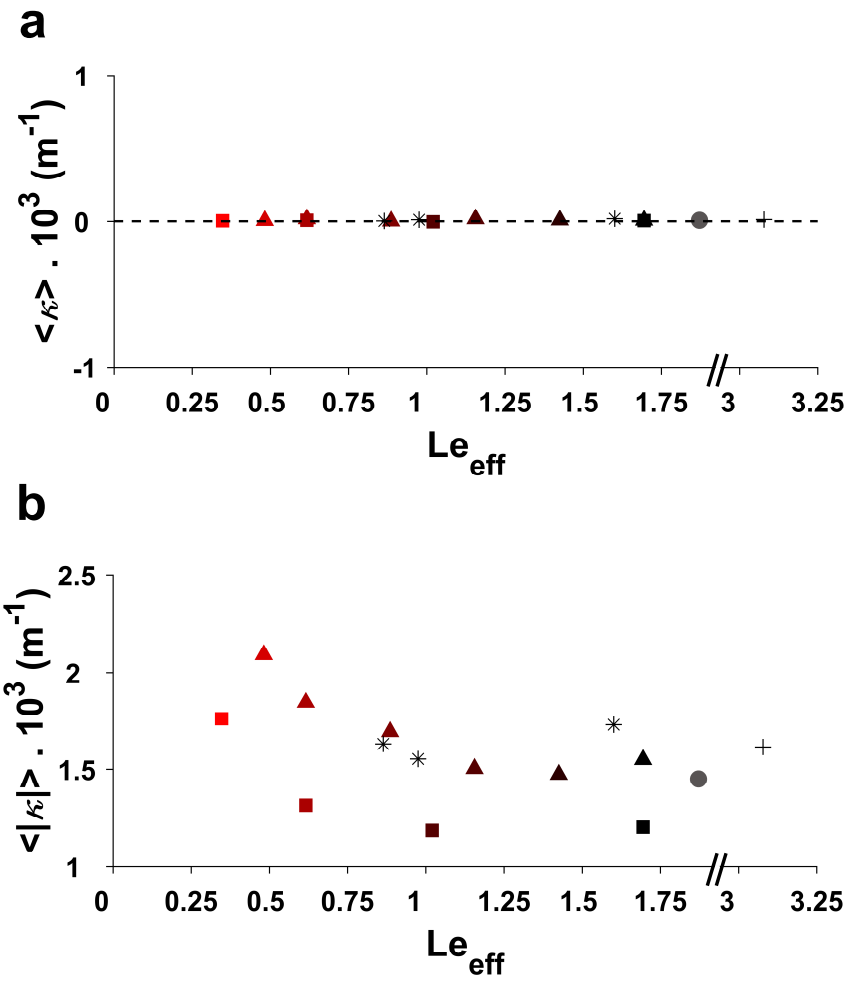

Figure 5.8 Flame-front curvature at various $\mathrm{Le_{eff}}$: (a) $\langle\kappa\rangle$, (b) $\langle|\kappa|\rangle$. Symbols are the same as Fig. 5.6 (d). The x-axis is broken to show the C_3H_8-He flame (plus) at $\mathrm{Le_{eff}} = 3.08$.

is comparable to the enhancement of FSA caused by increasing turbulence intensity by approximately 50 %. Similar scaling was observed in a previous DNS study of turbulent premixed flames in the thin reaction zone regime [54]. The dependence of $\langle\Sigma\rangle$ on flame-front curvature is illustrated in Fig. 5.9 (b), where a linear correlation is shown between $\langle\Sigma\rangle$ and $\langle|\kappa|\rangle$. These results demonstrate that differential diffusion causes an increase in FSA at constant turbulence intensities.

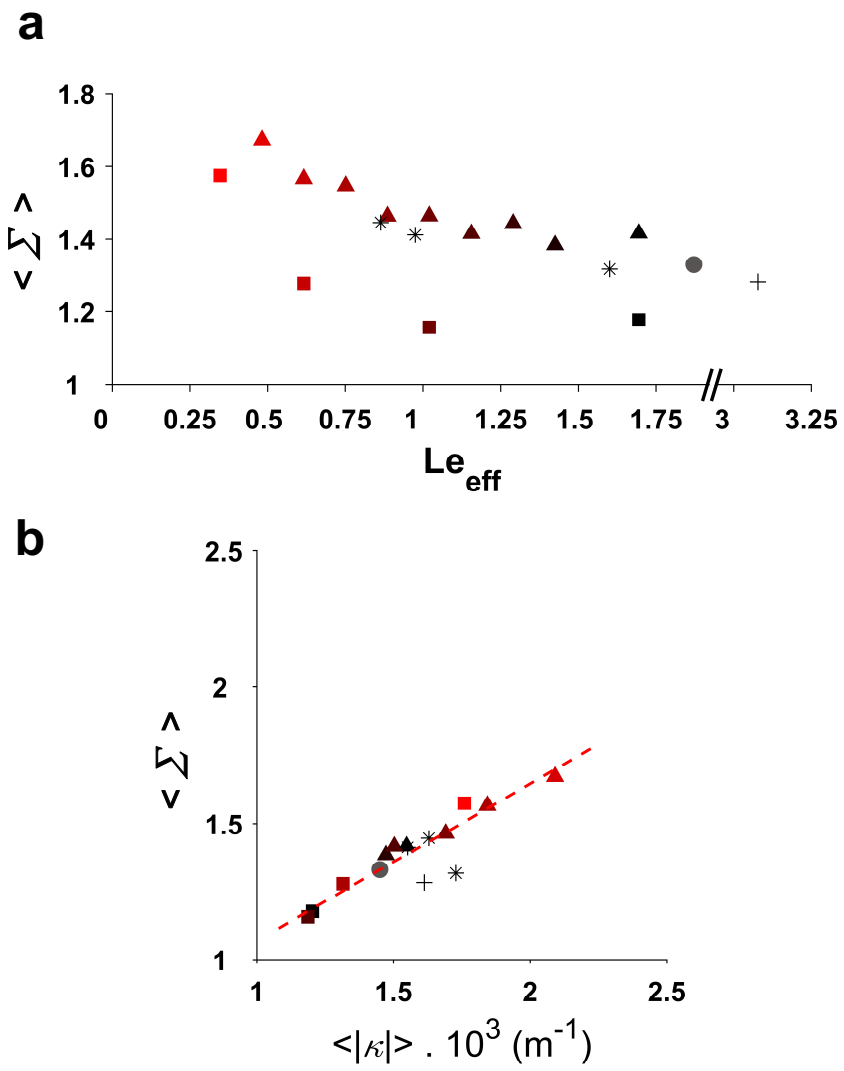

Figure 5.9 (a) Variations of $\langle \Sigma \rangle$ at various $\mathrm{Le_{eff}}$. Symbols are the same as Fig. 5.6 (d). The x-axis is broken to show the C_3H_8-He flame (plus) at $\mathrm{Le_{eff}} = 3.08$. (b) Correlations of $\langle \Sigma \rangle$ and $\langle |\kappa| \rangle$. Dashed line shows a linear fit: $\langle \Sigma \rangle$ = 0.577 ($\langle |\kappa| \rangle \times 10^3$) + 0.492.

5.4.4 Flame-front stretch

While laminar flames are stretched only due to the tangential hydrodynamic strain rate ($K_{\mathrm{s-t}}$), turbulent flames are stretched due to both $K_{\mathrm{s-t}}$ and the stretch effects of turbulent eddies through increasing flamelet curvature, as illustrated in Eq. 5.1. The two components of flame stretch are plotted in Fig. 5.10. Variations of the mean stretch imposed on turbulent flames due to flame curvature ($\langle \kappa \, S_{\mathrm{T}} \rangle$) are shown in Fig. 5.10 (a). This figure shows that the PDFs of $\kappa \, S_{\mathrm{T}}$ are normally

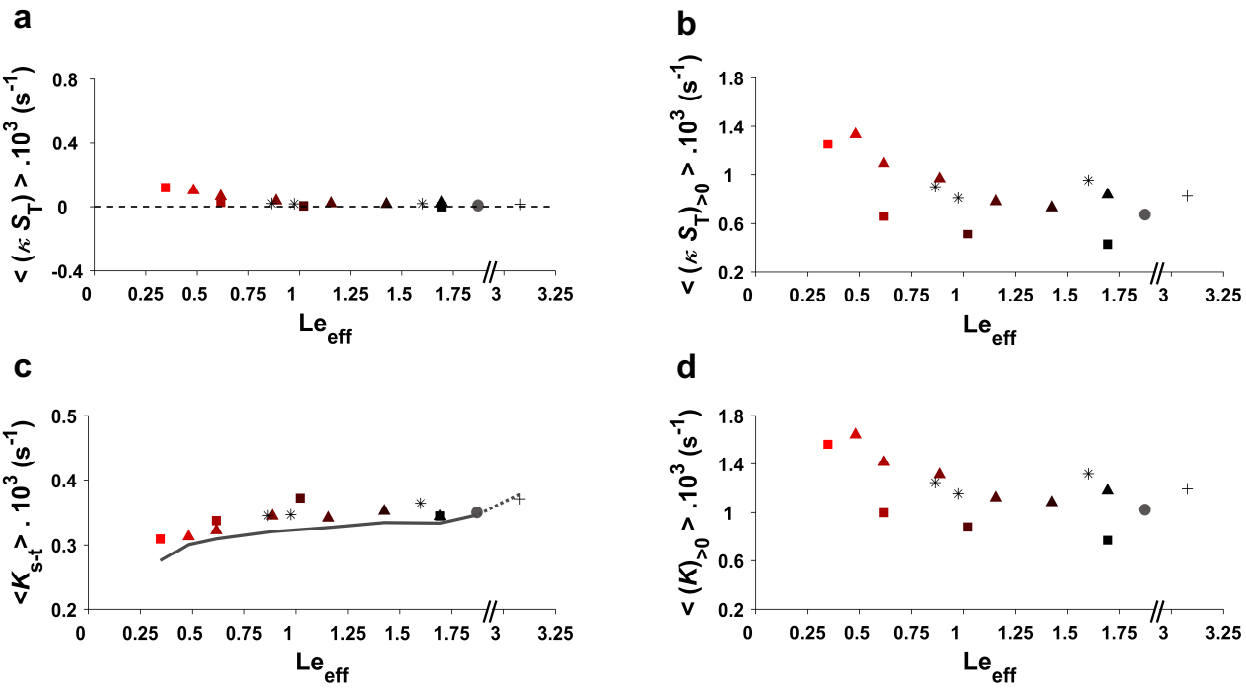

Figure 5.10 Components of flame stretch at various $\mathrm{Le_{eff}}$: (a) stretch imposed on turbulent flames due to flame curvature, (b) positive stretch imposed on turbulent flames due to flame curvature, (c) tangential hydrodynamic strain rate in turbulent (symbols) and laminar (line) flames, (d) total positive flame stretch imposed on turbulent flames. Symbols are the same as Fig. 5.6 (d). The x-axis is broken to show the C_3H_8-He flame (plus) at $\mathrm{Le_{eff}} = 3.08$.

distributed around zero with slight deviations towards the positively stretched flamelets for mixtures with $\mathrm{Le_{eff}} \ll 1$, which is consistent with $\langle \kappa \rangle \approx 0$ observed in Fig. 5.8 (a), as the flame-front fluctuates around the average flame location.

In order to highlight the effects of differential diffusion on the leading points of the flame front, the statistics of positively stretched flamelets are illustrated in Fig. 5.10 (b). Each segment of the flame front is positively stretched ($\kappa\, S_\mathrm{T} > 0$) when: (1) it is positively curved, and the leading edge velocity is positive, i.e., the flame moves towards the unburned reactants in the laboratory coordinate system, or (2) it is negatively curved and moves farther away from the fresh reactants. The PDFs of S_T (Fig. 5.6) illustrate that $\approx 86\,\%$ of the measured S_T values are positive; hence, $\approx 86\,\%$ of the data used in PDFs of flame stretch in Fig. 5.8 (b) are positively curved leading edges of the flame propagating into the fresh reactants. It is illustrated in Fig. 5.8 (b) that $\langle (\kappa\, S_\mathrm{T})_{>0} \rangle$ increases with decreasing $\mathrm{Le_{eff}}$ in mixtures with $\mathrm{Le_{eff}} < 1$, and is larger at higher turbulence intensities, consistent with flame speed and curvature data (Figs. 5.6 (d) and 5.8 (b)).

The tangential hydrodynamic strain rates (K_{s-t}) for flames at various $\mathrm{Le}_{\mathrm{eff}}$ are illustrated in Fig. 5.10 (c). In general, the two components of flame stretch in Figs. 5.10 (b) and 5.10 (c) show that the stretch caused by curvature is larger than the bulk strain rate in the highly turbulent flame experiments. The $\langle K_{s-t} \rangle$ remains almost constant in laminar and turbulent flames at various $\mathrm{Le}_{\mathrm{eff}}$, with the average value $\approx 336\,\mathrm{s}^{-1}$, as the bulk-flow velocity is constant in all experiments.

The mean total stretch imposed on turbulent flames is calculated using Eq. 5.1, and plotted against $\mathrm{Le}_{\mathrm{eff}}$ in Fig. 5.10 (d) for positively stretched flame-front segments. These results show values in the range of $700\,\mathrm{s}^{-1} \lesssim \langle K_{>0} \rangle \lesssim 1600\,\mathrm{s}^{-1}$. Variations of $\langle K_{>0} \rangle$ show that the total stretch imposed on the leading points of the flame front increases with decreasing $\mathrm{Le}_{\mathrm{eff}}$ for thermo-diffusively unstable mixtures with $\mathrm{Le}_{\mathrm{eff}} < 1$.

5.4.5 Turbulent burning rate

The effects of differential diffusion on the burning rate of turbulent premixed flames include the effects of local flamelet displacement velocity, as well as the effects of FSA, as illustrated in Eq. 5.2. Equation 5.2 is used to calculate the instantaneous turbulent burning rate (S_{T-LC}) for flames with various $\mathrm{Le}_{\mathrm{eff}}$, using the Σ and the average normalized S_T ($I_o \approx S_T/S_L^o$), over the entire flame front within the test domain, at time t. In order to quantify the effects of I_o and Σ on S_{T-LC}, the mean turbulent burning rate $\langle S_{T-LC} \rangle$ is extracted from the time series of S_{T-LC}, and plotted in Fig. 5.11 (a) for various $\mathrm{Le}_{\mathrm{eff}}$. S_{u-ref}/S_L^o values are also included to show the burning rate of laminar flames. The S_{T-LC} is almost constant with decreasing $\mathrm{Le}_{\mathrm{eff}}$ in mixtures with $\mathrm{Le}_{\mathrm{eff}} > 1$, and increases when $\mathrm{Le}_{\mathrm{eff}}$ falls below unity. The effect of $\mathrm{Le}_{\mathrm{eff}}$ on the burning rates of premixed stretched flames is not linear, with sharp increases in flames with $\mathrm{Le}_{\mathrm{eff}} \lesssim 0.75$ in both laminar and turbulent flames. The differences in the S_{T-LC} of laminar and turbulent flames are due to the effects of turbulent eddies in increasing flame stretch and creating/enhancing FSA, which results in increasing flame burning rates.

The ratio of the effects of the mean I_o and the mean Σ in increasing S_{T-LC} is plotted against $\mathrm{Le}_{\mathrm{eff}}$ and the normalized S_{T-LC} in Figs. 5.11 (b) and 5.11 (c), respectively. As shown in these figures, the ratio of these two parameters is almost constant ($\langle I_o \rangle / \langle \Sigma \rangle \approx 3.1$), and the results overlap over the wide range of Lewis numbers, and turbulence intensities, used in these experiments. The relative contribution of these two parameters in increasing S_{T-LC} can be obtained from this ratio. This analysis shows that I_o is responsible for approximately 76 % of the observed S_{T-LC}, and the remaining 24 % results from increasing FSA. This result shows the essential role of differential diffusion on turbulent burning rates, which needs to be considered in the study of turbulent flames.

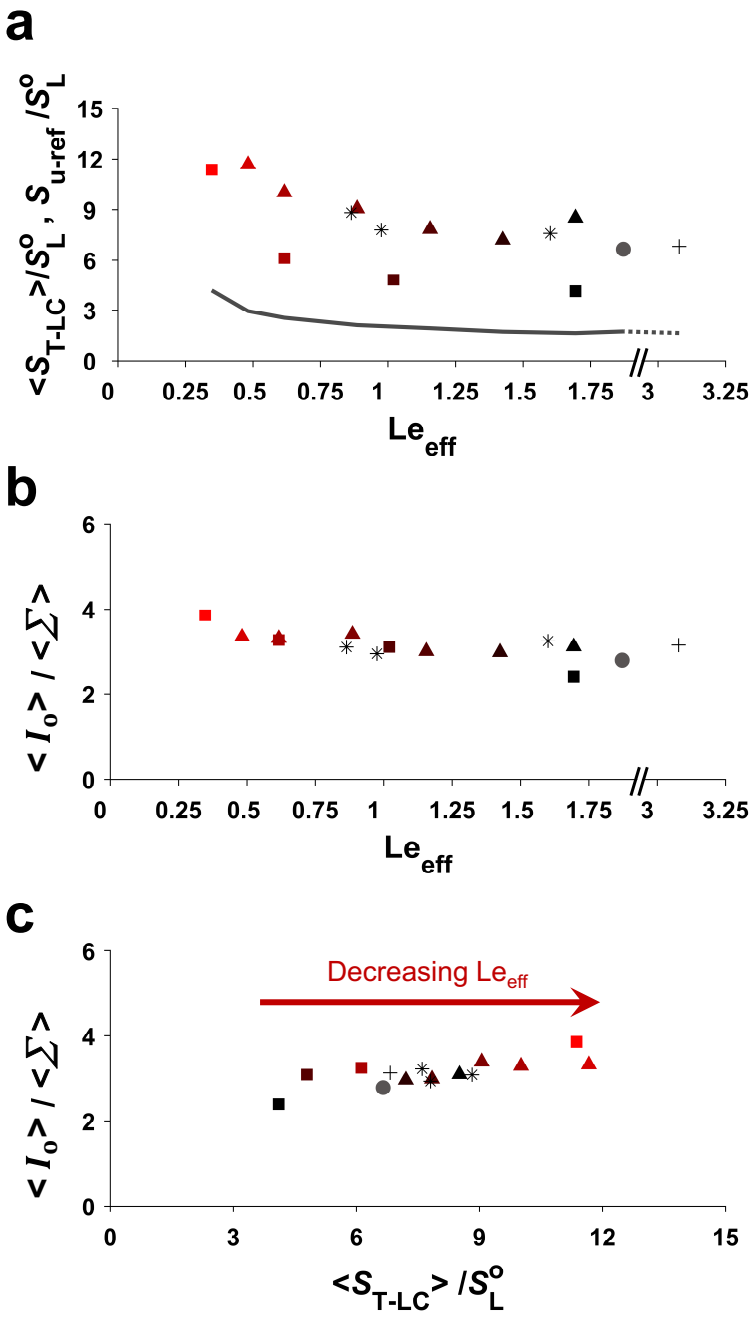

Figure 5.11 (a) Turbulent burning rates at various $\mathrm{Le_{eff}}$ in turbulent flames (symbols) compared to reference flame speeds in laminar flames (line). The x-axis is broken to show the C_3H_8-He flame (plus) at $\mathrm{Le_{eff}} = 3.08$. The relative contribution of the normalized $\langle S_\mathrm{T} \rangle$ ($\langle I_\mathrm{o} \rangle \approx \langle S_\mathrm{T} \rangle / S_\mathrm{L}^\mathrm{o}$) and $\langle \Sigma \rangle$ in increasing $S_{\mathrm{T-LC}}$ are plotted against: (b) $\mathrm{Le_{eff}}$, and (c) normalized $\langle S_{\mathrm{T-LC}} \rangle$. Symbols are the same as Fig. 5.6 (d).

5.4.6 Discussion − The effects of differential diffusion on turbulent burning rates

Variations of turbulent burning rates with decreasing $\mathrm{Le_{eff}}$, illustrated in Fig. 5.11 (a), correlate closely with flame location (Figs. 5.4 (b) and 5.4 (d)), local flamelet displacement velocity (Fig. 5.6 (d)), flame-front curvature (Fig. 5.8 (b)), flame-surface area (Fig. 5.9 (a)), and flame stretch (Fig. 5.10 (d)) at various $\mathrm{Le_{eff}}$. These results are consistent with the idea that, in thermo-diffusively unstable mixtures with $\mathrm{Le_{eff}} < 1$, when the flame front is perturbed, thermal-diffusive (TD) instabilities cause two main effects on flame propagation: (1) at the positively stretched portion of the flame front, the local velocity increases towards the fresh reactants due to the effects of differential diffusion, and (2) as the reactants approach the reaction zone in the negatively curved region along two side-by-side positively curved segments of the flame front, the fuel will preferentially diffuse out of the fresh reactants towards the positively curved leading edges, due to the higher molecular diffusion of the lighter fuels compared to the heavier oxidizer (i.e., preferential diffusion), and make the reactants leaner as they approach the reaction zone. This will decrease the propagation velocity in the negatively curved region; hence, the positively and negatively curved segments of the flame front move farther away from the average flame location. As illustrated in Fig. 5.8 (a), PDFs of curvature display a symmetric profile with a near-zero mean even for thermo-diffusively unstable mixtures with $\mathrm{Le_{eff}} < 1$, with no skewness towards positive curvature values. This shows that the flame-front curvature is equally negative as it is positive and that the increase in the average magnitude of flame curvature shown in Fig. 5.8 (b) is primarily associated with the preferential diffusion of the lighter fuels compared to the heavier oxidizer. A similar methodology was used in [92] for identifying the presence of DL hydrodynamic instabilities based on the skewness of the flame curvature PDF. This preferential diffusion results in increasing local curvature and stretch imposed on that location along the flame front, which further triggers the effects of differential diffusion in increasing local velocity, curvature, and flame stretch. Both these effects further amplify the initial wrinkle, and lead to a flame that has a larger FSA, which burns more reactants, and has higher local flamelet velocities; both effects increase the flame burning rates. Increasing average flame burning rates causes the thermo-diffusively unstable flames to climb up the steep bulk-velocity gradients in the stagnation flow, resulting in a significant relocation of these flames towards the bottom nozzle (Figs. 5.4 (b) and 5.4 (d)), and eventually leading to a flashback in mixtures with $\mathrm{Le_{eff}} \ll 1$. Flashback is a direct result of these higher turbulent burning rates due to variations in diffusive properties, at constant laminar flame speed, bulk-flow velocity, and turbulence intensity.

There are two main mechanisms that limit the perpetual increase in local flame velocities and

burning rates: (1) the destruction of FSA due to the flame-front segments merging at the trailing points, forming cusps, which reduces the flame-front curvature and flame stretch, leading to flamelets with smaller FSA, lower local velocities, and smaller flame burning rates, and (2) the propagation of leading points in all directions, which means that their radius of curvature increases in time, leading to a lower curvature; hence, putting a limit on the maximum flamelet velocity in that location along the flame front. Therefore, the average burning rate causes the flames to stabilize at some average location within the steep bulk-velocity gradients of the counterflow.

As illustrated in Fig. 5.6 (d) and Fig. 5.11 (a), the same overall curve of S_{T} versus $\mathrm{Le}_{\mathrm{eff}}$, as well as for $S_{\mathrm{T-LC}}$ versus $\mathrm{Le}_{\mathrm{eff}}$, are obtained for all mixtures, regardless of the fuel composition or inert gases used. These results indicate that the values of S_{T} and $S_{\mathrm{T-LC}}$, measured over a wide range of Lewis numbers, are not dependent on the fuel or oxidizing-gas mixture, and can be described fully by $\mathrm{Le}_{\mathrm{eff}}$ and turbulence intensity. Furthermore, Figs. 5.11 (b) and 5.11 (c) illustrate that the relative contribution of local flamelet velocities and FSA in increasing $S_{\mathrm{T-LC}}$ is not dependent on the fuel, oxidizing-gas mixture, or turbulence intensity, and the results overlap over a wide range of Lewis numbers.

Figure 5.9 (a), as well as numerous previous studies (e.g., [94, 96]) show that increasing turbulence intensity increases the FSA. In addition, Figs. 5.8 (b) and 5.10 (d) illustrate that increasing turbulence intensity increases the effects of differential diffusion in thermo-diffusively unstable mixtures ($\mathrm{Le}_{\mathrm{eff}} < 1$), due to the enhanced stretch imposed on flames through increasing flamelet curvature, which was also shown in [51]. These effects demonstrate that the effects of turbulence and differential diffusion are linked in increasing turbulent burning rates in mixtures with $\mathrm{Le}_{\mathrm{eff}} < 1$.

Flame-front cellular instabilities in premixed flames arise from a combination of both TD and DL hydrodynamic instabilities. While DL instabilities are typically neglected for small-scale flames at atmospheric pressure, due to the diffusional thickness of the flame, these effects are coupled to the effects of differential diffusion at high-pressure combustion for which DL instabilities can be substantially enhanced due to very thin flames. Recent studies show that turbulence triggers the production of instabilities, and may act to accentuate the burning rate by promoting intrinsic flame instabilities [53, 97], consistent with our observations that for thermo-diffusively unstable flames, turbulence increases both S_{T} and Σ. The discussion above shows that the effects of turbulence intensity, TD instabilities, and DL hydrodynamic instabilities may be interlinked during turbulent premixed flame propagation of mixtures with $\mathrm{Le}_{\mathrm{eff}} < 1$. Furthermore, in turbulent premixed flames, the local flame conformation, and overall combustion properties, such as turbulent burning rates and flame structure, are influenced by advection of these instabilities along the flame surface referred to as a *memory effect* [20]. This phenomenon suggests that the burning

rate and morphology of turbulent flames depend on both mixture properties, as well as geometry-dependent parameters [20, 92], which can be accounted for by the mean flame stretch modulated by the Markstein length [92], the former implicitly accounts for geometry-dependence [20], and the latter accounts for all diffusion processes occurring inside the flame zone [92]. The results represented in this study are consistent with this understanding.

While turbulence and DL hydrodynamic instabilities interact in the wrinkled/corrugated flamelet regimes, it was shown that for high turbulence intensities the effects of DL instabilities are predicted to diminish, and the flames are dominated by the turbulence in the vicinity of the thin reaction zone regime, in the corrugated flamelet regime [94, 95]. However, our results show that TD instabilities are effective in increasing turbulent flame speed even for highly turbulent flames, and there is currently no theory to predict these physics. This work, therefore, shows the need to advance combustion theory to produce models that can capture these effects for flames in real-world combustion systems to predict the performance of future fuel-flexible combustors, and the present results provide a valuable dataset for the validation of such theories.

5.5 Conclusions

The effects of differential diffusion on lean turbulent premixed flame location, local flamelet velocities, burning rates, and flame structure were investigated using counter-flow flames in the thin reaction zone regime. Various fuel-oxidizer-inert mixtures representative of a wide range of Lewis numbers were used in the context of fuel flexibility. Local instantaneous statistics of various flame parameters within the imaged plane were quantified as probability density functions using sufficiently large data sets to ensure statistical accuracy. These statistics showed that the effects of differential diffusion on the burning rates and the structure of turbulent premixed flames are important in the thin reaction zone regime ($1 < \mathrm{Ka_T} < 100$ and $\mathrm{Da_T} < 1$), and turbulence does not mask these effects, even if turbulent heat and mass transport are significantly enhanced over the laminar values.

The PDFs showed that, in turbulent premixed flames, local flamelet velocities and turbulent burning rates increase with decreasing $\mathrm{Le_{eff}}$ at a constant turbulence intensity and laminar flame speed. In addition to increasing local flamelet velocities, differential diffusion also increases both the flame-front curvature and flame-surface area in mixtures with $\mathrm{Le_{eff}} < 1$ at constant turbulence intensities, which increases turbulent burning rates. The effects of Lewis number are not linear; most results remain almost constant in mixtures with $\mathrm{Le_{eff}} > 1$, whereas they increase sharply with decreasing $\mathrm{Le_{eff}}$ in mixtures with $\mathrm{Le_{eff}} \lesssim 0.75$. The relative contribution of turbulent flamelet

velocities and flame-surface area, in increasing turbulent burning rates, is approximately 76 % and 24 %, respectively, and this proportion is not dependent on the fuel, oxidizing-gas mixture, or turbulence intensity, and the results overlap over a wide range of Lewis numbers. Furthermore, local flamelet velocities, burning rates, and structure parameters, i.e., flame-front curvature and flame-surface area, increase with increasing turbulence intensity, as commonly understood.

These results show that the effects of differential diffusion on turbulent premixed flame propagation of thermo-diffusively unstable mixtures in the thin reaction zone regime include the explicit effects on both increasing local flamelet displacement velocity, as well as increasing flame-surface area, as these two parameters are highly correlated. Furthermore, the effects of differential diffusion on various parameters of turbulent premixed flames, measured over a wide range of Lewis numbers, are not dependent on the fuel or oxidizing-gas mixture and can be described fully by $\mathrm{Le}_{\mathrm{eff}}$ and turbulence intensity.

Acknowledgment

This research was funded by the Natural Sciences and Engineering Research Council of Canada (grant No. I242349C0G) and Siemens Canada Limited under the Collaborative Research and Development program (NSERC-CRD). Support of the McGill Engineering Doctoral Awards (MEDA) program is also gratefully acknowledged.

References

[1] M.Z. Jacobson and M.A. Delucchi. “Providing all global energy with wind, water, and solar power, Part I: Technologies, energy resources, quantities and areas of infrastructure, and materials”. In: *Energy Policy* 39 (2011), pp. 1154–1169.

[2] H. Ibrahim, A. Ilinca, and J. Perron. “Energy storage systems-characteristics and comparisons”. In: *Renewable and Sustainable Energy Reviews* 12 (2008), pp. 1221–1250.

[3] L. Brennan and P. Owende. “Biofuels from microalgae - A review of technologies for production, processing, and extractions of biofuels and co-products”. In: *Renewable and Sustainable Energy Reviews* 14 (2010), pp. 557–577.

[4] Y. Hou, R. Vidu, and P. Stroeve. “Solar energy storage methods”. In: *Industrial & Engineering Chemistry Research* 50 (2011), pp. 8954–8964.

[5] J.M. Bergthorson. “Recyclable metal fuels for clean and compact zero-carbon power”. In: *Progress in Energy and Combustion Science* 68 (2018), pp. 169–196.

[6] J.M. Bergthorson and M.J. Thomson. “A review of the combustion and emissions properties of advanced transportation biofuels and their impact on existing and future engines”. In: *Renewable and Sustainable Energy Reviews* 42 (2015), pp. 1393–1417.

[7] Z. Huang, Y. Zhang, K. Zeng, B. Liu, Q. Wang, and D. Jiang. “Measurements of laminar burning velocities for natural gas–hydrogen–air mixtures”. In: *Combustion and Flame* 146 (2006), pp. 302–311.

[8] E. Hu, Z. Huang, J. He, C. Jin, and J. Zheng. “Experimental and numerical study on laminar burning characteristics of premixed methane–hydrogen–air flames”. In: *International Journal of Hydrogen Energy* 34 (2009), pp. 4876–4888.

[9] C. Tang et al. “Laminar burning velocities and combustion characteristics of propane–hydrogen–air premixed flames”. In: *International Journal of Hydrogen Energy* 33 (2008), pp. 4906–4914.

[10] P. Strakey, T. Sidwell, and J. Ontko. “Investigation of the effects of hydrogen addition on lean extinction in a swirl stabilized combustor”. In: *Proceedings of the Combustion Institute* 31 (2007), pp. 3173–3180.

[11] F. Halter, C. Chauveau, and I. Gökalp. “Characterization of the effects of hydrogen addition in premixed methane/air flames”. In: *International Journal of Hydrogen Energy* 32 (2007), pp. 2585–2592.

[12] B. Karlovitz, D.W. Denniston Jr, D.H. Knapschaefer, and F.E. Wells. "Studies on turbulent flames: A. Flame propagation across velocity gradients B. Turbulence measurement in flames". In: *Proceedings of the Combustion Institute* 4 (1953), pp. 613–620.

[13] M. Matalon. "On flame stretch". In: *Combustion Science and Technology* 31 (1983), pp. 169–181.

[14] A. Buschmann, F. Dinkelacker, T. Schäfer, M. Schäfer, and J. Wolfrum. "Measurement of the instantaneous detailed flame structure in turbulent premixed combustion". In: *Proceedings of the Combustion Institute* 26 (1996), pp. 437–445.

[15] Ö.L. Gülder and G.J. Smallwood. "Flame surface densities in premixed combustion at medium to high turbulence intensities". In: *Combustion Science and Technology* 179 (2007), pp. 191–206.

[16] F.T.C. Yuen and Ö.L. Gülder. "Turbulent premixed flame front dynamics and implications for limits of flamelet hypothesis". In: *Proceedings of the Combustion Institute* 34 (2013), pp. 1393–1400.

[17] R.W. Pitz, S. Hu, and P. Wang. "Tubular premixed and diffusion flames: Effect of stretch and curvature". In: *Progress in Energy and Combustion Science* 42 (2014), pp. 1–34.

[18] L.P.H. De Goey, T. Plessing, R.T.E. Hermanns, and N. Peters. "Analysis of the flame thickness of turbulent flamelets in the thin reaction zones regime". In: *Proceedings of the Combustion Institute* 30 (2005), pp. 859–866.

[19] R. Sankaran, E.R. Hawkes, J.H. Chen, T. Lu, and C.K. Law. "Structure of a spatially developing turbulent lean methane–air Bunsen flame". In: *Proceedings of the Combustion Institute* 31 (2007), pp. 1291–1298.

[20] J.F. Driscoll. "Turbulent premixed combustion: Flamelet structure and its effect on turbulent burning velocities". In: *Progress in Energy and Combustion Science* 34 (2008), pp. 91–134.

[21] F.T. Yuen and Ö.L. Gülder. "Dynamics of lean-premixed turbulent combustion at high turbulence intensities". In: *Combustion Science and Technology* 182 (2010), pp. 544–558.

[22] A. Marshall, J. Lundrigan, P. Venkateswaran, J. Seitzman, and T. Lieuwen. "Fuel effects on leading point curvature statistics of high hydrogen content fuels". In: *Proceedings of the Combustion Institute* 35 (2015), pp. 1417–1424.

[23] G. Damköhler. "The effect of turbulence on the combustion rate in gas compounds". In: *Z. Elektrochem. Angew. Phys. Chem.* 46 (1940), pp. 601–626.

[24] C.K. Law. "Dynamics of stretched flames". In: *Proceedings of the Combustion Institute* 22 (1989), pp. 1381–1402.

[25] J.H. Tien and M. Matalon. "On the burning velocity of stretched flames". In: *Combustion and Flame* 84 (1991), pp. 238–248.

[26] F.A. Williams. "Progress in knowledge of flamelet structure and extinction". In: *Progress in Energy and Combustion Science* 26 (2000), pp. 657–682.

[27] A.N. Lipatnikov and J. Chomiak. "Molecular transport effects on turbulent flame propagation and structure". In: *Progress in Energy and Combustion Science* 31 (2005), pp. 1–73.

[28] C.K. Law. *Combustion physics*. Cambridge university press, Cambridge, UK, 2010.

[29] P.A. Libby and F.A. Williams. "Structure of laminar flamelets in premixed turbulent flames". In: *Combustion and Flame* 44 (1982), pp. 287–303.

[30] Y.-C. Chen and R.W. Bilger. "Experimental investigation of three-dimensional flame-front structure in premixed turbulent combustion: II. Lean hydrogen/air Bunsen flames". In: *Combustion and Flame* 138 (2004), pp. 155–174.

[31] A. Amato, M. Day, R.K. Cheng, J. Bell, and T. Lieuwen. "Leading edge statistics of turbulent, lean, H_2–air flames". In: *Proceedings of the Combustion Institute* 35 (2015), pp. 1313–1320.

[32] P. Venkateswaran, A. Marshall, D.H. Shin, D. Noble, J. Seitzman, and T. Lieuwen. "Measurements and analysis of turbulent consumption speeds of H_2/CO mixtures". In: *Combustion and Flame* 158 (2011), pp. 1602–1614.

[33] H. Kobayashi, T. Tamura, K. Maruta, T. Niioka, and F.A. Williams. "Burning velocity of turbulent premixed flames in a high-pressure environment". In: *Proceedings of the Combustion Institute* 26 (1996), pp. 389–396.

[34] K. Yamamoto, M. Ozeki, N. Hayashi, and H. Yamashita. "Burning velocity and OH concentration in premixed combustion". In: *Proceedings of the Combustion Institute* 32 (2009), pp. 1227–1235.

[35] J. Furukawa, T. Hirano, and F.A. Williams. "Burning velocities of flamelets in a turbulent premixed flame". In: *Combustion and Flame* 113 (1998), pp. 487–491.

[36] J. Furukawa and F.A. Williams. "Flamelet effects on local flow in turbulent premixed Bunsen flames". In: *Combustion Science and Technology* 175 (2003), pp. 1835–1858.

[37] Y. Ikeda, J. Kojima, T. Nakajima, F. Akamatsu, and M. Katsuki. "Measurement of the local flamefront structure of turbulent premixed flames by local chemiluminescence". In: *Proceedings of the Combustion Institute* 28 (2000), pp. 343–350.

[38] E. Abbasi-Atibeh and J.M. Bergthorson. "Differential diffusion effects in counter-flow premixed hydrogen-enriched methane and propane flames". In: *Proceedings of the Combustion Institute* 37 (2019), pp. 2399–2406.

[39] E. Abbasi-Atibeh, S. Jella, and J.M. Bergthorson. "Fuel variation effects in propagation and stabilization of turbulent counter-flow premixed flames". In: *Journal of Engineering for Gas Turbines and Power* 141 (2018), p. 031024.

[40] K.N.C. Bray and R.S. Cant. "Some applications of Kolmogorov's turbulence research in the field of combustion". In: *Proceedings of the Royal Society of London Series A* 434 (1991), pp. 217–240.

[41] S. Kheirkhah and Ö.L. Gülder. "Consumption speed and burning velocity in counter-gradient and gradient diffusion regimes of turbulent premixed combustion". In: *Combustion and Flame* 162 (2015), pp. 1422–1439.

[42] J.D. Regele, E. Knudsen, H. Pitsch, and G. Blanquart. "A two-equation model for non-unity Lewis number differential diffusion in lean premixed laminar flames". In: *Combustion and Flame* 160 (2013), pp. 240–250.

[43] S.D. Salusbury and J.M. Bergthorson. "Maximum stretched flame speeds of laminar premixed counter-flow flames at variable Lewis number". In: *Combustion and Flame* 162 (2015), pp. 3324–3332.

[44] R.G. Abdel-Gayed, D. Bradley, M.N. Hamid, and M. Lawes. "Lewis number effects on turbulent burning velocity". In: *Proceedings of the Combustion Institute* 20 (1984), pp. 505–512.

[45] D. Bradley. "How fast can we burn?" In: *Proceedings of the Combustion Institute* 24 (1992), pp. 247–262.

[46] R.S. Barlow, M.J. Dunn, M.S. Sweeney, and S. Hochgreb. "Effects of preferential transport in turbulent bluff-body-stabilized lean premixed CH_4/air flames". In: *Combustion and Flame* 159 (2012), pp. 2563–2575.

[47] E. Boschek, P. Griebel, and P. Jansohn. "Fuel variability effects on turbulent, lean premixed flames at high pressures". In: *Proceedings of the ASME Turbo Expo: Turbine Technical Conference and Exposition. GT2007–27496* (2007).

[48] F. Dinkelacker, B. Manickam, and S.P.R. Muppala. "Modelling and simulation of lean premixed turbulent methane/hydrogen/air flames with an effective Lewis number approach". In: *Combustion and Flame* 158 (2011), pp. 1742–1749.

[49] V.R. Kuznetsov, V.A. Sabel'nikov, and P.A. Libby. *Turbulence and Combustion*. Hemisphere Publishing, Moscow, Russia, 1986.

[50] V.P. Karpov, A.N. Lipatnikov, and V.L. Zimont. "Flame curvature as a determinant of preferential diffusion effects in premixed turbulent combustion". In: *Advances in Combustion Science (Progress in Astronautics and Aeronautics)* 173 (1997), pp. 235–250.

[51] S. Yang, A. Saha, W. Liang, F. Wu, and C.K. Law. "Extreme role of preferential diffusion in turbulent flame propagation". In: *Combustion and Flame* 188 (2018), pp. 498–504.

[52] B. Savard and G. Blanquart. "Broken reaction zone and differential diffusion effects in high Karlovitz n-C_7H_{16} premixed turbulent flames". In: *Combustion and Flame* 162 (2015), pp. 2020–2033.

[53] Z. Liu, S. Yang, C.K. Law, and A. Saha. "Cellular instability in Le< 1 turbulent expanding flames". In: *Proceedings of the Combustion Institute* 37 (2019), pp. 2611–2618.

[54] I. Han and K.Y. Huh. "Roles of displacement speed on evolution of flame surface density for different turbulent intensities and Lewis numbers in turbulent premixed combustion". In: *Combustion and Flame* 152 (2008), pp. 194–205.

[55] P.J. Goix and I.G. Shepherd. "Lewis number effects on turbulent premixed flame structure". In: *Combustion Science and Technology* 91 (1993), pp. 191–206.

[56] R. Borghi. "On the structure and morphology of turbulent premixed flames". In: *Recent Advances in the Aerospace Sciences* (1985), pp. 117–138.

[57] N. Peters. *Turbulent combustion*. Cambridge university press, Cambridge, UK, 2000.

[58] L.W. Kostiuk, K.N.C. Bray, and T.C. Chew. "Premixed turbulent combustion in conterflowing streams". In: *Combustion Science and Technology* 64 (1989), pp. 233–241.

[59] E. Mastorakos, A.M.K.P. Taylor, and J.H. Whitelaw. "Extinction and temperature characteristics of turbulent counterflow diffusion flames with partial premixing". In: *Combustion and Flame* 91 (1992), pp. 40–54.

[60] L.W. Kostiuk, K.N.C. Bray, and R.K. Cheng. "Experimental study of premixed turbulent combustion in opposed streams: Part I—Nonreacting flow field". In: *Combustion and Flame* 92 (1993), pp. 377–395.

[61] L.W. Kostiuk, K.N.C. Bray, and R.K. Cheng. "Experimental study of premixed turbulent combustion in opposed streams: Part II–Reacting flow field and extinction". In: *Combustion and Flame* 92 (1993), pp. 396–409.

[62] E. Mastorakos, A.M.K.P. Taylor, and J.H. Whitelaw. "Extinction of turbulent counterflow flames with reactants diluted by hot products". In: *Combustion and Flame* 102 (1995), pp. 101–114.

[63] K. Sardi, A.M.K.P. Taylor, and J.H. Whitelaw. "Conditional scalar dissipation statistics in a turbulent counterflow". In: *Journal of Fluid Mechanics* 361 (1998), pp. 1–24.

[64] L.W. Kostiuk, I.G. Shepherd, and K.N.C. Bray. "Experimental study of premixed turbulent combustion in opposed streams. Part III–Spatial structure of flames". In: *Combustion and Flame* 118 (1999), pp. 129–139.

[65] D. Geyer, A. Kempf, A. Dreizler, and J. Janicka. "Turbulent opposed-jet flames: A critical benchmark experiment for combustion LES". In: *Combustion and Flame* 143 (2005), pp. 524–548.

[66] G. Coppola, B. Coriton, and A. Gomez. "Highly turbulent counterflow flames: A laboratory scale benchmark for practical systems". In: *Combustion and Flame* 156 (2009), pp. 1834–1843.

[67] F. Hampp and R.P. Lindstedt. "Quantification of combustion regime transitions in premixed turbulent DME flames". In: *Combustion and Flame* 182 (2017), pp. 248–268.

[68] A. Kempf, H. Forkel, J.-Y. Chen, A. Sadiki, and J. Janicka. "Large-eddy simulation of a counterflow configuration with and without combustion". In: *Proceedings of the Combustion Institute* 28 (2000), pp. 35–40.

[69] N. Bouvet, F. Halter, C. Chauveau, and Y. Yoon. "On the effective Lewis number formulations for lean hydrogen/hydrocarbon/air mixtures". In: *International Journal of Hydrogen Energy* 38 (2013), pp. 5949–5960.

[70] D.G. Goodwin, H.K. Moffat, and R.L. Speth. *Cantera: A software toolkit for chemical kinetics, thermodynamics, and transport processes*. Version 2.2.1, http://www.cantera.org, 2016.

[71] H.W. Liepmann. *Investigations on laminar boundary-layer stability and transition on curved boundaries*. Tech. rep. NACA Wartime Report W-107. ACR No. 3H30. 1943.

[72] J.M. Bergthorson. *Experiments and modeling of impinging jets and premixed hydrocarbon stagnation flames*. PhD thesis, California Institute of Technology, 2005.

[73] G. Coppola and A. Gomez. "Experimental investigation on a turbulence generation system with high-blockage plates". In: *Experimental Thermal and Fluid Science* 33 (2009), pp. 1037–1048.

[74] B. Böhm, O. Stein, A. Kempf, and A. Dreizler. "In-nozzle measurements of a turbulent opposed jet using PIV". In: *Flow, Turbulence and Combustion* 85 (2010), pp. 73–93.

[75] H. Tennekes and J.L. Lumley. *A First Course in Turbulence*. The MIT Press, Cambridge, USA, 1972.

[76] S.B. Pope. *Turbulent flows*. Cambridge University Press, Cambridge, UK, 2000.

[77] J.O. Hinze. *Turbulence*. McGraw-Hill, New York, USA, 1975.

[78] T. Lachaux, F. Halter, C. Chauveau, I. Gökalp, and I.G. Shepherd. "Flame front analysis of high-pressure turbulent lean premixed methane–air flames". In: *Proceedings of the Combustion Institute* 30 (2005), pp. 819–826.

[79] S.A. Filatyev, J.F. Driscoll, C.D. Carter, and J.M. Donbar. "Measured properties of turbulent premixed flames for model assessment, including burning velocities, stretch rates, and surface densities". In: *Combustion and Flame* 141 (2005), pp. 1–21.

[80] T. Pavlidis. *Algorithms for graphics and image processing*. Springer Science & Business Media, 2012.

[81] I.G. Shepherd. "Flame surface density and burning rate in premixed turbulent flames". In: *Proceedings of the Combustion Institute* 26 (1996), pp. 373–379.

[82] J.B. Bell et al. "Numerical simulation of a laboratory-scale turbulent V-flame". In: *Proceedings of the National Academy of Sciences* 102 (2005), pp. 10006–10011.

[83] M.Z. Haq, C.G.W. Sheppard, R. Woolley, D.A. Greenhalgh, and R.D. Lockett. "Wrinkling and curvature of laminar and turbulent premixed flames". In: *Combustion and Flame* 131 (2002), pp. 1–15.

[84] Y.-C. Chen. "Measurements of flame-front curvature based on Fourier transformation". In: *Combustion Theory and Modelling* 11 (2007), pp. 333–349.

[85] H. Kolla, J.W. Rogerson, and N. Swaminathan. "Validation of a turbulent flame speed model across combustion regimes". In: *Combustion Science and Technology* 182 (2010), pp. 284–308.

[86] P.J. Trunk, I. Boxx, C. Heeger, W. Meier, B. Böhm, and A. Dreizler. "Premixed flame propagation in turbulent flow by means of stereoscopic PIV and dual-plane OH-PLIF at sustained kHz repetition rates". In: *Proceedings of the Combustion Institute* 34 (2013), pp. 3565–3572.

[87] G. Hartung, J. Hult, R. Balachandran, M.R. Mackley, and C.F. Kaminski. "Flame front tracking in turbulent lean premixed flames using stereo PIV and time-sequenced planar LIF of OH". In: *Applied Physics B* 96 (2009), pp. 843–862.

[88] R. Abu-Gharbieh, G. Hamarneh, T. Gustavsson, and C.F. Kaminski. "Flame front tracking by laser induced fluorescence spectroscopy and advanced image analysis". In: *Optics Express* 8 (2001), pp. 278–287.

[89] R. Abu-Gharbieh, G. Hamarneh, T. Gustavsson, and C.F. Kaminski. "Level set curve matching and particle image velocimetry for resolving chemistry and turbulence interactions in propagating flames". In: *Journal of Mathematical Imaging and Vision* 19 (2003), pp. 199–218.

[90] I.R. Gran, T. Echekki, and J.H. Chen. "Negative flame speed in an unsteady 2-D premixed flame: A computational study". In: *Proceedings of the Combustion Institute* 26 (1996), pp. 323–329.

[91] S. Daniele, J. Mantzaras, P. Jansohn, A. Denisov, and K. Boulouchos. "Flame front/turbulence interaction for syngas fuels in the thin reaction zones regime: Turbulent and stretched laminar flame speeds at elevated pressures and temperatures". In: *Journal of Fluid Mechanics* 724 (2013), pp. 36–68.

[92] M. Zhang, A. Patyal, Z. Huang, and M. Matalon. "Morphology of wrinkles along the surface of turbulent Bunsen flames–Their amplification and advection due to the Darrieus–Landau instability". In: *Proceedings of the Combustion Institute* 37 (2019), pp. 2335–2343.

[93] G. Troiani, F. Creta, and M. Matalon. "Experimental investigation of Darrieus–Landau instability effects on turbulent premixed flames". In: *Proceedings of the Combustion Institute* 35 (2015), pp. 1451–1459.

[94] N. Fogla, F. Creta, and M. Matalon. "The turbulent flame speed for low-to-moderate turbulence intensities: Hydrodynamic theory vs. experiments". In: *Combustion and Flame* 175 (2017), pp. 155–169.

[95] S. Yang, A. Saha, Z. Liu, and C.K. Law. "Role of Darrieus–Landau instability in propagation of expanding turbulent flames". In: *Journal of Fluid Mechanics* 850 (2018), pp. 784–802.

[96] M. Day, J. Bell, P.-T. Bremer, V. Pascucci, V. Beckner, and M. Lijewski. "Turbulence effects on cellular burning structures in lean premixed hydrogen flames". In: *Combustion and Flame* 156.5 (2009), pp. 1035–1045.

[97] C.R. Bauwens, J.M. Bergthorson, and S.B. Dorofeev. “On the interaction of the Darrieus–Landau instability with weak initial turbulence”. In: *Proceedings of the Combustion Institute* 36 (2017), pp. 2815–2822.

Chapter 6

Conclusions

6.1 Summary of results

Fuel flexibility is important for next-generation combustor design, which enables various energy technologies to avoid burning fossil fuels by using renewable alternative fuels. Adaptability of new engines with renewable fuels will, ultimately, prevent the emission of new carbon, in the form of CO_2, into the environment; hence, mitigating global climate change, while benefiting from the inherent advantages of combustion-based engines, e.g., energy and power density. However, fuel flexibility significantly affects combustor operability properties, mainly due to variations in turbulent burning rates, through changing mixture reactivity, which is represented by unstretched laminar flame speed, and mixture diffusivity. Differential diffusion originates from the disparity between thermal-diffusivity and mass diffusivity at the flame front, which is represented by Lewis number, and is known to cause stretch sensitivity and thermal-diffusive instabilities in the propagation of premixed flames. The effects of differential diffusion on the propagation, stabilization, and structure of lean turbulent premixed flames were the focus of this study.

The goals of this thesis have been: (1) to design and build a counter-flow experimental apparatus capable of stabilizing near-adiabatic turbulent flames, in the thin reaction zone regime, against hot exhaust gases, which is also suitable for highly strained laminar flame experiments, (2) to develop diagnostic techniques enabling simultaneous flame-location detection and velocity field measurements, as well as temperature boundary condition measurements, (3) to develop data-processing tools to quantify instantaneous local flame properties, such as flame location, local flamelet velocities, flame burning rates, and parameters of turbulent flame structure, such as flame stretch, flame-front curvature, and flame surface area, and (4) to investigate the interactions between turbulence and thermal-diffusive instabilities at the flame-front, caused by the effects of differential diffusion, independent of mixture reactivity.

The hot-exhaust opposed-flow turbulent flame rig (HOTFR) is presented, and the design details

of HOTFR are discussed. In this study, strained counter-flow flames are used to investigate the effects of both components of flame stretch, i.e., bulk and local hydrodynamic strain rates, and local curvature, in the thin reaction zone regime. HOTFR allows laboratory-scale experiments closer to the relevant conditions of practical systems, such as gas-turbine engines and other combustors, and enables understanding the effects of differential diffusion in the thin reaction zone regime, where these measurements are thinly scattered in the current combustion research literature.

It was demonstrated through this study that the combination of high-speed particle image velocimetry (PIV) and Mie scattering flame tomography, using oil droplet seeding, can be used for simultaneous flame-location detection and velocity field measurements. Data-processing tools, developed through this study, enabled local instantaneous measurements of various flame parameters, rather than average properties. These measurements were statistically represented, using sufficiently large datasets, in the form of probability density functions (PDF), as time-averaged quantities do not yield local information on the physics of turbulent flame propagation.

The effects of turbulence and stretch sensitivity on the propagation and stabilization of lean turbulent premixed flames with variable Lewis numbers were investigated at increasing turbulence level. As the first incursion into the field of fuel flexibility, pure fuel-air mixtures of hydrogen-air ($\mathrm{Le} \ll 1$), methane-air ($\mathrm{Le} \approx 1$), and propane-air ($\mathrm{Le} > 1$), representative of various thermo-diffusive properties, were studied. In these experiments, turbulence intensity was increased by increasing bulk-flow velocity. Increasing turbulence intensity enhances both flame surface area, as well as the stretch imposed on flames due to the increasing flame-front curvature. Increasing flame surface area leads to a flame that burns more reactants; however, this effect is similar for all mixtures. Therefore, these results demonstrated that the statistics of local instantaneous flame location and turbulent flamelet velocities are sensitive to the effects of differential diffusion at increasing turbulence level. With increasing flame stretch, in hydrogen-air flames, thermo-diffusively unstable mixtures with $\mathrm{Le} \ll 1$, local flamelet velocities increased considerably compared to the laminar flame speed, due to the effects of differential diffusion. Slight differences were observed in local flamelet velocities of H_2-air and CH_4air flames while the differences in global turbulent burning rates, shown implicitly by the PDFs of flame location, were significant in these flames.

While the effects of mixture reactivity on turbulent burning rates are well studied, most studies report the combined effects of the mixture reactivity and diffusivity properties, whereas, fewer studies have focused only on the effects of differential diffusion on the propagation of premixed flames. In the next experimental campaign, the unstretched laminar flame speed of the mixtures, the bulk-flow properties, and the temperature boundary condition were kept constant, in order to only focus on the effects of differential diffusion in the thin reaction zone regime at constant turbulence intensities. The spatial resolution of the PIV measurements was also improved by 31 %,

through modifications on the camera lens system, compared to the previous experiments. These experiments investigated the effects of differential diffusion on flame location and local flamelet velocities for lean premixed flames with distinct effective Lewis numbers ($\mathrm{Le_{eff}}$). Furthermore, a brief discussion on the structure parameters of turbulent premixed flames, including flame stretch and flame-front curvature was also presented. In the context of fuel flexibility, fuel blends of hydrogen, which is a clean alternative for fossil fuels, and conventional hydrocarbons, i.e., methane and propane, were studied in air, where the variations of $\mathrm{Le_{eff}}$ were mainly due to a change in fuel diffusivity of the mixtures. The effects of differential diffusion in increasing turbulent burning rates were only observed in H_2-enriched C_3H_8-air flames when $\mathrm{Le_{eff}} < 1$ at H_2 contents of larger than $60\,\%$ (by volume), whereas, these effects were observed in H_2-enriched CH_4-air flames over the whole range of H_2 content, all having $\mathrm{Le_{eff}} < 1$. However, PDFs of flame velocity showed that local displacement velocities only slightly increased with increasing H_2 content due to the effects of differential diffusion. These results further implied that there must also be an effect of differential diffusion on flame surface area at constant turbulence intensities, which was also illustrated by a clear increase in flame-front curvature when $\mathrm{Le_{eff}}$ fell below unity.

In the last part of this thesis, the effects of differential diffusion on various flame parameters of lean premixed flames, such as flame location, local flamelet velocities, burning rates, and flame structure parameters, including flame stretch, flame-front curvature, and flame surface area, were investigated in the thin reaction zone regime. These effects were studied at two levels of turbulence intensity, generated using a star-shaped turbulence-generating plate, which was placed at two different distances from the nozzle exit. In these experiments, the unstretched laminar flame speed, the bulk-flow properties, and the temperature boundary condition were kept constant; hence, this study focused on the effects of differential diffusion, independent of mixture reactivity, at each turbulence level. A wide range of fuels and fuel blends were used in combination with various oxidizer-inert mixtures to form mixtures with very distinct effective Lewis numbers, by varying both fuel diffusivity and thermal diffusivity of the mixture, through H_2 enrichment and dilution. In these experiments, the effective Lewis number was in the broad range of $0.3 < \mathrm{Le_{eff}} < 3.1$, which covers a wide range as seen in typical combustion systems. The comprehensiveness of this study allows general conclusions to be drawn on the effects of differential diffusion on the propagation of turbulent premixed flames, rather than generating fuel-specific conclusions. Laminar flame measurements were also reported as a reference of comparison to study the effects of flame stretch in the absence of curvature effects in highly strained counter-flow flames. The spatial resolution of the PIV measurements was further improved by $4\,\%$ ($\approx 343\,\mu$m), which showed that the PIV measurements were approaching the resolution limit of the diagnostic technique in obtaining independent velocity vectors.

These measurements showed that the effects of differential diffusion on the burning rate and the structure of turbulent premixed flames are important in the thin reaction zone regime ($1 < \mathrm{Ka_T} < 100$ and $\mathrm{Da_T} < 1$), where turbulent heat and mass transport are significantly enhanced over the laminar values. Furthermore, the stretch sensitivity of turbulent premixed flames are not dependent on the fuel or oxidizing-gas mixture, and can be described fully by the effective Lewis number and turbulence intensity. The effects of differential diffusion on various flame parameters are not linear, as these parameters remain almost constant with decreasing $\mathrm{Le_{eff}}$ in mixtures with $\mathrm{Le_{eff}} > 1$, whereas, these effects become significant when $\mathrm{Le_{eff}} \lesssim 0.75$. It was also demonstrated that, in turbulent premixed flames with $\mathrm{Le_{eff}} < 1$, differential diffusion increased the flame-front curvature and the flame surface area at constant turbulence intensities, which showed that turbulence is not the only factor influencing the flame-front topology in turbulent premixed flames.

Finally, this study illustrated that, at constant turbulence intensities, differential diffusion increases the burning rate of turbulent flames in thermo-diffusively unstable mixtures ($\mathrm{Le_{eff}} < 1$) through two main mechanisms: (1) increasing local flamelet displacement velocity, and (2) increasing flame surface area. Furthermore, the relative contribution of these two parameters in increasing turbulent burning rates is approximately 76 % and 24 %, respectively. These results show that, over a wide range of Lewis numbers, this proportion is not dependent on the fuel, oxidizing-gas mixture, or turbulence intensity, and can be described fully by the effective Lewis number.

6.2 Contributions

This thesis presents several important contributions to the advancement of turbulent premixed combustion science and fuel-flexible combustion technology. These contributions are:

1. A counter-flow apparatus was designed and built at the Alternative Fuels Laboratory (AFL) at McGill University, which is capable of stabilizing near-adiabatic turbulent premixed flames in the thin reaction zone regime. The rig has a compact geometry, excellent optical accessibility, and well-defined boundary conditions, which reduce the complexity, and facilitate laser-diagnostic measurements and computational combustion modeling. Furthermore, diagnostic techniques were developed, which enables simultaneous flame-location detection and velocity field measurements.

2. Diagnostic techniques were developed that allows simultaneous flame-location detection and velocity-field measurements using particle image velocimetry (PIV) and Mie scattering

flame tomography. Furthermore, data-processing tools were developed through this study to quantify high-speed particle image velocimetry (PIV) and Mie scattering flame tomography data. These processing tools are used to extract local instantaneous statistics of various flame parameters. This set of processing tools is widely applicable for post-processing of data in various fields of combustion research using laser-based diagnostic techniques.

3. Experiments were designed that specifically focused on the interactions between turbulence and thermal-diffusive instabilities in the propagation of turbulent premixed flames independent of mixture reactivity. The results of this study are important in understanding the effects of differential diffusion on the propagation and structure of turbulent premixed flames in the thin reaction zone regime. We measured significant variations in turbulent burning rates, due to the effects of differential diffusion, that will likely affect the operability of fuel-flexible combustors in real-world engines, such as blowout, flashback, and dynamic stability. Furthermore, the comprehensiveness of this study allows to draw general conclusions on the effects of differential diffusion rather than generating fuel-specific conclusions.

4. This thesis shows the need to advance the combustion theory to produce models that can capture the effects of differential diffusion for flames in real-world combustion systems, in order to predict the performance of future fuel-flexible combustors. The results of this thesis are of sufficient detail that they provide valuable datasets for the validation of such theories. Furthermore, this thesis shows that there is no need for different models to capture the effects of Lewis number for various fuel and oxidizing-gas mixtures, as these effects can be described fully by the effective Lewis number and turbulence intensity.

Fuel flexibility in practical devices brings large uncertainty in the design process, which, currently, can only be addressed through costly trial and error studies. The improved scientific understanding of the basic issues behind the combustor operability and flame stability with variable fuel compositions, and improved predictive capabilities of turbulent premixed combustion models, will reduce the cost of product development while reducing the carbon footprint of energy technologies that simultaneously produce lower levels of air contaminants.

6.3 Future research directions

As a next step to this study, future research may include similar experiments for larger L/δ_{L} values, in order to explore the interactions between differential diffusion and turbulence for larger L/δ_{L}, and to ensure that the turbulence can force the flame even at large L/δ_{L}. This can be done either by

making bigger burners, which increase the characteristic length scale of the apparatus, or by going to higher pressures with the same rig, as the increasing pressure would minimally affect L, while drastically reduce the flame thickness. By changing L/δ_{L}, we would also change the characteristic size of the turbulence to the characteristic critical stretch rate (or curvature) for the formation of the Darrieus–Landau and thermo-diffusive cellular instabilities.

Fuel flexibility research in turbulent premixed combustion is still at an early stage. An improved understanding of the basic and applied combustion thermo-physics is necessary to develop improved turbulent combustion models, as design tools, that enable prediction of the effects of fuel flexibility. By improving turbulent combustion models, and increasing confidence in combustion CFD as a design tool, product design will be improved and the achievement of higher technology readiness levels will be simplified and less costly.

Furthermore, it is often argued in the combustion research community that there is a need to consider time-dependent flame dynamics imposed by different types of instabilities, in order to generate more rigorous flamelet libraries in turbulent premixed combustion modeling using the laminar flamelet approach. To continue in this direction, the dynamic response of laminar premixed flames with variable fuel-oxidizer-inert compositions, representative of mixtures with distinct thermo-diffusive properties, can be experimentally investigated. In particular, these experiments can be focused on the transient response of flames with variable fuel compositions to bulk mass flow rate oscillations, non-uniform fuel-oxidizer-inert mixture (stratification), interactions with controlled vortices, and acoustic instabilities. Various fuels and fuel-oxidizer-inert mixtures can be used to represent a wide variety of renewable alternative fuels, conventional fuels, and fuel blends. Such studies will provide fundamental knowledge on the effects of different types of instabilities on flame parameters, such as burning rates and scalar structure of flames with various fuel compositions.

The design of the current counter-flow apparatus can be modified to design a unique experimental rig, which allows aerodynamically stabilized inwardly propagating premixed cylindrical flames. The rig is capable of stabilizing flames that are nearly unstretched; hence, is a unique experimental case essential to investigate the separate effects of curvature and strain rate, and to analyze transient flame response to various flame instabilities. Laser-based diagnostic techniques, such as high-speed PIV coupled with Mie scattering flame tomography used in the current study, or high-speed PIV coupled with OH-PLIF, can be used for simultaneous flame-location detection and velocity field measurements. Furthermore, processing tools, developed during this thesis, can be modified and extended for instantaneous local and global measurements in inwardly propagating premixed cylindrical flames.

Understanding the effects of differential diffusion on the burning rates and structure of turbulent premixed flames, as well as the transient response of premixed flames with variable fuel compositions to various flame instabilities, will improve predictive capabilities of turbulent premixed combustion models toward designing fuel-flexible combustors with reduced emissions and higher performance.

Appendix A

The design details of HOTFR

A.1 Top burner design details

The Ceramic burner at the top of the HOTFR (Fig. 2.1) is composed of a ceramic nozzle manufactured by casting zirconium oxide, or zirconia (ZrO_2) with a maximum temperature of 2500 K. The ceramic nozzle is enclosed inside a stainless steel jacket used for attaching the ceramic nozzle to the aluminum base plate. A Corundum-mullite (70% Al_2O_3) water-cooled ceramic honeycomb is placed inside the ceramic nozzle as a flame-holder. The temperature of the honeycomb and the surface temperature of the stainless steel jacket are monitored using K-type thermocouples. The lower portion of the stainless steel jacket and the base plate are water-cooled for safety. The design drawings of various components of the top nozzle assembly are illustrated in Figs. A.1, A.2, and A.3.

A part was designed and manufactured using machinable wax (Fig. A.2) that fits into the stainless steel jacket and forms a hollow cavity of the ceramic nozzle shape, which is used as a mold for casting the ceramic nozzle. To cast the ceramic nozzle, the casting mold was filled with the mixture of the zirconium oxide powder and its activator and was left on a shaking table to remove air bubbles and prevent cracks in the nozzle. The shrinkage rate of the casting paste was 1.5 %; therefore, a prolonged and even drying process is required to prevent cracks in the ceramic part. De-molding of the ceramic nozzle was followed by 24 hours of air-drying at room temperature. Then, the nozzle was temperature-cured through a two-step process: (1) a low temperature curing process at 110 °C, where the ceramic nozzle was heated from the room temperature to 110 °C gradually at 2 °C/min, and was left at 110 °C for 2 hours, and (2) a high temperature curing process at 950 °C, where the ceramic nozzle was heated from 110 °C to 950 °C at 5 °C/min, and was left at 950 °C for 2 hours. The high-temperature curing increases the strength of the ceramic part against thermal and mechanical shocks.

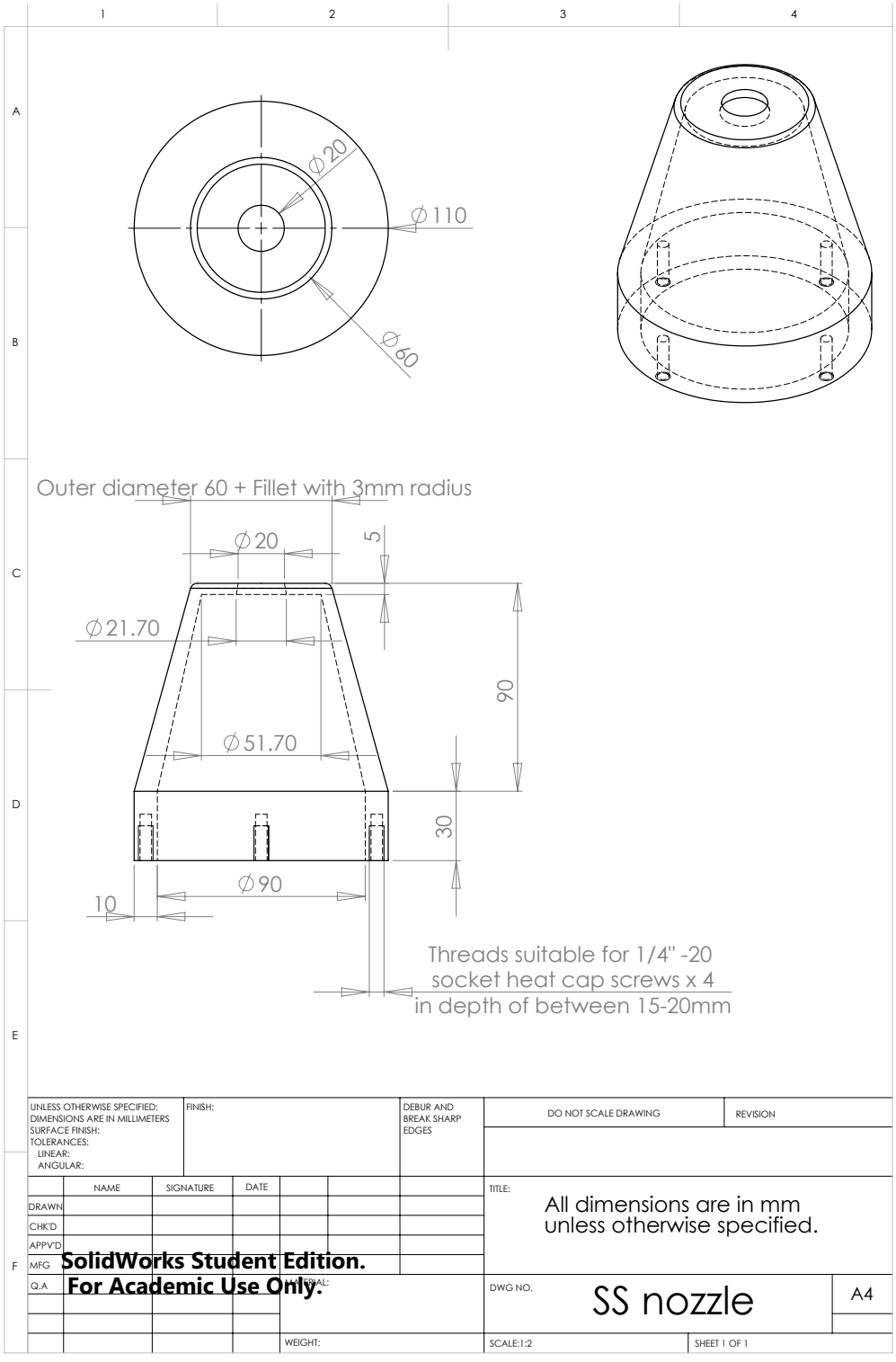

Figure A.1 Design drawing of the stainless steel jacket holding the ceramic burner.

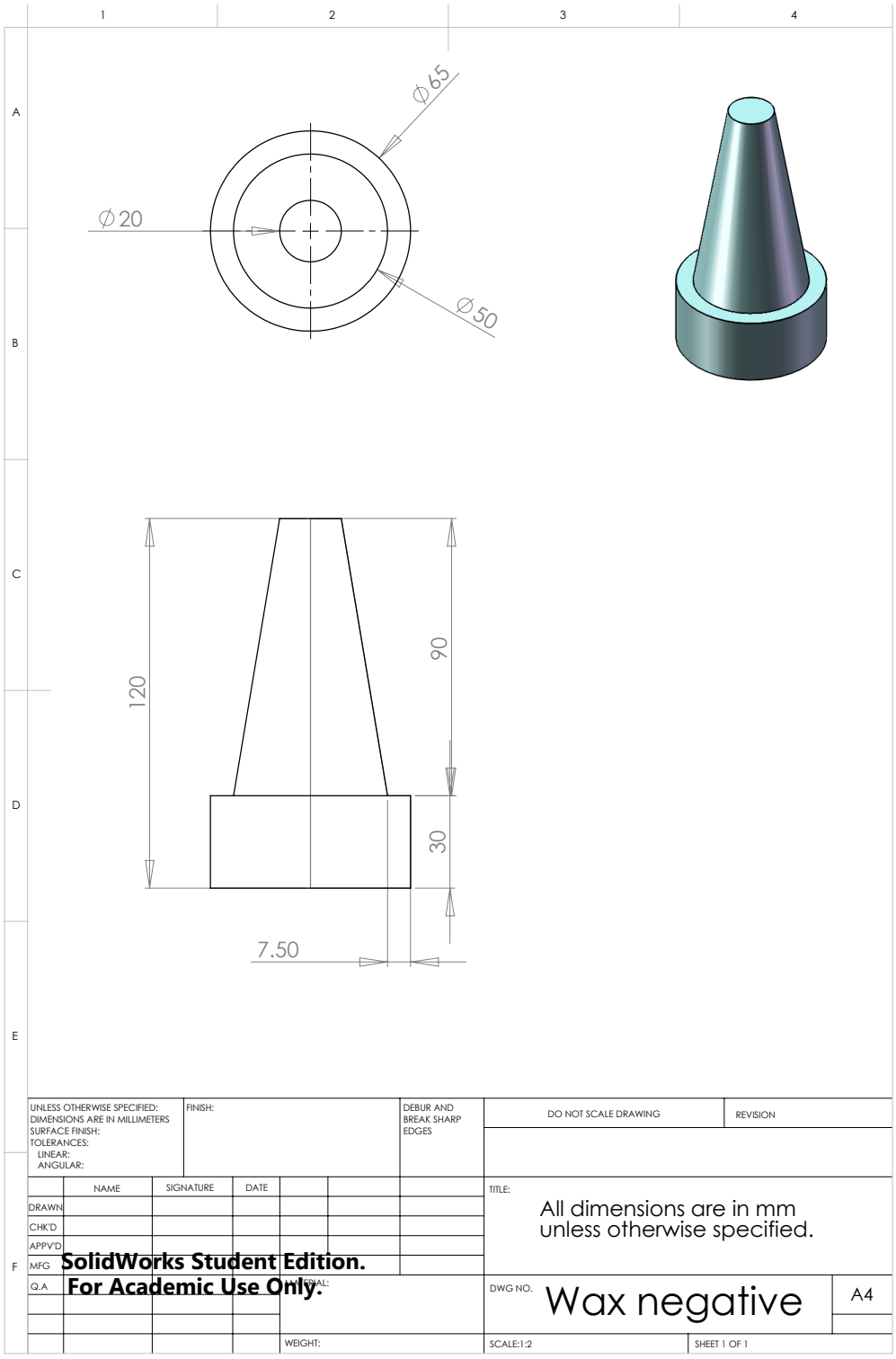

Figure A.2 Design drawing of the wax-negative used to make the casting mold of the ceramic nozzle.

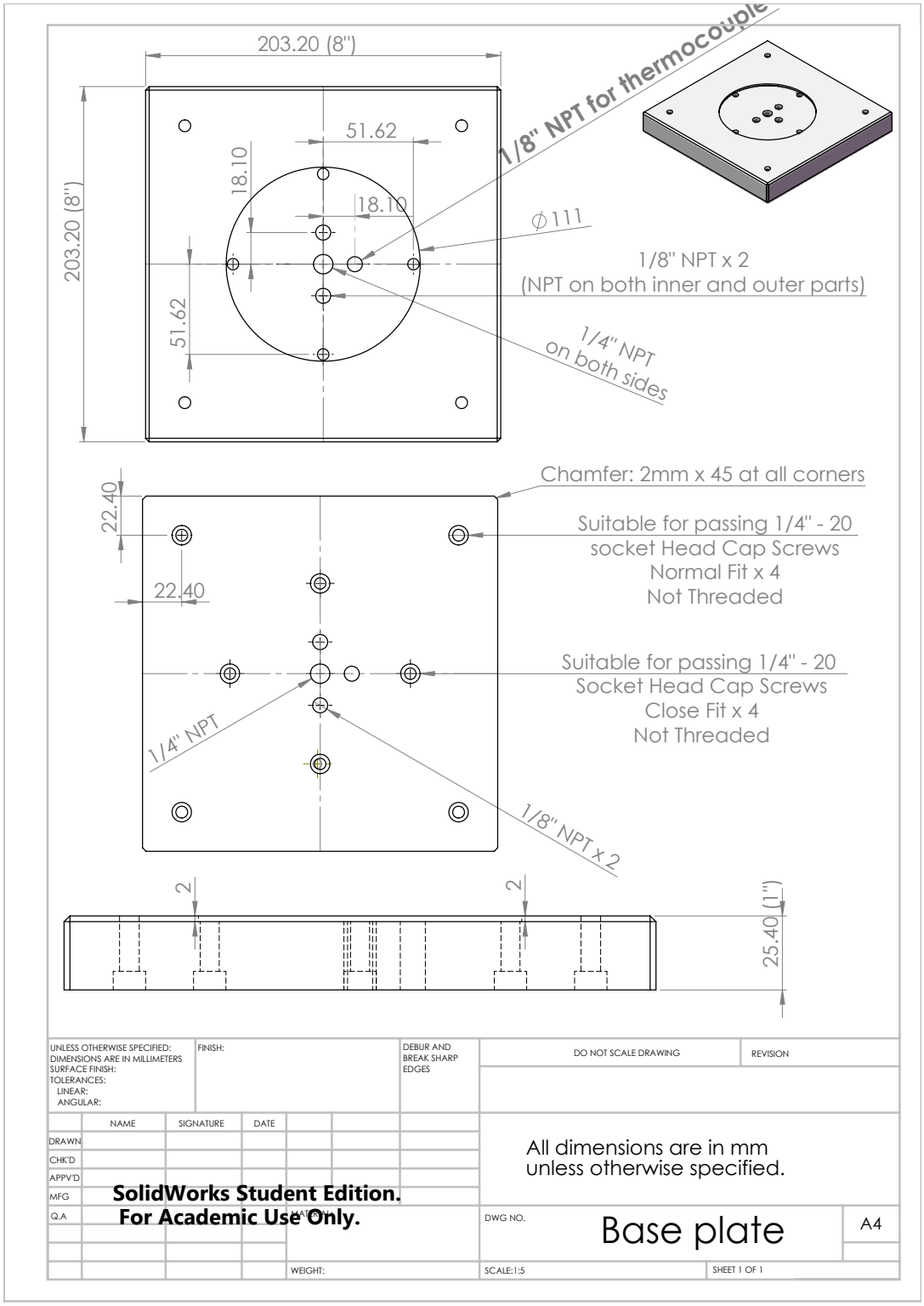

Figure A.3 Design drawing of the base plate of the ceramic burner.

A.2 Turbulence-generating plates design details

In HOTFR, high-blockage turbulence-generating plates are used to generate high-intensity turbulence in a confined system while preserving axisymmetric uniformity. The MCJ-TGP with 5 jets (Fig. 2.2), used in the experiments in Chapter 3, was previously designed and used in the turbulent premixed combustion research at the AFL [1, 2].

Multiple TGP designs were tested by Coppola and Gomez [3] in order to achieve higher turbulence intensity and better uniformity for the same bulk flow. Based on this study, a star-shaped turbulence-generating plate (S-TGP) was designed through this thesis. The design drawing of the S-TGP is illustrated in Fig. A.4. The S-TGP was used in the experiments in Chapters 4 and 5, and its performance in generating turbulence is illustrated in Sections 4.3.2 and 5.3.2.

A.3 Bottom nozzle design details

Various components of the bottom nozzle assembly in HOTFR (Fig. 2.1) are modified versions of the components designed by the AFL in 2011 and used in [1, 2]. Various components of the bottom nozzle assembly are illustrated in Fig. A.5. The interior contour of the nozzle contraction is defined by polynomials that minimize the formation of Taylor-Görtler vortices [4] in the concave portion of the profile, and minimize the angle-of-attack in the convex portion [5]. In general, the design is modified for compactness, easy assembly, convenience in gas delivery, and safety (e.g., multiple o-rings embedded in the modified design make the setup entirely leakproof). The base plate is modified to accommodate the outlet pipe of the atomizer (inner diameter of $d = 25.4\,\text{mm}$), and the co-flow plenum is modified to deliver more uniform co-flow.

Figures A.6−A.11 give the design drawings of various components of the bottom nozzle assembly.

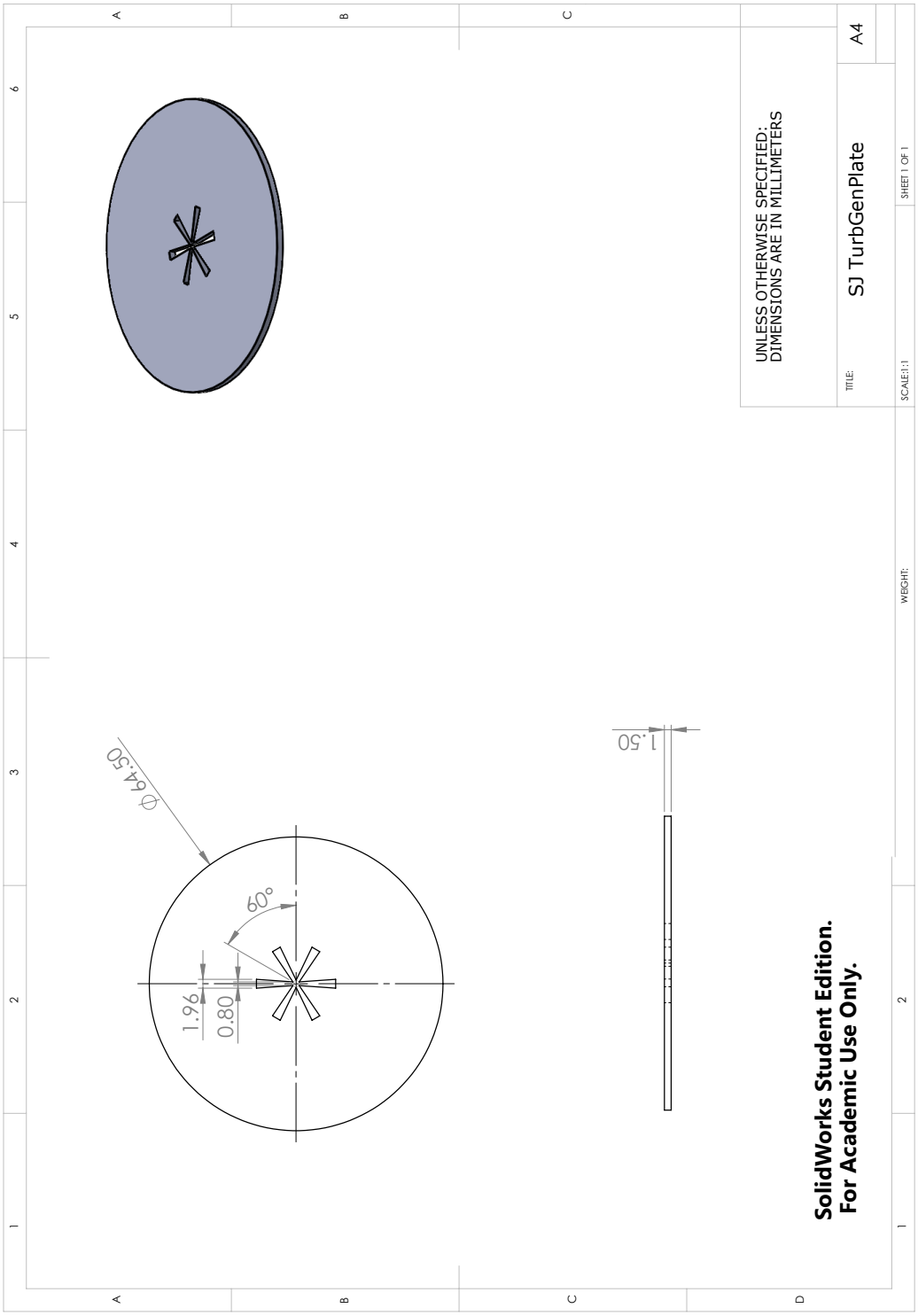

Figure A.4 Design drawing of S-TGP.

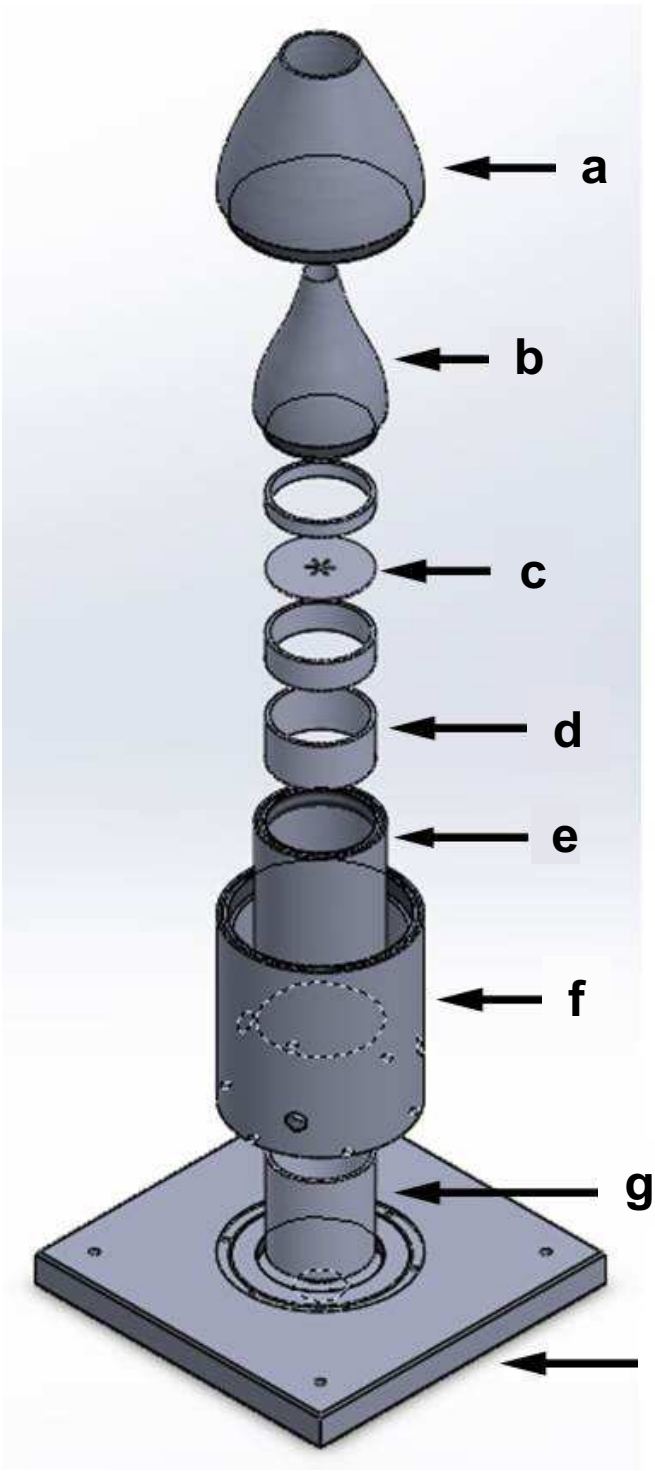

Figure A.5 Various components of the bottom nozzle assembly: (a) co-flow nozzle, (b) nozzle for premixed fuel and oxidizing-gas mixture, (c) S-TGP, (d) spacer, (e) plenum for premixed fuel and oxidizing-gas mixture, (f) co-flow plenum, (g) diffuser, and (h) base plate.

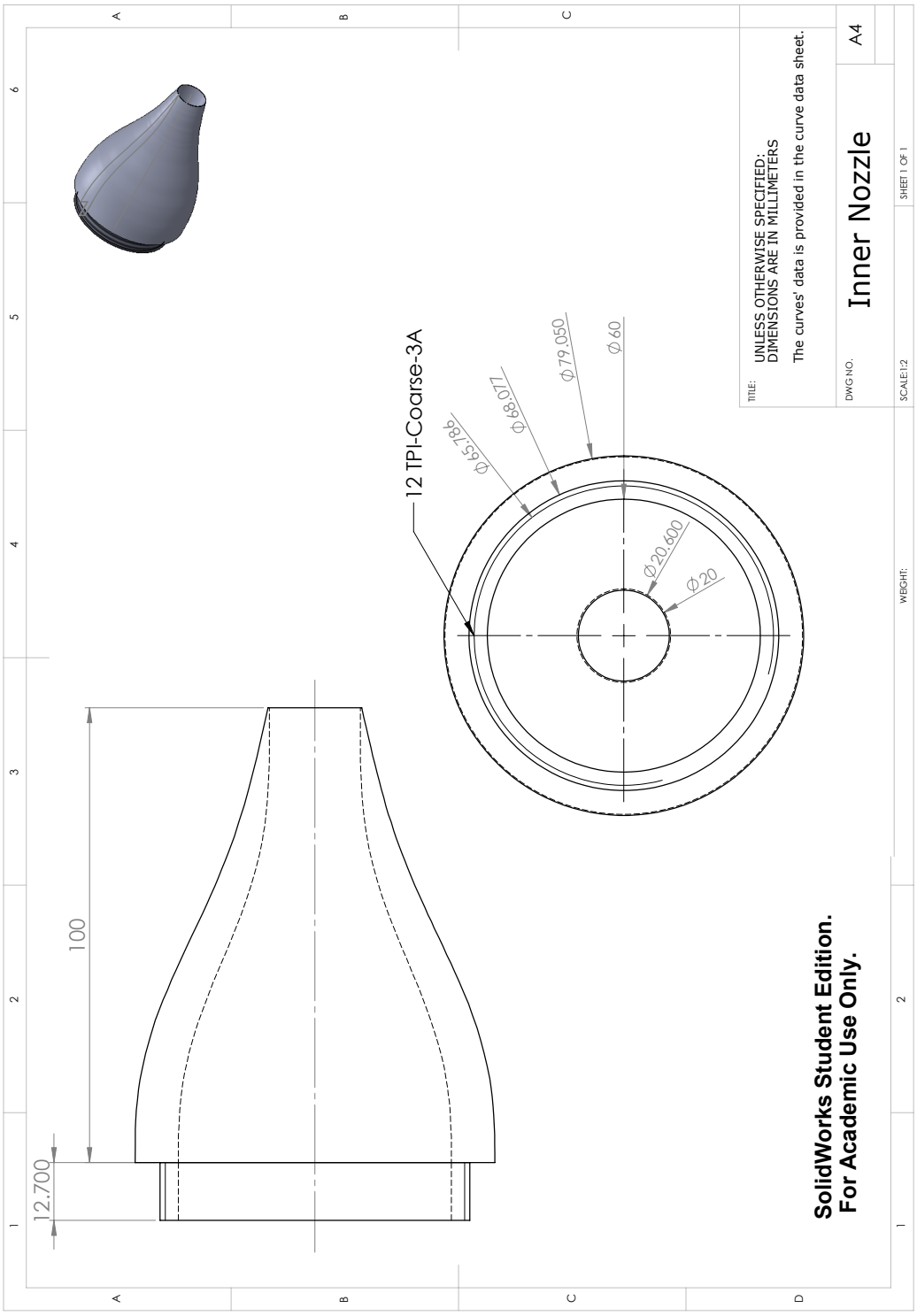

Figure A.6 Design drawing of the inner nozzle for premixed fuel and oxidizing-gas mixture.

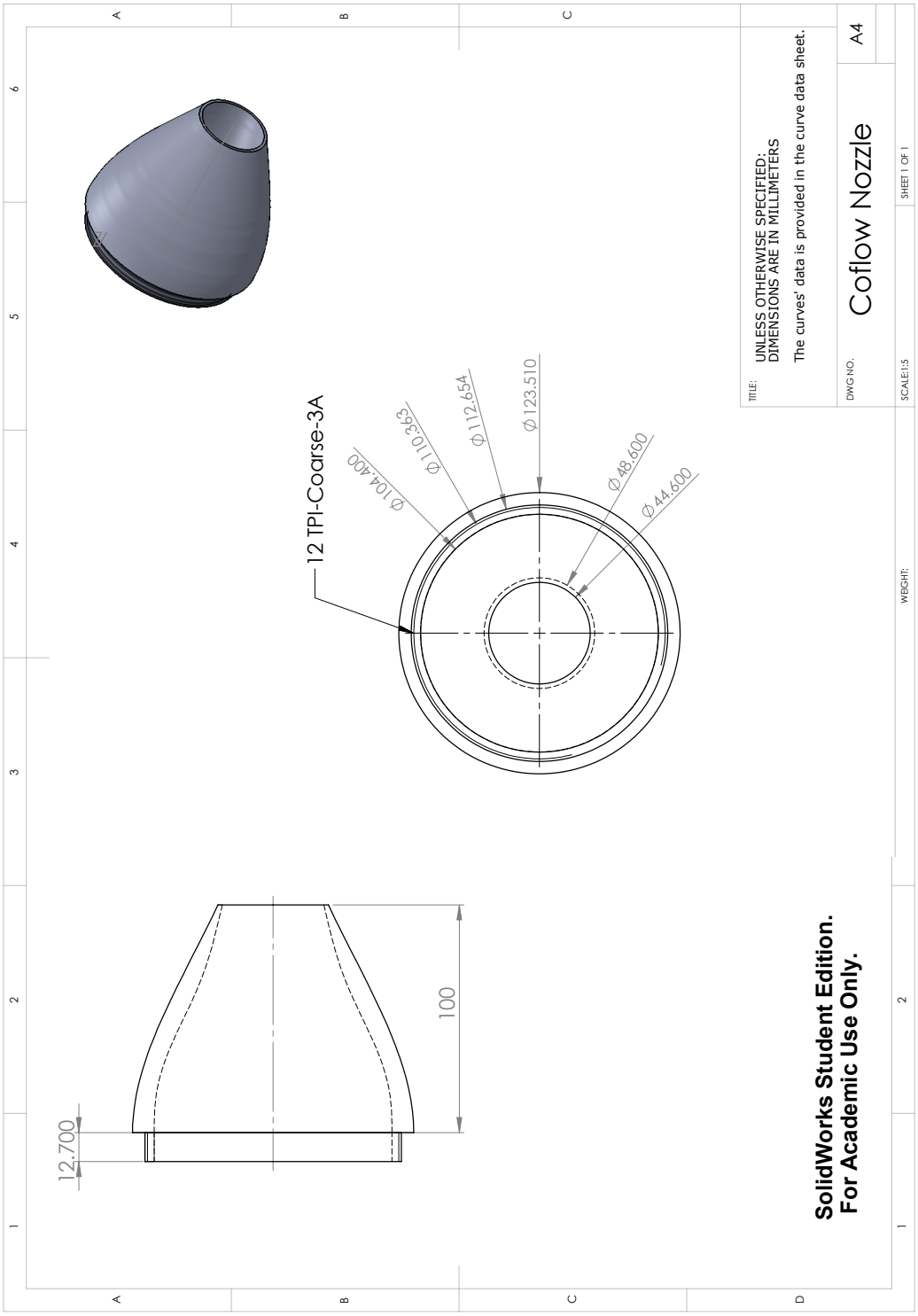

Figure A.7 Design drawing of the co-flow nozzle.

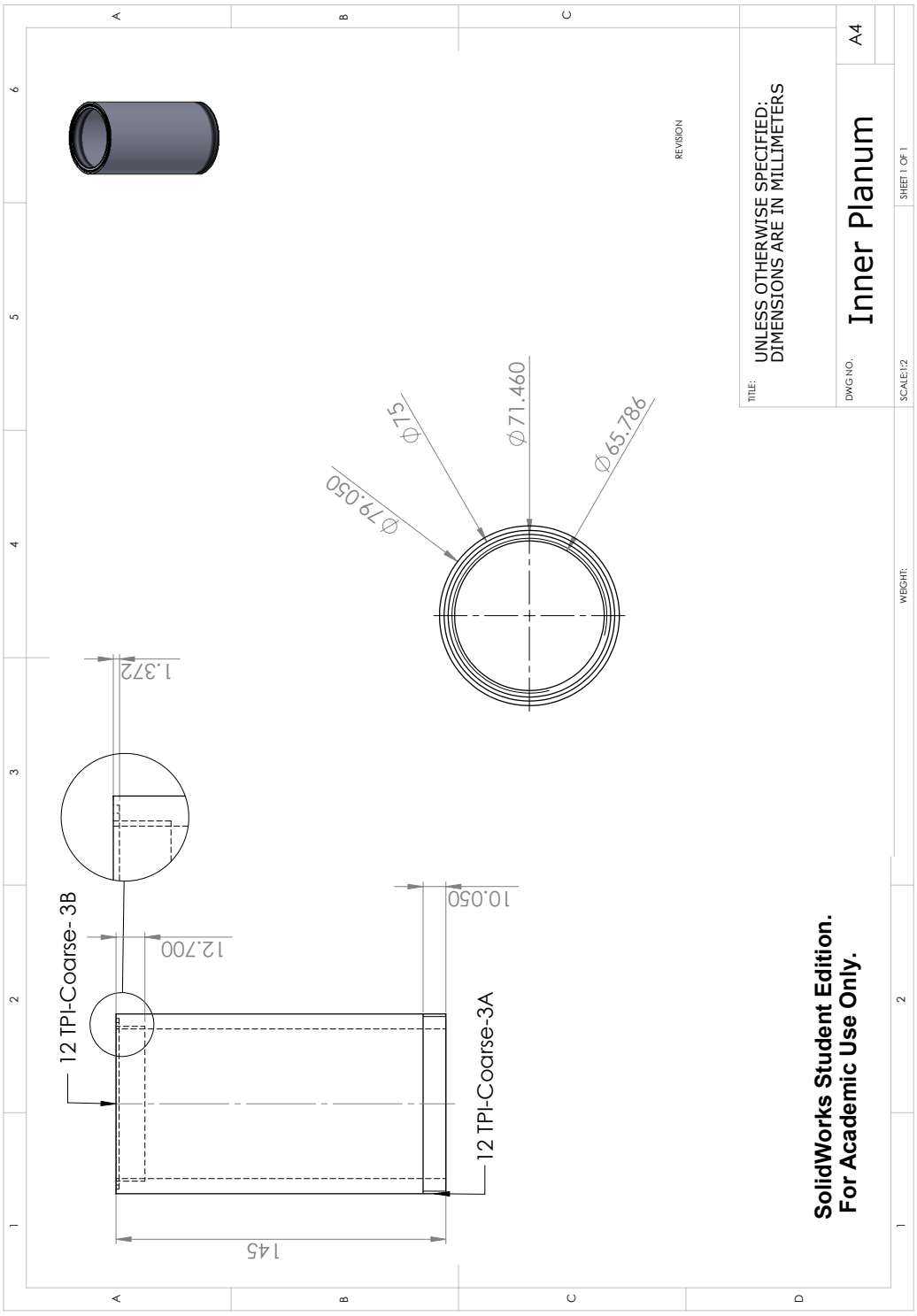

Figure A.8 Design drawing of the inner plenum for premixed fuel and oxidizing-gas mixture.

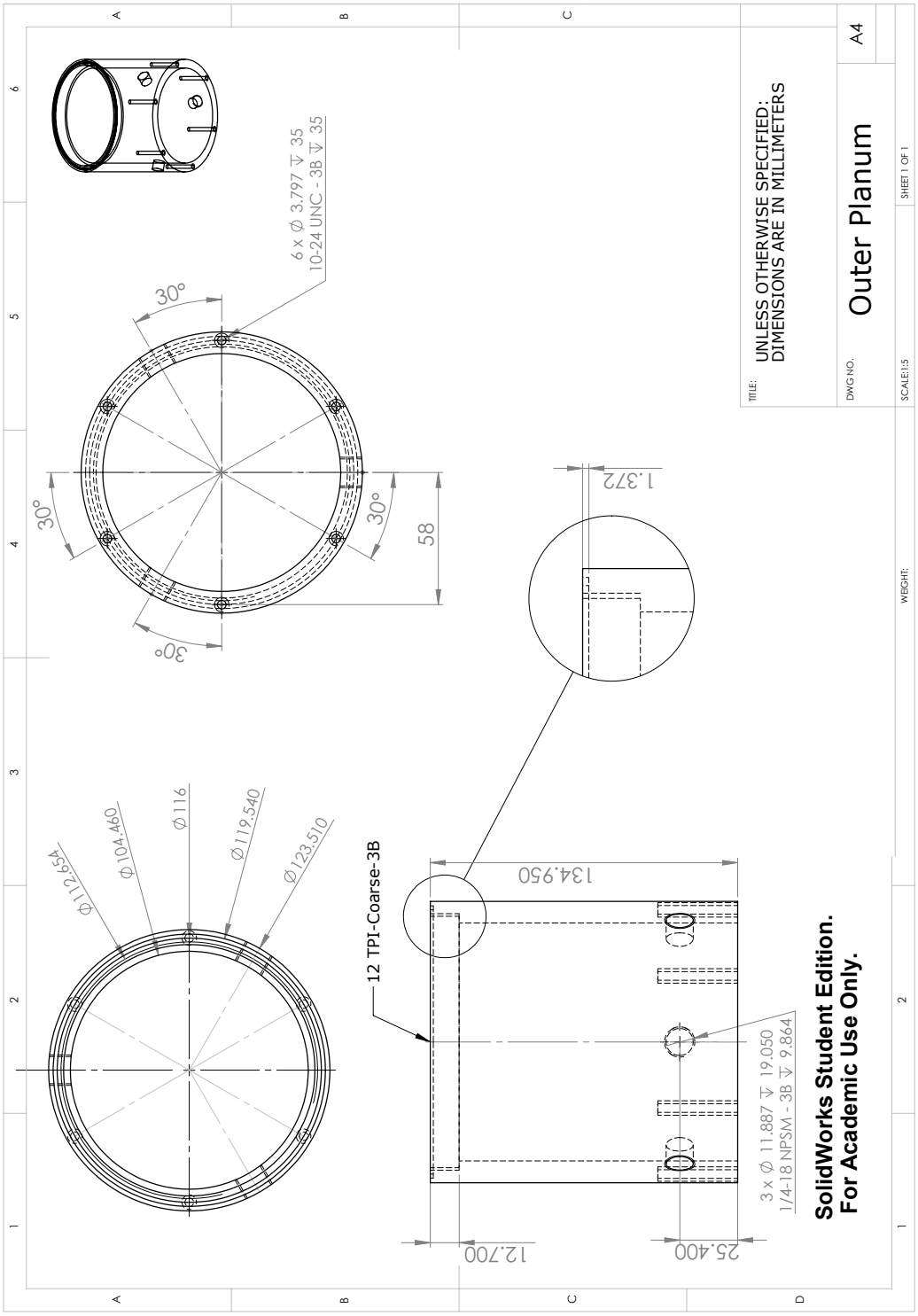

Figure A.9 Design drawing of the co-flow plenum.

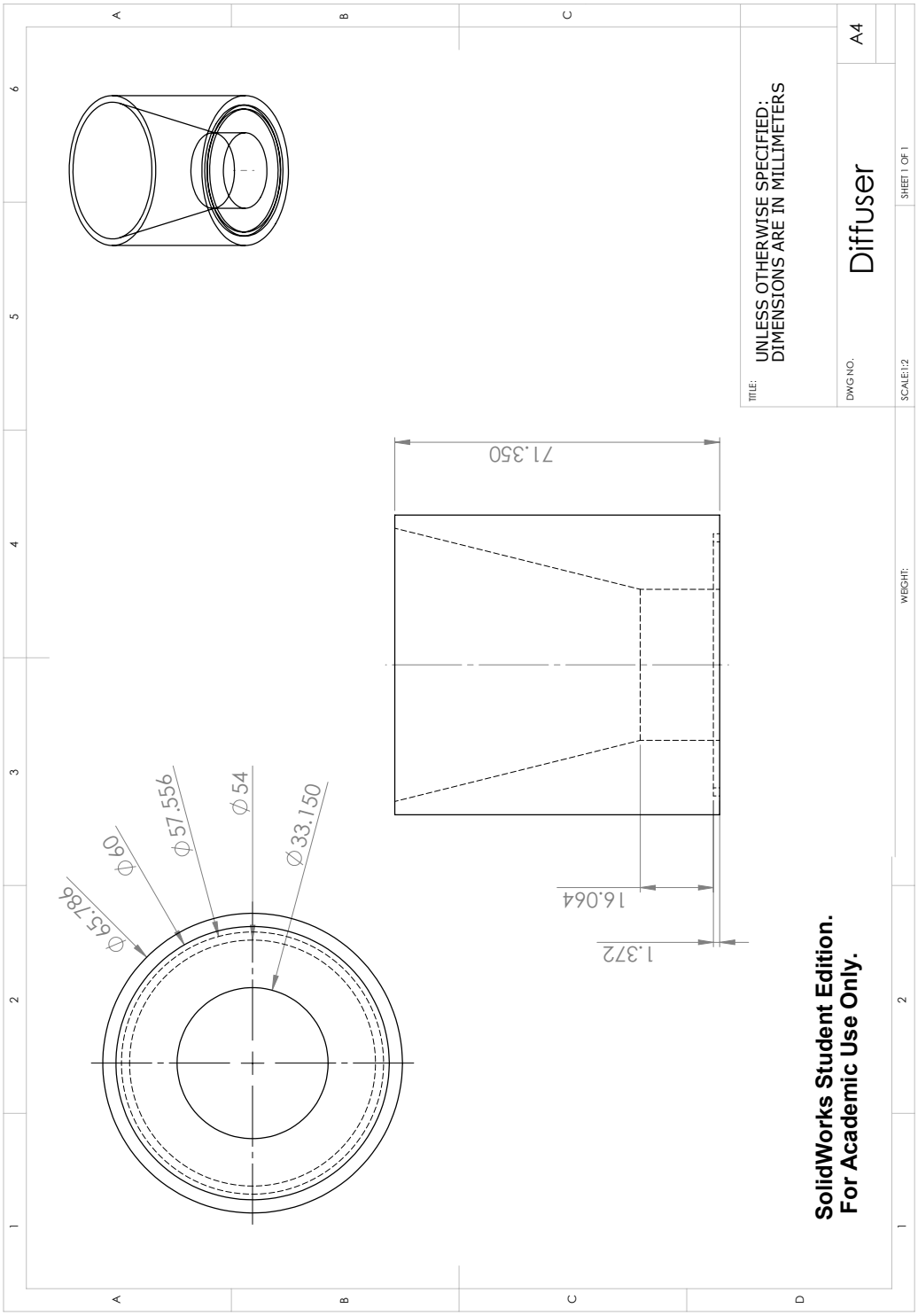

Figure A.10 Design drawing of the diffuser.

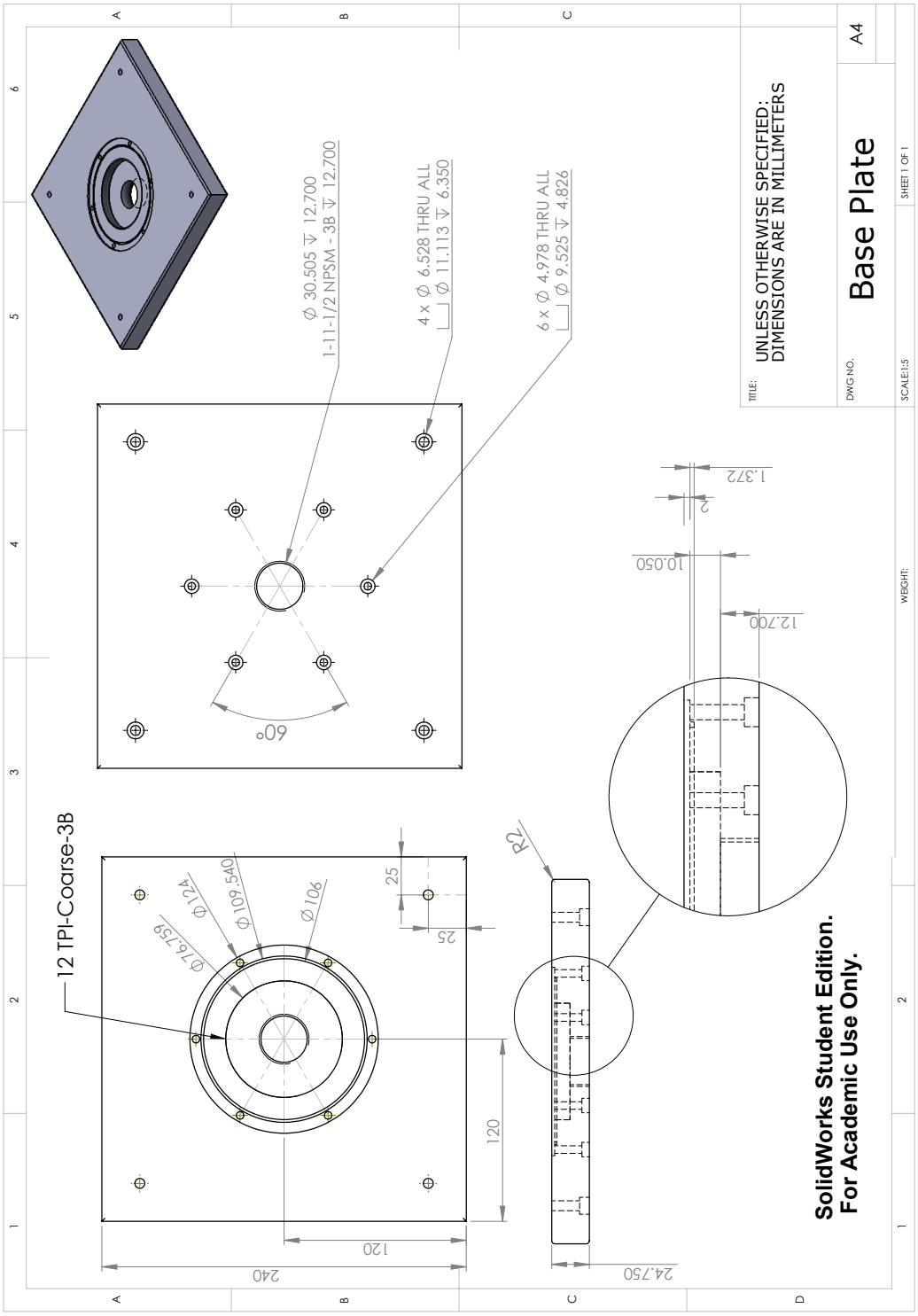

Figure A.11 Design drawing of the bottom nozzle base plate.

Appendix B

Temperature measurement of the hot exhaust gases at the ceramic burner exit

The temperature of the hot exhaust gases at the ceramic burner exit (T_{CB}) is measured using R-type thermocouples (platinum-13% rhodium alloy at the positive lead, and platinum at the negative lead) at 5 mm distance from the nozzle exit. Thermocouple readings are to be corrected for heat losses due to radiation, convection, and conduction, to prevent serious deviations from the actual value. Extrapolating the measured temperature to a zero diameter using different wire (bead) diameters is one possible methodology to do this correction, as theoretically, a thermocouple bead of a zero diameter would have no heat loss [6, 7]. In this study, three R-type thermocouples with three different wire (bead) diameters were used to measure T_{CB}: $d_{\mathrm{TC1}} = 51\,\mu$m, $d_{\mathrm{TC2}} = 127\,\mu$m, and $d_{\mathrm{TC3}} = 203\,\mu$m.

The thermocouple reading temperature (T_{TC}) can be expressed as [7–9]:

$$T_{\mathrm{TC}} = T_{\mathrm{CB}} + \gamma d_{\mathrm{TC}}^{q} \tag{B.1}$$

where d_{TC} is the lead wire or thermocouple bead diameter, q is a numerical constant, and γ is a numerical value, which is a function of the heat losses due to the radiation, convection, and conduction [10]. In order to calculate q, the thermocouple bead is estimated as a cylinder, and flow properties and mixture characteristics, such as the Reynolds number (Re), Prandtl number (Prtl), and mixture thermal conductivity (λ) are calculated in Cantera [11] for the flow at the nozzle exit. Convection heat transfer correlations [12] are used to calculate the Nusselt number (Nu) and the convection heat transfer coefficient. These calculations result in: $q = 0.6425$, and a linear extrapolation at $d = 0$ on T_{TC} vs d_{TC}^{n} plots is used to correct the temperature for heat losses, and estimate T_{CB}, as well as γ values.

The temperature profiles at the nozzle exit and the radial temperature distribution along the text section are illustrated in Fig. B.1. In HOTFR, the equivalence ratio of the CH_4-air flame and the

U_{CB} are adjusted within the operability (flashback and blowout) limits to balance the momentum and provide temperatures close to T_{ad} of the fuel and oxidizing gas mixture at the stagnation surface. It is illustrated in Fig. B.1 that, by increasing ϕ and U_{CB}, T_{CB} approaches T_{ad}. The radial temperature profiles are fairly constant within the test domain, and the repeatability in measuring T_{CB} is verified by multiple measurements to be $\approx 1\,\%$ of the reading.

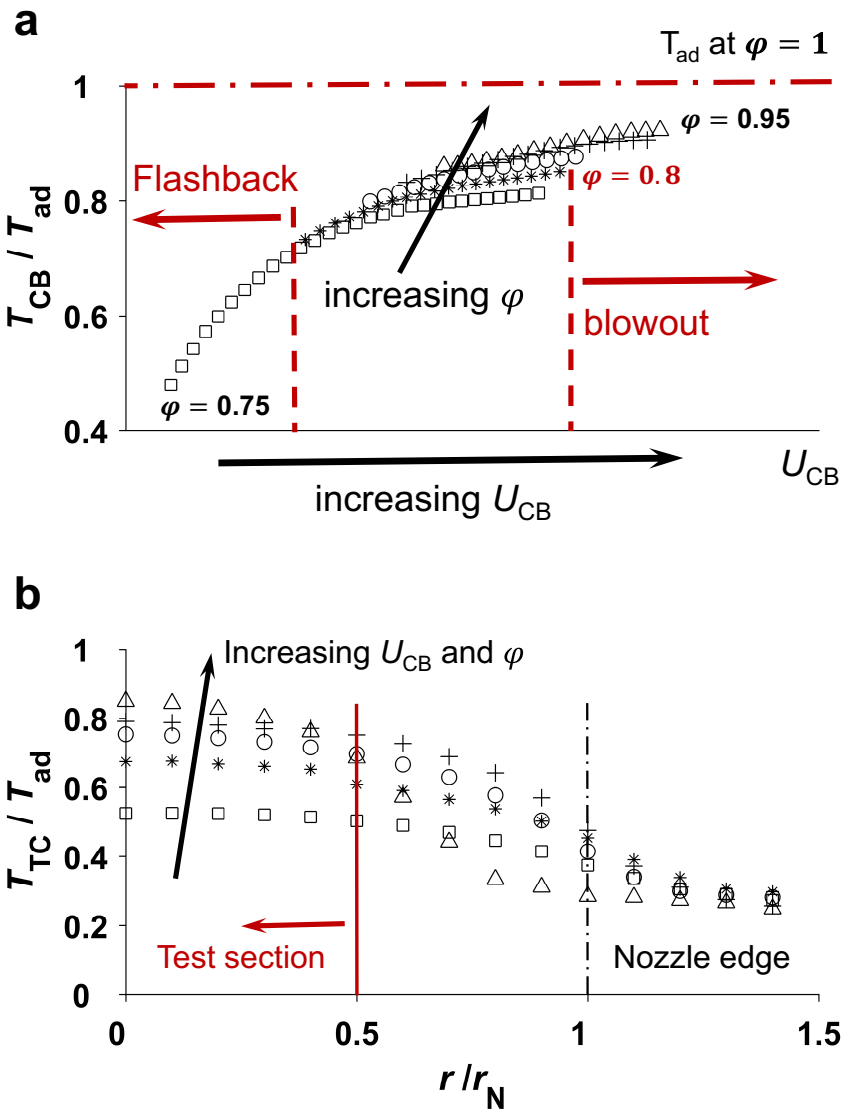

Figure B.1 T_{CB} profiles measured at 5 mm distance from the nozzle exit: (a) T_{CB} profiles at increasing U_{CB} and ϕ, highlighting flashback and blowout regions for a CH_4-air mixture at $\phi = 0.8$, (b) radial profiles of T_{TC} ($d_{\mathrm{TC3}} = 203\mu m$). Temperatures are normalized by T_{ad} of stoichiometric CH_4-air flame.

Appendix C

Uncertainty in particle image velocimetry (PIV)

In PIV, tracer particles are seeded into the flow, and a quantitative velocity field calculation is accomplished by measuring the spatial displacement of tracer particles over a fixed time interval. In PIV, it is assumed that the velocity of the tracer elements is equal to the flow velocity, however, the velocity-lag of these particles, due to particle inertia (relaxation time, or Stokes time) in the regions of high velocity gradients, and thermophoretic in the regions of high temperature gradients, introduces some uncertainties in the flow velocity measurement.

Newton's second law describes the equation of motion for a tracer element in a 1D flow, where the sum of the forces acting on the tracer particle (ΣF) is expressed as: $\Sigma F = m_{\mathrm{P}} a_{\mathrm{P}} = m_{\mathrm{P}} \left(\mathrm{d}u_{\mathrm{P}}/\mathrm{d}t\right)$, where m_{P} is the mass of a spherical particle, a_{P} is the particle acceleration, and u_{P} is the particle velocity. During PIV runs, various forces are effective on the tracer particles, such as the gravitational force, pressure-gradient force, Stokes-drag force, fluid-inertial force, unsteady-drag force, and thermophoretic force.

In these experiments, atomized oil droplets are used as seeding particles, which is a common seeding method in PIV. Oil density is considerably larger than the density of the bulk fuel-oxidizer-inert mixture carrying these atomized droplets; hence, the force terms containing the unburned-mixture density, such as pressure gradient, apparent mass, and unsteady drag can be neglected [13]. Furthermore, as shown in [14], the gravitational force has a small effect on micron-sized tracer particles in PIV experiments, and can also be neglected. Therefore, in order to estimate the PIV uncertainty in calculating the velocity vector field, the principal sources of uncertainty, in these turbulent experiments, are considered to be due to the particle inertia (relaxation time or Stokes time) and thermophoresis (F_{TP}) [15], with small contributions from the camera and laser sheet perpendicularity, and the calibration. In this study, measurements of the root-mean-square (rms) of the fluctuating component of the velocity (u' in the axial direction, and v' in the radial direction),

which describes the intensity of the turbulence, as well as the instantaneous local convective velocity upstream of the flame front (S_{u}), are desired. The convective velocity is measured upstream of the flame front, in the unburned-mixture region prior to the high temperature gradient zone of the flame, where the temperature is lower than the flash point of the oil ($T < 576\,\mathrm{K}$). Therefore, a good estimation would leave the resulting equation of motion for an oil droplet with the Stokes-drag force (F_{SD}) exerted on a particle, as thermophoretic force can also be neglected in analyzing the uncertainty of S_{u}, due to a low-temperature-gradient zone.

Considering the Stokes drag force in the low-Reynolds-number flow, the ratio of the tracer particle velocity to the unburned gas velocity is derived, with the details of the various terms available in [13–17]:

$$\frac{u_{\mathrm{P}}}{u_{\mathrm{g}}} = \frac{1}{1 + C_{\mathrm{KW}}\,\tau_{\mathrm{s}}\,\sigma_{\mathrm{u}}} \tag{C.1}$$

In this equation, C_{KW} is the Knudsen-Weber slip-correction factor [16, 17], τ_{s} is the relaxation time, or stokes time, and σ_{u} is the fluid velocity gradient. The stokes time (τ_{s}) is defined as: $\tau_{\mathrm{s}} = (\rho_{\mathrm{P}}\, d_{\mathrm{P}}^2) \,/\, (18\mu)$, where μ is the unburned gas viscosity, d_{P} is the oil droplet diameter ($\approx 1\,\mu$m), and ρ_{P} is the oil density. Furthermore, using the integral length scale (L) and u', as a relevant length scale, and a characteristic velocity scale, in these experiments, respectively, σ_{u} can be estimated as: $\sigma_{\mathrm{u}} = (\mathrm{d}u_{\mathrm{g}}/\mathrm{d}x) = (2\,u'/L)$. Experimental conditions and uncertainty details, caused by particle inertia, for turbulent combustion experiments in Chapters 3 and 5 are listed in Tables C.1 and C.2, respectively. It should be noted that these calculations are done at the nozzle exit. As listed in these tables, the uncertainty in the velocity measurements, caused by particle inertia in these experiments, is less than 0.5%.

Table C.1 Uncertainty details, caused by particle inertia, for PIV measurements in Chapter 3, at increasing $U/S_{\mathrm{L}}^{\mathrm{o}}$ and $u'/S_{\mathrm{L}}^{\mathrm{o}}$, at the nozzle exit: C_3H_8-air at $\phi = 0.7$ ($S_{\mathrm{L}}^{\mathrm{o}} = 0.197$ m/s), CH_4-air at $\phi = 0.6$ ($S_{\mathrm{L}}^{\mathrm{o}} = 0.115$ m/s), and H_2-air at $\phi = 0.19$ ($S_{\mathrm{L}}^{\mathrm{o}} = 0.875$ m/s).

	$U/S_{\mathrm{L}}^{\mathrm{o}}$	$u'/S_{\mathrm{L}}^{\mathrm{o}}$	$\tau_{\mathrm{s}}\,\sigma_{\mathrm{u}} \times 10^3$	C_{KW}	Uncertainty (%)
C_3H_8	4.6	1.4	0.74	1.15	0.09
	13.5	4.6	2.41	1.15	0.28
	21.1	6.5	3.40	1.15	0.39
	26.4	9.1	3.98	1.15	0.45
CH_4	8.8	2.5	0.64	1.15	0.07
	25.1	8.1	2.16	1.15	0.25
	35.8	11.2	3.17	1.15	0.36
	48.7	15.8	3.55	1.15	0.41
H_2	13.1	3.5	0.80	1.16	0.09
	32.2	10.9	2.25	1.16	0.26
	42.9	16.2	2.86	1.16	0.33
	63.4	19.8	3.88	1.16	0.45

Table C.2 Uncertainty details, caused by particle inertia, for PIV measurements in Chapter 5, at constant bulk-flow properties and constant $S_{\mathrm{L}}^{\mathrm{o}} = 0.115$ m/s, at the nozzle exit.

	Fuel (%) (Vol.)	O_2 balance diluent (%) (Vol.)	Diluent (%) (Vol.)	ϕ	T_{ad} (K)	$\mathrm{Le}_{\mathrm{eff}}$	$U/S_{\mathrm{L}}^{\mathrm{o}}$	$u'/S_{\mathrm{L}}^{\mathrm{o}}$	$\tau_{\mathrm{s}}\,\sigma_{\mathrm{u}} \times 10^3$	C_{KW}	Uncertainty (%)
High turbulence	C_3H_8	21	$60\,N_2 + 40\,He$	0.45	1513	3.08	41.3	10.5	2.32	1.18	0.27
	C_3H_8	21	N_2	0.56	1631	1.87	38.3	9.8	2.18	1.18	0.26
	C_3H_8	21	$60\,N_2 + 40\,CO_2$	0.79	1823	1.69	39.5	10.4	2.29	1.14	0.26
	$80\,C_3H_8 + 20\,H_2$	21	$60\,N_2 + 40\,CO_2$	0.77	1795	1.43	40.4	9.7	2.19	1.15	0.25
	$60\,C_3H_8 + 40\,H_2$	21	$60\,N_2 + 40\,CO_2$	0.75	1762	1.16	39.7	9.7	2.50	1.15	0.29
	$40\,C_3H_8 + 60\,H_2$	21	$60\,N_2 + 40\,CO_2$	0.71	1709	0.89	42.2	10.3	2.77	1.15	0.32
	$20\,C_3H_8 + 80\,H_2$	21	$60\,N_2 + 40\,CO_2$	0.63	1617	0.62	39.1	10.7	2.45	1.16	0.28
	$10\,C_3H_8 + 90\,H_2$	21	$60\,N_2 + 40\,CO_2$	0.57	1532	0.48	38.2	10.8	2.48	1.16	0.29
	CH_4	21	$60\,N_2 + 40\,He$	0.47	1542	1.60	39.5	11.1	1.19	2.29	0.27
	CH_4	21	N_2	0.60	1669	0.98	37.7	10.4	1.15	2.45	0.28
	CH_4	21	$60\,N_2 + 40\,CO_2$	0.88	1896	0.86	38.3	10.4	1.15	2.25	0.26
Low turbulence	C_3H_8	21	$60\,N_2 + 40\,CO_2$	0.79	1823	1.69	38.6	7.8	1.61	1.14	0.18
	$50\,C_3H_8 + 50\,H_2$	21	$60\,N_2 + 40\,CO_2$	0.73	1740	1.02	42.6	6.3	1.66	1.15	0.19
	$20\,C_3H_8 + 80\,H_2$	21	$60\,N_2 + 40\,CO_2$	0.63	1617	0.62	41.1	6.0	1.44	1.16	0.17
	H_2	21	$60\,N_2 + 40\,CO_2$	0.48	1440	0.35	37.6	7.8	1.67	1.17	0.20

Furthermore, in quantifying the velocity field using PIV, some uncertainties originate from the processing algorithm, and correlation statistics of the PIV software. In order to estimate this uncertainty, it is assumed that the velocity of a laminar flame, in the cold region close to the nozzle exit, must remain constant throughout the experiment, at a constant mass flow rate. In each laminar flame experiment, 1000 PIV images are taken in 100 ms. In Fig. C.1 (a), the mean axial velocity ($\overline{U}$) for the CH_4-air flame (see Table 5.1) is plotted in the axial direction (z) from the nozzle exit up to 5 mm above the nozzle exit at the nozzle centerline. Furthermore, in Fig. C.1 (b), $\overline{U}$ is plotted in the radial direction at 1 mm above the nozzle exit. The rms of the fluctuating component of the velocity in the axial direction ($\pm u'$) is shown at each PIV grid on the $\overline{U}$ profiles in both axial and radial velocity profiles shown in Fig. C.1. The average of the normalized fluctuations $\langle(u'/\overline{U})\rangle$ in the axial (Fig. C.1 (a)) and the radial (Fig. C.1 (b)) profiles are approximately 0.0142 and 0.005, respectively. These calculations estimate the uncertainty in the PIV software for quantifying the velocity field as $\approx 1.42\,\%$ and $\approx 0.5\,\%$ for the axial and the radial velocity profiles, respectively.

In this study, the total uncertainty in the PIV velocity measurements is estimated as the combination of the two sources of uncertainties discussed in this Appendix. Considering the uncertainty of the axial velocity profiles estimated above, the total PIV uncertainty is estimated as $\pm 1.51\,\%$.

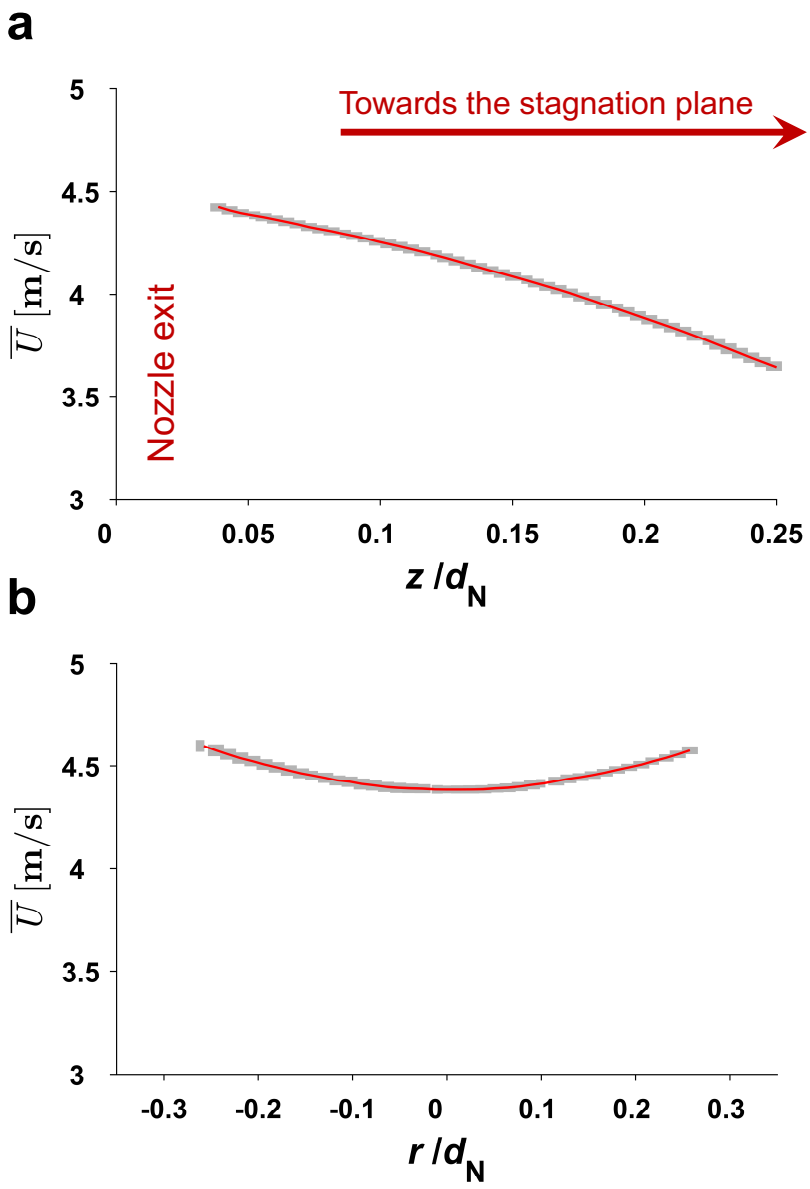

Figure C.1 Sample uncertainty calculations, caused by the correlation statistics in the PIV software, showing $\overline{U}$ (solid line), and $\pm u'$ (shadow around the solid line): (a) in the axial direction in the cold region close to the nozzle exit, and (b) in the radial direction at 1 mm above the nozzle exit.

Appendix D

Uncertainty in flame-front tracking

The PIV resolution in capturing the flame front introduces some uncertainty in instantaneous flame-front location measurements using flame-surface tracking methods used in this study. The main sources of this uncertainty in localizing the flame front are: the mean tracer particle distance in the test domain (l_{p}), oil droplet lifetime at the flame front (droplet evaporation time) (τ_{evap}), uncertainties imposed by filtering processes during post-processing procedure (l_{Filt}), over-saturation of pixels caused by intense illumination from larger oil droplets in the PIV images (l_{I}). In order to compute the seeding density and the mean distance between tracer particles, l_{p} is calculated by comparing the saturated and original PIV images and averaging over $1000-2000$ PIV images. The distance traveled by the flame front, as it sweeps over the oil droplets during τ_{evap}, is defined as the evaporation distance (l_{evap}). τ_{evap} is calculated as: $\tau_{\mathrm{evap}} = d_{\mathrm{p}}^2/E$, where d_{p} is the largest oil droplet diameter ($d_{\mathrm{p}} \approx 2\mu$m), and E is the evaporation constant:

$$E = \frac{8\lambda}{\rho c_{\mathrm{p}}} \ln\left(1 + \frac{c_{\mathrm{p}}(T_\infty - T_{\mathrm{s}})}{h_{\mathrm{fg}}}\right) \tag{D.1}$$

where λ is the thermal conductivity of the blend of oil and reactants mixture, ρ_{l} and c_{p} are the density and heat capacity of the oil at room temperature, respectively, T_∞ is the domain temperature estimated as: $T_\infty = (T_{\mathrm{ad}} + T_{\mathrm{room}})/2$, T_{s} is the flash point temperature of the canola oil (576 K), and h_{fg} is the specific enthalpy of vaporization of the canola oil estimated as h_{fg} of octadecanoic acid, which is the main composition of the canola oil. Therefore, $l_{\mathrm{evap}} = \tau_{\mathrm{evap}} \times S_{\mathrm{F}_{\mathrm{max}}}$, where $S_{\mathrm{F}_{\mathrm{max}}}$ is extracted from the PDFs of S_{F}, as explained in Chapter 2. Some uncertainties are also imposed by the different filters used to enhance the intensity images, the main source being a Median filter, which has a size of 5×5 pixels; hence, introducing $l_{\mathrm{Filt}} \approx 2.5$ pixels of uncertainty in estimating the flame-front location. Furthermore, over-saturation of pixels, caused by intense illumination from larger oil droplets, occupies ≈ 2 pixels in PIV images ($l_{\mathrm{I}} \approx 2$ pixels). The detailed results of the uncertainty calculations in flame-front tracking, at increasing $U/S_{\mathrm{L}}^{\mathrm{o}}$ and $u'/S_{\mathrm{L}}^{\mathrm{o}}$ (experiments reported in Chapter 3), are listed in Table D.1. The total uncertainty is obtained by quadrature:

Table D.1 Various sources of uncertainty in flame-front tracking at increasing $U/S_{\mathrm{L}}^{\mathrm{o}}$ and $u'/S_{\mathrm{L}}^{\mathrm{o}}$: C_3H_8-air at $\phi = 0.7$ ($S_{\mathrm{L}}^{\mathrm{o}} = 0.197$ m/s), CH_4-air at $\phi = 0.6$ ($S_{\mathrm{L}}^{\mathrm{o}} = 0.115$ m/s), and H_2-air at $\phi = 0.19$ ($S_{\mathrm{L}}^{\mathrm{o}} = 0.875$ m/s). Uncertainty values are normalized by the related diffusive laminar flame thickness (δ_{L}).

	$U/S_{\mathrm{L}}^{\mathrm{o}}$	$u'/S_{\mathrm{L}}^{\mathrm{o}}$	$l_{\mathrm{p}}/\delta_{\mathrm{L}}$	$l_{\mathrm{evap}}/\delta_{\mathrm{L}}$	$l_{\mathrm{Filt}}/\delta_{\mathrm{L}}$	$l_{\mathrm{I}}/\delta_{\mathrm{L}}$	$l_{\mathrm{Total}}/\delta_{\mathrm{L}}$
C_3H_8	4.6	1.4	0.887	0.009	0.330	0.264	0.983
	13.5	4.6	0.367	0.028	0.330	0.264	0.560
	21.1	6.5	0.415	0.045	0.330	0.264	0.594
	26.4	9.1	0.245	0.058	0.330	0.264	0.492
CH_4	8.8	2.5	0.556	0.006	0.188	0.150	0.606
	25.1	8.1	0.261	0.024	0.188	0.150	0.356
	35.8	11.2	0.301	0.033	0.188	0.150	0.387
	48.7	15.8	0.156	0.042	0.188	0.150	0.290
H_2	13.1	3.5	0.487	0.054	0.158	0.126	0.530
	32.2	10.9	0.249	0.207	0.158	0.126	0.382
	42.9	16.2	0.305	0.316	0.158	0.126	0.483
	63.4	19.8	0.187	0.384	0.158	0.126	0.473

$l_{\mathrm{Total}} = \sqrt{l_{\mathrm{p}}^2 + l_{\mathrm{evap}}^2 + l_{\mathrm{Filt}}^2 + l_{\mathrm{I}}^2}$. As listed in Table D.1, the total uncertainty in flame-front tracking, for experiments reported in Chapter 3, is within the range of $0.290 \leq (l_{\mathrm{Total}}/\delta_{\mathrm{L}}) \leq 0.983$. In Chapters 4 and 5, the experimental conditions are close to the highest turbulence intensity case reported in Chapter 3. Therefore, the total uncertainty in flame-front tracking is estimated as $(l_{\mathrm{Total}}/\delta_{\mathrm{L}}) \lesssim 0.5$, in these experiments.

Appendix E

The effects of deviations from adiabatic conditions at the stagnation surface on flame speed

In the counter-flow apparatus used in this study (HOTFR), a set of laminar flame experiments is used to estimate the effects of the stagnation surface temperature on the stretched laminar flame speed ($S_{\mathrm{u-ref}}$). The temperature of the stagnation surface is estimated by the temperature of the hot exhaust gases (T_{CB}), which is measured at 5 mm distance from the ceramic nozzle exit. While the temperature of the hot exhaust gases was kept constant at $T_{\mathrm{CB}} = 1786\,\mathrm{K}$ in all experiments reported in the article, using a methane-air (CH_4-air) flame at equivalence ratio (ϕ) of 0.7, the adiabatic flame temperature (T_{ad}) of the studied combustible mixtures varied in the range of $1440\,\mathrm{K} \leq T_{\mathrm{ad}} \leq 1896\,\mathrm{K}$.

In order to assess the effects of deviations from adiabatic conditions at the stagnation surface on $S_{\mathrm{u-ref}}$, a new set of laminar flame experiments were performed. This new set of experiments includes various flames with distinct effective Lewis number ($\mathrm{Le_{eff}}$) and T_{ad}, such as the propane flame diluted with helium (C_3H_8+He) at $\mathrm{Le_{eff}} = 3.08$ ($\phi = 0.45$ and $T_{\mathrm{ad}} = 1513$ K), propane flame diluted with carbon dioxide (C_3H_8+CO_2) at $\mathrm{Le_{eff}} = 1.69$ ($\phi = 0.79$ and $T_{\mathrm{ad}} = 1823$ K), hydrogen-enriched (90 % by volume) propane flame diluted with carbon dioxide ($10C_3H_8$+$90H_2$+CO_2) at $\mathrm{Le_{eff}} = 0.48$ ($\phi = 0.57$ and $T_{\mathrm{ad}} = 1532$ K), and methane flame in air (CH_4-air) at $\mathrm{Le_{eff}} = 0.97$ ($\phi = 0.76$ and $T_{\mathrm{ad}} = 1939$ K), stabilized against hot exhaust gases at various stagnation surface temperatures between $1786\,\mathrm{K} \leq T_{\mathrm{CB}} \leq 2012\,\mathrm{K}$. In these experiments, T_{CB} was controlled by the equivalence ratio of the CH_4-air flame at the top nozzle. Please refer to Table 5.1 for other details of the combustible mixtures.

The effects of stagnation surface temperature on $S_{\mathrm{u-ref}}$ measurements are illustrated in Fig. E.1 (a), where the laminar flame velocity is normalized by $S_{\mathrm{u-ref}}$ at $T_{\mathrm{CB}} = 1786\,\mathrm{K}$, and is plotted against

the difference between the adiabatic flame temperature of a specific flame and the temperature of the stagnation surface, $T_{\mathrm{CB}} - T_{\mathrm{ad}}$, normalized by T_{ad}. The vertical and the horizontal lines show the adiabatic stagnation surface, where $T_{\mathrm{CB}} \approx T_{\mathrm{ad}}$, and the experiments at $T_{\mathrm{CB}} = 1786\,\mathrm{K}$, respectively. From the data reported in Fig. E.1 (a), it can be estimated that the deviations from adiabatic conditions at the stagnation surface cause an average variation in $S_{\mathrm{u-ref}}$ measurements of approximately $0.164\,S_{\mathrm{L}}^{\mathrm{o}}$ per 100 K temperature difference between T_{CB} and T_{ad}.

Figure E.1 (b) shows the difference between the measured $S_{\mathrm{u-ref}}$ at constant $T_{\mathrm{CB}} = 1786\,\mathrm{K}$, and the estimated $S_{\mathrm{u-ref}}$ values if they would have been measured under adiabatic conditions at the stagnation surface, i.e., $T_{\mathrm{CB}} \approx T_{\mathrm{ad}}$ of the given flame, for H_2-enriched C_3H_8+CO_2 flames. This difference in $S_{\mathrm{u-ref}}$ values, $|\Delta_{\langle S_{\mathrm{u-ref}}\rangle}|$, is an estimation of the effect of using a constant T_{CB}, rather than varying T_{CB} to match the T_{ad} of a given mixture at each experiment. In these flames, T_{ad} reduces from 1823 K to 1440 K by reducing ϕ at constant $S_{\mathrm{L}}^{\mathrm{o}}$. $|\Delta_{\langle S_{\mathrm{u-ref}}\rangle}|$ is calculated as:

$$|\Delta_{\langle S_{\mathrm{u-ref}}\rangle}| = |\langle S_{\mathrm{u-ref}}\rangle_{T_{\mathrm{CB}}=1786\,K} - \langle S_{\mathrm{u-ref}}\rangle_{\mathrm{ad}}| \tag{E.1}$$

Figure E.1 (b) illustrates that deviations from the adiabatic stagnation surface cause variations in $S_{\mathrm{u-ref}}$ values of $(|\Delta_{\langle S_{\mathrm{u-ref}}\rangle}|/S_{\mathrm{L}}^{\mathrm{o}}) < 0.6$. These estimated variations are much smaller than the increase in $S_{\mathrm{u-ref}}$ with increasing H_2 enrichment caused by the effects of differential diffusion, illustrated in this study.

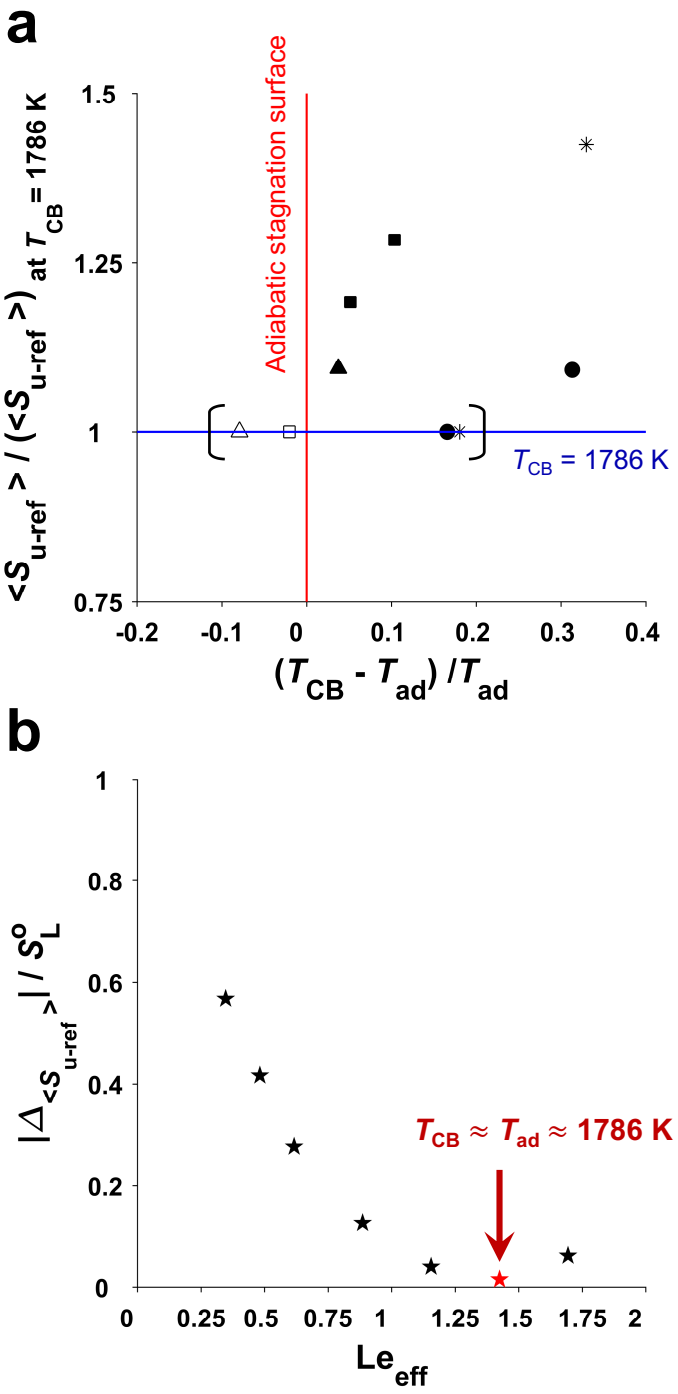

Figure E.1 (a) The effects of deviations from adiabatic stagnation surface on $S_{\mathrm{u-ref}}$ of flames at various $\mathrm{Le_{eff}}$: C_3H_8+He (star), C_3H_8+CO_2 (square), $10C_3H_8$+$90H_2$+CO_2 (circle), and CH_4-air at $\phi = 0.76$ (triangle). (b) The difference between the measured $S_{\mathrm{u-ref}}$ at $T_{\mathrm{CB}} = 1786\,\mathrm{K}$, and the estimated $S_{\mathrm{u-ref}}$ values at $T_{\mathrm{CB}} \approx T_{\mathrm{ad}}$ of the given flame, during H_2 enrichment of C_3H_8+CO_2 flames.

References

[1] S.D. Salusbury and J.M. Bergthorson. “Maximum stretched flame speeds of laminar premixed counter-flow flames at variable Lewis number”. In: *Combustion and Flame* 162 (2015), pp. 3324–3332.

[2] S.D. Salusbury, E. Abbasi-Atibeh, and J.M. Bergthorson. “The effect of Lewis number on instantaneous flamelet speed and position statistics in counter-flow flames with increasing turbulence”. In: *Proceedings of the ASME Turbo Expo: Turbine Technical Conference and Exposition. GT2017-64821* (2017).

[3] G. Coppola and A. Gomez. “Experimental investigation on a turbulence generation system with high-blockage plates”. In: *Experimental Thermal and Fluid Science* 33 (2009), pp. 1037–1048.

[4] H.W. Liepmann. *Investigations on laminar boundary-layer stability and transition on curved boundaries*. Tech. rep. NACA Wartime Report W-107. ACR No. 3H30. 1943.

[5] J.M. Bergthorson. *Experiments and modeling of impinging jets and premixed hydrocarbon stagnation flames*. PhD thesis, California Institute of Technology, 2005.

[6] V. Hindasageri, R.P. Vedula, and S.V. Prabhu. “Thermocouple error correction for measuring the flame temperature with determination of emissivity and heat transfer coefficient”. In: *Review of Scientific Instruments* 84 (2013), p. 024902.

[7] G.E. Glawe, R. Holanda, and L.N. Krause. *Recovery and radiation corrections and time constants of several sizes of shielded and unshielded thermocouple probes for measuring gas temperature*. Tech. rep. NASA: NASA-TP-1099, E-9289. 1978.

[8] G.E. Glawe, F.S. Simmons, and T.M. Stickney. *Radiation and recovery corrections and time constants of several chromel-alumel thermocouple probes in high-temperature, high-velocity gas streams*. Tech. rep. NASA: NACA-TN-3766. 1956.

[9] D. Bradley and K.J. Matthews. “Measurement of high gas temperatures with fine wire thermocouples”. In: *Journal of Mechanical Engineering Science* 10 (1968), pp. 299–305.

[10] P. Siewert. *Flame front characteristics of turbulent lean premixed methane/air flames at high-pressure*. PhD thesis, Swiss Federal Institute of Technology, Zurich, 2006.

[11] D.G. Goodwin, H.K. Moffat, and R.L. Speth. *Cantera: A software toolkit for chemical kinetics, thermodynamics, and transport processes*. Version 2.2.1, http://www.cantera.org, 2016.

[12] T.L. Bergman and F.P. Incropera. *Fundamentals of heat and mass transfer*. John Wiley & Sons, Hoboken, New Jersey, USA, 2011.

[13] C.J. Sung, C.K. Law, and R. L Axelbaum. "Thermophoretic effects on seeding particles in LDV measurements of flames". In: *Combustion Science and Technology* 99 (1994), pp. 119–132.

[14] F.N. Egolfopoulos and C.S. Campbell. "Dynamics and structure of dusty reacting flows: inert particles in strained, laminar, premixed flames". In: *Combustion and Flame* 117 (1999), pp. 206–226.

[15] J.M. Bergthorson and P.E. Dimotakis. "Particle velocimetry in high-gradient/high-curvature flows". In: *Experiments in Fluids* 41 (2006), pp. 255–263.

[16] M.D. Allen and O.G. Raabe. "Slip correction measurements of spherical solid aerosol particles in an improved Millikan apparatus". In: *Aerosol Science and Technology* 4 (1985), pp. 269–286.

[17] L. Talbot. "Thermophoresis-A review". In: *Progress in Astronautics and Aeronautics* 74 (1981), pp. 467–488.